Advances in Civil Engineering

Sensitivity Analysis of Stability and Deformation of Underground Structures 2021

Lead Guest Editor: Bingxiang Yuan
Guest Editors: Jingjing Meng, Yonghong Wang, S. P. Pradhan, and Zhijun Xu

Sensitivity Analysis of Stability and Deformation of Underground Structures 2021

Advances in Civil Engineering

Sensitivity Analysis of Stability and Deformation of Underground Structures 2021

Lead Guest Editor: Bingxiang Yuan
Guest Editors: Jingjing Meng, Yonghong Wang, S. P. Pradhan, and Zhijun Xu

Contents

Development Assessment of the Coal Industry of China Based on the Minimum Deviation Comprehensive Weight Evaluation Model
Shihua Ren, Dezhi Zheng, Yang Qu, Rongjun Qin, Xiaomiao Jiao, and Jinyan Bai
Research Article (11 pages), Article ID 5248324, Volume 2021 (2021)

Comparisons of Two Approaches for Geotechnical Model Calibration with Scarce Data
Yuanxin Lei, Huifen Liu, and Zhixiong Lu
Research Article (12 pages), Article ID 4245051, Volume 2021 (2021)

Decision Making of Curriculum Attainment Degree for Engineering Geology Based on Fuzzy Set Theory
Binbin Yang, Shuting Du, Xiaoming Zhao, Dongqi Tang, and Changde Yang
Research Article (6 pages), Article ID 1743778, Volume 2021 (2021)

Hindawi
Advances in Civil Engineering
Volume 2022, Article ID 7734078, 12 pages
https://doi.org/10.1155/2022/7734078

Research Article

Deformation and Fracture Characteristics of Coal Gangue Interbedded Samples under Loading and Unloading Conditions

Jisheng Xue and Tielin Zhao

China Coal Research Institute, Beijing 100013, China

Correspondence should be addressed to Jisheng Xue; xuejisheng@tdkcsj.com

Received 20 February 2022; Revised 10 June 2022; Accepted 13 June 2022; Published 14 July 2022

Academic Editor: Zhijun Xu

The dynamic sedation of the coal mine production is alternate or superimposed in coal rocks, which causes crack unevenness due to the presence of jacquards, causing unregistered coal blocks. By observing the deformation and fracture characteristics of coal-rock interbedding specimens with different gangue ratio under different stress paths, this paper studies the fracture instability mechanism and fracture characteristics of coal-rock interbedding, analyzes the progressive failure process and fracture opening model of coal-rock interbedding, and uses GDEM software to simulate the triaxial loading and unloading failure characteristics of coal-rock samples. The results show that the ratio of gangue inclusion has a significant effect on the structural strength of coal rock interbedding; with the unloading, the coal rock interbedding of the top coal body will be damaged and destroyed to varying degrees and asynchronously, the coal rock interbedding of the top coal body will present various forms of failure characteristics according to the changes of horizontal stress gradient in the vertical direction; the progressive failure process of coal rock interbedding under loading and unloading conditions can be divided into three stages. As the jigs are raised, the crack nonstable expansion stress of the composite coal body sample is gradually increased; and the rising ratio of the jacket X is not complete. The striped conjugated shear failure characteristics are more obvious; the different combined coal gangue tester shows microcrack near the peripheral loading boundary, and as the loading axis pressure increases, the fracture distribution range and density are increased; the rock layer is present. The tensile fracture is destroyed, and the coal seam exhibits shear destruction of intensive cracks; different test pieces produce significant tensile destruction on one side of the unloaded boundary; the greater the loaded axial pressure of the specimen, the greater the damage degree of the specimen after unloading; the damage degree of two coal and one rock specimens is the largest, the damage degree of one coal and one rock specimens is in the middle, and the damage degree of one coal and two rock specimens is the smallest.

1. Introduction

Due to the complexity of coal-forming environment, gangue is often associated with coal roof. With the increase of coal roof thickness, coal-gangue interbed is the most common in extra-thick coal roof [1, 2]. A large number of on-field experience and laboratory studies show that the gangue layer in coal roof can cause poor caving performance and low recovery rate of top coal during fully mechanized caving mining of extra-thick coal roof. The reason is that the storage of gangue layer causes uneven development of fracture damage in top coal body, which is the main reason for aggravating coal deformation [3–8]. In the mining process, the disturbance of dynamic and static load alternates or superposes on the gangue coal roof, resulting in the excessive deformation bearing capacity of the coal body on the top of coal-gangue interbed, which leads to the failure instability or shear slip of the composite coal-gangue mass, resulting in irreversible large deformation, and the caving lumpiness of the top coal increases. The failure process of composite roof coal body is similar to the loading and unloading process. In the process of working face advancing, the coal body in the coal roof of coal-gangue interlayer experiences the failure through loading and unloading under the influence of the front abutment pressure [9–13]. The study shows that the controlling factors affecting the instability of coal mass are mainly the direction of stress, the rate of stress change, the physical and mechanical strength, and the friction properties of coal mass [14, 15].

Research reports on the failure of coal-gangue interbed focus on the uniaxial failure characteristics of coal-gangue interbed under dynamic and static loads and pay more attention to the influence of coal-gangue interbed on roof caving and impact liability. Zhu et al. [16] used standard rock specimens of 50 mm to study the uniaxial compression failure characteristics of coal-gangue interbeds with different thicknesses and inclinations. When the combination angle is less than 45°, the main failure is split failure, and when the combination angle is greater than 45°, the failure is shear failure along the interface. Wu et al. [17] used physical similarity simulation experiment to analyze the stress distribution and evolution law of coal-gangue interbedded roof and found that the advance pressure generated by mining led to the failure of coal-gangue interbedded roof, roof separation, subsidence, and caving. Zhang et al. [18] explained the factors influencing the mechanics and failure characteristics of combined coal-gangue through uniaxial and triaxial compressive tests of coal-gangue specimens in different combination forms and proposed that the failure of combined coal-gangue under load is mainly tensile failure and shear failure of coal body, and the damage of coal body can induce the damage or failure of rock body to a certain extent. Nie et al. [19, 20] found through laboratory tests that the fracture characteristics of combined coal-gangue mass in the process of uniaxial compression are different from those of single coal-gangue mass, and the fracture is progressive and the main fracture mechanism is shear failure. Zhao et al. [21, 22] combined the two-body interaction theory to explain the elastic rebound and strain localization characteristics of the two-body interaction system and proposed that the combined coal-gangue specimens could reflect the basic mechanical phenomena in the process of rock burst. Huang and Liu [23] studied the dynamic failure characteristics of coal-gangue under different loading speeds through the uniaxial loading test of combined coal-gangue. Liu et al. [24–26] carried out the study on the influencing factors of the bursting liability of combined coal-gangue, studied the bursting liability of combined coal-gangue by comparing the characteristics of coal-gangue combination obtained from the test, and obtained the correlation between the bursting liability of combined coal and various physical and mechanical parameters. Xie et al. [27, 28] analyzed the difference between single and aggregate mechanical properties through uniaxial and triaxial compression tests of combined coal-gangue and established a biophysical model, providing a theoretical basis for the study of biophysical stability. The failure mechanism of coal-gangue interbed may be the failure caused by the change of uniaxial stress condition from uniaxial stress condition to uniaxial stress condition, and the failure forms of coal body under different stress paths are obviously different. In the process of coal mining, the negative impact on production is mainly caused by the unloading process of coal-gangue interbed after the pressure rises. It is of great significance to clarify the unloading failure mechanism of coal-gangue interbed. Unloading rate, triaxial stress, soft structural plane, and gangue ratio all have an impact on the failure characteristics of coal-gangue interbed.

Figure 1: Coal-gangue interbed specimens.

The structure of single coal-gangue surface and simple combination of structural plane deformation and instability of coal-gangue damage characteristics for more in-depth research and roof caving in thick coal roof mining help to effectively control impact ground pressure and roadway instability but with compound roof coal in coal-gangue under static loading, the failure mechanism of fracture characteristics of the research is not comprehensive enough. In particular, there are few research works on the failure and instability of coal-gangue interbedded top and the influence of gangue ratio on the failure. In this paper, the failure mechanism and failure characteristics of the coal-gangue specimens with different ratios of gangue were studied by observing the deformation and failure laws of the coal-gangue specimens with different ratios of gangue.

2. Test Method

2.1. Specimens. In this paper, 150 mm × 150 mm × 150 mm coal-gangue interbed specimens were selected, and all specimens were taken from the same intact unweathered coal-gangue blocks. The specimen was produced in Madaotou Coal Mine in Datong, Shanxi Province; the embedded depth is 350 m. Coal bodies with dense and uniform texture were selected and bonded with gangue after processing. Each end face of the specimen was polished in the rock specimen processing workshop, and the size error of each direction of the specimen was less than 0.1 mm. The angle error of each face measured by the square is less than 0.1°. Before the experiment, the specimens were stored for half a month and dried naturally for the experiment. As shown in Figure 1, three combinations are selected according to different coal roof proportions, which are divided into three conditions: two coals and one gangue, one rock and one coal, and two rocks and one gangue.

2.2. Test Equipment and Test Principle. The failure and instability of rock mass are the result that the microdamage in rock mass accumulates to produce the main fracture surface

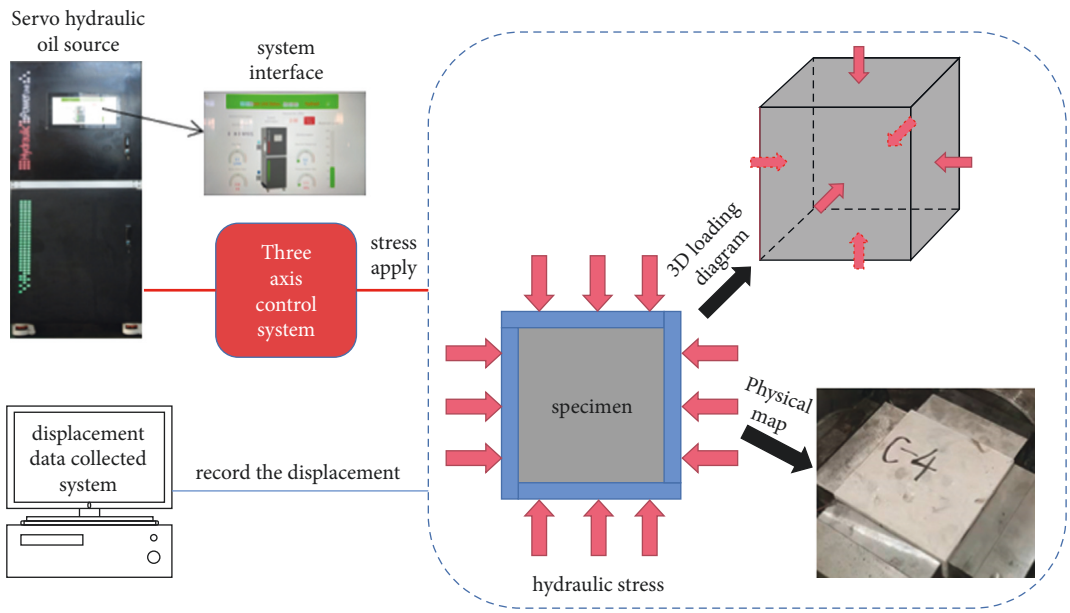

Figure 2: Principle of rock mechanics test system.

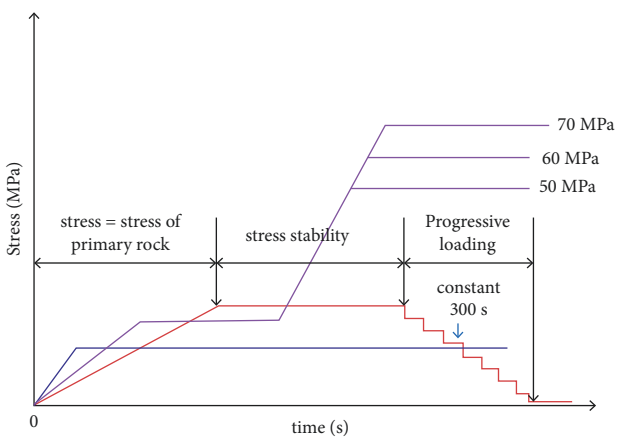

Figure 3: Stress loading and unloading test plan.

under the inducement of external force. The failure and instability of rock mass are a typical nonlinear failure. The study shows that the slight change of initial conditions in nonlinear system may lead to the great difference of the final failure form. For the research object of coal-gangue interbed, which is composed of a variety of rocks, there is a natural soft interface between coal body and rock stratum, and the thicknesses of gangue and coal-gangue interbed interface are bound to affect the deformation and failure characteristics of coal-gangue interbed specimens under the action of loading and unloading caused by mining, as well as the fracture structure generated within them.

In order to study the macroscopic and microscopic characteristics of deformation and fracture of coal-gangue interbedded specimens under loading and unloading conditions, the loading and unloading tests of coal-gangue interbedded specimens and CT scanning of fracture structures in rock mass were carried out by using true triaxial press and industrial microscopic CT imaging system, respectively. The principle of the test system is shown in Figure 2. The true triaxial rock press machine and CT scanning equipment used in this paper were provided by Central South University and Taiyuan University of Technology, respectively. The maximum load of the equipment is 2 000 kN, the loading rate is 10 N–10 kN/s, the accuracy is ±1%, the displacement measurement range is 0–200 mm, the measurement accuracy is <±0.5% FS, and the resolution of the minimum displacement is 0.001 mm.

2.3. Loading and Unloading Plans. The true triaxial loading mechanical test system was used to conduct mechanical tests on coal-gangue interbedded specimens to study the failure characteristics of coal-gangue under specific loading and unloading paths conforming to the advanced abutment pressure curve. The maximum principal stress in vertical bedding direction is the main factor causing the interbed in coal-gangue. According to the field measurement results, the axial pressures of 70 MPa, 60 MPa, and 50 MPa are taken, the maximum horizontal principal stress is 11.84 MPa, and the minimum horizontal principal stress is 6 MPa. The loading and unloading tests of coal-rock interbedded structure specimens under three kinds of combination conditions were carried out, respectively. According to the relevant test provisions of rock mechanics, the loading rate is 1 kN/s and the unloading rate is 0.2 kN/s. The loading plan is shown in Figure 3, y-axis refers to vertical stress (MPa). The vertical stress direction is the direction of the vertical specimen bedding, and the maximum horizontal principal stress direction is the unloading direction.

As shown in the table and figures, the most axial pressure of loading plan 1 is 70 MPa, the most axial pressure of loading plan 2 is 60 MPa, the most axial pressure of loading plan 3 is 50 MPa, and the specimen numbers and loading experiment plan are shown in Table 1.

Table 1: Specimens and the according load plan.

Specimen number	The type of specimens	Ratio of gangue (%)	Load plan
A3	One rock and one coal	50	Plan 2
A5	One rock and one coal	50	Plan 1
A6	One rock and one coal	50	Plan 3
B2	Two coals and one rock	33.3	Plan 2
B4	Two coals and one rock	33.3	Plan 1
B6	Two coals and one rock	33.3	Plan 3
C4	Two rocks and one coal	67.7	Plan 3
C5	Two rocks and one coal	67.7	Plan 2
C6	Two rocks and one coal	67.7	Plan 1

3. Deformation Characteristics of Specimens under Different Loading and Unloading Conditions

3.1. Failure Characteristics of Coal-Gangue Interbed Specimens. After the loading and unloading test, micro-CT was used to observe the crack morphology in the specimen. Figure 4 shows the micro-CT scanning results of the coal-gangue interbed specimen after loading and unloading. Among the 9 specimens, specimen C6 did not have integrity after loading and unloading and was not scanned. After analyzing the CT scanning results of each group of test pieces after loading and unloading test, the samples of coal rock combination with different gangue ratio have different failure characteristics, the sample has experienced the process of initial fracture compression, micro fracture development, interconnection, and finally the formation of through macro fractures, the failure mode is tension shear composite failure, the macrocracks of the specimen are obvious after failure.

Under the loading condition of plan 1, two rocks and one gangue specimen C6, one rock and one coal specimen A5, and two coals and one gangue specimen B4, all specimens were destroyed after unloading. Specimen C6 was destroyed after the experiment, and the specimen had no integrity after the experiment. The integrity of specimen A5 was damaged before the experiment, and there were obvious cracks and structural planes. It could be found that the cracks were mainly parallel to the direction of the minimum principal stress, and the fracture plane was x-shaped conjugate shear failure. The integrity of gangue was significantly stronger than that of coal. The deformation of specimen B4 with two rocks and one gangue in the vertical direction and unloading direction is obvious, and the longitudinal fractures are developed. The fracture plane generated during the failure is parallel to the direction of the minimum horizontal principal stress, and the fracture is in the x-shaped conjugate shear failure mode.

Under the loading condition of plan 2, specimen C5 and two coals and one gangue B2, all specimens were damaged after unloading, while specimen A3 showed no obvious damage. The fracture plane orientation generated by specimen C5 with two rocks and one gangue is mostly parallel to the nonunloading direction, and the number of cracks in the specimens and the failure degree of the specimens are obviously smaller than those of specimen C6. The fracture plane orientation generated after loading of specimen B2 was mostly parallel to the nonunloading direction, and the number of cracks in the specimens and the failure degree of the specimens were significantly smaller than those of specimen B4.

Under the loading condition of plan 3, specimen C4 and specimen B6, no obvious failure occurred in all specimens after unloading, but obvious failure occurred in one rock and one coal A6. The rupture surface of specimen A6 is perpendicular to the unloading direction.

The interbedded specimens of coal-gangue undergo the process of initial fracture compression, microfracture development, mutual connectivity, and finally the formation of penetrating macro fracture. The failure mode is mainly pull-shear composite failure, and the macrofracture is obvious after the failure. The interbedded specimens of one rock and one coal show incomplete X-type conjugate shear failure characteristics. The coal specimens and rock specimens in the interbedded specimens of two coals and one gangue exhibit relatively independent and incomplete X-type conjugate shear failure characteristics, and transverse cracks are formed on the top of the coal specimens due to compression. The two-rock one-coal interbedded specimens exhibit systematic and incomplete *X*-type conjugate shear failure characteristics.

In the loading and unloading experiment of true triaxial simulation of real mining stress, the failure degree of samples with different gangue inclusion ratio is different under different loading conditions, statistics of the distribution of fragmentation after sample failure are shown in Figure 5, one coal one rock and two coal one rock samples have less damage after loading and unloading, the integrity of the sample is high, and the block cracks are concentrated in 12~15 cm. In the sample of one coal and two rocks, 60% of the failure lumpiness is concentrated in 12~15 cm, mainly in rock, and the failure lumpiness of coal is concentrated in 3~9 cm.

The size effect of coal-gangue mass after loading and unloading test is the reflection of its inherent structural complexity, which is due to the existence of fracture network system in rock mass and the joint influence of loading and unloading process. Coal-gangue physical and mechanical properties and particle distribution, as well as defects, such as joint distribution, showed a greater difference, the stress distribution of local stress and strain in different position is different, there will always be in the rock a very obvious damage crack, and this is the main cause of rock damage condition, thus, to some extent, limiting the development of

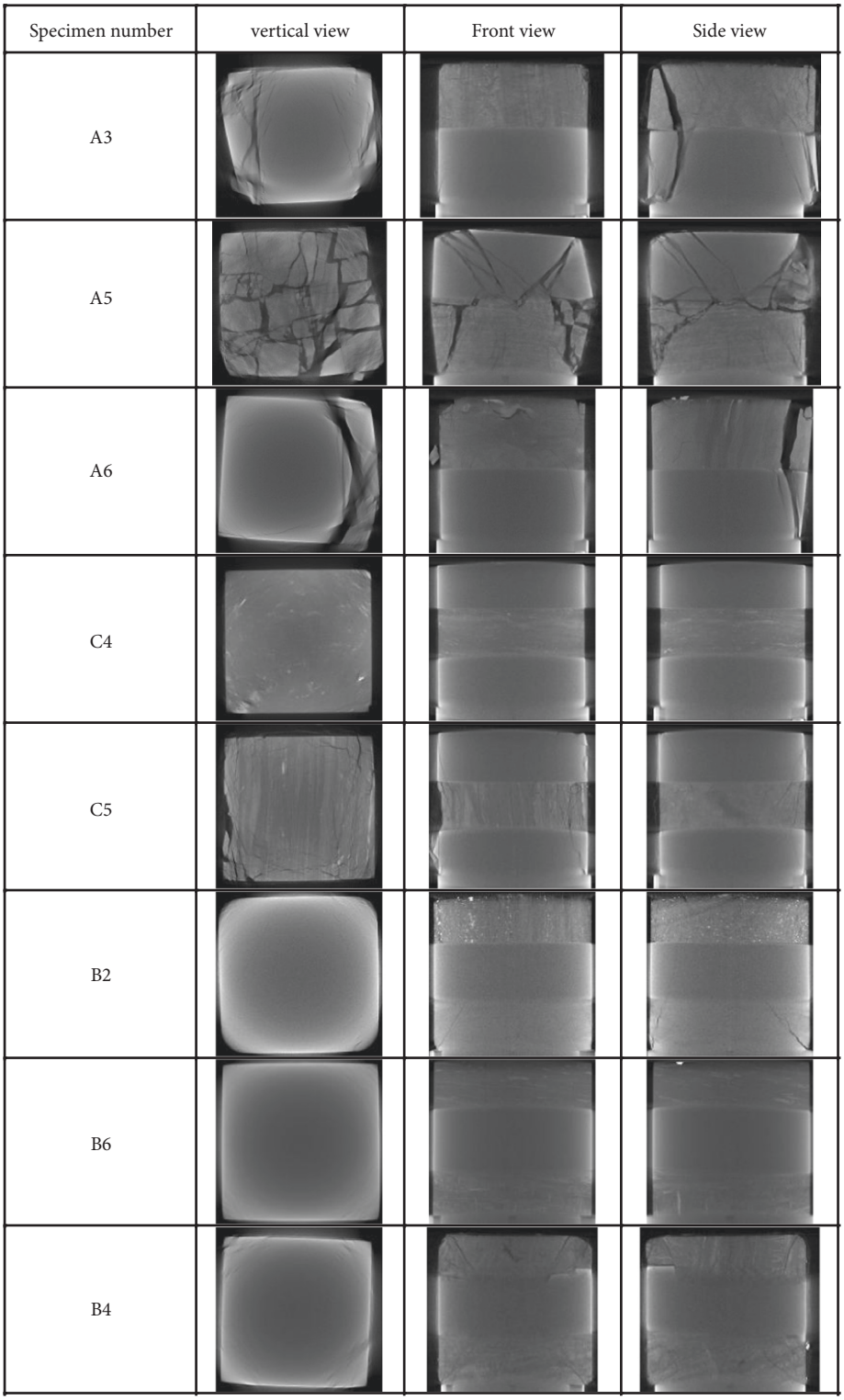

Figure 4: Micro-CT scanning results of coal-rock interbedding specimen after loading and unloading.

some of the other weak small cracks. The fragmentation resulting in damage is large.

3.2. Deformation Characteristics of Coal-Gangue Interbed Specimens with Different Ratios of Gangue. Loading and unloading tests were carried out under three axial pressures for each ratio of gangue. Figure 6 shows the body stress-strain curves of different ratio of gangue under different loading plans.

The specific results are as follows.

Under the vertical stress of 70 MPa, the stress-strain curve under each ratio of gangue shows the following: when

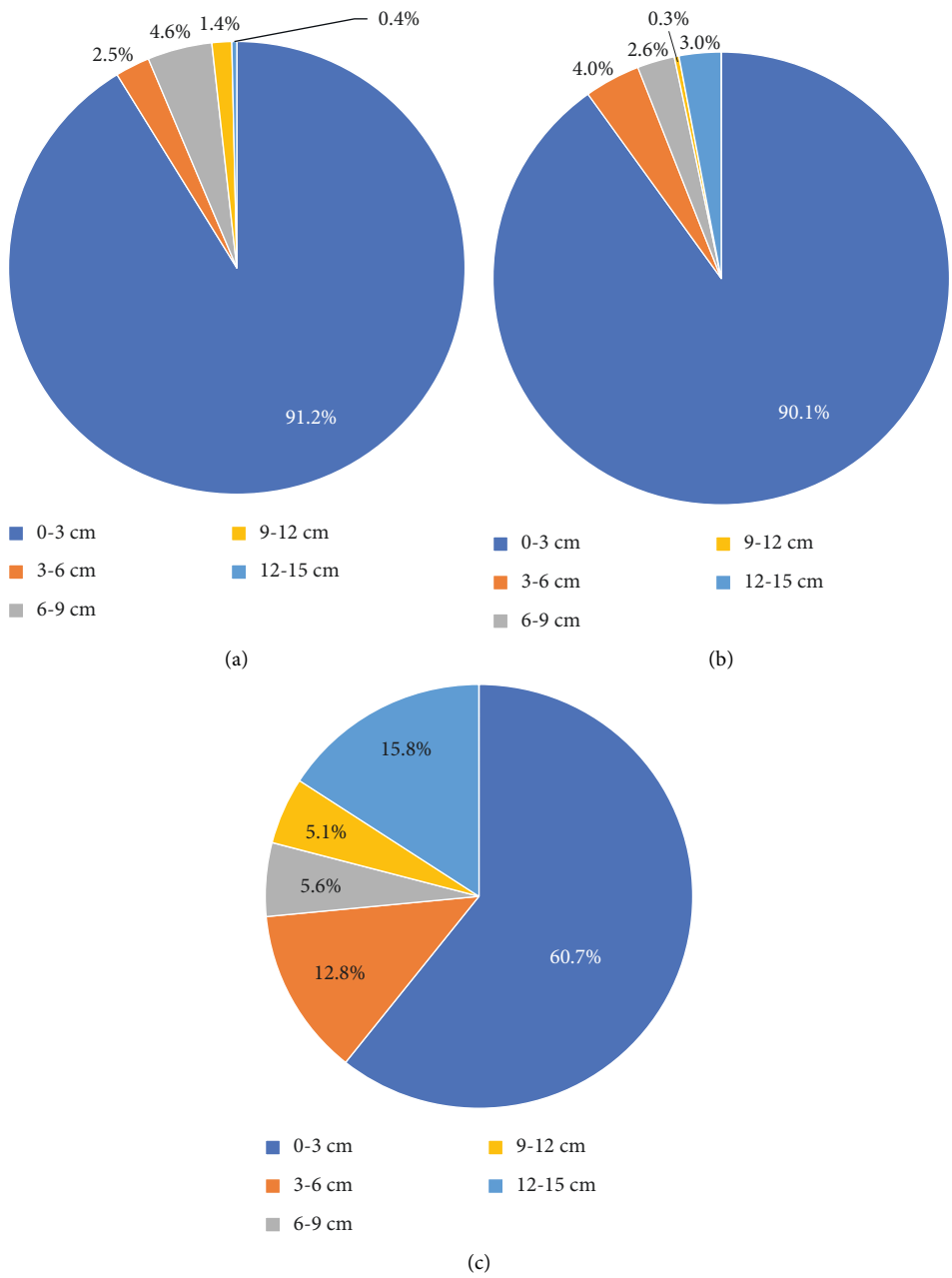

Figure 5: The block scale proportional distribution of different specimens. (a) One coal and one rock; (b) two coals and one rock; (c) one coal and two rocks.

the volume stress is low, one rock and one coal exhibit dilatation, while the other two groups of specimens do not exhibit dilatation, and the volume strain fluctuates or rises step by step with the increase of the volume stress. After that, the volume strain increases with the increase of volume stress, and the volume strain decreases with the increase rate of volume stress at 33.63 MPa. It can be found from the loading curve that when the volume stress reaches 33.63 MPa, the increase of volume stress is caused by the increase of spindle stress. When the bulk stress reaches 92 MPa, the bulk stress begins to decrease. Due to the difference of the loading and unloading paths and the new plastic deformation in the unloading process, the bulk strain decreases faster in the unloading stage than in the loading stage. The specimens with two rocks and one gangue, one rock and one coal, and two coals and one gangue failed at 77.79 MPa, 78.19 MPa, and 79.29 MPa, respectively, and the corresponding partial stresses were 70.42 MPa, 71.62 MPa, and 69.42 MPa, respectively. By comparing the volumetric stress-strain curves of specimens with different ratios of gangue at 33.63 MPa–92 MPa, it can be found that the increase rate of volumetric strain in this section decreases with the increase of the ratio of gangue.

Under the vertical stress of 60 MPa, the stress-strain curves under the conditions of various gangue ratios show the following: when the bulk stress is low, dilatancy occurs in

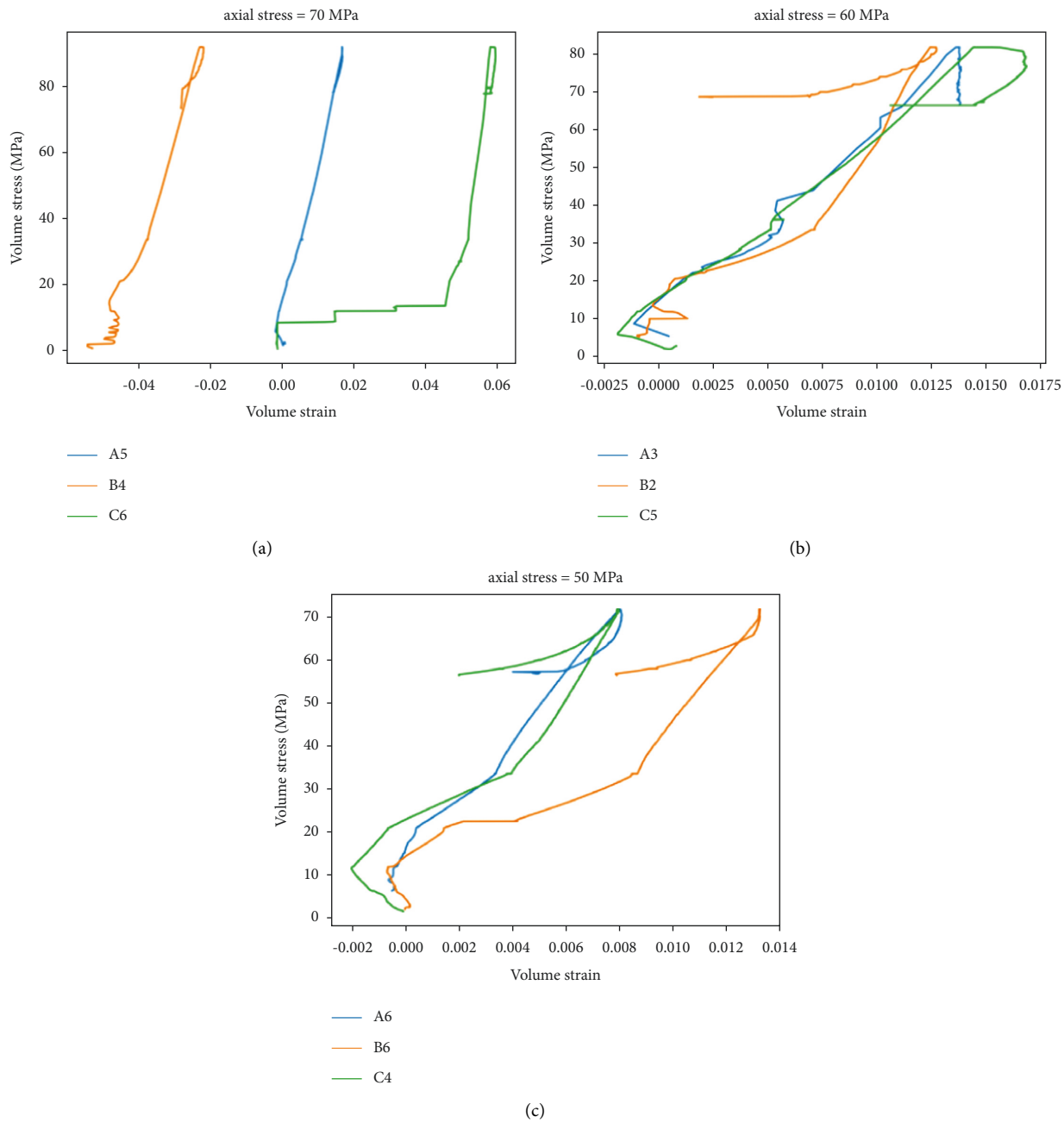

Figure 6: Volume stress-strain curve under different maximum vertical stress. (a) Maximum vertical stress = 70 MPa; (b) maximum vertical stress = 60 MPa; (c) maximum vertical stress = 50 MPa.

the specimens with one rock and one coal and two rocks and one gangue. The dilatancy does not occur in the specimens with two coals and one gangue. Around 20 MPa, the expansion volume offsets the previous dilatancy volume strain. After that, the bulk strain increases with the increase of bulk stress, and the bulk strain decreases with the increase rate of bulk stress at 35 MPa. From the loading curve, it can be found that the main shaft stress increases when the bulk stress reaches 35 MPa, and the stress-strain curves of one rock and one coal and two rocks and one gangue between 35 and 82 MPa are basically the same. When the bulk stress reaches 82 MPa, the bulk stress begins to decrease. Due to the difference of the loading and unloading paths and the new plastic deformation in the unloading process, the bulk strain decreases faster in the unloading stage than in the loading stage. By comparing the volumetric stress-strain curves of specimens with different ratios of gangue between 35 MPa and 82 MPa, it can be found that the volumetric strain rising rate decreases with the increase of the ratio of gangue. The specimens with two rocks and one gangue, one rock and one coal, and two coals and one gangue failed at 66.45 MPa, 66.45 MPa, and 68.94 MPa, respectively, and the corresponding partial stresses were 65.1 MPa, 65.1 MPa, and 60.12 MPa, respectively.

Under the vertical stress of 50 MPa, the stress-strain curve under the conditions of each gangue ratio shows the following: when the volume stress is low, dilatation phenomenon occurs in the specimens of one coal and one coal as well as two coals and onecoal. No dilatation occurs in the specimens of two coals and one rock. After that, the volume strain increases with the volume stress increasing, and the volume strain decreases with the growth rate of the volume stress at 34 MPa. From the loading curve, it can be found that when the volume stress reaches 34 MPa, the increase of the volume stress is caused by the increase of the principal axis stress. The volume strain increment of the three specimens is basically the same between 34 and 72 MPa. When the bulk stress reaches 72 MPa, the bulk stress begins to decrease. Due to the difference of the loading and unloading paths and the possible new plastic deformation during the unloading process, the bulk strain decreases faster in the unloading stage than in the loading stage. After loading and unloading, the specimens with one rock and one coal and two coals and one gangue were destroyed at 57.32 MPa and 56.67 MPa, respectively, and the corresponding partial stress was 53.36 MPa and 54.66 MPa, respectively.

Based on the test results of the three groups of loading conditions, the influence of different gangue ratio on the mechanical properties of coal-gangue interbed specimens can be obtained. The influence of gangue ratio on the structural strength of coal-gangue interbed is significant, mainly reflected in the two following aspects: (a) With the decrease of the ratio of gangue, the deformation in the direction of the maximum principal stress increases, while the deformation in the unloading direction does not change significantly. The corresponding volume strain increases, indicating that the deformation required before specimen failure increases. (b) As the ratio of gangue increases, the critical volume stress for failure of coal-gangue interbedded structure rises, indicating that the higher the ratio of gangue in unloading process, the stronger the stability of coal-gangue interbedded structure.

3.3. Changes in Bulk Modulus of Specimens with Different Ratios of Gangue. The bulk modulus between the body stress of 20 MPa and the maximum principal stress during loading and unloading was calculated, as shown in Table 2.

As the ratio of gangue increases, the bulk modulus of coal-gangue interbedded sample decreases. The correlation between the ratio of gangue and the bulk modulus is drawn, as shown in Figure 7. The relationship between the ratio of gangue and the bulk modulus of coal-gangue interbedded sample is quadratic polynomial.

Table 2: The bulk modulus of specimen with different gangue ratio.

Specimens number	The type of specimens	Bulk modulus (Pa)
A3	One rock and one coal	4909.339
A5	One rock and one coal	6181.396
A6	One rock and one coal	6796.158
	Average value	**5962.298**
B2	One rock and two coals	5083.113
B4	One rock and two coals	4534.259
B6	One rock and two coals	4236.436
	Average value	**4617.936**
C4	Two rocks and one coal	4812.791
C5	Two rocks and one coal	4659.832
C6	Two rocks and one coal	3169.501
	Average value	**4214.041**

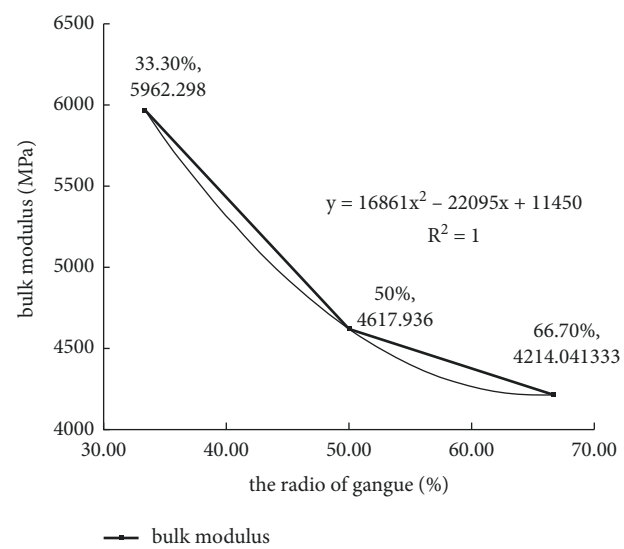

Figure 7: The relationship between gangue ratio and bulk modulus.

4. Numerical Simulation Analysis of Fracture Characteristics of Coal-Rock Interbedding

4.1. Numerical Modeling and Simulation Solutions. Generally, the computational domains include the continuous state, discontinuous state, or partially continuous state, which correspond to the FEM, DEM, and CDEM domains. Conventionally, the FEM domain is used for fully continuous problems, and the DEM domain for fully discontinuous problems. Meanwhile the Continuous Discontinuous Element Method (CDEM) couples the finite element calculation with the discrete element calculation, which conducts finite element calculation inside the block elements and conducts discrete element calculation at the block elements boundary. Through the fracture of interface elements, not only can the deformation and motion characteristics of the material in the continuous state and the discontinuous state be simulated, but also the progressive failure process of the material from the continuous body to the discontinuous body can be realized. In this paper, considering the influence of coal seam gangue, the high-efficiency numerical simulation software GDEM based on CDEM theory is used to conduct numerical simulation research on the failure process of coal-rock interbedded specimens under triaxial loading.

To study the influence law of coal and gangue on the mixed-bed specimen failure, based on the specimen types of laboratory tests, the numerical models of one-coal two-rock specimen, one-coal one-rock specimen, and two-coal one-

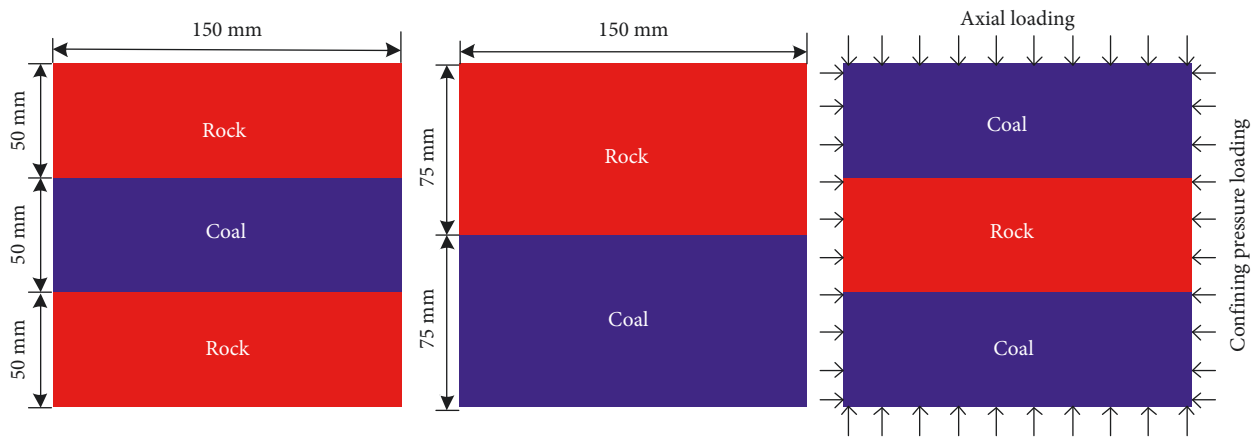

Figure 8: Numerical models and boundary conditions.

Table 3: Micromechanical parameters of coal-rock sample.

	Density (kg/m^3)	Elastic modulus (Pa)	Poisson's ratio	Cohesion (MPa)	Tensile strength (MPa)	Internal friction angle (°)
Rock	2500	8.51e9	0.26	20.2	27.04	30.0
Coal	1300	2.69e9	0.34	14.6	19.68	26.0

rock specimen are generated. The element number of numerical model is 22500, and the width of numerical model is 150 mm. For one-coal two-rock specimen and two-coal one-rock specimen, the heights of rock layer and coal layer in numerical model are 50 mm. For one-coal one-rock specimen, the heights of rock layer and coal layer are 75 mm. To simulate the triaxial loading of rock test, the vertical compressive stress is applied to the upper and lower surfaces of numerical model to simulate the axial loading, and the horizontal compressive stress is applied to the left and right surfaces of numerical model to simulate the confining pressure loading. The size of the model size and boundary conditions numerical specimen is 150 mm × 150 mm, as shown in Figure 8.

According to the mechanical test results of the rock specimen, the mesomechanical parameters of the coal-rock specimen in the simulation are obtained through numerical inversion, as shown in Table 3.

A large number of research works indicate that the maximum principal stress in the vertical bedding direction is the main factor causing the coal-gangue interbedding. Therefore, based on the experimental scheme of coal-rock specimens, three axial pressures of 50 MPa, 60 MPa, and 70 MPa are, respectively, used in the numerical simulation, and the maximum horizontal principal stress is 12 MPa. The simulations of loading and unloading process of coal-rock specimens under three combination conditions are carried out. During the simulation, uniformly distributed compressive stresses of 50 MPa, 60 MPa, and 70 MPa are, respectively, applied to the upper and lower surfaces of the coal-rock specimen, and the uniformly distributed horizontal compressive stress of 12 MPa is applied to the left and right surfaces of the coal-rock specimen. During the loading process, when the simulation iterates for 100,000 steps, the loading process ends, and the damage and failure degree of the coal-rock specimen is analyzed. To simulate the failure mechanism of the coal-rock structure under the asymmetric load of mining disturbance during the coal mining process, the simulation scheme of unloading the confining pressure on one side of the specimen is adopted to study the failure mechanism of the coal-rock sample.

4.2. Specimen Failure Characteristics during Unloading. Under the axial pressure of 50 MPa, 60 MPa, and 70 MPa and confining pressure of 12 MPa, after unloading the confining pressure on the right side of the specimen, the failure results of the coal-rock specimen under different combination conditions are shown in Figure 9.

From Figure 9, for one rock-one coal specimen, under the axial pressure of 50 MPa, the confining pressure of 12 MPa is unloaded, the length of the crack from the unloading boundary to the middle of the specimen gradually shortens, and the length of the crack in the coal seam is smaller than that of the rock layer; however, there are obvious fracture zones in the coal seam. With the increase of the loading axial pressure, the coal-rock specimen presents a tendency to fly outwards after unloading the confining pressure, and the tendency of the coal seam to fly away is more obvious. With the increase of the loading axial pressure, the width of the oblique fracture zone in the coal seam increases significantly after the confining pressure. For the one-rock two-coal specimen, with the increase of the loading axial pressure, the distribution range of the cracks in the specimen increases after unloading the confining pressure. The upper and lower coal seams of the specimen are thrown out symmetrically after unloading the confining pressure; however, there is no obvious tendency of being thrown away in the middle rock layer, and the specimen as a whole showed a concave failure shape. For the two-rock one-

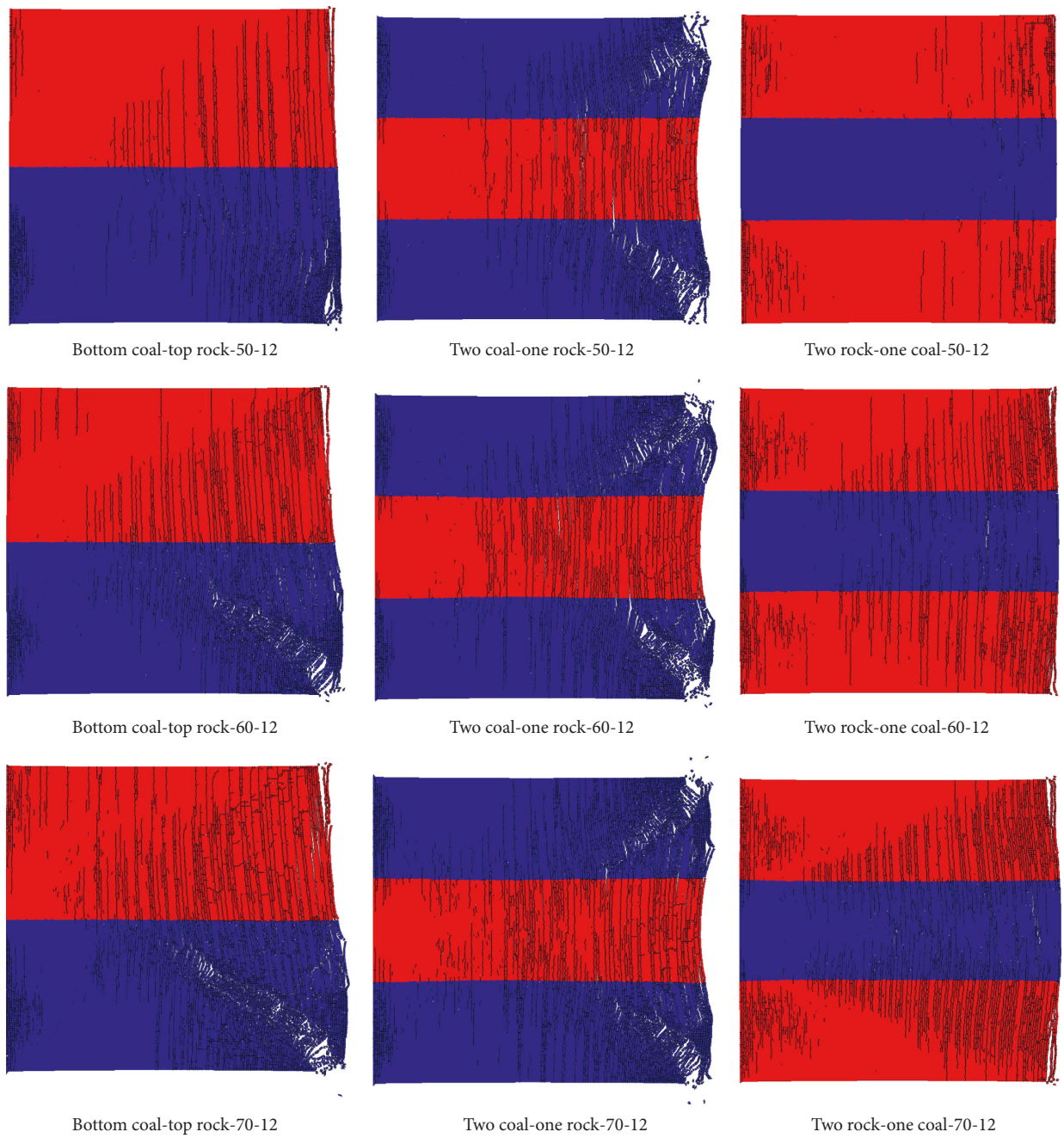

Figure 9: Failure results of rock sample after unloading the confining pressure. (a) Bottom coal-top rock, 50-12; (b) top coal-one rock, 50-12; (c) two rocks-one coal, 50-12; (d) bottom coal-top rock, 60-12; (e) top coal-one rock, 60-12; (f) two rocks-one coal, 60-12; (g) bottom coal-top rock, 70-12; (h) top coal-one rock, 70-12; (i) two rocks-one coal, 70-12.

coal specimen, under the axial pressure of 50 MPa, the upper and lower rock layers of the specimen are obviously fractured after unloading confining pressure, and the damage degree of the middle coal seam is weaker. Under the axial pressure of 60 MPa and 70 MPa, the cracks in coal and rock layers of sample are obvious after unloading. Under different loading and unloading conditions, the two-rock one-coal specimens show a convex failure form in which the central coal seam protrudes outwards. As a whole, the greater the loading axial pressure, the greater the damage degree of different coal-rock specimens after unloading; different specimens all produce significant unloading-tensile failure on the side of the unloading boundary; the failure degree of the two-coal one-rock specimen is greater than that of the one-coal one-rock specimen which is greater than that of the one-coal two-rock specimen.

5. Conclusions

(1) The influence of the proportion of coal-rock interbed structure is significant, mainly embodied in the two following aspects; first, with the proportion of dirt

band down the direction of maximum principal stress deformation on the rise, change of the direction of the unloading deformation is not obvious, the corresponding volume strain increases, the characterization of the specimen to before the damage deformation increases; second, as the ratio of gangue decreases, the critical volume stress of coal-gangue interbedded structure increases, indicating that the higher the ratio of gangue in unloading process, the stronger the stability of coal-gangue interbedded structure.

(2) Under the condition that the maximum horizontal principal stress value is determined, with the unloading process, different degrees of asynchronous damage and failure will occur in the coal-gangue interbedded layer of top coal body. In the vertical direction, the coal-gangue interbedded layer of top coal body presents various types of failure characteristics according to the change of horizontal stress gradient.

(3) The interbedded specimens of coal-gangue undergo a process of initial fracture compression, microfracture development, mutual connectivity, and finally the formation of penetrating macrofractures. The failure mode is mainly pulse-shear composite failure, and the macrofractures are obvious after the failure. When the maximum horizontal principal stress is greater than 60 MPa, the specimen after unloading is relatively broken, and the size of block cracks is concentrated in 12–15 cm. With the increase of the ratio of gangue, the incomplete X-type conjugate shear failure is more obvious.

(4) During the triaxial loading process, the coal-gangue interlayer specimens with different combinations generate the microfractures near the confining pressure loading boundary. After unloading confining pressure, different specimens all generate obvious tensile failure on the side of the unloading boundary. The greater the loading axial pressure, the greater the damage degree of the specimen after unloading. The damage degree of the two-coal one-rock specimen is greater than that of the one-coal one-rock specimen which is greater than that of the one-coal two-rock specimen.

Data Availability

The data used to support the findings of this study are available from the corresponding author upon request.

Conflicts of Interest

The authors declare that there are no conflicts of interest regarding the publication of this paper.

Acknowledgments

This work was supported by the National Key Research and Development Program (2018YFC0604506) and Science and Technology Innovation and Entrepreneurship Fund Special Project of Tiandi Technology Co., Ltd. (2020-TD-ZD016).

References

[1] Y. Luo, *Research on Evolution of Roof Force Chain and Top Coal Failure Law in Fully Mechanized Caving Stope*, Master Thesis of Anhui University of Science and Technology, Anhui, China, degree programs, 2016.

[2] J. C. Wang and Z. H. Wang, "The failure mechanism of top coal in fully mechanized caving mining under the combined action of loading and unloading," *Tongmei Science and Technology*, vol. 155, no. 3, p. 1~7, 2017.

[3] J. P. Zuo, J. L. Pei, J. F. Liu, and R. D. Peng, "Acoustic emission behavior and space-time evolution mechanism in the process of coal and rock fracture," *Chinese Journal of Rock Mechanics and Engineering*, vol. 30, no. 8, pp. 1564–1570, 2011.

[4] B. X. Liu, J. L. Huang, Z. Y. Wang, and L. Liu, "Study on damage evolution and acoustic emission characteristics of uniaxial compression coal and rock," *Chinese Journal of Rock Mechanics and Engineering*, vol. 28, no. S1, pp. 3234–3238, 2009.

[5] E. Y. Wang and X. Q. He, "Experimental study on electromagnetic radiation of coal and rock deformation and fracture," *Chinese Journal of Geophysics*, no. 1, pp. 131–137, 2000.

[6] X. R. Ge, J. X. Ren, and Y. B. Pu, "CT dynamic test of triaxial mesoscopic damage evolution law of coal and rock," *Chinese Journal of Rock Mechanics and Engineering*, no. 5, pp. 497–502, 1999.

[7] B. Bai, N. Qingke, Z. Yike, W. Xiaolong, and H. Wei, "Co-transport of heavy metals and SiO 2 particles at different temperatures by seepage," *Journal of Hydrology*, vol. 597, 2020.

[8] B. Yuan, Z. Li, W. Chen et al., "Influence of groundwater depth on pile-soil mechanical properties and fractal characteristics under cyclic loading," *Fractal and Fractional*, vol. 6, no. 4, p. 198, 2022.

[9] Y. D. Jiang, Y. S. Pan, and F. X. Jiang, "Mechanism and prevention of rock burst in coal mining in my country," *Journal of Coal Science*, vol. 39, no. 2, pp. 205–213, 2014.

[10] Y. J. Yang, Y. Song, and J. Chu, "Experimental study on strength and deformation characteristics of coal and rock under cyclic loading," *Chinese Journal of Rock Mechanics and Engineering*, no. 1, pp. 201–205, 2007.

[11] Y. X. Xia, J. F. Pan, and Y. J. Wang, "Research on coal rock fracture and stress distribution characteristics based on high-precision microseismic monitoring," *Journal of Coal Science*, vol. 36, no. 2, pp. 239–243, 2011.

[12] B. Yuan, L. Zihao, C. Yiming et al., "Mechanical and microstructural properties of recycling granite residual soil reinforced with glass fiber and liquid-modified polyvinyl alcohol polymer," *Chemosphere*, vol. 286, 2021.

[13] B. Yuan, Z. Li, and Z. Zhao, "Experimental study of displacement field of layered soils surrounding laterally loaded pile based on transparent soil," *Journal of Soils and Sediments*, vol. 4, pp. 1–12, 2021.

[14] B. Bai, R. Zhou, G. Cai, W. Hu, and G. Yang, "Coupled thermo-hydro-mechanical mechanism in view of the soil particle rearrangement of granular thermodynamics," *Computers and Geotechnics*, vol. 137, Article ID 104272, 2021.

[15] P. S. Xie, Y. Y. Zhang, and Y. L. Zhang, "Instability law of interlayer roof in large dip angle and high mining height and its influence on support," *Chinese Journal of Coal*, vol. 46, no. 2, pp. 344–356, 2021.

[16] C. J. Zhu, C. Ma, and J. X. Zhou, "Mechanical properties and failure characteristics of composite coal-rock mass under the coupling of dynamic and static loads," *Journal of Coal*, vol. 38, 2021.

[17] Y. P. Wu, W. H. Liu, Y. L. Zhang, and W. B. Yang, "Deformation and failure characteristics of overlying rock in coal-rock interbedded roof with large dip angle and large mining height," *Mining Research and Development*, vol. 40, no. 9, p. 5, 2020.

[18] Z. T. Zhang, J. F. Liu, L. Wang, and M. Zhao, "Experimental study on the influence of combination method on the mechanical properties and failure characteristics of coal-rock combination," *Chinese Journal of Coal*, vol. 37, no. 10, pp. 1677–1681, 2012.

[19] B. S. Nie, X. Q. He, and C. W. Zhu, "Study on mechanical properties and electromagnetic emission during the fracture process of combined coal-rock," *Procedia Earth and Planetary Science*, vol. 1, no. 1, pp. 281–287, 2009.

[20] Z. H. Zhao, W. M. Wang, L. H. Wang, and C. Dai, "Compression-shear strength criterion of coal-rock combination model considering interface effect," *Tunnelling and Underground Space Technology*, vol. 47, pp. 193–199, 2015.

[21] S. K. Zhao, Y. Zhang, and R. J. Han, "Numerical simulation of impact tendency evolution of combined coal-rock structure," *Journal of Liaoning University of Engineering and Technology (Natural Science Edition)*, vol. 32, no. 11, pp. 1441–1446, 2013.

[22] Z. H. Chen, C. A. Tang, and R. Q. Huang, "A double rock sample model for rockbursts," *International Journal of Rock Mechanics and Mining Sciences*, vol. 34, no. 6, pp. 991–1000, 1997.

[23] B. X. Huang and J. W. Liu, "The effect of loading rate on the behavior of samples composed of coal and rock," *International Journal of Rock Mechanics and Mining Sciences*, vol. 61, pp. 23–30, 2013.

[24] J. X. Liu, C. A. Tang, and W. C. Zhu, "Study on coal-rock series combination model and rock burst mechanism," *Chinese Journal of Geotechnical Engineering*, vol. 26, no. 2, pp. 276–280, 2004.

[25] C. P. Lu, L. M. Dou, and X. R. Wu, "Experimental study on the evolution of the impact tendency and the acousto-electric effect of the combined coal and rock," *Chinese Journal of Rock Mechanics and Engineering*, vol. 26, no. 12, pp. 2549–2555, 2007.

[26] L. M. Dou, J. C. Tian, and C. P. Lu, "Study on electromagnetic radiation law of combined coal and rock impact damage," *Chinese Journal of Rock Mechanics and Engineering*, vol. 24, no. 19, pp. 3541–3544, 2005.

[27] H. P. Xie, Z. H. Chen, and H. W. Zhou, "A preliminary study on the two-body mechanical model based on the interaction between engineering body and geological body," *Chinese Journal of Rock Mechanics and Engineering*, vol. 24, no. 9, pp. 1457–1464, 2005.

[28] J. P. Zuo, H. P. Xie, and A. M. Wu, "Study on the failure mechanism and mechanical properties of deep coal-rock individual and assemblage," *Chinese Journal of Rock Mechanics and Engineering*, vol. 30, no. 1, pp. 84–92, 2011.

Hindawi
Advances in Civil Engineering
Volume 2022, Article ID 1369171, 12 pages
https://doi.org/10.1155/2022/1369171

Research Article

Laboratory Tests on Open-Close Pile Jacking and Load Bearing Characteristics in Saturated Clay Soil

Qiang Song,[1] Teng Zhang,[2,3] Guangyu Zhou,[4] Hongzhong Li,[5] Xianghou Li,[6] Yishun Jiang,[6] Peng Zhao,[6] Weihui Tian,[7] Yonghong Wang,[2,8] Chuantong Zhang,[9] and Huining Liu[10]

[1]*Qingdao Vocational and Technical College of Hotel Management, Qingdao 266100, China*
[2]*School of Civil Engineering, Qingdao University of Technology, Qingdao 266033, China*
[3]*Qingdao Green Technology Geotechnical Engineering Co., Ltd., Qingdao 266033, China*
[4]*Department of Hydraulic Engineering, Shandong Water Conservancy Vocational College, Rizhao 276826, China*
[5]*Guangdong Province Communications Planning & Design Institute Co., Ltd., Guangzhou, China*
[6]*Shandong Luqiao Group Co., Ltd., Jinan, China*
[7]*Powerchina Northwest Engineering Corporation Limited, Xian, China*
[8]*Cooperative Innovation Center of Engineering Construction and Safety in Shandong Blue Economic Zone, Qingdao 266033, China*
[9]*China State Construction Zhongxin Construction Engineering Co., Ltd., Shandong Branch, Qingdao, China*
[10]*Shandong Hi-Speed Engineering Construction Group Co. Ltd., Jinan, China*

Correspondence should be addressed to Yonghong Wang; hong7986@163.com

Received 25 February 2022; Accepted 17 May 2022; Published 15 June 2022

Academic Editor: Angelo Aloisio

The stress characteristics of the pile-soil interface have an important influence on the effect and long-term bearing capacity of jacked piles. In order to obtain the stress characteristics of the pile-soil interface of the jacked pile in clay, the development law of pore water pressure and earth pressure for open- and closed-end jacked piles during the pile jacking process was studied using indoor model tests based on a saturated soft clay foundation. Test results show that, during the pile jacking process, the excess pore water pressure, earth pressure, and effective earth pressure at the pile-soil interface all increase gradually along penetration depth, and the increasing trend first increases linearly and then increases sharply at the pile end. The excess pore water pressure at the pile-soil interface of an open-end pile is smaller than that of a closed-end pile. The earth pressure and effective earth pressure at the pile-soil interface of the closed-end pile show a "lateral pressure degradation," and the degradation becomes more and more significant with increasing depth. The pile-soil interface adhesion coefficient increases with increasing penetration depth, and the greater the adhesion coefficient is, the higher the tightness between the pile and soil will be. As a method of determining the interfacial tightness between the pile and soil, the adhesion coefficient is closely related to the excess pore water pressure and earth pressure generated during the pile jacking process and can accurately reflect the mechanical mechanism of pile jacking in saturated viscous soil. Results of this contribution can provide reference for theoretical research on the mechanical pile jacking mechanism in saturated viscous soil.

1. Introduction

Jacked piles are a significant component of many construction projects; hence, improving jacked pile technology is an urgent need [1–4]. The process of jacked pile sinking is considered to be static uniform speed penetration, and the pile side resistance is generated by the friction between the pile soil. Driven pile is sunk by the impact load of the pile hammer acting on the pile top, and the pile side resistance is generated under the action of the nonlinear pile soil with a large deformation of the dynamic height. However, many aspects of current jacked pile research are lacking [5–8]. Stress characteristics at the pile-soil interface have significant influence on the pile jacking process and long-term bearing

capacity. The variation law of excess pore pressure and earth pressure caused by pile jacking is also significant [9, 10]. At present, scholars at home and abroad primarily use theoretical methods to study changes in earth pressure and pore water pressure caused by jacked pile penetration. Cao et al. [11] studied the pile side pressure, excess pore water pressure, and pile side soil displacement in the pile jacking process based on circular hole expansion theory and obtained the earth pressure, pore water pressure, and shallow soil displacement around the pile under various conditions. Tehrani et al. [12] further modified the theoretical solution for circular hole expansion theory on pile body resistance and pile-soil effect by considering the surface roughness and obtained the change rule of earth pressure in the radial direction and with depth. Burns and Mayne [13] obtained the variation law of pore water pressure in the pile jacking permeation in fine sand, silt, and soft soil and carried out function fitting in combination with the theory of circular hole expansion. Sagaseta [14] examined pore water pressure and earth pressure using the strain path method by considering the influence of depth change on soil displacement and continuity of the pile penetration process. Hoang et al. [15] investigated the pile installation effects on the behaviors of jacked in piles through three simulation techniques. Both the experimental results and calculated results using three techniques agreed well and indicated that ground consolidation caused by pile installation increases the pile bearing capacity and the pile shaft resistance. Xue et al. [16] studied the experimental tests of four RC pile specimens backfilled with different damping material to assess their effect on the soil-structure hysteretic response. Theoretical formulas are commonly unable to accurately apply the actual mechanical conditions of practical projects, so the distribution rules of excess pore water pressure and earth pressure around piles obtained by theoretical research methods are nongeneral and difficult to be popularized.

On the basis of field tests, some scholars have obtained the variation rules for the excess pore water pressure and earth pressure in the pile jacking process. Hwang et al. [17] found that the dynamic change of pore pressure was closely related to the pile penetration process by embedding sensors in the affected soil layer at a certain distance around the pile to observe the pore water pressure and earth pressure of the full-length pile during the pile jacking process. Cooke and Price [18] pushed a test pile into overconsolidated London clay and tested the pore water pressure of the soil around the pile after the jacking pile. Pestana et al. [19] compared and analyzed the dissipation law and influence range of the excess pore water pressure based on a large number of field tests and believed that measuring excess pore water pressure could effectively predict property changes in foundation soil. Doherty and Gavin [20], based on the field tests, discussed the pore water pressure in the pile jacking process, and the end condition has a certain influence on the pore water pressure. The excess pore water pressure and earth pressure caused by jacked pile construction obtained by field test have a guiding significance for pile foundation construction.

In the pile jacking process, excess pore water pressure and earth pressure at the pile-soil interface are different from excess pore water pressure and earth pressure in the soil within a given range around the pile. Lehane [21], based on field tests, found that soil pressure at the pile-soil interface at various positions decreased with increasing h/B (h is the distance between the sensor and the pile end; B is the pile diameter). Bond and Jardine [22] comprehensively and accurately tested the pore water pressure and effective radial stress at the pile-soil interface during the pile jacking process and under static loading. Kou et al. [23] studied the law of pore water pressure dissipation when the jacked pile penetrates into silt deposited soil based on field tests. Liu et al. [24] examined the performance of an open pile penetrating into a silty layer using an indoor model test and obtained the accumulation law for excess pore water pressure in the soil. Studying the changes in excess pore water pressure and earth pressure at the pile-soil interface caused by pile jacking in cohesive soil is of great significance.

Accurately measuring the interfacial earth pressure and pore water pressure caused by jacked pile penetration and determining the degree of bonding between piles and soil through the variation law of effective earth pressure at the pile-soil interface in the pile jacking process are the major difficulties in studying the pile jacking mechanism. In practical engineering applications, pile jacking is mostly used in clay soil. Clay soil can better reproduce the actual working state of pile jacking, so it is necessary to carry out a pile jacking penetration mechanism in clay soil foundations study [25, 26]. At present, there are relatively few studies on the stress characteristics at the pile-soil interface during the pile jacking process in viscous soil, especially comparative studies on open- and closed-end piles. Aiming at the plugging effect caused by the open pipe pile in the process of pile jacking, a more detailed experimental study of "soil plug resistance" in the separation of pile immersion resistance can be carried out [27]. Obtaining the variation law of excess pore pressure and earth pressure caused by pile jacking is urgent and necessary. This article is based on open- and closed-end model piles with sensors as well as pile jacking and static load laboratory tests in viscous soil. The variation law of excess pore water pressure and earth pressure at pile-soil interface generated in the pile jacking process and under static loading is obtained, and the concept expressed by the adhesion coefficient of the compaction degree between the pile-soil and earth pressure is determined. Results of this study can provide reference for theoretical research on mechanical pile jacking in saturated viscous soil.

2. Theoretical Calculation Method for Pore Water Pressure

Simulating the pile penetration process is a relatively complex problem in theory. At present, the data measured in field or indoor pile penetration processes indicate that most of the earth pressure and pore water pressure can be estimated using cylindrical hole expansion theory. For the saturated elastic and completely plastic material subject to the Mohr-Coulomb yield criterion, the total stress increment caused by expansion of the cylindrical hole [28] is

$$\text{In the plastic zone } \begin{aligned} \Delta\sigma_r &= 2c_u \ln\left(\frac{R_p}{r}\right) + c_u, \\ \Delta\sigma_\theta &= 2c_u \ln\left(\frac{R_p}{r}\right) - c_u, \\ \Delta\sigma_z &= 2c_u \ln\left(\frac{R_p}{r}\right), \end{aligned} \tag{1}$$

$$\text{In the elastic zone } \begin{aligned} \Delta\sigma_r &= c_u \ln\left(\frac{R_p}{r}\right), \\ \Delta\sigma_\theta &= -c_u \ln\left(\frac{R_p}{r}\right), \\ \Delta\sigma_z &= 0. \end{aligned} \tag{2}$$

$\Delta\sigma_r$, $\Delta\sigma_\theta$, and $\Delta\sigma_z$ are, respectively, the radial, tangential, and vertical stress increment; R is the distance from the pile center; R_p is the radius of plastic zone; C_u is the undrained soil shear strength.

The pore water pressure increment can be calculated according to the Henkel formula [29], as follows:

$$\Delta u = \beta\Delta\sigma_{\mathrm{OCT}} + \alpha\Delta\tau_{\mathrm{OCT}}, \tag{3}$$

where $\Delta\sigma_{\mathrm{OCT}}$ and $\Delta\tau_{\mathrm{OCT}}$ are the normal stress increment and shear stress increment of octahedron, respectively, β and α are Henkel pore water pressure parameters, and $\beta = 1$ for saturated soil.

The relationship between the Henkel pore water pressure parameter α and Skempton pore water pressure parameter A is as follows [30]:

$$\alpha = 0.707\,(3A - 1). \tag{4}$$

By substituting (1), (2), and (4) into (3), the formula for calculating the excess pore water pressure in the soil around the pile can be obtained:

$$\begin{aligned} &\text{in the plastic zone } \frac{\Delta u}{C_u} = 2\ln\left(\frac{R_p}{r}\right) + 1.73A - 0.58, \\ &\text{in the elastic zone } \frac{\Delta u}{C_u} = 0.578\,(3A - 1)\left(\frac{R_p}{r}\right)^2, \\ &\text{on the surface of the pile } \frac{\Delta u_{\max}}{C_u} = \ln\left[\frac{E}{2(1+\mu)C_u}\right] + 1.73A - 0.58, \\ &\text{the radius of the plastic zone is } \frac{R_p}{r_0} = \sqrt{\frac{E}{2(1+\mu)C_u}}, \end{aligned} \tag{5}$$

where E is the elastic modulus of soil, μ is Poisson's ratio of soil, and R_0 is the pile radius.

3. Test Scheme

3.1. Model Box and Preparation of Foundation. The model test was carried out in a large-scale model box in the Qingdao University of Technology laboratory (Figure 1).

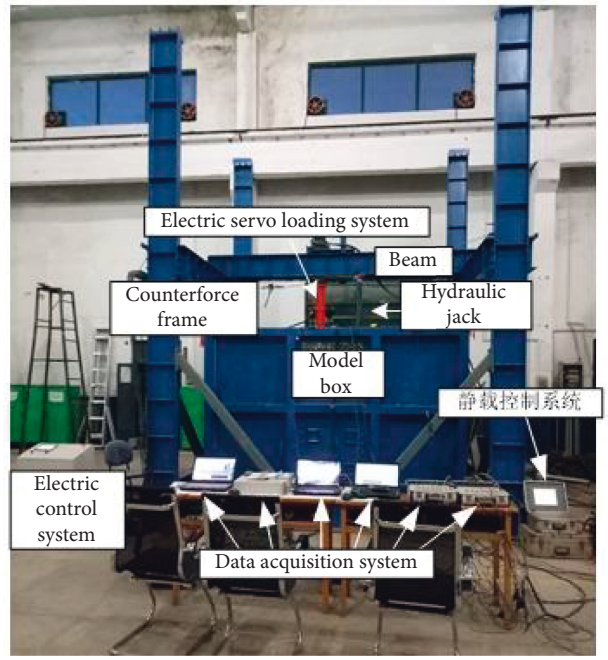

Figure 1: Large model test device.

The large-scale model's length × width × height is 2800 mm × 2800 mm × 2000 mm, and the model is placed on a base measuring 4 000 mm × 4 000 mm (length × width). The viscous soil used in the test comes from a silty clay layer, and the field soil samples are dried, crushed, screened, and sprayed with water to consolidate the soil [31]. The basic physical indexes of foundation soil after preparation are shown in Table 1.

3.2. Test Piles. In this paper, 2 test piles, TP1 and TP2, were tested using the indoor model test. The model pile was designed using aluminum material, with an elastic modulus of 72 GPa and Poisson's ratio of 0.3. According to similarity theory, the length of model piles TP1 and TP2 is 1000 mm, the outer diameter is 140 mm, and the inner diameter is 100 mm. Closed-end model pile TP1 is a single-wall model pipe pile with round pipe, and the pile end was installed using a flat plate with the same diameter as the pile. In order to effectively monitor the soil plug resistance on the inner wall of the pile, a double-wall open-end pipe pile TP2 was developed. A 20 mm gap was created between the inner and outer piper to create installation space for the microsensor and avoid damage to the sensor by soil entering into the pile.

3.3. Sensor Layout. In order to obtain the earth pressure and pore water pressure at the pile-soil interface, a silicon piezoresistive sensor was embedded in the model pile (Figure 2) [32]. The sensor range is specially customized according to the model experiments' earth pressure value, and the smaller the sensor's range, the smaller the sensor size. The earth pressure sensor and pore water pressure sensor surface are completely flush with the model pile surface. A silicon piezoresistive earth pressure sensor and pore water pressure

Table 1: Physical and mechanical parameters of foundation soil.

Soil classification	Relative density ds	Unit weight γ/(kN/cm^3)	Moisture content w (%)	Liquid limit w_L (%)	Plastic limit w_P (%)	Plasticity index I_p (%)	Cohesion c (kPa)	Internal friction angle φ/(o)	Compression modulus $E_{s1\text{-}2}$ (MPa)
Clay soil	2.73	18.0	35	35	21.2	13.5	14.4	8.6	3.3

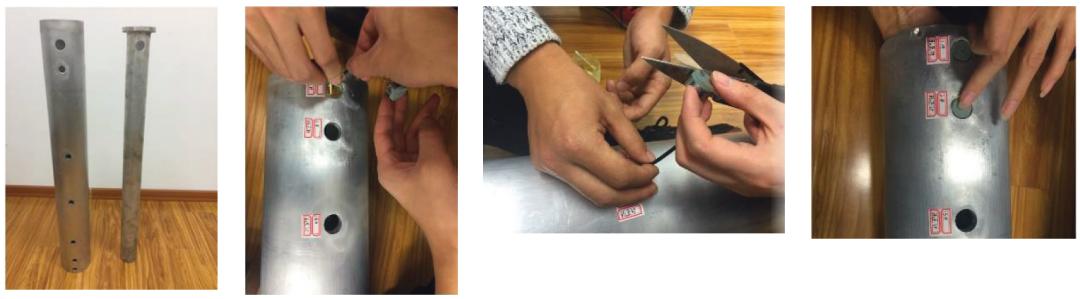

(a) (b) (c) (d)

Figure 2: Images showing the sensor installation process (unit: mm): (a) opening, (b) applying glue, (c) protection, and (d) installation.

sensor are installed on the same horizontal section using the same installation method. Six soil pressure and pore water pressure sensors were installed at unequal distances on the surface of the model pile, with a spacing of 50 mm, 100 mm, 200 mm, 200 mm, and 300 mm, respectively. The sensors were numbered 1#~6# from the pile end to the pile top, corresponding to $h/L = 1/20$, 1/10, 1/5, 2/5, 3/5, and 9/10 (h is the height between the sensor and pile end; L is the length of model pile). The force of the pile body near the pile end is significantly greater than the upper part of the pile body during pile jacking, and the closer it is to the pile end, the more obvious the effective radial stress degradation of the pile-soil interface is. Installing sensors at unequal distances on the surface of the model pile is beneficial to studying the length effect of the pile and the effective radial stress degradation of the pile interface caused by the length effect, which is conducive to accurately estimating the pile side friction resistance.

By placing temperature self-compensated fiber Bragg grating earth pressure sensor on the pile top loading platform, the change in pile jacking resistance can be obtained. A FS2200RM demodulator was used to automatically collect and save the FBG sensor data during the pile jacking process. The earth pressure and pore water pressure at the pile-soil interface were collected in real time using a CF3820 high-speed static signal test analyzer.

3.4. Experimental Scheme. The open and closed two pile types are sinking in the same test conditions. One time load is performed during the pile sinking process, the pile sinking speed is 300 mm/min, and the pile sinking depth is 900 mm. The soil layer of this test is homogeneous. To make the most of the test conditions, the open and closed piles are pressed into the soil in the middle of the model box. In this paper, through the development of open model piles and closed model piles with interface sensors, the indoor test of jacked sinking piles in open piles and closed piles in clay soil was carried out, and the changes in excess pore pressure and earth pressure of the pile-soil interface were studied.

4. Pile Jacking Test Results and Analysis

4.1. Pile Jacking Pressure during Pile Jacking. The pile jacking pressure was measured according to the total wavelength difference and the temperature wavelength difference during the pile jacking process using a temperature self-compensation pressure sensor. The pile jacking pressure formula is as follows [33]:

$$F = \frac{\Delta\lambda_B}{K_\varepsilon} A_p, \tag{6}$$

where F is pile jacking pressure, kN, $\Delta\lambda_B$ is the wavelength difference, nm, K_ε is the sensitivity coefficient, nm/MPa, and A_p is the cross-sectional area of the pile, m^2.

The change curve of pile jacking pressure with penetration depth during pile jacking is shown in Figure 3. TP1 and TP2 pile jacking pressure varies with penetration depth in a similar way, but TP1 has a larger pile jacking pressure, and the pile jacking pressure of TP1 is 15.8% greater than that in TP2 at the end of pile jacking because test pile TP2 is an open-end pipe pile, which forms a soil plug during the pile jacking process. The actual soil plug height of the model pile was small and the soil plug height was 329 mm when the burial depth was 900 mm. As a result, the pile jacking resistance and pile jacking pressure will be small. With continuous penetration of the pile into the soil, the stress state of the open-end pile gradually becomes similar to that of the closed-end pipe pile. The open pile is converted from a shallow partial occlusion that penetrates into the initial stage to a soil plug and will produce a plug effect; as the pile body penetrates, the earth plug is inside the pipe pile. The walls generate increasing friction until they are close to the degree

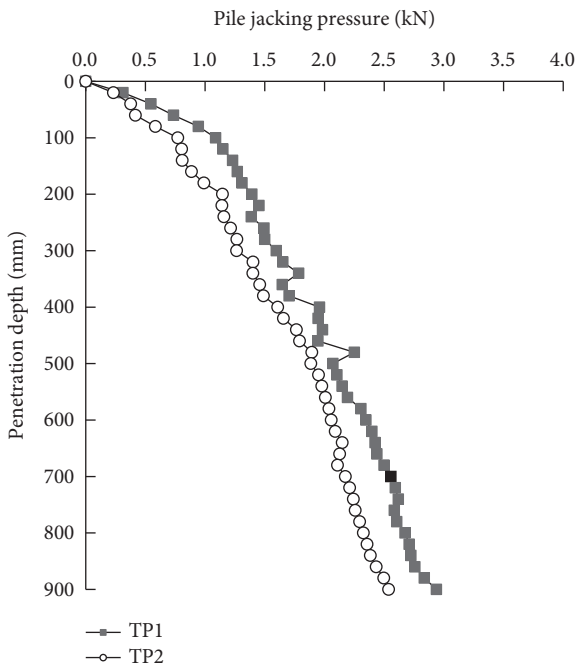

Figure 3: Pile driving pressure for open-end and closed-end piles.

of complete occlusion, presenting the sinking characteristics of closed piles.

4.2. Analysis of Excess Pore Water Pressure at Pile-Soil Interface. Pore water pressure is directly measured using a silicon piezoresistive pore water pressure sensor. The excess pore water pressure is the difference between the measured total pore water pressure and the hydrostatic pressure. The hydrostatic pressure is constant, and the change is the excess water pressure during pile jacking process and static load test process:

$$u_c = u - u_a, \tag{7}$$

where u_c is the excess pore water pressure, kPa, u is the total pore water pressure, kPa, and u_a is hydrostatic pressure, kPa.

With the increase of the depth of soil entry, the pressure of the soil covered around the pile increases, the extrusion and shearing effect of the soil around the pile become more and more intense, and the squeezing effect on the deep soil during the pile sinking process is more obvious. Under different penetration depths, the excess pore water pressure gradually increases with increasing depth, and the increasing trend is approximately a straight line at first followed by a sudden increase (Figure 4, the numbers of the legend in Figure 4 represent the penetration depths). During the pile jacking process, due to the continuous disturbance and compression of soft soil, too much pore water pressure is easily generated while the soil at the pile end suffers the greatest disturbance, so the excess pore water pressure at the pile end increases faster with increasing depth. At the same depth, excess pore water pressure decreases with increasing penetration depth because the amount of friction increases with increasing penetration depth, the soil is constantly disturbed, and the radial earth pressure on the pile side is gradually released, leading to a decrease in excess pore water pressure with increasing penetration depth at a certain depth.

By comparing the variation trend of excess pore water pressure between TP1 and TP2, it can be found that, with increasing depth, excess pore water pressure for test pile TP1 is generated faster because test pile TP1 is a closed-end pile, which has a significant soil squeezing effect in the pile jacking process and has a greater soil disturbance and radial deformation. As a result, the excess pore water pressure of test pile TP1 increases faster. As pile TP1 has a more significant soil squeezing effect than TP2, the excess pore water pressure for test pile TP1 is 1.04~1.24 times that of TP2.

4.3. Analysis of Earth Pressure at the Pile-Soil Interface. The change law of earth pressure at the pile-soil interface of the two test piles is consistent with the penetration depth (Figure 5). The deformation in the pile sinking process cannot be fully recovered after a certain time after the end of the pile, the radial effect force still exists, and the deformation during the loading process is superimposed on the deformation of the pile. Lateral earth pressure increases rapidly near the pile end with increasing depth because the area near the pile end has the greatest soil disturbance and produces the strongest compaction effect, and there is a compaction zone at the pile end, within which the overburden soil is heavy and the actual contact area of the pile soil is the largest, leading to a maximum earth pressure at the pile-soil interface and the fastest growth rate. At the same depth, the earth pressure at the pile-soil interface decreases with increasing penetration depth because at this depth, with increasing penetration depth, the amount of friction increases gradually, and there is a mud film between the pile and soil, which releases the earth pressure at the pile-soil interface. Therefore, the earth pressure at the pile-soil interface at the same depth decreases with increasing depth.

Compared with pile TP2, the earth pressure at the pile-soil interface of pile TP1 was higher, and the maximum earth pressure was 13.1% higher than that of pile TP2 because test pile TP1 is a closed-end pile, and its compaction effect is more significant than that of the open-end pile TP2 with the same diameter (Figure 5). Pile TP1 also has a greater disturbance to the soil; therefore, the earth pressure at the pile-soil interface of the test pile TP1 is larger.

4.4. Analysis of Effective Earth Pressure at the Pile-Soil Interface. The effective earth pressure at the pile-soil interface can be calculated by the following formula:

$$\sigma' = \sigma - \mu_c, \tag{8}$$

where σ' is the effective earth pressure, kPa, σ is the total earth pressure, kPa, and μ_c is the excess pore water pressure, kPa.

The curve of the effective earth pressure at the pile-soil interface is similar to that at the pile-soil interface with varying earth pressure with depth (Figure 6). The effective

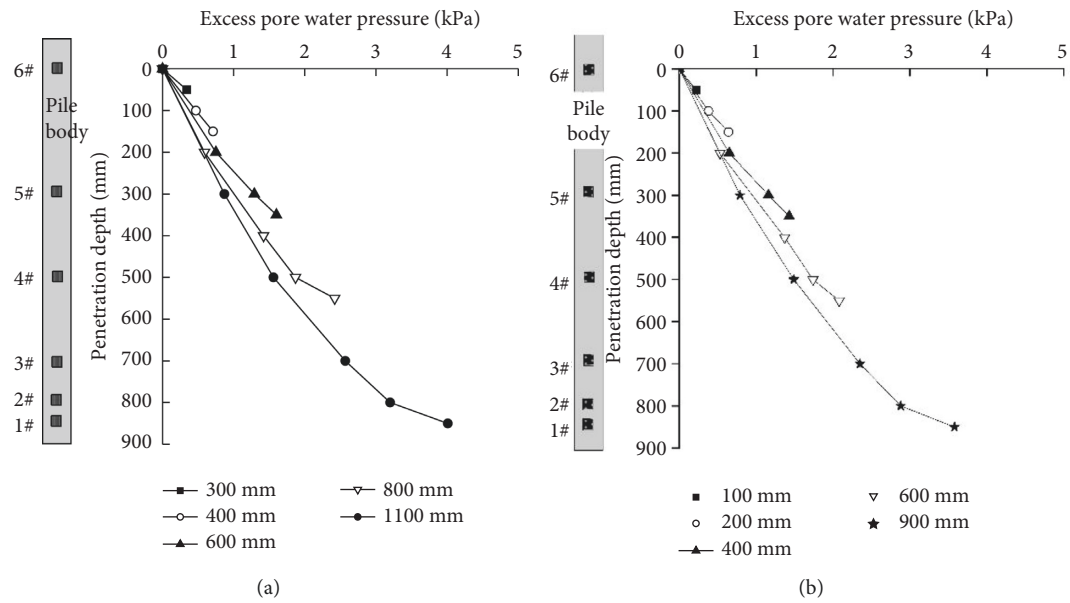

Figure 4: Excess pore water pressure distribution diagram for test piles TP1 and TP2 during the sinking process: (a) TP1, (b) TP2.

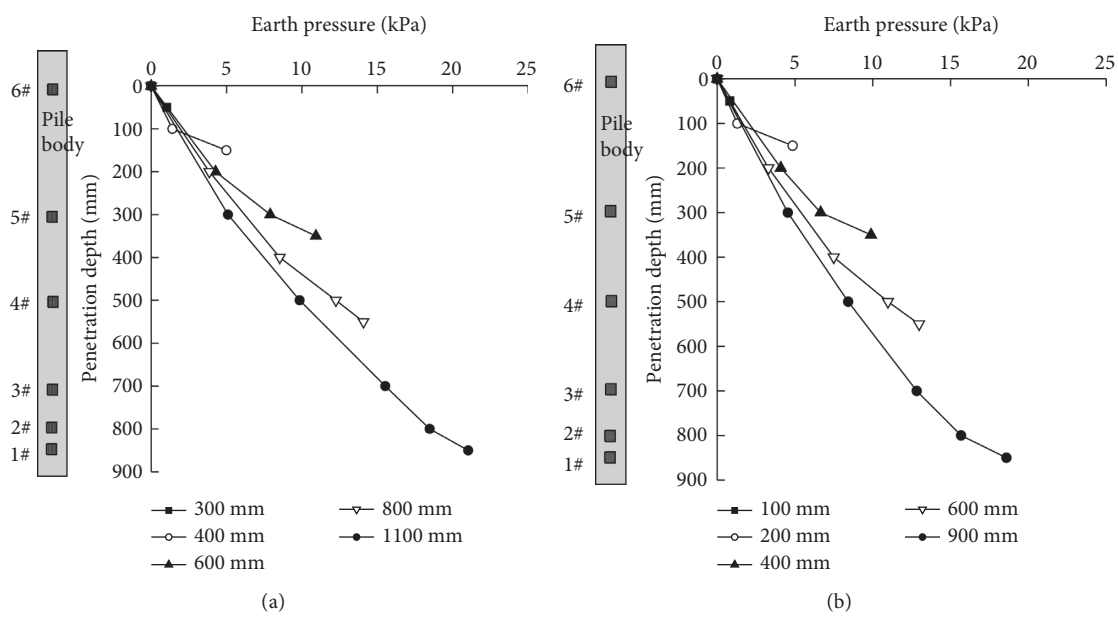

Figure 5: Distribution of earth pressure for test piles TP1 and TP2 during pile jacking: (a) TP1, (b) TP2.

earth pressure at the pile-soil interface increases gradually with increasing penetration depth and increases faster at the pile end due to the increased soil squeezing effect. At the same depth, the effective earth pressure at the pile-soil interface deteriorates. The effective earth pressure at the pile-soil interface is an important part of the earth pressure at the pile-soil interface. The degradation of effective earth pressure at the pile-soil interface is the main reason for the degradation of pile side friction. The experimental results further confirm that there is a degradation effect of pile side friction resistance at the same depth in the penetration process, and the relative distance of pile end h/D has a certain influence on pile side friction resistance, and when calculating pile side friction resistance, due to the friction resistance of the inner side of the open pile, it is necessary to consider the influence of the soil plug effect on the outer friction resistance of the pile.

Because the ratio between the excess pore water pressure and the earth pressure at the pile-soil interface is small, the effective earth pressure at the pile-soil interface of pile TP1 is also greater than that of pile TP2. Because pile TP1 is a closed-end pile, the effective earth pressure at the pile-soil interface of pile TP1 during the whole pile jacking process is 1.7%~23.7% higher than that of pile TP2.

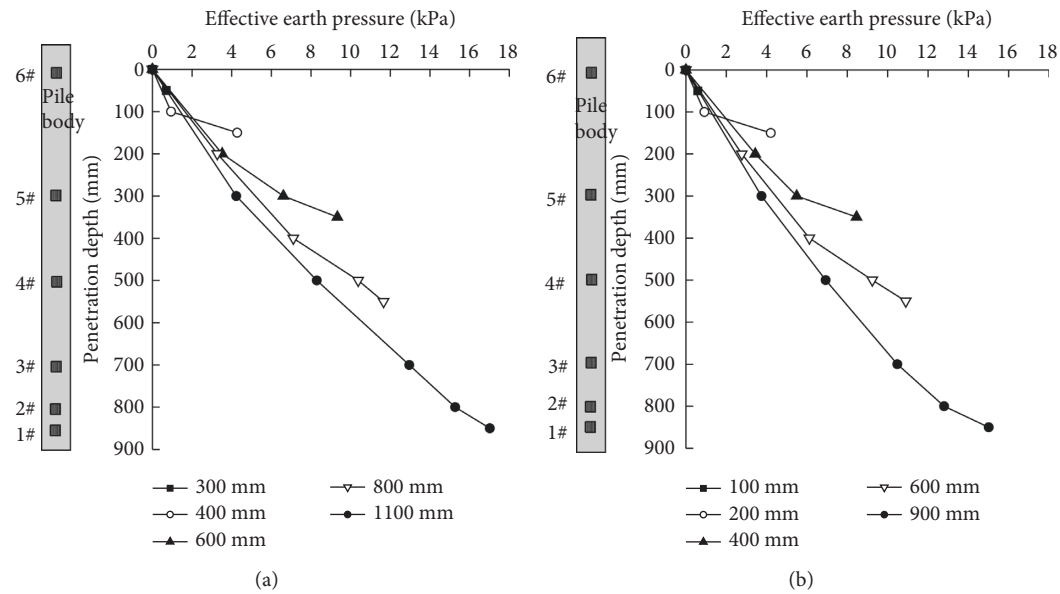

Figure 6: Distribution of effective earth pressure on test piles TP1 and TP2 during pile jacking: (a) TP1, (b) TP2.

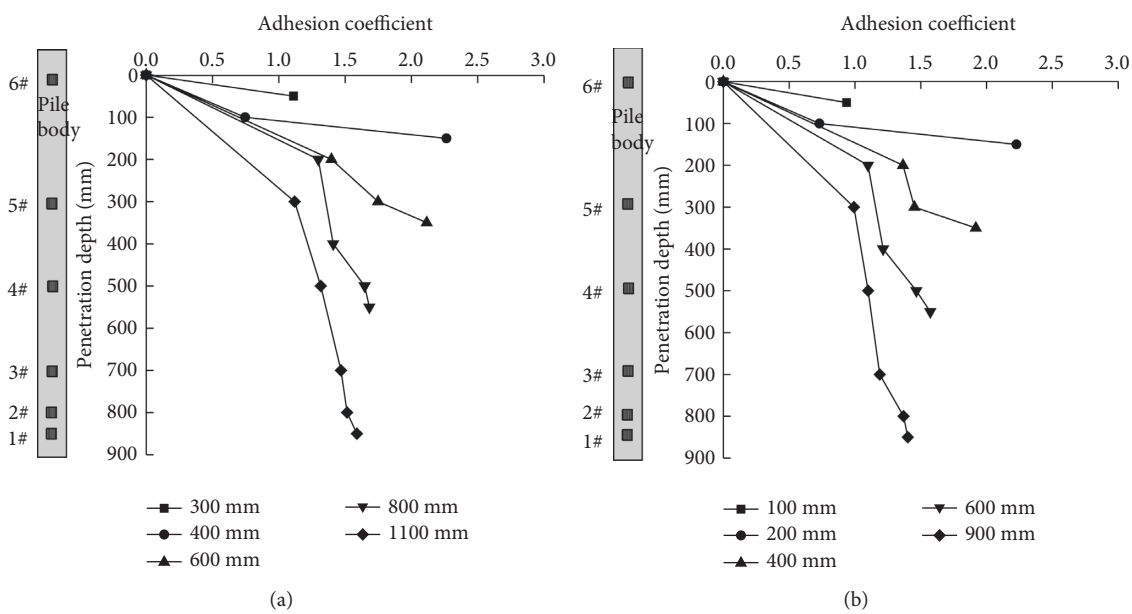

Figure 7: Change trend of adhesion coefficient of the pile-soil interface during pile jacking process: (a) TP1, (b) TP2.

4.5. Analysis of Pile-Soil Interface Adhesion Coefficient. The pile-soil interface adhesion coefficient represents the adhesion degree between the pile and soil; that is, the adhesion coefficient is equal to the ratio of effective earth pressure P' and horizontal deadweight stress σ_{cx} at the pile-soil interface. The adhesion coefficient t_c can be customized according to the following formula:

$$t_c = \frac{P'}{\sigma_{cx}}, \tag{9}$$

where when $t_c = 0$, the pile and soil is isolated. At $t_c > 1$, the effective earth pressure is greater than the original horizontal deadweight stress due to compaction.

The greater the effective earth pressure at the pile-soil interface, the greater the adhesion coefficient of the pile-soil interface and the higher the adhesion degree between the pile and soil, that is, the larger the actual contact area between pile and soil.

The adhesion coefficient at different pile depths increases with increasing penetration depth and is greater than 1 at greater depths because with increasing depth, the soil squeezing effect increases gradually, the effective earth pressure at the pile-soil interface increases at a faster speed, and the value is higher than the horizontal deadweight stress, and the higher amplitude increases with depth, so the adhesion coefficient of the pile-soil interface increases with

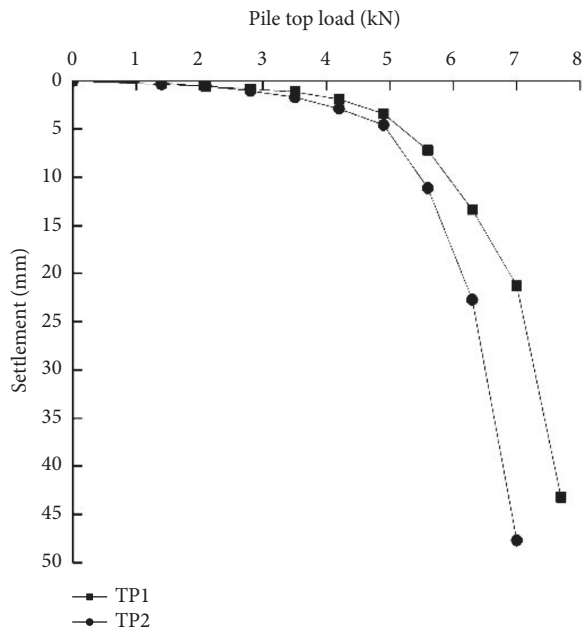

Figure 8: Q-s curve.

penetration depth (Figure 7). It further indicates that the higher the effective earth pressure at the pile-soil interface, the tighter the adhesion between pile and soil and the greater the actual contact area between pile and soil, which is manifested as a gradual increase in pile side resistance. At the same depth, the adhesion coefficient decreases gradually with increasing depth. The reasons are as follows: with increasing depth, the amount of shear and friction at the same depth increases, the pile side stress is gradually released, the effective earth pressure at the pile-soil interface decreases, and the adhesion coefficient of the pile-soil interface decreases with increasing depth. The degree of adhesion between piles and soil is weakened, indicating that the pile side resistance degrades along with the depth at the same depth.

5. Static Load Test Results and Analysis

5.1. Q-s Curve Analysis. Q-s curves can reflect load transfer behavior, pile-soil interactions, and pile failure mode; hence, analyzing Q-s curves is helpful for examining the vertical compressive bearing behavior of a single pile. The pile top settlement of test piles TP1 and TP2 changes with pile top load (Figure 8).

The Q-s curves of the two test piles show a steep drop (Figure 8). The curve is roughly divided into three stages: when the load is less than 3.5 kN, the curve is approximately straight line; when the load of test pile TP1 is greater than 3.5 kN and less than 6.3 kN, and the load of TP2 is greater than 3.5 kN and less than 5.6 kN, the curve entered the bending section; when the load of test pile TP1 is greater than 6.3 kN and TP2 is greater than 5.6 kN, the curve showed a steep drop. The soil around the pile will yield in the last two stages.

When the final load is applied, the pile top displacement values of test piles TP1 and TP2 are 43.24 mm and 47.72 mm, respectively, reaching the test end conditions specified in the code [26]. The ultimate bearing capacities of the two test piles in soft soil are 7.0 kN and 6.3 kN, respectively. After pile compression is completed, the pore water pressure in the soil beside the pile gradually dissipates over time, the soil reconsolidates, and the soil strength gradually recovers. The final pressures of test piles TP1 and TP2 are 2.94 kN and 2.54 kN, respectively. After 30 days of static load testing, the vertical bearing capacities of a single TP1 and TP2 pile were measured to be 2.38 and 2.48 times the final pressure, respectively. With the development of thixotropic recovery and consolidation aging, bearing capacity significantly increases. Compared with TP1, the final pressure and vertical bearing capacity of TP2 are smaller, but after the rest period, the development of bearing capacity is similar to TP1. The reason is that test pile TP2 is an open-end pile, which will produce soil plug in the process of pile jacking, and the soil plug is basically closed at the end of pile jacking. After the rest period, the soil plug and the pile wall are more closely bonded, and the soil around the pile is gradually consolidated and restored. It is more similar to the stress state of the closed-end pile, so the development of the bearing capacity is similar after the rest period.

5.2. Analysis of Results of Excess Pore Water Pressure at the Pile-Soil Interface. Under the action of various loads, the excess pore water pressure of pile TP2 increases gradually with increasing depth (Figure 9). The curve above 800 mm is steep; that is, the development of excess pore water pressure is slow with increasing depth. The curve below 800 mm becomes shallower; that is, the excess pore water pressure grows faster with increasing depth because in the process of static loading, the pile and soil undergo relative displacement and soil disturbance increase near the pile end, resulting in a rapid increase in excess pore water pressure at the pile end. With increasing load at the same depth, the excess pore water pressure at the pile-soil interface increases gradually. With increasing pile top load, the relative displacement between pile and soil increases, the soil compaction degree increases, and the excess pore water pressure at the pile-soil interface increases.

Compared with the value of the excess pore water pressure generated in the pile jacking process and under static load, the excess pore water pressure generated under static load is smaller. When the pile top load is 7.0 kN, the maximum excess pore water pressure at the pile end is 1.46 kPa, which is only 40.8% of the excess pore water pressure generated during pile jacking. The relative displacement between the pile and soil is small during static loading, the disturbance degree is small, and the compaction degree of soil is also small. In the pile jacking process, soil is continuously expelled outward, which causes significance disturbance to the soil, and the excess pore water pressure generated during pile jacking is large.

5.3. Analysis of Earth Pressure at the Pile-Soil Interface. Under the pile top load at all levels, the earth pressure at pile-soil interface increases in a straight line with increasing

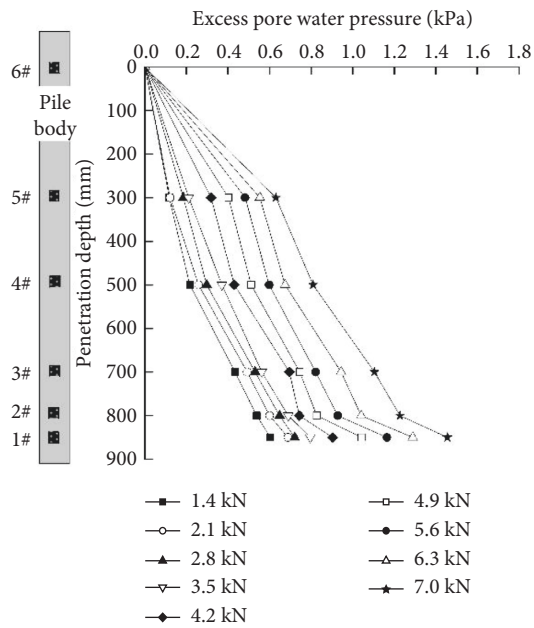

Figure 9: Change in excess pore water pressure of test pile TP2 with depth under various loads.

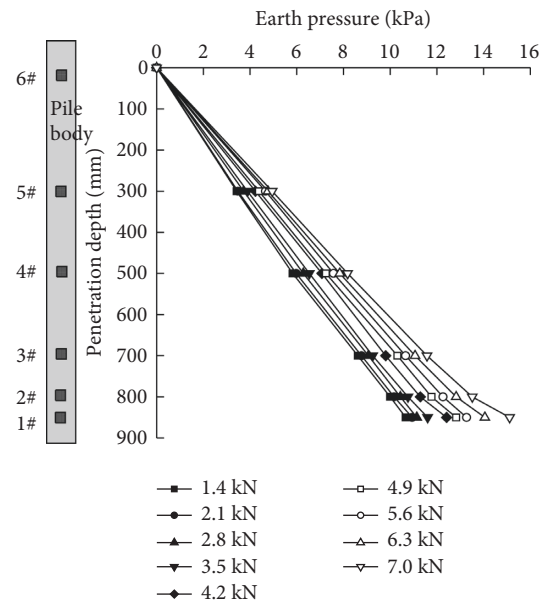

Figure 10: Variation of earth pressure at the pile-soil interface of TP2 with depth under various loads.

depth (Figure 10). The overburden soil weight increases with increasing depth, which makes the earth pressure at the pile-soil interface increase gradually. At the same depth, the earth pressure at the pile-soil interface gradually increases with increasing pile top load, and the increasing amplitude also shows a gradual increasing trend. With increasing pile top load, the pile top settlement increases, and the radial earth pressure increases with the soil compaction degree increasing.

Compared with the earth pressure at the pile-soil interface in the pile jacking process, the earth pressure at the pile-soil interface in the process of static load is smaller because the pile jacking mechanism is different from that of static loading. Pile jacking is a dynamic process, in which the soil around the pile is continuously displaced, the soil squeezing effect is strong, the generated earth pressure at the pile-soil interface is large, and the earth pressure "degrades" with increasing penetration depth at the same depth. In the static loading process, the pile top settlement is relatively small. Due to the small compaction degree of the pile top settlement relative to the surrounding soil, the earth pressure at the pile-soil interface is relatively small. In the static load process, the duration of each loading stage is relatively long, and the strength of disturbed soil gradually recovers.

5.4. Analysis of Effective Earth Pressure at the Pile-Soil Interface. The effective earth pressure at the pile-soil interface is similar to the change curve of earth pressure in Figure 10 (Figure 11). The effective earth pressure at the pile-soil interface increases gradually with increasing depth and increases approximately in a straight line. The effective earth pressure is the difference between the earth pressure and the excess pore water pressure, which only accounts for 3.4%~12.7% of the earth pressure and plays a small role. Therefore,

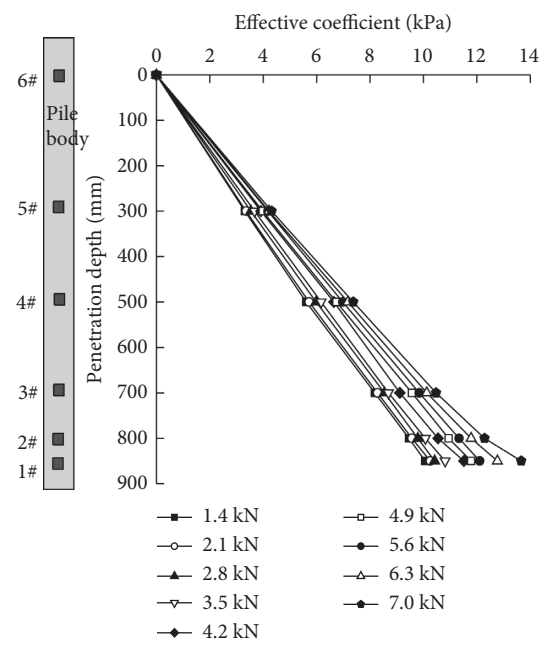

Figure 11: Variation curve of effective earth pressure of TP2 with depth under various loads.

the variation trend of the effective earth pressure at the pile-soil interface is similar to that of the earth pressure. With increasing pile top load, the amplitude of effective earth pressure gradually increases, and the closer it is to the pile end, the larger the amplitude increase is: the maximum is 0.0274 kPa/mm. With increasing pile top load, the compaction effect of the pile on soil increases gradually, and the closer it is to the pile end, the stronger the compaction effect becomes. In addition, compared with the pile jacking process, due to the longer load holding time in the static loading process, the pile body settlement is smaller, the soil

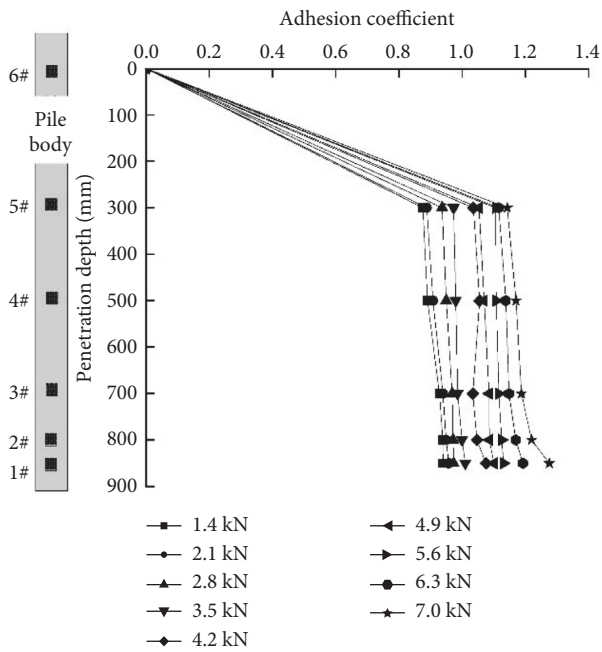

Figure 12: Variation curve of TP2 adhesion coefficient with depth under various loads.

squeezing effect is weaker, and the effective earth pressure on the side of the pile is also smaller. The adhesion coefficient values in this paper are slightly less than the values based on Meyerhof failure mode of ultimate bearing capacity.

5.5. Analysis of Adhesion Coefficient of the Pile-Soil Interface. Under the action of various loads, adhesion coefficient increases gradually with increasing depth, and when the pile top load is small, the pile side resistance shows a trend of large up and small down (Figure 12). Under the action of pile top load, pile settlement occurs, and with increasing depth, the actual contact area between pile and soil increases, resulting in a gradual increase of adhesion coefficient with the depth. The pile side resistance is gradually exerted from top to end, and the pile side resistance caused by the lower soil layer is less when the load is small. With increasing pile top load, the pile side resistance of the upper soil layer is gradually fully exerted, while that of the lower soil layer begins exerting. Under the action of maximum pile top load, the pile side resistance always increases with depth.

At the same depth, with increasing pile top load, adhesion coefficient increases gradually, indicating that the adhesion degree between piles and soil increases gradually. With increasing pile top load, the pile top settlement gradually increases and the earth pressure at the pile-soil interface increases, which results in increasing the actual contact area between the pile and soil, increasing the adhesion degree between the pile and soil and showing that the pile side resistance increases with increasing pile top load at the same depth. Numerically, the adhesion coefficient at the position of the #1 to #5 sensors ranges within 0.875–1.275, which is approximately 1, indicating that the earth pressure in the static loading process is approximately the static earth pressure.

6. Conclusion

In this paper, through large-scale indoor model tests of open- and closed-end pile jacking in saturated viscous soil, the change rules of effective earth pressure and adhesion coefficient at the pile-soil interface during pile jacking and static load test are examined, and the following conclusions are drawn:

(1) Under different pile depths, the excess pore water pressure, earth pressure, and effective earth pressure at the pile-soil interface of the open- and closed-end pile increase gradually with penetration depth, and the increase trend is approximately a straight line at first, followed by a sudden increase at the pile end. The soil squeezing effect of the closed-end pile is more significant than that of the open-end pile. The excess pore water pressure for closed-end pile is 1.04~1.24 times the open-end pile. The maximum earth pressure at the pile-soil interface of closed-end pile was 13.1% higher than that of open-end pile. At the same penetration depth, the excess pore water pressure, earth pressure, and effective earth pressure decrease with increasing penetration depth; that is, there is a "side pressure degradation" phenomenon, and the "degradation" phenomenon of open- and closed-end pile is consistent.

(2) The excess pore water pressure and effective earth pressure of the pile-soil interface gradually increase with the depth increasing during the pile sinking process. The incremental amplitude is related to the different h/D positions of the pile body at the end of the pile sinking. The increment amplitude decreases as h/D increases. The incremental amplitude of the closed-end pile at the same h/D position is greater than that of the open-end pile.

(3) Compared with the excess pore water pressure, the earth pressure and effective earth pressure generated during pile jacking and the force generated during static loading are relatively small. The maximum excess pore water pressure at the pile end is only 40.8% of the excess pore water pressure generated during pile jacking. Earth pressure does not "degrade" during static loading.

(4) In static load test, adhesion coefficient increases with increasing depth. At the same depth, with increasing pile top load, adhesion coefficient and adhesion degree of the pile-soil interface gradually increase.

Data Availability

The data used to support the findings of this study are available from the corresponding author upon request.

Conflicts of Interest

The authors declare that they have no conflicts of interest.

Acknowledgments

This research was supported by the National Key Research and Development Plan (2021YFE0113400).

References

[1] J. Yang, L. G. Tham, P. K. K. Lee, and S. T. F. Chan, "Behaviour of jacked and driven piles in sandy soil," *Géotechnique*, vol. 56, no. 4, pp. 245–259, 2006.

[2] Z. Wang, L. Miao, and F. Wang, "Theoretical and numerical analysis of jacked pile in sand," in *Proceedings of the Geo Congress 2012: State of the Art and Practice in Geotechnical Engineering*, pp. 245–254, Oakland, CA, USA, 2012.

[3] L. Li, J. Li, D. A. Sun, and L. Zhang, "Time-dependent bearing capacity of a jacked pile: an analytical approach based on effective stress method," *Ocean Engineering*, vol. 143, pp. 177–185, 2017.

[4] L. M. Zhang and H. Wang, "Field study of construction effects in jacked and driven steel H-piles," *Géotechnique*, vol. 59, no. 1, pp. 63–69, 2009.

[5] S. Yan, Z. Jia, W. Liu, and J. Li, "Research on the large diameter and supper long pile running under self-weight in the ocean engineering," *Journal of Coastal Research*, vol. 73, no. sp1, pp. 809–814, 2015.

[6] D. Chaney, K. Demars, and J. H. Chin, "Tests on model jacked piles in calcareous sand," *Geotechnical Testing Journal*, vol. 19, no. 2, p. 164, 1996.

[7] W. Lee, W.-J. Lee, S.-B. Lee, and R. Salgado, "Measurement of pile load transfer using the Fiber Bragg Grating sensor system," *Canadian Geotechnical Journal*, vol. 41, no. 6, pp. 1222–1232, 2004.

[8] G.-W. Li, H.-F. Pei, J.-H. Yin, X.-C. Lu, and J. Teng, "Monitoring and analysis of PHC pipe piles under hydraulic jacking using FBG sensing technology," *Measurement*, vol. 49, pp. 358–367, 2014.

[9] J. P. Cater, M. F. Randolph, and C. P. Wroth, "Stress and pore pressure changes in clay during and after the expansion of a cylindrical cavity," *International Journal for Numerical and Analytical Methods in Geomechanics*, vol. 3, no. 4, pp. 305–322, 1979.

[10] S.-L. Shen, J. Han, H.-H. Zhu, and Z.-S. Hong, "Evaluation of a dike damaged by pile driving in soft clay," *Journal of Performance of Constructed Facilities*, vol. 19, no. 4, pp. 300–307, 2005.

[11] L. F. Cao, C. I. Teh, and M. F. Chang, "Undrained cavity expansion in modified Cam clay I: theoretical analysis," *Géotechnique*, vol. 51, no. 4, pp. 323–334, 2001.

[12] F. S. Tehrani, F. Han, R. Salgado, M. Prezzi, R. D. Tovar, and A. G. Castro, "Effect of surface roughness on the shaft resistance of non-displacement piles embedded in sand," *Géotechnique*, vol. 66, no. 5, pp. 1–15, 2016.

[13] S. E. Burns and P. W. Mayne, "Pore pressure dissipation behavior surrounding driven piles and cone penetrometers," *Transportation Research Record: Journal of the Transportation Research Board*, vol. 1675, no. 1, pp. 17–23, 1999.

[14] C. Sagaseta, "Analysis of undrained soil deformation due to ground loss," *Géotechnique*, vol. 37, no. 3, pp. 301–320, 1987.

[15] L. T. Hoang, K. X. Dao, X. Xiong, and T. Matsumoto, "Performance analysis of a jacked-in single pile and pile group in saturated clay ground," *Soils and Foundations*, vol. 62, no. 1, Article ID 101094, 2022.

[16] J. Xue, A. Aloisio, Y. Lin, M. Fragiacomo, and B. Briseghella, "Optimum design of piles with pre-hole filled with high-damping material: experimental tests and analytical modeling," *Soil Dynamics and Earthquake Engineering*, vol. 151, Article ID 106995, 2021.

[17] J.-H. Hwang, N. Liang, and C. H. Chen, "Ground response during pile driving," *Journal of Geotechnical and Geoenvironmental Engineering*, vol. 127, no. 11, pp. 939–949, 2001.

[18] R. W. Cooke and G. Price, "Strains and displacements around friction piles," in *Proceedings of the 8th International Conference on Soil Mechanics and Foundation Engineering*, pp. 53–60, Moscow, 1973.

[19] J. M. Pestana, C. E. Hunt, and J. D. Bray, "Soil deformation and excess pore pressure field around a closed-ended pile," *Journal of Geotechnical and Geoenvironmental Engineering*, vol. 128, no. 1, pp. 1–12, 2002.

[20] P. Doherty and K. Gavin, "Shaft capacity of open-ended piles in clay," *Journal of Geotechnical and Geoenvironmental Engineering*, vol. 137, no. 11, pp. 1090–1102, 2011.

[21] B. M. Lenane, *Experimental Investigations of Pile Behaviour Using Instrumental Field piles [Dissertation]*, University of London (Imperial College), London, 1992.

[22] A. J. Bond and R. J. Jardine, "Shaft capacity of displacement piles in a high OCR clay," *Géotechnique*, vol. 45, no. 1, pp. 3–23, 1995.

[23] H. L. Kou, M. Y. Zhang, and F. Yu, "Shear zone around jacked piles in clay," *Journal of Performance of Constructed Facilities*, vol. 29, no. 6, Article ID 04014169, 2015.

[24] J. W. Liu, Z. M. Zhang, F. Yu, and Z.-Z. Xie, "Case history of installing instrumented jacked open-ended piles," *Journal of Geotechnical and Geoenvironmental Engineering*, vol. 138, no. 7, pp. 810–820, 2012.

[25] M. Y. Fattah, B. S. Zbar, and F. S. Mustafa, "Effect of soil saturation on load transfer in a pile excited by pure vertical vibration," *Proceedings of the Institution of Civil Engineers - Structures and Buildings*, vol. 174, no. 2, pp. 132–144, 2021.

[26] Y.-Y. Wang, S.-K. Sang, M.-Y. Zhang, D.-S. Jeng, B.-X. Yuan, and Z.-X. Chen, "Laboratory study on pile jacking resistance of jacked pile," *Soil Dynamics and Earthquake Engineering*, vol. 154, Article ID 107070, 2022.

[27] M. Y. Fattah and W. H. S. Al-Soudani, "Bearing capacity of closed and open ended pipe piles installed in loose sand with emphasis on soil plug," *Indian Journal of Geo-Marine Sciences*, vol. 45, no. 5, pp. 703–724, 2016.

[28] A. J. Abbo and S. W. Sloan, "A smooth hyperbolic approximation to the Mohr-Coulomb yield criterion," *Computers & Structures*, vol. 54, no. 3, pp. 427–441, 1995.

[29] Y.-Q. Tang, Z.-D. Cui, X. Zhang, and S.-K. Zhao, "Dynamic response and pore pressure model of the saturated soft clay around the tunnel under vibration loading of Shanghai subway," *Engineering Geology*, vol. 98, no. 3-4, pp. 126–132, 2008.

[30] R. M. Buckley, R. J. Jardine, S. Kontoe, and B. M. Lehane, "Effective stress regime around a jacked steel pile during installation ageing and load testing in chalk," *Canadian Geotechnical Journal*, vol. 55, no. 11, pp. 1577–1591, 2018.

[31] "The national standards compilation group of people's Republic of China," *GB/T50123-1999 Standard for Soil Test Method*, China Planning Press, Beijing, 1999.
[32] Y. Wang, X. Liu, M. Zhang, and S. S. Yang, "Field test of excess pore water pressure at pile-soil interface caused by PHC pipe pile penetration based on silicon piezoresistive sensor," *Sensors*, vol. 20, no. 10, Article ID 2829, 2020.
[33] M. Yegian and G. Wrights, "Lateral soil resistance displacement relationships for pile fundation in soft clays," in *Proceedings of the Offshore Technology Conference*, Houston, Texas, April 1973.

Hindawi
Advances in Civil Engineering
Volume 2022, Article ID 3245305, 8 pages
https://doi.org/10.1155/2022/3245305

Research Article

Health Assessment of Foundation Pit Based on the Fuzzy Analytical Hierarchy Process

Jinbo Sun,[1] Ke Sun,[2,3] Liang Gong,[1] Sheng Gu,[1] and Hao Hao[4]

[1]*School of Civil Engineering, Southeast University, Nanjing 211189, Jiangsu, China*
[2]*School of Civil Engineering and Architecture, Jiangsu University of Science and Technology, Zhenjiang 212100, China*
[3]*College of Civil Engineering, Nanjing Tech University, Nanjing 211816, China*
[4]*Management Committee of China (Nanjing) Software Valley, Nanjing 210012, Jiangsu, China*

Correspondence should be addressed to Ke Sun; sunke27@163.com and Liang Gong; 12600244@qq.com

Received 19 December 2021; Accepted 10 May 2022; Published 30 May 2022

Academic Editor: S. P. Pradhan

Many monitoring indexes affect the health condition of foundation pits to different extents. How to use a massive on-site monitoring dataset to quantitatively assess the health of foundation pits is a problem that deserves due consideration. This paper proposes a foundation pit health assessment model based on the fuzzy analytical hierarchy process (AHP) method. First, factors affecting the health of foundation pits are classified by the AHP, a hierarchical factor system for foundation pit health assessment is established, and the index scale method is used to assign weights to assessment factors at different hierarchical levels. Combined with the fuzzy mathematical method, the membership functions of four health degree levels (A to D) are constructed, and the determination range of each health degree level is given to realize the quantitative calculation of the health condition from the bottom-level assessment factor to the overall foundation pit. Considering that each assessment factor involves many monitoring points and different monitoring data, a comprehensive assessment operator is also constructed to highlight the most adverse impact. Finally, the proposed model is used to perform a health assessment of an actual foundation pit project, and the variation in the foundation pit health during the entire monitoring period is obtained. The health grade of the foundation pit is determined to be B, which is a basically healthy condition consistent with the on-site inspection results.

1. Introduction

With the continuous growth of the global population and the development of urbanization, infrastructure construction is booming, and the number of foundation pit accidents consequently shows a significant increasing trend, which not only increases economic investment and delays the construction period but also endangers the safety and property of people nearby, causing adverse social impacts. Therefore, accurately monitoring and assessing the health condition of foundation pits, understanding their existing or potential weaknesses, and determining the necessary remedial measures to ensure their safety and reliability are continually popular topics [1–4].

Studies on foundation pit problems were initially focused on the deformation and reliability of foundation pit support structures. Terzaghi et al. [5] proposed a total stress analysis method to estimate the relationship between excavation stability and support load. This classical theory is still in use today. Later, Bjerrum and Eide [6], Matsuo and Kawamura [7], and Hashash and Whittle [8] each analyzed the mechanisms of various failure modes and the influences of uncertain factors of foundation pit support systems and carried out reliability analyses and system reliability assessments. As foundation pits deepen and widen, deformation of their structure will cause changes in the surrounding environment and structure, potentially leading to severe engineering accidents [9–13]. To address this problem, structural health monitoring technology has been popularized in large-scale foundation pit projects. By deploying various types of sensors, it is possible to accurately monitor the changes in the support structure of the foundation pit structure and the

surrounding environment [14–17]. However, there are many indexes that can be monitored, and it is not easy to determine the impact of each index on the overall health of the foundation pit. This is especially problematic when the monitoring data of different measurement points differ greatly for the same index. Therefore, effectively using a large amount of monitoring data to effectively determine the health condition of the overall foundation pit is an urgent problem [18].

On this basis, this paper proposes a foundation pit health assessment model based on the fuzzy analytical hierarchy process (AHP) method, and on-site monitoring data are applied to quantitatively calculate and assess the health of the foundation pit to verify the validity of the method.

2. Method and Procedure

The fuzzy AHP method is a comprehensive assessment method combining fuzzy mathematics [19] and the analytic hierarchy process [20]. With this method, the fuzzy transformation principle and the maximum membership principle are used to comprehensively consider the degree of association between the thing being assessed and each of its attributes and to determine its grade or type. The AHP can decompose a complex multiobjective decision-making problem into several individual indexes or several levels according to specific criteria and then obtain the assessment score of each index through a quantitative calculation method to provide the optimal assessment decision for the objective. The characteristic of this method is that human subjective judgment is mathematical and thinking, which can provide a basis for quantitative evaluation index, selection of optimal scheme, and system risk assessment, and has been widely used in the engineering field.

The basic idea of the fuzzy AHP method is to decompose the problem according to the nature and general goal of the multiobjective evaluation, form a hierarchical substructure from bottom to top, and then carry out a systematic quantitative assessment with the fuzzy mathematics method. Therefore, when using fuzzy AHP to make decisions, it can be generally divided into the following four steps:

(1) The problem is analyzed, the causal relationship between various factors in the system is determined, and a multilevel hierarchical structure model for multiple elements of the system objective is established.

(2) Weight assignment, that is, the factors of the same level (grade) and the factors of the higher level, is compared in pairs as criteria and determined their relative importance according to the evaluation scale. Pairwise comparisons using linguistic terms yield a set of weights for each level in the hierarchy, as shown in Table 1.

(3) The membership function of quantitative evaluation of a single factor can be established by the fuzzy mathematics method, and the health interval and corresponding threshold of each evaluation factor are determined.

(4) Systematic calculations use field monitoring data to assess the health of the foundation pit and provide guidance for subsequent work.

The operating procedure aiming at the foundation pit engineering health assessment is shown in Figure 1, and the detailed process will be described later.

3. Health Assessment Model

3.1. Assessment Factors and Weight Assignment. The health of a foundation pit is affected by various factors such as the geological condition, construction process, and surrounding environment. Items available for monitoring are many and unfixed, including retaining walls (piles), supports, columns, groundwater levels, neighboring buildings, and pipelines. At present, much experience in foundation pit construction has been accumulated with the rapid development of China's urbanization. In reference to the "Technical Code for Construction Safety of Deep Building Foundation Excavations" [21], the factors that determine the health of a foundation pit are subdivided level by level from top to bottom using the AHP.

The top level shows the overall health condition of the foundation pit, which is defined as the assessment factor T.

T is determined by both the structure of the foundation pit and the surrounding environment, so the assessment factor set of the second level can be defined as

$$T = \{C_1 \quad C_2\}, \tag{1}$$

where C_1 represents the health condition of the structure of the foundation pit, and C_2 represents the health condition of the environment around the foundation pit. C_1 and C_2 are further subdivided to obtain the bottom assessment factor set.

$$\begin{aligned} C_1 &= \{P_1 \quad P_2 \quad P_3 \quad P_4 \quad P_5\}, \\ C_2 &= \{P_6 \quad P_7 \quad P_8 \quad P_9\}, \end{aligned} \tag{2}$$

where P_1 to P_5 represent the settlement of the retaining wall, the horizontal displacement of the retaining wall, the horizontal displacement of the retained soil, the settlement of the column pile, and the axial force of the support, respectively, and P_6 to P_9 represent the settlement of the underground pipeline, settlement of the building, ground settlement, and groundwater level, respectively. P_1 to P_9 are the variables that must be monitored specifically in a general foundation pit project.

Weights should be assigned to each factor within the hierarchical structure. There is no specific criterion for the assignment. Referring to related research and expert experience [22], the importance of each factor within the hierarchical structure is compared pairwise. The index scale method [23] was used to assign weights, and the results are shown in Figure 2.

3.2. Health Condition Assessment Set. The ideas of structural health assessment are basically the same, most of which are implemented through hierarchical classification and the scoring method. In this paper, the health conditions of

Table 1: Linguistic terms.

	Equal importance	Moderate importance	High importance	Very high importance	Extreme importance	General expression
1 ~ 9 scale	1	3	5	7	9	m $m = 1 \sim 9$
Exponential scale	9^0 (1)	$9^{(1/9)}$ (1.277)	$9^{(3/9)}$ (2.08)	$9^{(7/9)}$ (4.237)	$9^{(9/9)}$ (9)	$9^{(K/9)}$ $K = 0 \sim 9$

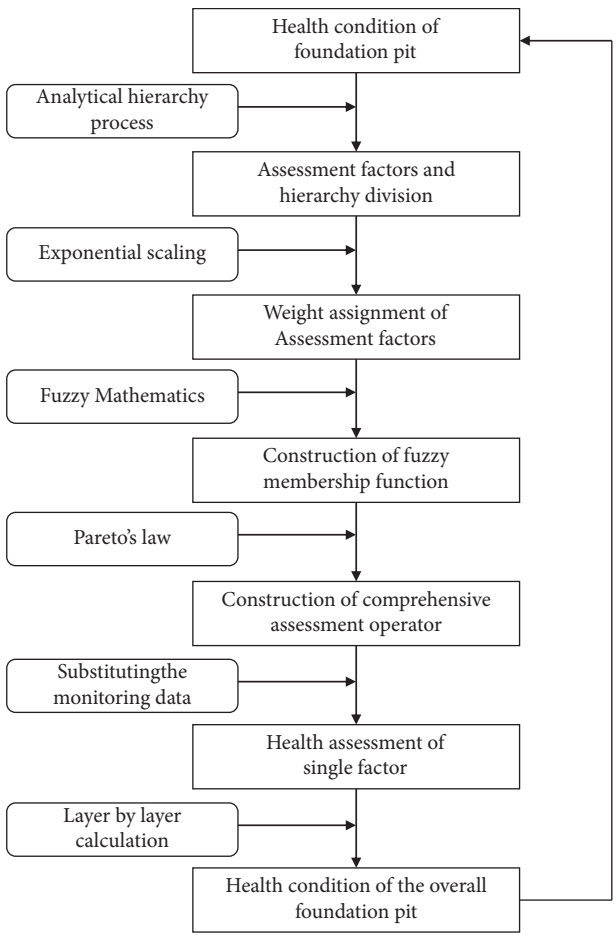

Figure 1: Health assessment process of foundation pit.

various assessment factors for a foundation pit are divided into four levels, A to D, corresponding to very healthy, basically healthy, subhealthy, and unhealthy conditions. The assessment set H is defined as

$$H = \{H_1, H_2, H_3, H_4\}, \tag{3}$$

where H_1 to H_4 correspond to the health grades of A to D. The level vector of the assessment set, G, is established as

$$G = [\,4 \;\; 3 \;\; 2 \;\; 1\,]. \tag{4}$$

3.3. Membership Functions and Grading Ranges. As the correlation between monitoring factors and the health condition of foundation pit is not clear, there is a certain ambiguity, and then, the fuzzy membership function is used to calculate the membership degree of the bottom-level factors in the hierarchical structure for foundation pit health assessment of the health assessment set G. Assuming that the health of a foundation pit project is linearly related to the actual monitoring data of each factor, the membership function of the health grades can be constructed using the triangular distribution and trapezoidal distribution in fuzzy mathematics, as shown in Figure 3.

In Figure 3, K_1 to K_3 are the thresholds for the four health ranges, whose values vary with the objects of assessment factors and must be determined based on engineering practice and industry standards. In Figure 3, the membership functions for the four health grades (A to D) are as follows:

$$\mu_A(x) = \begin{cases} 1, & x < a_1, \\ \dfrac{x - a_2}{a_1 - a_2}, & a_1 \le x \le a_2, \\ 0, & x > a_2, \end{cases} \tag{5}$$

$$\mu_B(x) = \begin{cases} 0, & x < a_1, \\ \dfrac{x - a_1}{a_2 - a_1}, & a_1 \le x \le a_2, \\ \dfrac{x - a_3}{a_2 - a_3}, & a_2 < x \le a_3, \\ 0, & x > a_3, \end{cases} \tag{6}$$

$$\mu_C(x) = \begin{cases} 0, & x < a_2, \\ \dfrac{x - a_2}{a_3 - a_2}, & a_2 \le x \le a_3, \\ \dfrac{x - a_4}{a_3 - a_4}, & a_3 < x \le a_4, \\ 0, & x > a_4, \end{cases} \tag{7}$$

$$\mu_D(x) = \begin{cases} 0, & x < a_3, \\ \dfrac{x - a_3}{a_4 - a_3}, & a_3 \le x \le a_4, \\ 1, & x > a_4, \end{cases} \tag{8}$$

where x is the independent variable and is taken as the monitoring value of each bottom-level assessment factor (P_1 to P_9); a_1 to a_4 are the range segmentation parameters, which have the following linear relationship with K_1 to K_3 [24]:

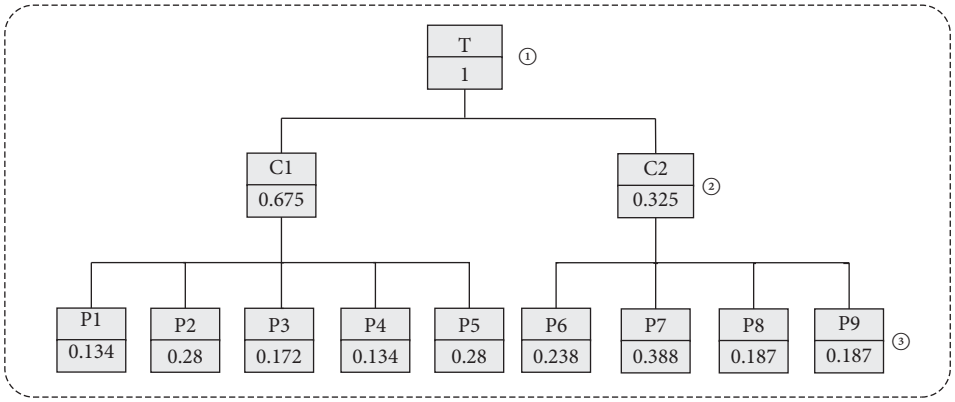

Figure 2: Hierarchical structure and weight assignment of assessment factors.

$$\begin{bmatrix} a_1 \\ a_2 \\ a_3 \\ a_4 \end{bmatrix} = \begin{bmatrix} 0.8 & & & \\ 0.5 & 0.5 & & \\ & 0.5 & 0.5 & \\ & & & 1.2 \end{bmatrix} \begin{bmatrix} K_1 \\ K_2 \\ K_3 \end{bmatrix}. \quad (9)$$

After the values of a_1 to a_4 are determined by (9), the monitoring value x of each factor is, respectively, substituted into equations (6)–(9) to obtain the membership matrix for the health grade of the bottom-level assessment factor.

$$Q = [\mu_A(x) \;\; \mu_B(x) \;\; \mu_C(x) \;\; \mu_D(x)]^T. \quad (10)$$

Multiplying the membership matrix Q by the grade vector G, the health assessment value R of the bottom-level factor can be obtained as

$$R = G \bullet Q = [4 \;\; 3 \;\; 2 \;\; 1] \begin{bmatrix} \mu_A(x) \\ \mu_B(x) \\ \mu_C(x) \\ \mu_D(x) \end{bmatrix}. \quad (11)$$

Combined with the linear features of the above fuzzy membership functions, the grading ranges of the four health grades corresponding to the R values are determined and listed in Table 2. The assessment of the health condition of each factor in the hierarchical structure can be carried out using this table.

3.4. Comprehensive Assessment Operator. The comprehensive assessment operator is a mathematical operation that uses the assessment values of multiple subitems to obtain the overall assessment result. For each bottom-level assessment factor that affects the health of a foundation pit, multiple sets of measurement points are generally set up for data acquisition. Because the monitoring data of different measuring points affect the health of a foundation pit differently, to highlight the most dangerous measurement points while considering the common influence of all other measurement points, a comprehensive assessment operator S is constructed as follows:

$$S = \alpha \cdot S_1 + \beta \cdot S_2, \quad (12)$$

where S_1 is the worst health assessment value of all measurement points ($R_{\min}$); S_2 is the average of the health assessment values at other measurement points; and α and β represent the weights of S_1 and S_2, respectively, whose values are taken as, preferably in reference to Pareto's law [25], $\alpha = 0.8$, $\beta = 0.2$.

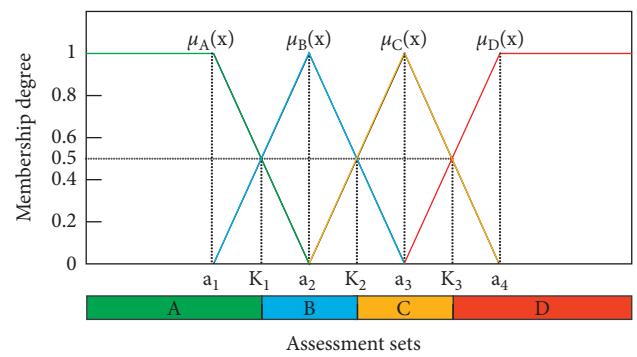

Figure 3: Membership function of the health grades.

Table 2: Quantitative classification of health conditions.

Grades	Remark	Vector value	Health value range
A	Very healthy	4	3.2–4
B	Basically healthy	3	2.4–3.2
C	Subhealthy	2	1.6–2.4
D	Unhealthy	1	1–1.6

4. Case Study

4.1. Project Overview and Data Collection. The foundation pit had a basement construction area of 21,800 m^2. The foundation soil within a 70-m depth of the shallow site belongs to quaternary sediments, which mainly consist of clayey soil, silty soil, and sandy soil. The field-measured stable groundwater level has a buried depth of 0.50 m to 2.00 m. To ensure the safety and health of the foundation pit project and its surrounding environment during the construction period, informationalized construction monitoring of the foundation pit was implemented. The monitoring factors and corresponding measurement points are shown in Table 3.

Table 3: Monitoring factors and corresponding measurement points.

Factors	Description	Measurement points label
P_1	Settlement of retaining wall	CQ1 ~ CQ24
P_2	Horizontal displacement of retaining wall	CX1 ~ CX21
P_3	Horizontal displacement of retained soil	TX1 ~ TX21
P_4	Settlement of column pile	CL1 ~ CL23
P_5	Axial force of support	CZ1 ~ CZ15
P_6	Settlement of underground pipeline	CM1 ~ CM24
P_7	Settlement of building	CF1 ~ CF45
P_8	Ground settlement	DB1 ~ DB25
P_9	Groundwater level	SW1 ~ SW21

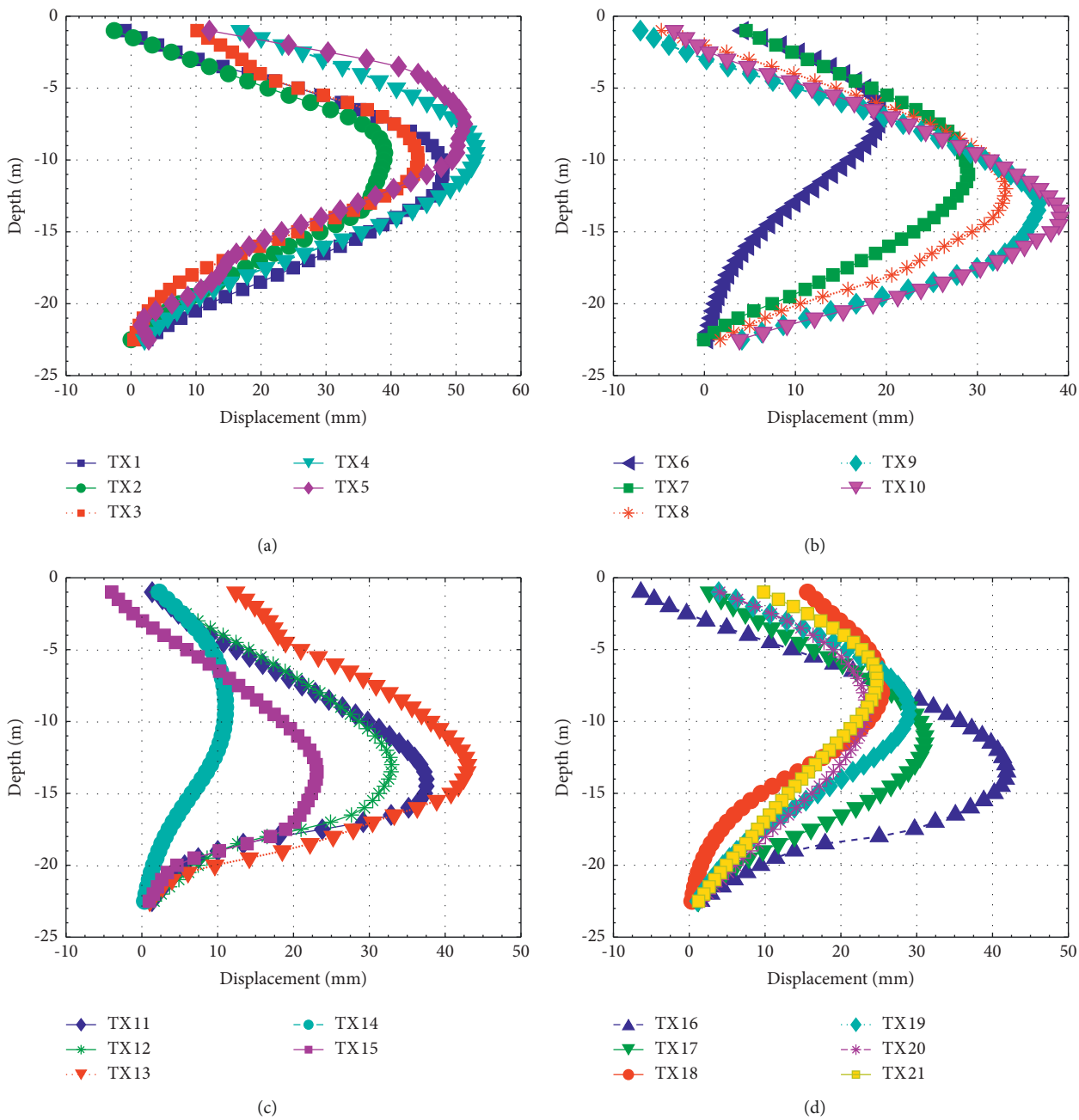

Figure 4: Horizontal displacement of the retained soil in a certain period. (a) Measurement points TX1-TX5. (b) Measurement points TX6-TX10. (c) Measurement points TX11-TX15. (d) Measurement points TX16-TX21.

Table 4: Health ranges division of monitoring factors.

Factors\grades	A	B	C	D
P_1 (mm)	[0, 10)	[10, 20)	[20, 30)	[30, +∞)
P_2 (mm)	[0, 10)	[10, 30)	[30, 50)	[50, +∞)
P_3 (mm)	[0, 10)	[10, 30)	[30, 50)	[50, +∞)
P_4 (mm)	[0, 10)	[10, 20)	[20, 30)	[30, +∞)
P_5 (kN)	[0, 3000)	[3000, 5000)	[5000, 7000)	[7000, +∞)
P_6 (mm)	[0, 10)	[10, 20)	[20, 30)	[30, +∞)
P_7 (mm)	[0, 10)	[10, 20)	[20, 30)	[30, +∞)
P_8 (mm)	[0, 10)	[10, 20)	[20, 30)	[30, +∞)
P_9 (mm)	[0, 200)	[200, 600)	[600, 1000)	[1000, +∞)

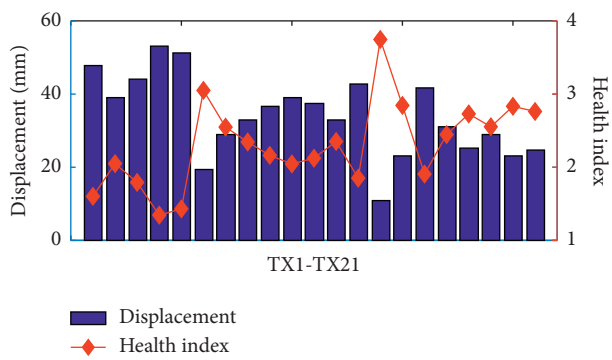

Figure 5: Horizontal displacement and health value of retained soil.

Foundation pit monitoring is not the focus of this paper and will be described in another work. Due to space limitation, the monitoring data of 21 measuring points of P_3 (i.e., horizontal displacement of the retained soil) in a certain period are shown in Figure 4.

4.2. Health Assessment and Analysis. First, a health assessment of the bottom-level factors was performed. In reference to the "Technical Code for Monitoring of Building Excavation Engineering" [26], the health ranges of each factor are divided as shown in Table 4.

The health assessment of the P_3 factor (i.e., the horizontal displacement of the retained soil) is taken as an example. Referring to Table 3, the threshold values K_1, K_2, and K_3 of the health ranges of the factor P_3 can be determined as 10, 30, and 50, respectively. Substitution into equation (10) gives the values of health range segmentation parameters a_1 to a_4 of the factor P_3.

$$\begin{bmatrix} a_1 \\ a_2 \\ a_3 \\ a_4 \end{bmatrix} = \begin{bmatrix} 0.8 & & & \\ 0.5 & 0.5 & & \\ & 0.5 & 0.5 & \\ & & & 1.2 \end{bmatrix} \begin{bmatrix} 10 \\ 30 \\ 50 \end{bmatrix} = \begin{bmatrix} 8 \\ 20 \\ 40 \\ 60 \end{bmatrix}. \quad (13)$$

Substitution of a_1 to a_4 into equations (6)–(9) gives the membership functions for the four health grades of the factor P_3. The monitoring values of the maximum horizontal displacements at measurement points TX1 to TX21 are substituted successively to obtain the membership matrix Q of each measurement point in terms of the four health classes. Finally, (11) is used to obtain the health assessment value R for the 21 measuring points. The results are shown in Figure 5.

The minimum health value in Figure 5—namely, 1.35 for measurement point TX4—and the average of health assessment value of the other 20 measurement points are substituted into (12) to obtain the comprehensive health assessment value of 1.55 for the factor P_3.

The same approach can be used to obtain the health values of all bottom-level assessment factors except P_3. Combined with the hierarchical structure and factor weights for foundation pit health assessment as shown in Figure 2, the weighted calculation is performed upward level by level to obtain the overall health assessment value of 2.55 for the foundation pit in a certain monitoring period, as shown in Figure 6. Referring to Table 1, the health of the foundation pit is graded as B—that is, a basically healthy condition. The factor P_3 lowered the overall health value of the foundation pit. Therefore, in a later stage, it is necessary to focus on the monitoring of the horizontal displacement of the retained soil at measurement point TX4 and even take necessary remedial measures.

Finally, the monitoring data of each period can be substituted into the calculation in batches to obtain the evolution of the foundation pit health over time during the entire monitoring period. As shown in Figure 7, the health condition of the foundation pit shows a trend of exponential decrease with time, and the health value dropped rapidly during the first month of monitoring, decreasing from 3.3 to approximately 2.6. In the later stage, the health

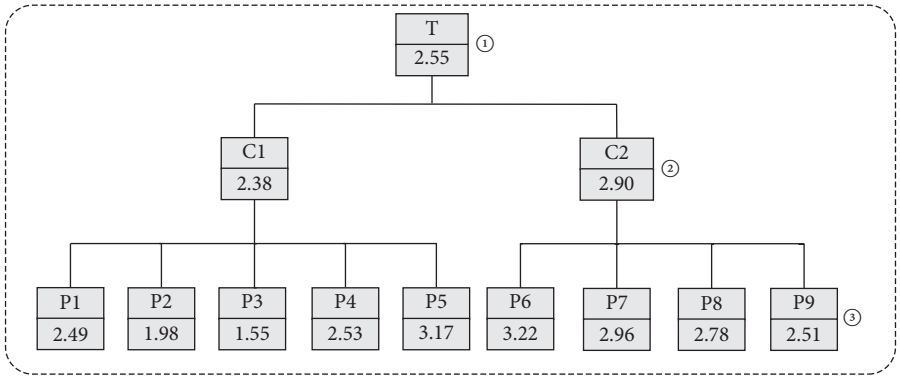

Figure 6: Health assessment results of the foundation pit in a certain period.

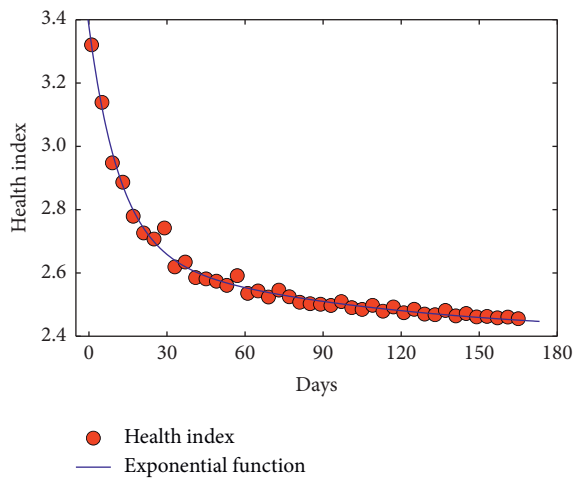

Figure 7: The evolution of foundation pit health state during the monitoring cycle.

value increased with time and gradually stabilized and remained at approximately 2.5. In general, the foundation pit was in a relatively healthy condition, consistent with the results of the on-site inspection, which found no obvious accidents.

5. Conclusions

In this paper, the fuzzy AHP method was applied to the health assessment of foundation pit projects. The specific outcomes are as follows:

(1) The AHP was used to subdivide various factors affecting the health of a foundation pit, a multilevel foundation pit health assessment factor system was established, and an index scale method was used to assign weights to each factor.

(2) The fuzzy mathematical method was used to construct a four-level health membership function of the assessment factor and a comprehensive assessment operator, which can quantitatively assess the health condition from the bottom-level factors to the overall foundation pit.

(3) Based on actual pit health monitoring data, a full-cycle health assessment of the foundation pit was performed using the established health assessment model. The health value of the foundation pit was consistently above 2.4, achieving a health grade of B. Therefore, the foundation pit was determined to be in a basically healthy condition, which agreed with the actual conditions at the site.

Data Availability

The data used to support the findings of this study are partly included within the article, and the rest data are available from the corresponding author upon request.

Conflicts of Interest

The authors declare that they have no conflicts of interest.

Acknowledgments

The work reported in this paper was partially funded by the Natural Science Foundation of Jiangsu Province (Grant no. BK20170574), the National Natural Science Foundation of China (Grant no. 51978317), the Key Laboratory of Ministry of Education for Geomechanics and Embankment Engineering, Hohai University (Grant no. B210204004), and the Industry-University-Research Collaboration Project of Jiangsu Province (Grant no. BY2021022).

References

[1] R. B. Peck, "Deep excavations and tunnelling in soft ground," *Proc.int.conf.on Smfe*, vol. 225-290, 1969.

[2] J. A. Hudson, *Excavation, Support and Monitoring*, Elsevier, Amsterdam, Netherlands, 1993.

[3] A. Brencich, "Deep trench, landslide and effects on the foundations of a residential building: a case study," *Engineering Structures*, vol. 32, no. 7, pp. 1821–1829, 2010.

[4] C. H. Juang, L. Wang, H. S. Hsieh, and S. Atamturktur, "Robust geotechnical design of braced excavations in clays," *Structural Safety*, vol. 49, pp. 37–44, 2014.

[5] K. Terzaghi, R. B. Peck, and G. Mesri, "Soil mechanics in engineering practice," *Soil Science*, vol. 68, no. 5, pp. 149-150, 1948.

[6] L. Bjerrum and O. Eide, "Stability of strutted excavations in clay," *Géotechnique*, vol. 6, no. 1, pp. 32–47, 1956.
[7] M. Matsuo and K. Kawamura, "Design method of deep excavation of cohesive soil based on the reliability theory: soils found, v20, n1, march 1980, p61–75," *International Journal of Rock Mechanics and Mining Sciences & Geomechanics Abstracts*, vol. 18, no. 1, p. 9, 1981.
[8] Y. M. A. Hashash and A. J. Whittle, "Ground movement prediction for deep excavations in soft clay," *Journal of Geotechnical Engineering*, vol. 122, no. 6, pp. 474–486, 1996.
[9] T. D. O'Rourke, "Ground movements caused by braced excavations," *Journal of the Geotechnical Engineering Division*, vol. 107, no. 9, pp. 1159–1178, 1981.
[10] Sugimoto and Takao, "Prediction for the maximum settlements of ground surface by open cut," *Doboku Gakkai Ronbunshu*, vol. 373, pp. 113–120, 1986.
[11] M. D. Bolton and W. Powrie, "Behaviour of diaphragm walls in clay prior to collapse," *Géotechnique*, vol. 38, no. 2, pp. 167–189, 1988.
[12] H.-M. Lin and F. C. Hadipriono, "Problems in deep foundation construction in taiwan," *Journal of Performance of Constructed Facilities*, vol. 4, no. 4, pp. 259–270, 1990.
[13] C. Y Ou, P. G. Hsieh, and D. C. Chiou, "Characteristics of ground surface settlement during excavation," *Canadian Geotechnical Journal*, vol. 30, no. 5, pp. 758–767, 1993.
[14] B. J. Wang, L. Ke, B. Shi, and G. Q. Wei, "Test on application of distributed fiber optic sensing technique into soil slope monitoring," *Landslides*, vol. 6, no. 1, pp. 61–68, 2009.
[15] C. Piao, G. Wei, and C. Yong, "Study on the BOTDR-based distributed detection of the pile foundation bearing capacity," in *Proceedings of the International Conference on Electric Technology & Civil Engineering*, Lushan, China, April 2011.
[16] Y. J. Yin, X. L. Liu, and Y. M. Qian, "Research on the deformation monitoring of deep foundation pit engineering," *Advanced Materials Research*, vol. 889-890, pp. 1383–1387, 2014.
[17] W. Xie and Pengcheng, "Monitoring of deep foundation pit support and construction process in soft soil area of pearl river delta," *IOP Conference Series: Earth and Environmental Science*, vol. 128, Article ID 012097, 2018.
[18] O. Moselhi, T. Hegazy, and P. Fazio, "Potential applications of neural networks in construction," *Canadian Journal of Civil Engineering*, vol. 19, no. 19, pp. 521–529, 1992.
[19] L. A. Zadeh, "Fuzzy sets," *Information and Control*, vol. 8, no. 3, pp. 338–353, 1965.
[20] T. L. Saaty, "Axiomatic foundation of the analytic hierarchy process," *Management Science*, vol. 32, no. 7, pp. 841–855, 1986.
[21] Ministry of Housing and Urban-Rural Development of the People's Republic of China, *Technical Code for Construction Safety of Deep Building Foundation Excavations*, China Architecture & Building Press, JGJ311-2013, Beijing, China, 2013.
[22] D. I. Kim, W. S. Yoo, H. Cho, and K. I. Kang, "A fuzzy ahp-based decision support model for quantifying failure risk of excavation work," *KSCE Journal of Civil Engineering*, vol. 18, no. 7, pp. 1966–1976, 2014.
[23] H. A. Donegan, F. J. Dodd, and T. B. M. McMaster, "A new approach to ahp decision-making," *Journal of the Royal Statistical Society*, vol. 41, no. 3, pp. 295–302, 1992.
[24] W. Zhang, Ke Sun, C. Lei et al., "Fuzzy analytic hierarchy process synthetic evaluation models for the health monitoring of shield tunnels," *Computer-Aided Civil and Infrastructure Engineering*, vol. 29, no. 9, pp. 676–688, 2014.
[25] M. Hardy, "Pareto's law," *The Mathematical Intelligencer*, vol. 32, no. 3, pp. 38–43, 2010.
[26] Ministry of Housing and Urban-Rural Development of the People's Republic of China, *Technical Code for Monitoring of Building Excavation Engineering*, China Planning Press, GB50497-2016, Beijing, China, 2016.

Hindawi
Advances in Civil Engineering
Volume 2022, Article ID 3056668, 22 pages
https://doi.org/10.1155/2022/3056668

Research Article

Mechanical Behavior of Loess Tunnels Caused by Surface Water Joints Infiltration

Qingfu Li, Ming Liu, and Yingqiao Yu

School of Water Conservancy Engineering, Zhengzhou University, Zhengzhou 450003, China

Correspondence should be addressed to Ming Liu; lmxiaoyu@gs.zzu.edu.cn

Received 26 December 2021; Revised 9 May 2022; Accepted 12 May 2022; Published 30 May 2022

Academic Editor: Zhijun Xu

Many researchers have conducted a vast amount of research on water sensitivity and joint seepage in loess tunnels. However, studies on the mechanical effects of shallow buried loess tunnels under the influence of joint dominant seepage are still insufficient. In this study, we simulate the seepage range of loess tunnels with joints, and we use this seepage range to numerically simulate the mechanical properties of shallow buried loess tunnels. Studies have shown that the permeability coefficient and the number of joints are the key factors that affect the amount of surface water infiltration. An increase in the permeability coefficient on the order of 5×10^{-3} m/s will cause the surface water to pour into the ground and rapidly form a saturated soak zone on the liner, while an increase in the number of joints will increase the width and formation rate of the saturated zone. The results of the tunnel mechanics simulation show that the surface settlement and the surrounding rock displacement increase with the increase of the wetted area of the vault; the effect of arch footing water immersion on the surface settlement and the surrounding rock displacement is most significant for the same wetted area width. Compared with the three-stage method, the center cross diaphragm (CRD) method of excavation can better control the surface and the surrounding rock settlement under waterlogged conditions. In particular, the lining settlement on the waterlogged side can be effectively controlled, and the overall settlement of the tunnel is more uniform.

1. Introduction

Loess is a loose-packed powder soil formed in the Quaternary period, and it is widely distributed in arid and semiarid areas [1]. Loess deposits cover $6.5 \times 10^4 \text{km}^2$ in China, of which about $4 \times 10^4 \text{km}^2$ is collapsible loess [2]. The Q_3 and Q_4 loess formed in Upper Pleistocene and Holocene has the characteristics of no layering as well as loose texture and pore development. The unique metastable structure of loess will be destabilized and collapsed into small micropores when this soil is influenced by rain seepage, which is macroscopically manifested as a sudden decrease in strength and a large deformation after water immersion [3, 4]. The special metastable structure of collapsible loess is prone to collapse and large deformation beyond the normal level under the influence of construction disturbance and moisture immersion [5]. Self-weight wet-submerged loess surrounding rock in the immersion of water after a significant drop in strength produces a large deformation. Additionally, the self-supporting capacity of the surrounding rock is greatly reduced, and the stress redistribution caused by uneven settlement and the bias effect causes the tunnel lining to be in an unfavorable state of stress or even damage [6].

Loess joints are fracture gaps in the loess for which the soil is not significantly displaced along both sides of the fractures. Loess joints are with a certain degree of open fissures; during the surface rainwater infiltration, loess joints especially through the joints can often form the advantage of surface water infiltration channel [7]. Under the condition of high intensity infiltration of surface water, water will preferentially infiltrate along the dominant infiltration channels such as joint fissures, and the infiltration volume is extremely high, sometimes even up to 20 times of the infiltration volume in the uniform infiltration stage [8]. In the initial stage of the high intensity infiltration of surface water,

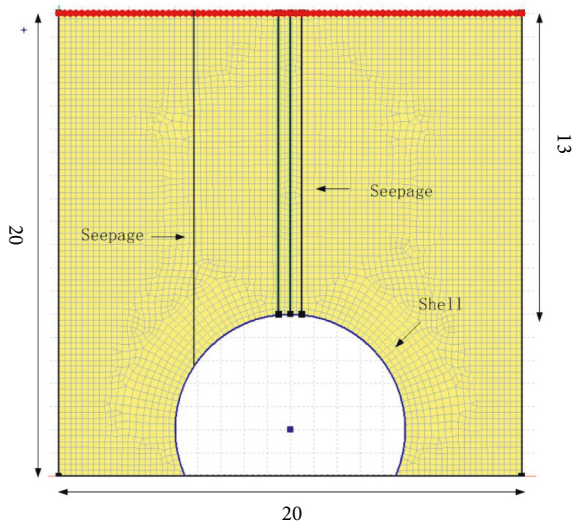

Figure 1: Model of loess joint seepage.

Table 1: Working condition setting of loess joint seepage.

Case	Location of the joints	Number of joints	Permeability coefficient of joints
Case 1	Vault	1	2×10^{-3} m/s
Case 2	Vault	2	2×10^{-3} m/s
Case 3	Vault	3	2×10^{-3} m/s
Case 4	Vault	1	5×10^{-3} m/s
Case 5	Arch shoulder	1	5×10^{-3} m/s

the tunnel perimeter rock will undergo severe uneven waterlogging, and the strength and deformation of the waterlogged loess perimeter rock will increase dramatically, resulting in stress redistribution and reduced self-supporting capacity within the perimeter rock, which will in turn lead to increased stress or bias pressure on the tunnel lining, deteriorating the mechanical properties of the lining and leaving the lining in a stress-unfriendly state. The lining stress behavior is very different from that of the perimeter rock before the wetting [9–14]. Due to the ultrahigh water head, water leakage through tunnel joints is a major concern during a tunnel's service life [15]. Segmental joints are vulnerable parts of the lining structure in precast shield tunnels, from both the structural (lower stiffness compared to main segments) and nonstructural (potential water leakage points) perspectives [16, 17]. Segmental joints act as a weak link in the tunnel lining in terms of both structural responses (due to the lower stiffness and strength compared to the main segments) and the serviceability considerations (high risk of water/gas leakage) [18]. Water leakage through segmental joints is a clutch issue for shield tunnels during both the construction and operation stages [19, 20]. For a modern underwater tunnel subjected to high water head, the segments are required to cast by the high-performance concrete with excellent quality and very low permeability [21].

The mechanical properties of loess are very different under dry and wet conditions [22, 23]. Therefore, the study of the lining force characteristics of shallow buried loess tunnels under the influence of dominant flow is of vital importance to the prevention and control loess tunnel lining diseases. The authors simulate the possible joint seepage field by means of theoretical studies and numerical simulations and perform simulated calculations and analyses of tunnel forces under the influence of joint seepage, with a view to providing guidance and insight for the design and construction events of shallow buried loess tunnels affected by joints seepage.

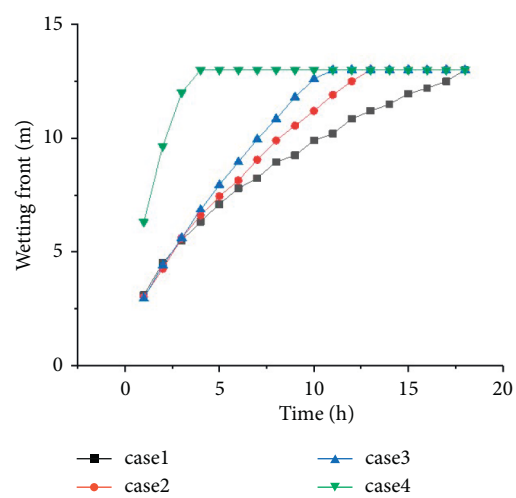

Figure 2: 24% wetting front depths of Case 1, Case 2, Case 3, and Case 4.

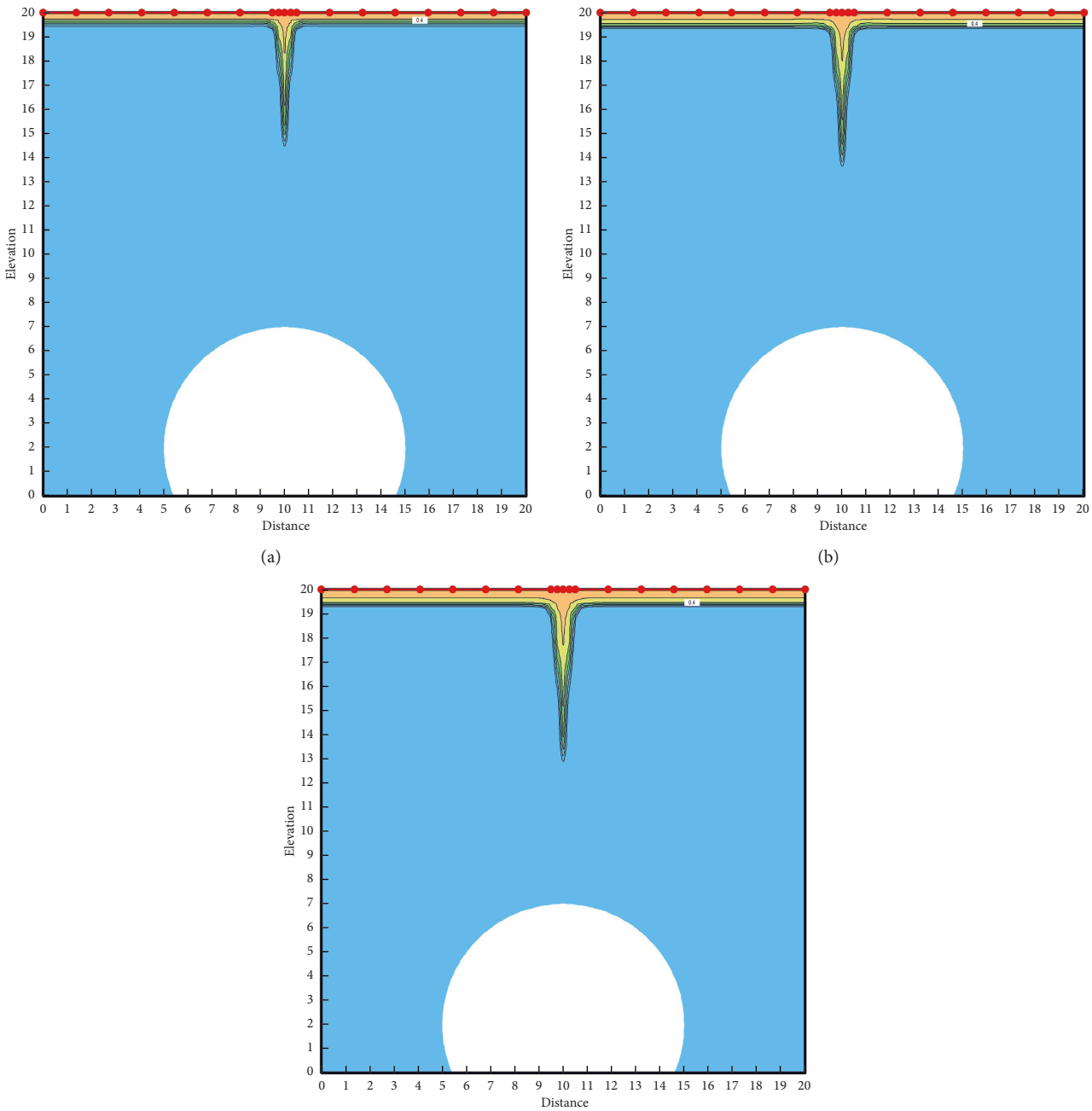

Figure 3: Case 1 3rd, 4th, and 5th hour seepage fields. (a) 3rd hour seepage field. (b) 4th hour seepage field. (c) 5th hour seepage field.

2. Seepage Numerical Simulation

2.1. Numerical Simulation. In this section, numerical simulations of seepage are performed for the established model of loess containing joints using the numerical simulation software GeoStudio. Figure 1 shows the seepage numerical calculation model and grid size. The longitudinal calculation range is 20 m, the vertical calculation ranges of both lateral sides are 20 m including 13 m buried depth. A circular impermeable layer was set at the bottom to simulate the tunnel lining, impermeable boundaries were set at the sides and bottom, and a 0.02 m pressure head was set at the top to simulate surface water accumulation. The saturated permeability coefficient of the loess is set to $5e-6$ m/s with an initial moisture content of 12%. The joints are located at the top and left sides of the impermeable layer. The length of the vault joints is 13 m, the left side joints are 20 m, and the size of the joints unit is 25 cm × 2.5 cm. The equivalent permeability coefficients of the joints are 2×10^{-3} m/s and 5×10^{-3} m/s, and four cases of 1, 2, and 3 joints directly above the impermeable layer and 1 joint above the left of the impermeable layer are set. The working conditions are shown in Table 1.

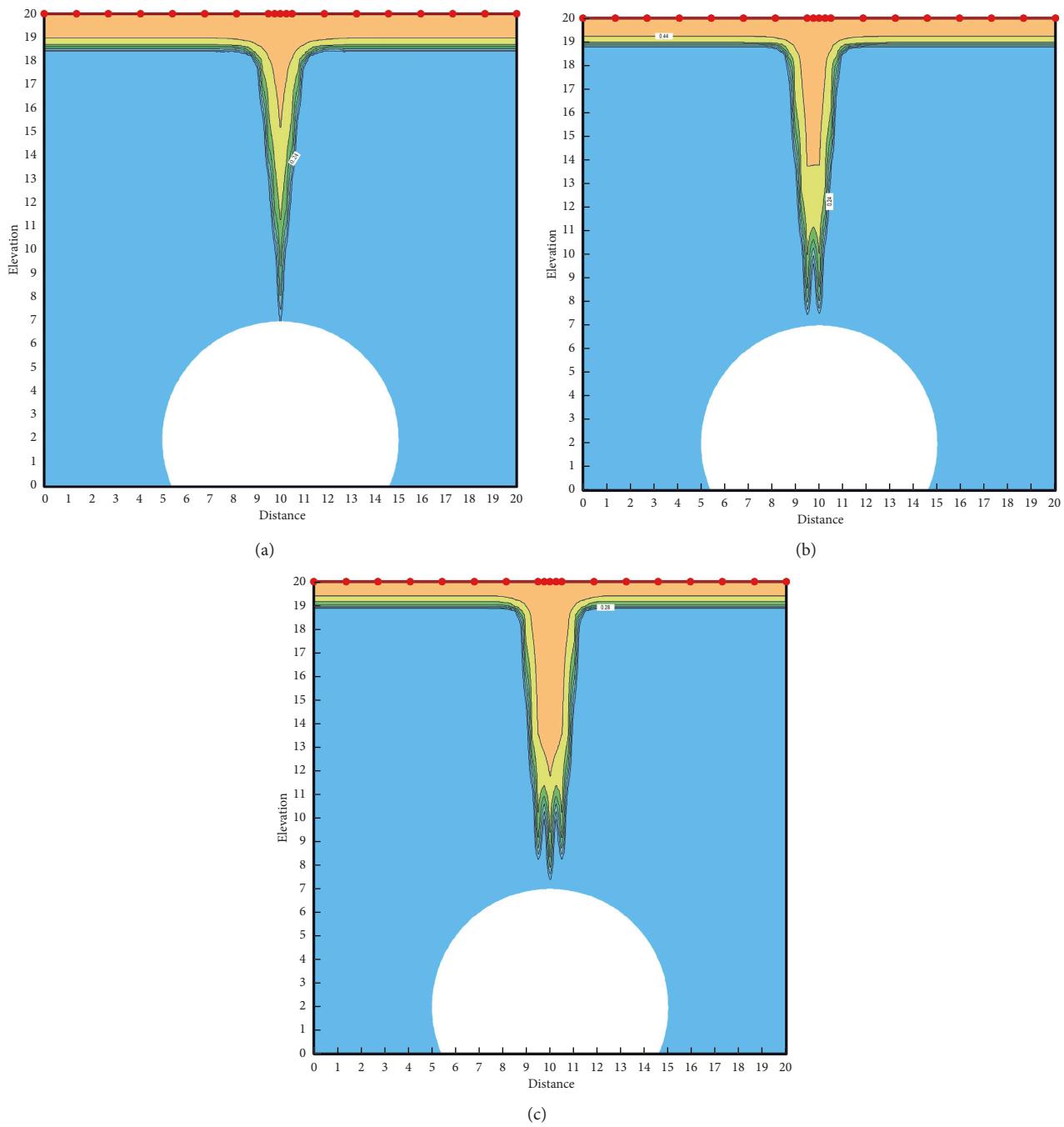

Figure 4: Seepage field of 1 hour before the wetting front touches the impermeable layer in Case 1, Case 2, and Case 3. (a) Case 1. (b) Case 2. (c) Case 3.

2.2. Results of Numerical Investigation. The 24% wetting front depths of Case 1, Case 2, Case 3, and Case 4 after the surface water started to infiltrate are shown in Figure 2. It can be seen that Case 1, Case 2, and Case 3 are three cases with the same nodal permeability coefficient, and their wetting fronts contact the impermeable layer after 11, 13, and 18 hours of the start of infiltration, respectively. The depth of the wetting front is relatively close within the first 3 hours of the beginning of infiltration, indicating that the number of nodules at the beginning of infiltration has less influence on the advance rate of the wetting front. After 3 hours, the infiltration rate of 1 and 2 joints began to slow down and the advancing depth curve of the wetting front leveled off, while the infiltration rate of 3 joints remained basically the same and the advancing depth curve of the wetting front kept increasing linearly. Six hours after the start of infiltration, the advance of the wetting front in Case 1 slowed down further, while the advance of the wetting front in Case 2 did not decrease significantly.

Figure 3 shows the seepage field of Case 1 at the 3rd, 4th, and 5th hours after the start of infiltration. From the figure, it can be seen that, from the 3rd hour onwards, the region of

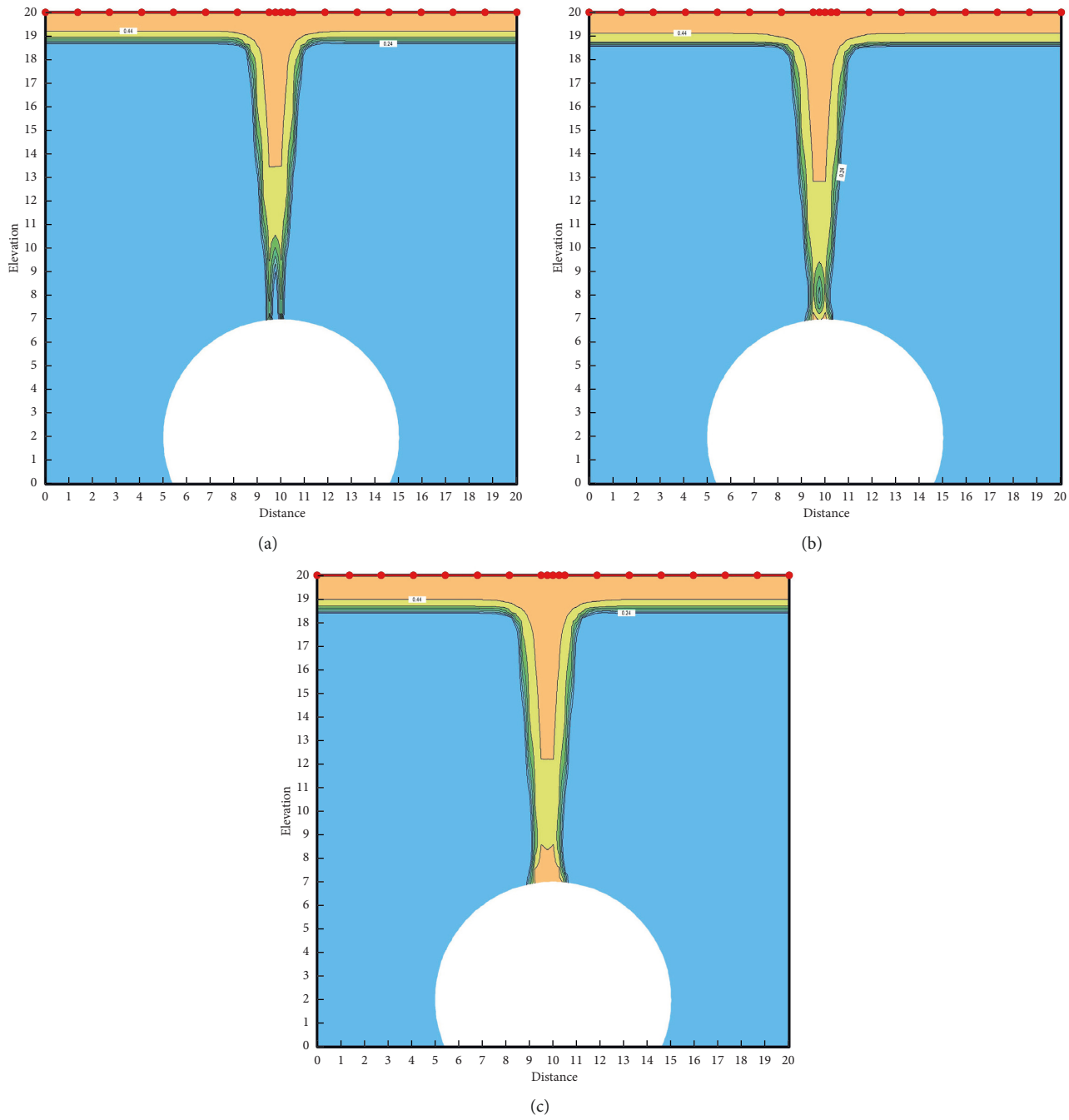

Figure 5: Seepage field after the 0th, 2nd, and 4th hours of contacting the impermeable layer by the wetting front in Case 2. (a) Hour 0 seepage field. (b) 2nd hour seepage field. (c) 4th hour seepage field.

40% water content starts to develop to both sides with the joints as the center, and the increase in lateral infiltration is precisely the reason for the further decrease in the forward speed of the wetting front of Case 1. This phenomenon can also be observed in Case 2, where both Case 1 and Case 2 have a phase where the saturation zone expands, and the advancing speed of the wetting front decreases, after which the advancing speed of the wetting front is further stabilized. However, this phase is shorter in Case 2. Case 2 and Case 3 have greater infiltration per unit time due to the increase in the number of nodules, bringing a wider and deeper saturation zone while also allowing a greater depth of advancement of the 24% moisture content wetting front.

Figure 4 shows the seepage fields of the wetted fronts before contacting the impermeable layer for 1 hour in Case 1, Case 2, and Case 3. As can be seen in Figure 4, the depth of the saturated zone under the working condition of 1 joint is less than half of the depth of the wetting front at 24% water content, and the saturation zone is conical in shape with a very narrow width. The depth of the saturation zone is greatly

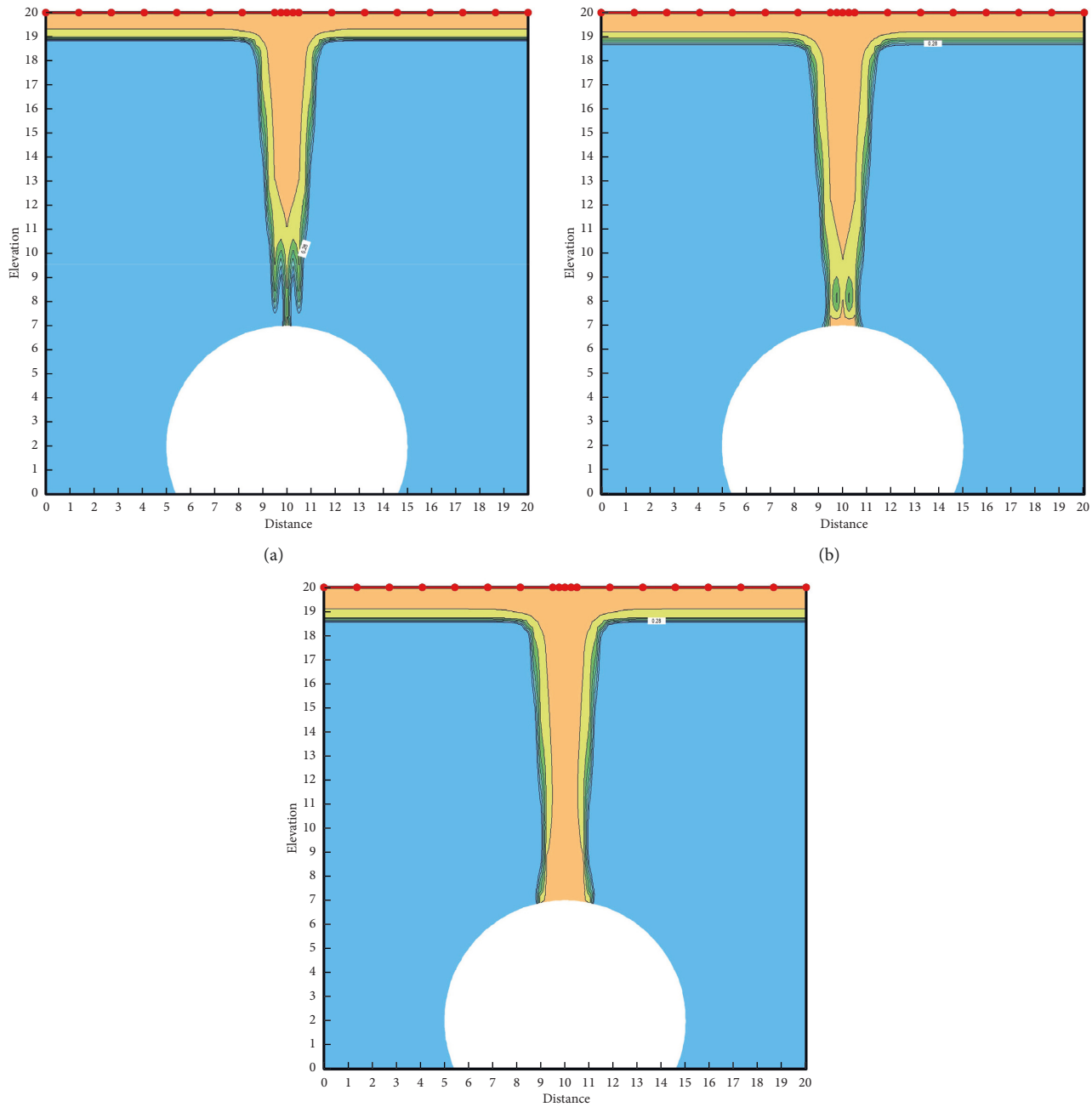

Figure 6: Seepage field after the 0th, 2nd, and 4th hours of contacting the impermeable layer by the wetting front in Case 3. (a) Hour 0 seepage field. (b) 2nd hour seepage field. (c) 4th hour seepage field.

increased for the cases of 2 joints and 3 joints. The depth of the saturation zone reaches half of the wetting front of 24% water content in Case 2 and 2/3 of the wetting front of 24% water content in Case 3. The width of the saturation zone also increases with the increase of the number of joints. It can be assumed that the increase in the number of joints contributes to the increase in the depth and width of the saturated zone, and the increase in the depth and width of the saturated zone also accelerates the advance of the wetting front.

Figures 5 and 6 show the seepage fields after the 0th, 2nd, and 4th hours of contacting the impermeable layer for the wetting front in working conditions 2 and 3, respectively. It can be seen that the number of joints has a significant effect on the extent of the saturation zone after the wetting front contacts the impermeable layer. Compared with that in Case 3, the saturation zone in Case 2 appears slower and smaller in width, and Case 2 does not have the rapid penetration of the saturation zone in Case 3. At the same time, both working conditions showed a parallel distribution of equal water content lines after the wetting front contacted the impermeable layer, forming a rectangular wetting zone in the soil.

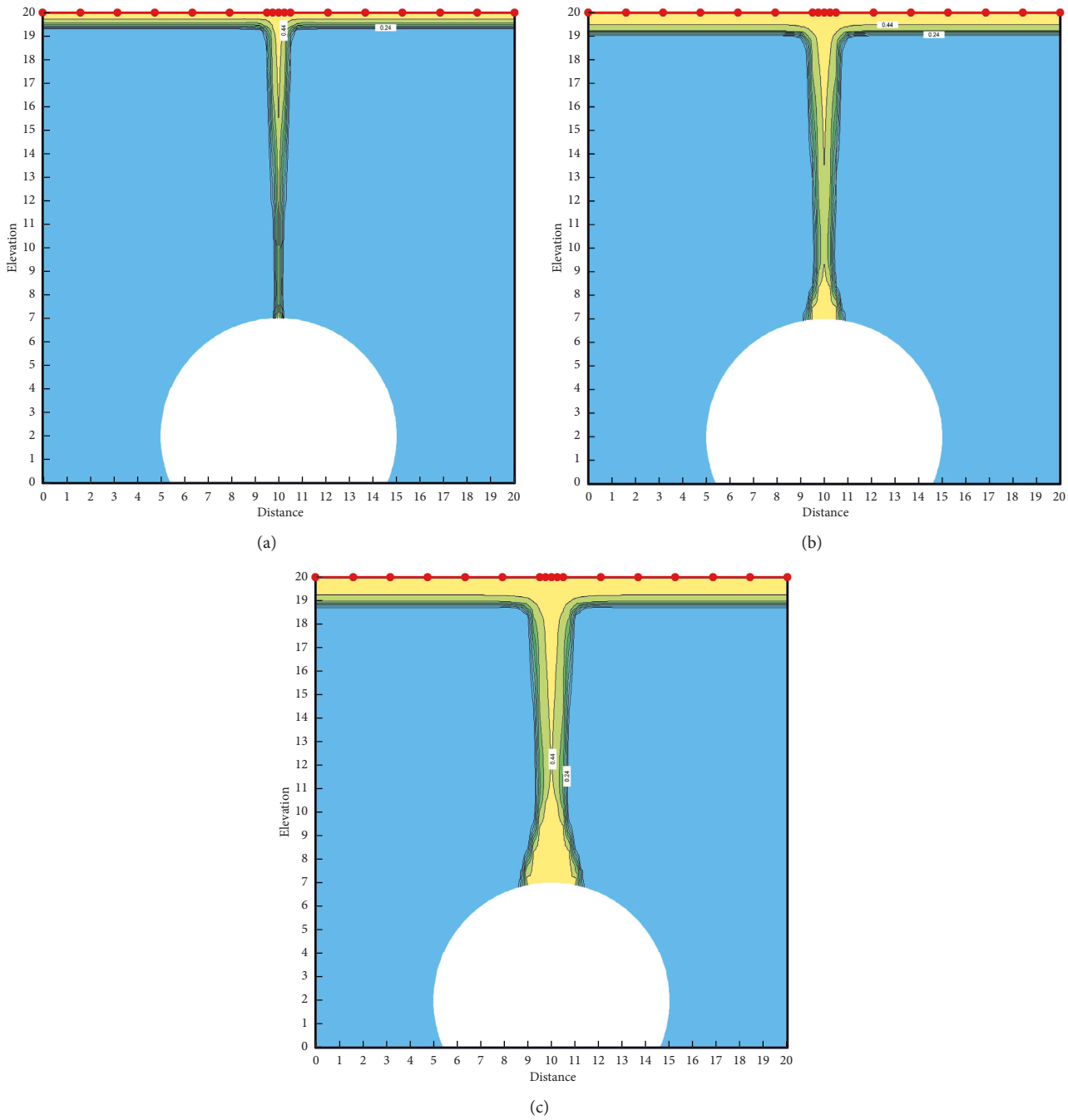

Figure 7: Seepage field after 4, 8, and 12 hours of infiltration in Case 4. (a) Seepage field after 4 hours. (b) Seepage field after 8 hours. (c) Seepage field after 12 hours.

Figure 7 shows the seepage field after 4, 8, and 12 hours of infiltration at the beginning of working Case 4. It can be seen that, in the surface water infiltration process species, the infiltration coefficient of 5×10^{-3} m/s joints will cause surface water to fill the ground. The infiltration of water between 4 and 8 hours is mainly in the impermeable layer above the siltation, so that the soil above the impermeable layer quickly reaches saturation. The saturation area on the impermeable layer reaches the maximum width, and the width gradually decreases upward, and the central part of the soil is in a state of near saturation but is not saturated. The saturated area is gradually connected upwards and downwards within 8 to 12 hours, but the width of the saturated area in the middle is very small, which fully indicates that the surface water infiltration is irrigation type, and the lateral infiltration coefficient is much smaller than the longitudinal infiltration coefficient. The infiltrated water mainly accumulates at the bottom, which causes the formation of a very wide saturated area in the upper part of the impermeable layer.

Figure 8 shows the seepage field at the beginning of infiltration after 6, 9, and 12 hours of working Case 5. It can

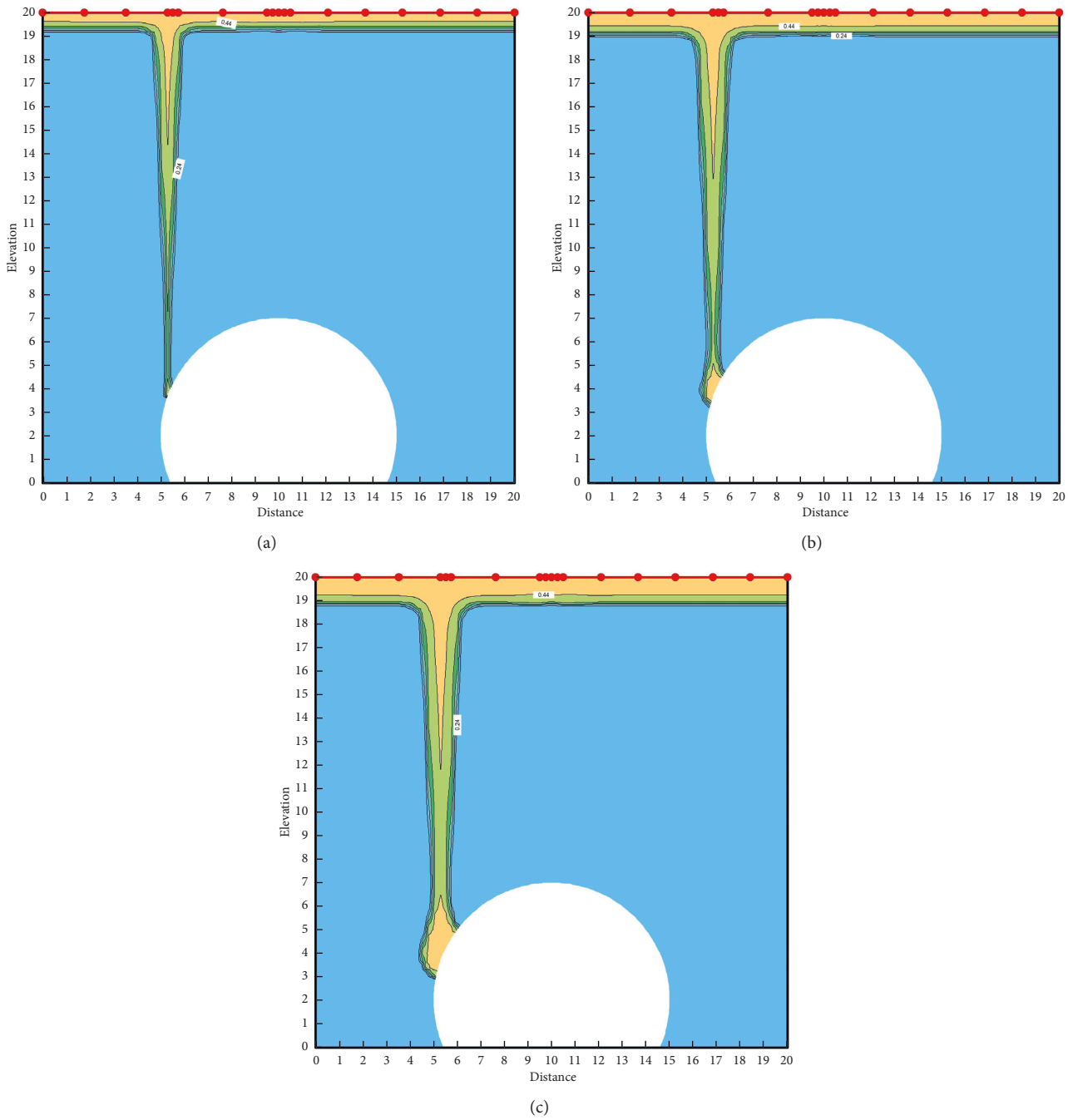

Figure 8: Seepage field after 6, 9, and 12 hours of infiltration in Case 5. (a) Seepage field after 6 hours. (b) Seepage field after 9 hours. (c) Seepage field after 12 hours.

be seen from the figure that seepage fields of working condition 5 and working condition 4 are similar; both of them have a high saturation area of 40% water content after the wetting front touches the impermeable layer for 1 hour. Then the infiltrated water mainly accumulates at the lowest end of the joints and on the impermeable layer, and a relatively large saturation area will be formed on the impermeable layer. Unlike working condition 4, in working condition 5, the infiltrating water flows below the impermeable layer under the action of gravity, and it moves from the arch shoulder and arch side to the foot of the arch, forming a saturated area with a small top and a large bottom.

2.3. Numerical Simulation Analysis considering Liner Drainage System. Road tunnel is equipped with drainage system which contains circular, longitudinal, as well as horizontal drainage pipes behind the lining. The drainage effect of the tunnel lining should be taken into account when performing seepage simulations related to perimeter rock

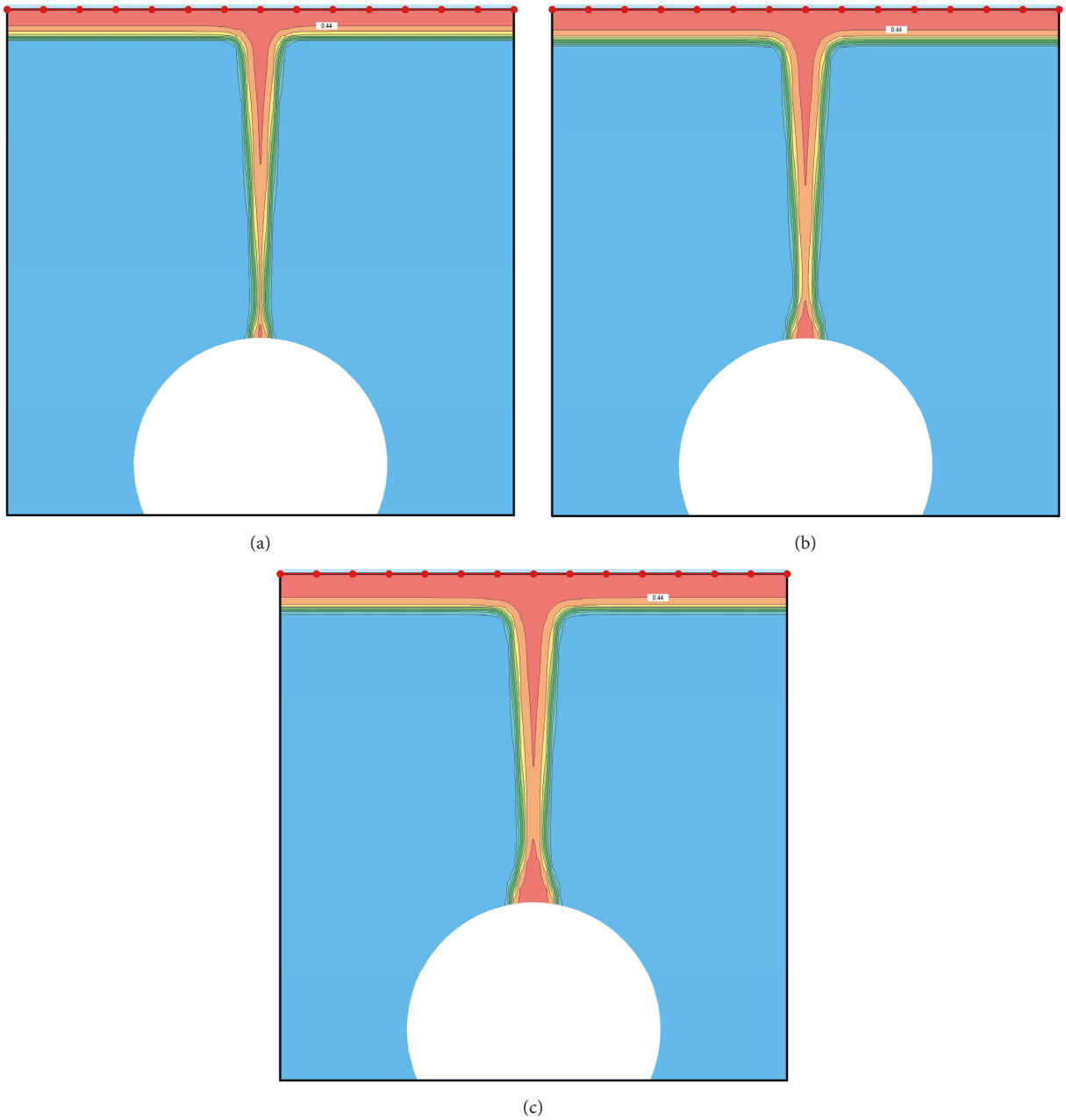

Figure 9: Seepage field after 8, 10, and 12 hours of infiltration in Case 1, lining without drainage system. (a) Seepage field after 8 hours. (b) Seepage field after 10 hours. (c) Seepage field after 12 hours.

seepage. To simplify the calculation process and by reviewing the relevant literature, the tunnel lining is simplified to a permeable surface in the simulations in this chapter to simulate the perimeter rock seepage under effective working conditions of the lining drainage system.

Figures 9 and 10 show the seepage flow field of Case 1 for the liner without and with drainage system, respectively. It can be seen that the surrounding rock at the edge of the tunnel lining is saturated at the 8th hour, regardless of whether the tunnel lining has drainage or not. However, with the increase of seepage time, the seepage fields of the two different working conditions appear to be significantly different. When the tunnel lining does not have drainage capacity, the saturated area at the top of the tunnel will expand rapidly, creating a large saturated area at the top of the tunnel in just 2 hours. When the tunnel lining had drainage capacity, the saturated zone of the surrounding rock at the top of the tunnel showed no significant growth in width or height after the 8th hour formation. It can be seen that the most important role of the existence of the lining drainage system is to effectively prevent the problem of water accumulation in the surrounding rock of the tunnel. When the liner drainage system is present, a near-rectangular seepage field

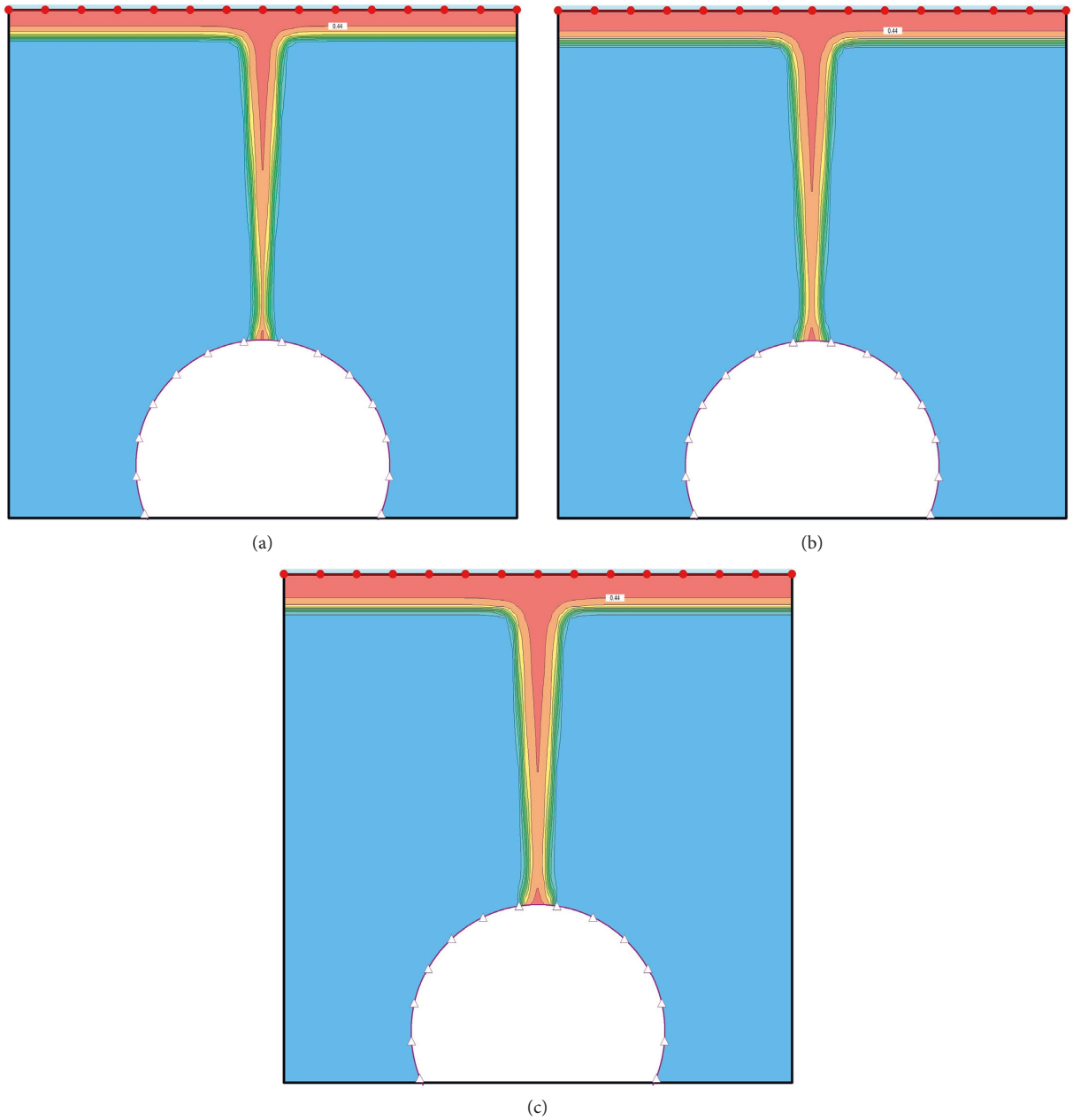

(a) (b) (c)

Figure 10: Seepage field after 8, 10, and 12 hours of infiltration in Case 1, lining with drainage system. (a) Seepage field after 8 hours. (b) Seepage field after 10 hours. (c) Seepage field after 12 hours.

centered at the joint position is formed in the surrounding rock.

3. Influence of Joint Seepage on the Mechanical Behavior of Existing Tunnels

3.1. Analytical Model and Calculation Parameters. According to the viewpoint of elastic mechanics, the model is simplified to a plane strain problem for study, and a two-dimensional calculation model is established. The model size is 50 m × 35 m, the width of the tunnel is 10 m, the height is 7 m, and the model size is set to five times of the tunnel size to ensure the accuracy of the calculation. Horizontal and vertical displacement constraints are set at the bottom of the model, horizontal displacement constraints are set on both sides of the model, the top is a free surface, and the computational model and mesh are shown in Figure 11.

In this model, the stress field of the loess stratum in its natural state is calculated according to the material properties in Table 2, and the ideal elastoplastic principal structure model with the Mohr–Coulomb strength criterion is used to calculate the tunnel. The tunnel is excavated by killing the unit, and the C20 concrete lining with a thickness of 25 cm and anchor rod support are applied after 30 steps of calculation to simulate the construction method of applying the lining immediately after excavation. The concrete lining

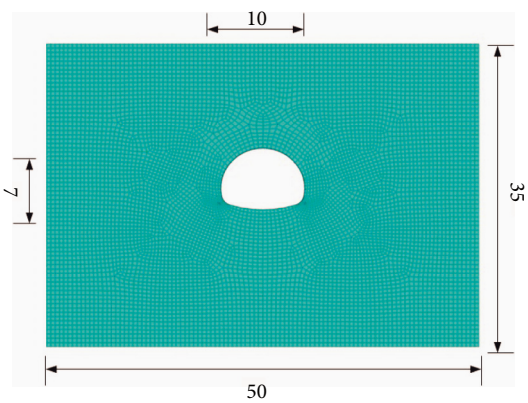

Figure 11: Numerical calculation model of tunnel.

Table 2: Material parameters.

Loess	Gravity (kN/m^3)	Cohesive force (kPa)	φ (ϕ/°)	Elastic modulus (MPa)	Poisson's ratio (μ)
Natural water content	15.2	36	26	22.62	0.32
Water immersion	17.7	9	18	2.26	0.32

Table 3: Material parameters.

Material category	Gravity (kN/m^3)	Elastic modulus (GPa)	Poisson's ratio (μ)	K (GPa)	G (GPa)
Lining	25	25.3	0.2	17.5	13.1

Table 4: Material parameters.

Material category	Gravity (kN/m^3)	Yield strength (MPa)	E (GPa)	Diameter (mm)	Poisson's ratio (μ)	Length (m)
Bolts	78.5	500	200	42	0.2	2.5

is simulated using the shell unit (the concrete lining is simulated by shell unit (shell), and the anchor rod is simulated by anchor cable unit (cable)). Material properties of the surrounding rock are based on existing literature [24, 25]. The properties of each material are shown in Tables 3 and 4.

Different joints locations and permeability coefficients will produce saturated areas with different locations and widths. Five working conditions are set up as shown in Table 5 and Figure 12 according to the different joints locations and permeability strengths.

Table 5: Working condition setting.

Case	Infiltration depth (m)	Joint distribution	Infiltration width (m)
1	2	—	-
2	2	Arch vault	3
3	2	Arch vault	5
4	2	Spandrel	3
5	2	Arch foot	3

3.2. Surface Settlement Analysis. The surface settlement curves of the five working conditions after the rainfall-induced waterlogging of the surrounding rock are shown in Figure 13. It can be seen that the settlement curve after the immersion of the surrounding rock has a quadratic parabolic distribution, and there is a strong correlation between the surface settlement and the location of the surrounding rock immersion. In Case 1, there is only uniform infiltration, the settlement trough width is about 25 m, the settlement curve is symmetrical along the central axis of the tunnel, and the maximum settlement occurs directly above the tunnel vault with a settlement value of 7.49 mm. The settlement troughs of the other four conditions with nodal infiltration are all enlarged, with the settlement trough of Case 2 exceeding 45 m.

The settlement curves of Case 2 and Case 3, which are symmetrical in the infiltration and wetting zone of the joint, are symmetrical along the central axis of the tunnel as in Case 1, and the maximum settlement also occurs directly above the vault, with settlement values of 14 mm and 21.8 mm. We introduce the concept of a settlement trough to illustrate the effect of the presence of the tunnel on the

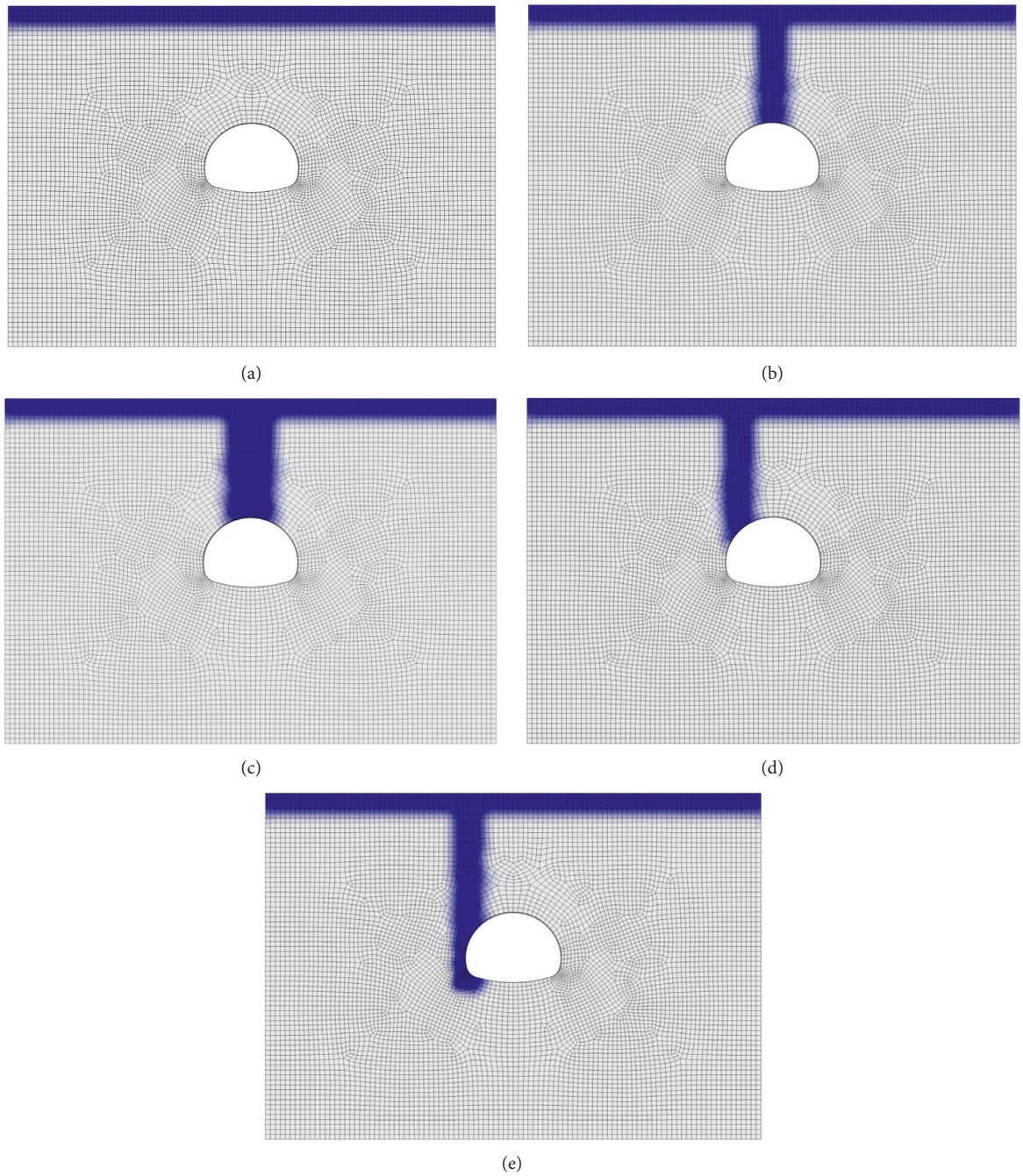

Figure 12: Working condition setting. (a) Case 1. (b) Case 2. (c) Case 3. (d) Case 4. (e) Case 5.

settlement of the surrounding rock. We approximated the settlement trough curve as a quadratic parabola, taking the 2 m uniformly infiltrated loess settlement plane as the x-axis, and the range of the settlement trough is determined according to the two intersection points of the parabola and the x-axis. Among the five working conditions, the surface settlement value of working condition 3 is the largest, and the settlement trough of Case 3 is significantly larger than those of Case 1 and Case 2, reaching about 50 meters. This indicates that the increase of the submerged water range significantly affects the surface settlement range and depth.

The width of the immersed area is the same for Case 4, Case 5, and Case 2, but the maximum settlement has increased, and the settlement trough is wider. It can be seen that the settlement value of Case 5 is further expanded, the settlement trough is significantly wider and deeper, and the settlement above the vault is larger, indicating that the influence of the arch foot dip on the surface settlement is more significant.

3.3. Surrounding Rock Displacement Analysis. The monitoring points of rock displacement data are shown in

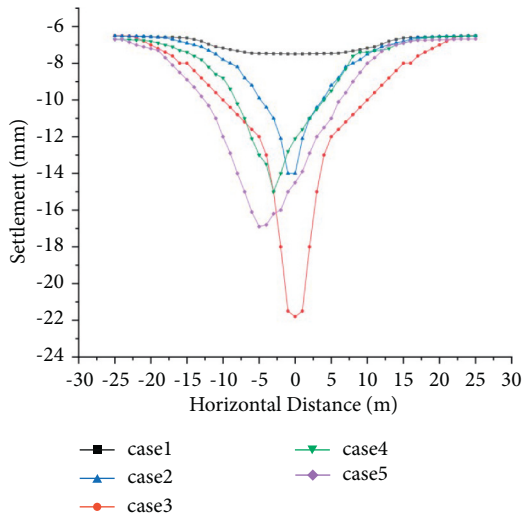

Figure 13: Surface settlement in each working condition.

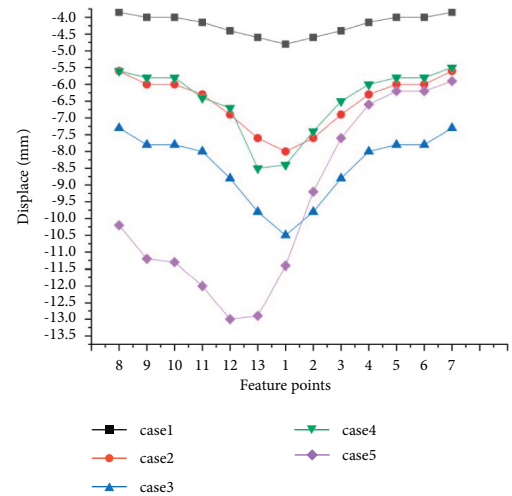

Figure 15: Settlement folding diagram of surrounding rock for each working condition.

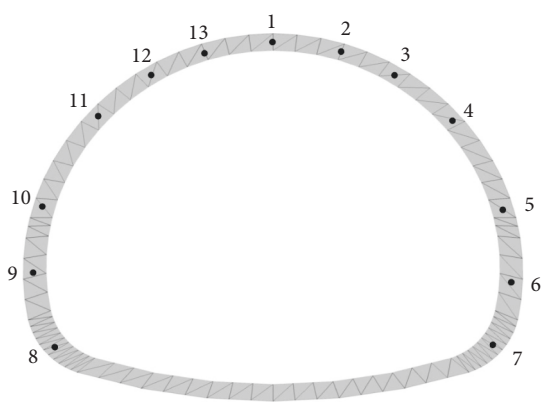

Figure 14: Surrounding rock displacement monitoring point.

Figure 14, and a total of 13 monitoring points including arch top, arch shoulder, arch foot, and arch waist are set.

Figure 15 shows the vertical displacements of each characteristic point after the waterlogging of the surrounding rock for the five working conditions.

It can be seen that a certain amount of settlement occurs at each characteristic point in Case 1, among which the settlement value of the vault is the largest, and the settlement of each part of the lining is symmetrically distributed with the central axis as the center. This symmetry also appears in Case 2 and Case 3.

In Case 2 and Case 3, where the arch is submerged in water, there is a significant increase in arch settlement, and the settlement curve has a secondary parabolic distribution with the central axis of the arch as the symmetry axis, and the tunnel shows a flattening trend.

The maximum settlement value of Case 2 is increased by about 83% compared with Case 1. With the increase of the dip range of the arch, the self-weight of the surrounding rock increases and the bearing capacity of the surrounding rock decreases. The vertical displacement of each characteristic point in Case 3 has increased, among which the settlement value of the arch top has increased the most, an increase that is 119% higher than that of Case 1.

The submerged areas of both Case 4 and Case 5 are located on the left side of the tunnel, with Case 4 being located above the vault and Case 5 on the left side and left foot of the tunnel. It can be seen that the overall settlement of Case 4 is similar to that of Case 2, except that the settlement curve of Case 4 is asymmetrically distributed, and the maximum settlement occurs at the left arch shoulder and at the top of the arch. Figure 16 shows the vertical rock displacement cloud of Case 5. It can be seen that the surrounding rock on the submerged side of the tunnel in Case 5 showed significant settlement.

Figures 17 and 18 show the horizontal displacement clouds of the surrounding rock for Case 4 and Case 5. It can be seen that water immersion on the left side of the tunnel causes the overall displacement of the tunnel to the right. In Case 4, the tunnel as a whole is compressed and flattened. The left side of the surrounding rock displaced to the left and the right side displaced to the right, with the right side having a greater displacement value. In working condition 5, due to the waterlogging of the arch foot, the soil arch effect of the tunnel surrounding rock is destroyed, and the bearing capacity is greatly reduced, and there is a tendency for the tunnel to be displaced to the right as a whole. In particular, the displacement of the right is significantly increased.

4. Impact of Joint Seepage on Tunnel Construction

4.1. Numerical Simulation Program. This section describes how the shallow buried loess tunnel is simulated for working Case 2, working Case 3, working Case 4, and working Case 5 using two construction methods: the three-step method and the Cross middle door method, that is, CRD.

The model and grouping of the three-step construction method are shown in Figure 19. The simulation procedure is as follows: first, the model is established, values are assigned to the surrounding rock, boundary conditions are applied, and the simulation of the wet zone is carried out after the

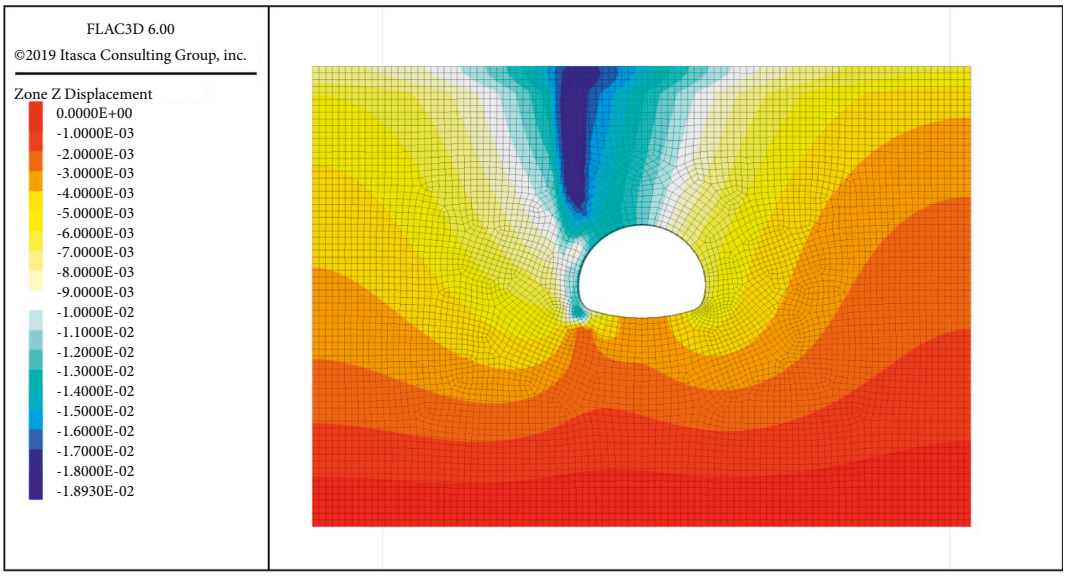

Figure 16: Case 5 vertical displacement cloud of surrounding rock.

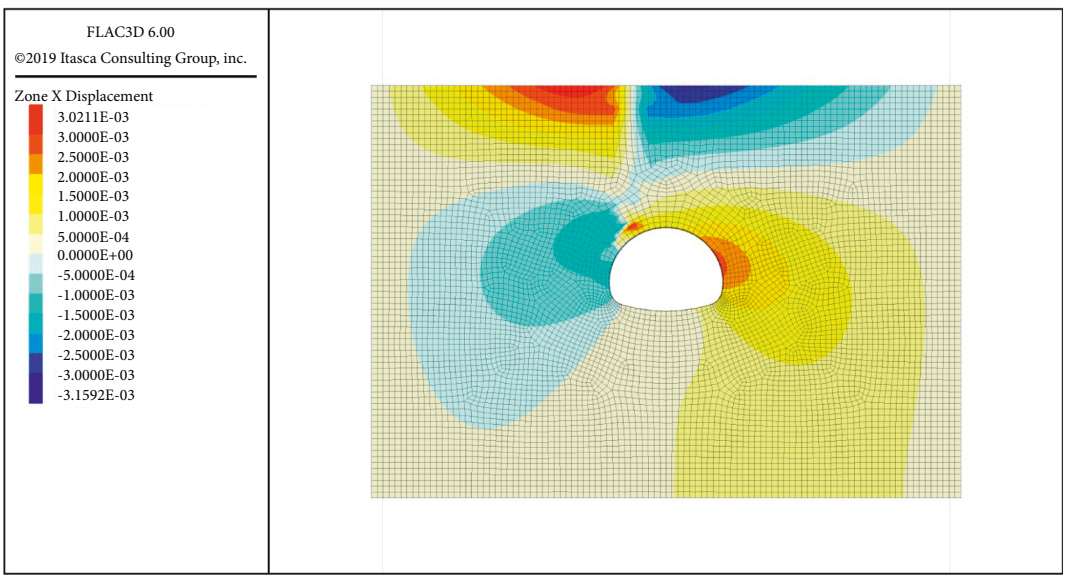

Figure 17: Case 4 horizontal displacement cloud of surrounding rock.

initial equilibrium. After calculating the stress in the wet zone, the displacement and velocity are zeroed to start the excavation, and the concrete lining and anchor support are applied according to the excavation of step A. The excavation of step B, the concrete lining, and anchor support are applied. Finally, the excavation of step C, the concrete lining, and anchor support are applied.

The model and grouping for the construction of the CRD method are shown in Figure 20. The simulation procedure is as follows. Firstly, the model is built, values are assigned to the surrounding rock, boundary conditions are imposed, and the wet zone after the initial equilibrium is simulated. After calculating the stress in the wet zone, the displacement and velocity are zeroed, and the excavation is started. According to the excavation of the upper left A step, the concrete lining and anchor support are applied. The upper right B step is excavated, and the concrete lining and anchor support are applied. The lower left C step is excavated, and the concrete lining and anchor support are applied. Finally, the lower right D step is excavated, and the concrete lining and anchor support are applied.

4.2. Surface Settlement Analysis. The tunnels have different flooding conditions, and the surface settlement is generated after the excavation was completed using different excavation methods. The surface settlement curves after the completion of the excavation by the three-step method and the CRD method are shown in Figures 21 and 22.

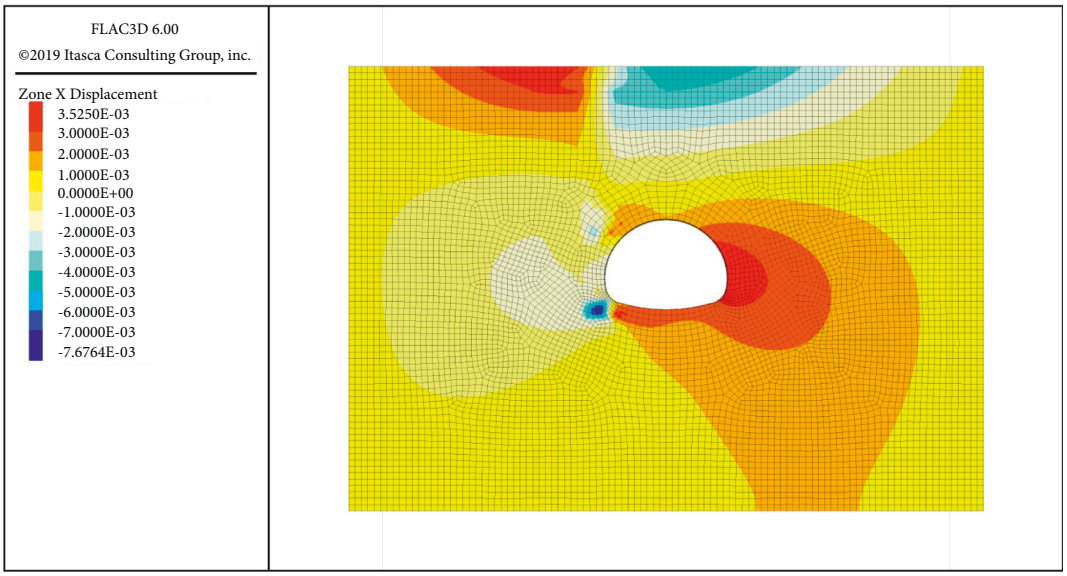

Figure 18: Case 5 horizontal displacement cloud of surrounding rock.

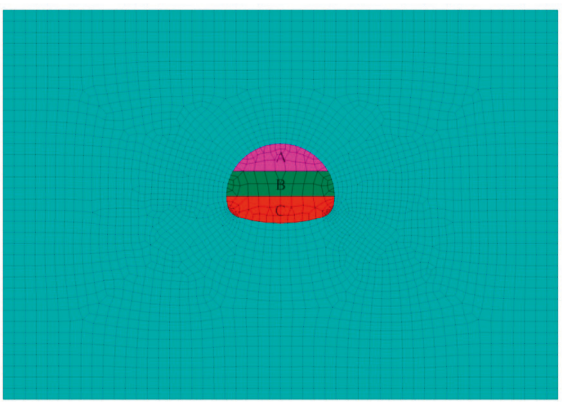

Figure 19: Numerical calculation model of three-step method construction.

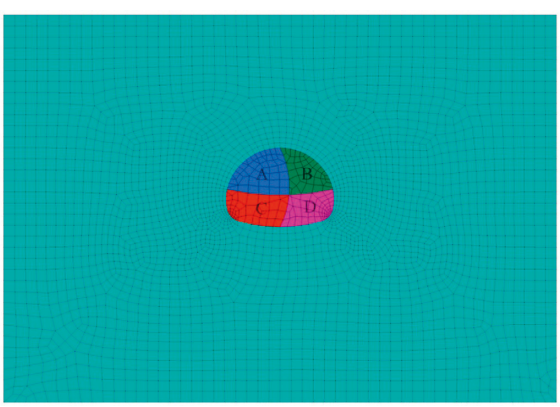

Figure 20: Numerical calculation model of CRD method construction.

It can be seen from Figure 19 that the surface soil showed a certain settlement trend after the completion of the construction of the three-stage method under each soaking

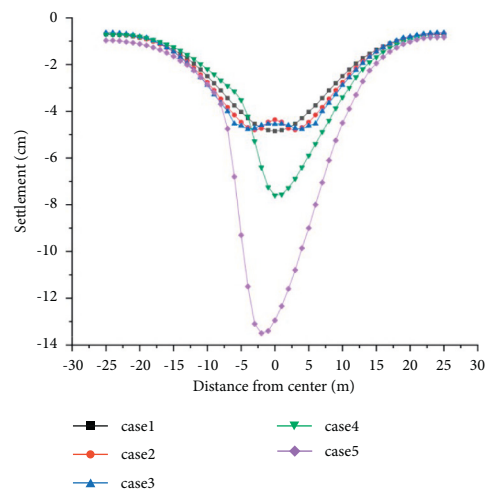

Figure 21: Surface displacement after the completion of the three-step method construction.

condition, and, with the increase of the vault soaking area, the vault settlement in Case 3 increased slightly compared with that in Case 2, but the increase was small. Figure 23 shows the vertical ground stress cloud of Case 2, which shows that the vertical stress in the middle of the submerged area is increased, the soil arch effect is produced on both sides, and the soil in the middle is extruded and raised.

The width of the submerged area in Case 4 and Case 5 is the same as that in Case 2, but the surface settlement is much larger than that in Case 1, with the maximum settlement value in Case 4 increasing by 60% compared with that in Case 2 and the maximum settlement value in Case 5 increasing by 185% compared with that in Case 2. It can be seen that the surface settlement caused by the arch shoulder and the arch foot dip condition is much larger than that of the arch top dip condition. Figure 24 shows the vertical ground stress cloud diagram of Case 5. It can be seen from

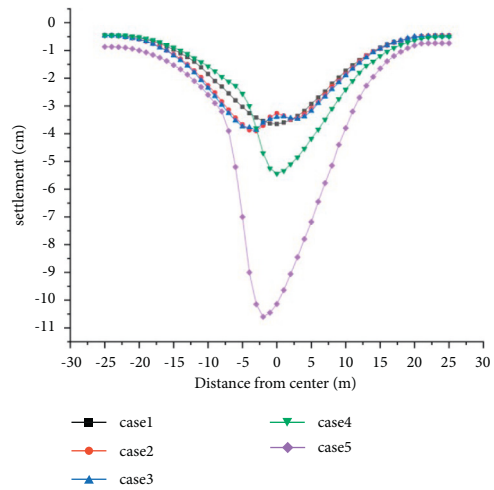

Figure 22: Surface displacement after the completion of the CRD method construction.

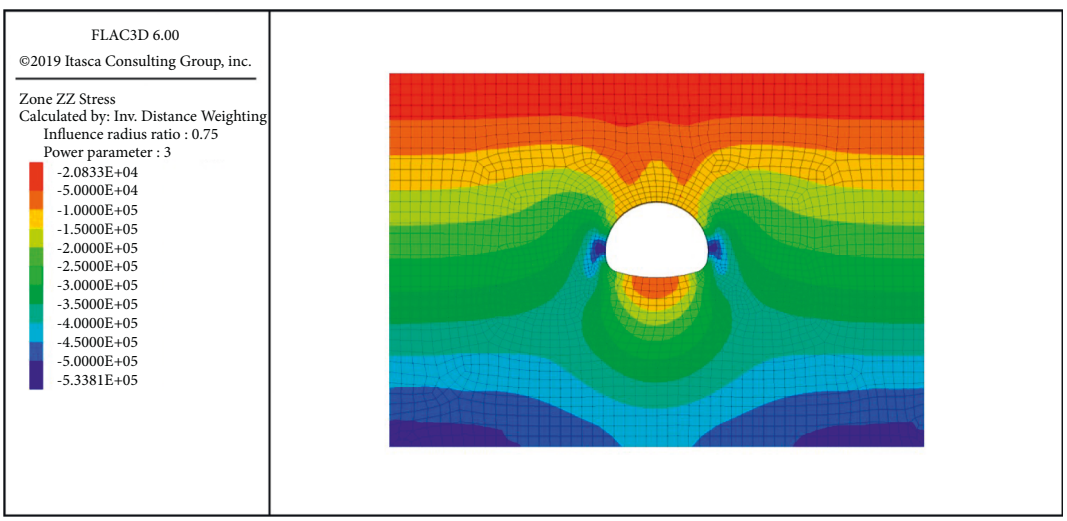

Figure 23: The vertical ground stress cloud of Case 2.

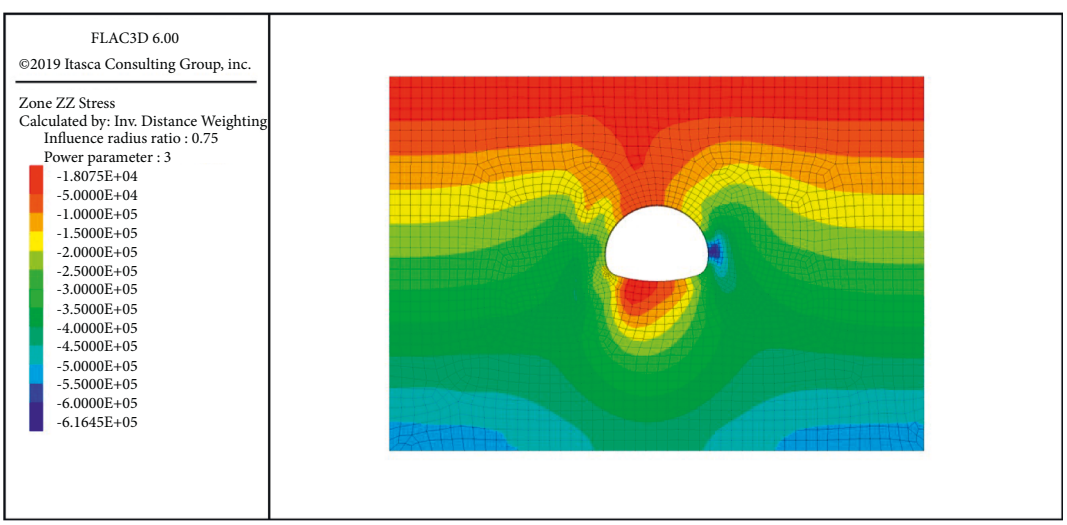

Figure 24: The vertical ground stress cloud of Case 5.

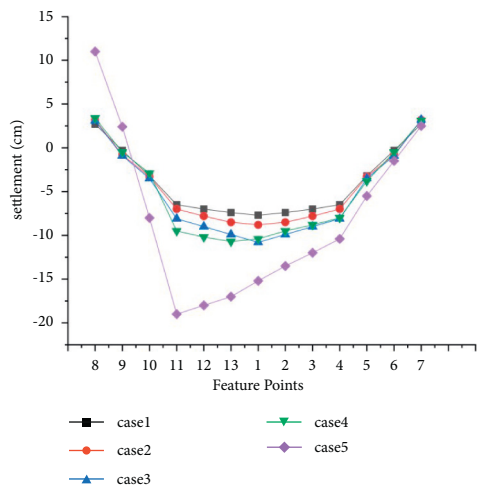

Figure 25: Vertical displacement of the surrounding rock after the completion of the three-step method.

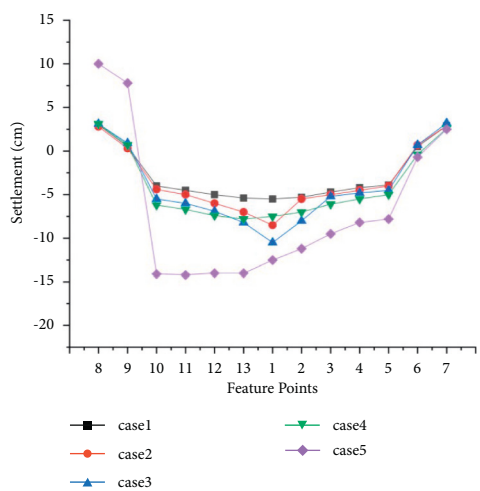

Figure 26: Vertical displacement of the surrounding rock after the completion of the CRD method.

Table 6: Vertical displacement of each working condition after excavation completion (cm).

Feature points	Case 1		Case 2		Case 3		Case 4		Case 5	
	Three-step	CRD	Three-step	CRD	Three-step	CRD	Three-step	CRD	Three-step	CRD
1	−7.7	−5.5	−8.8	−8.5	−10.8	−10.5	−10.4	−7.5	−15.2	−12.5
2	−7.4	−5.3	−8.5	−5.5	−9.9	−8	−9.5	−7	−13.5	−11.2
3	−7	−4.7	−7.8	−5	−9	−5.2	−8.8	−6.1	−12	−9.5
4	−6.5	−4.2	−7	−4.5	−8.1	−4.8	−8	−5.5	−10.4	−8.2
5	−3.2	−3.9	−3.3	−4	−3.5	−4.5	−3.8	−5	−5.5	−7.8
6	−0.3	0.5	−0.8	0.7	−0.9	0.7	−0.5	−0.4	−1.5	−0.7
7	2.7	2.9	3.2	2.9	3.2	3.2	3.1	2.6	2.5	2.5
8	2.7	3	3.2	2.8	3.1	3.1	3.4	3.1	11	10
9	−0.3	0.5	−0.8	0.3	−0.9	0.9	−0.5	0.7	2.4	7.8
10	−3.2	−4	−3.3	−4.4	−3.5	−5.5	−2.9	−6.2	−8	−14.1
11	−6.5	−4.5	−7	−5	−8.1	−6	−9.5	−6.7	−19	−14.2
12	−7	−4.9	−7.8	−6	−9	−6.9	−10.2	−7.4	−18	−14
13	−7.4	−5.3	−8.5	−7	−9.9	−8.2	−10.7	−7.8	−17	−14

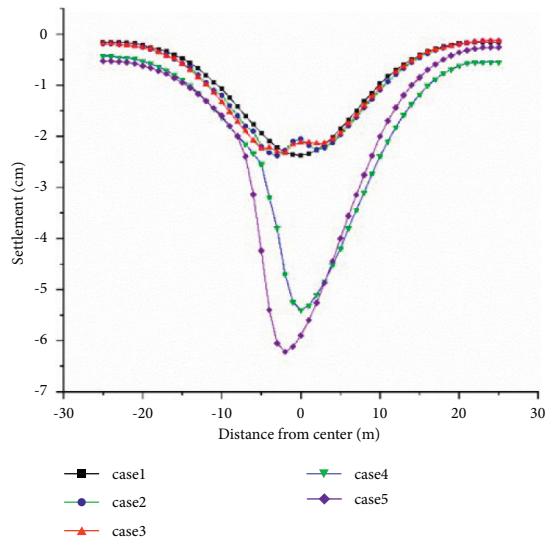

Figure 27: Surface displacement after the completion of the A-C-B-D sequence construction.

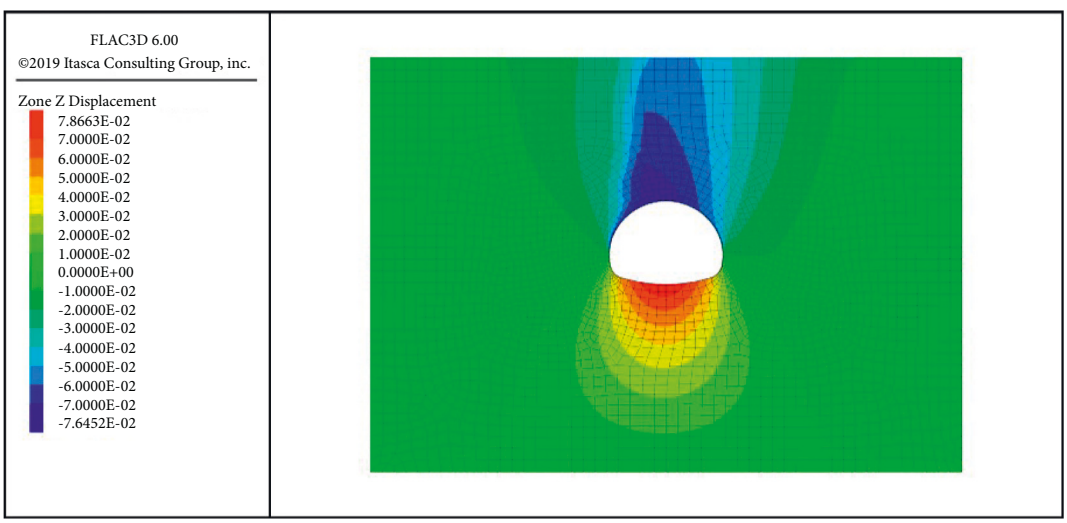

(a)

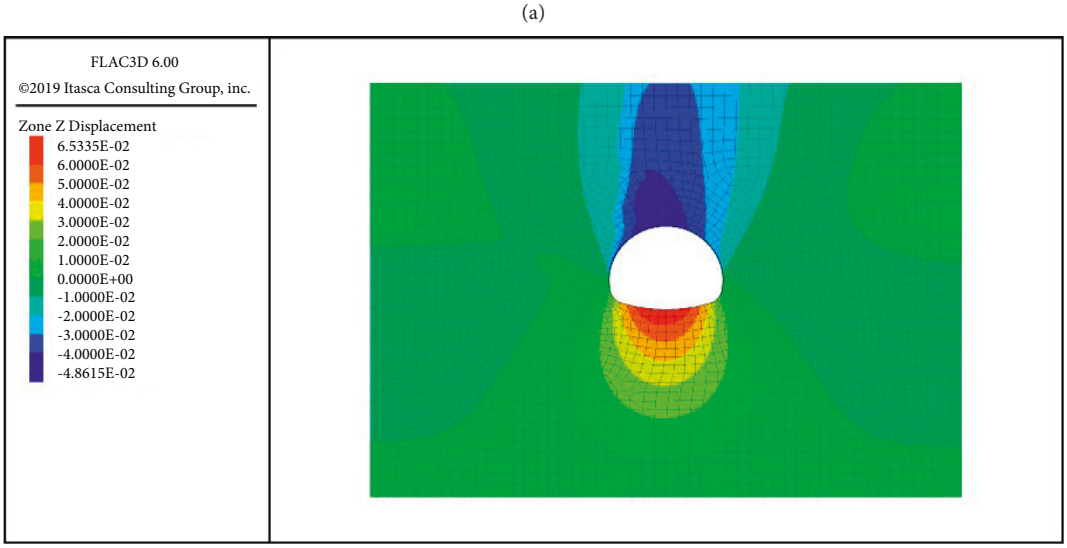

(b)

Figure 28: Case 4 vertical displacement cloud of surrounding rock. (a) A-B-C-D sequence. (b) A-C-B-D sequence.

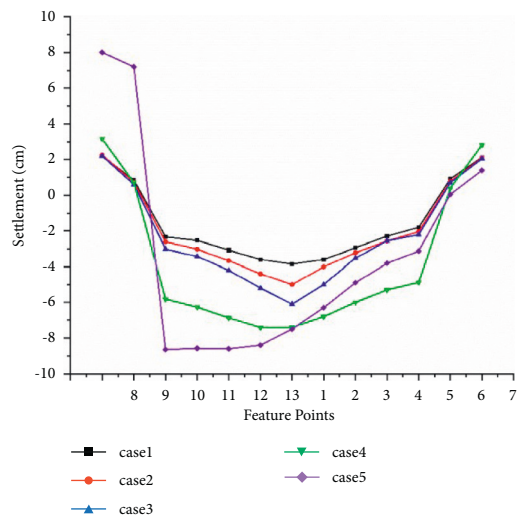

Figure 29: Vertical displacement of the surrounding rock after the completion of the A-C-B-D sequence construction.

Table 7: Vertical displacement of each working condition after excavation completion (cm).

Feature points	Case 1		Case 2		Case 3		Case 4		Case 5	
	A-B-C-D	A-C-B-D	A-B-C-D	A-C-B-D	A-B-C-D	A-C-B-D	A-B-C-D	A-C-B-D	A-B-C-D	A-C-B-D
1	−5.5	−3.8	−8.5	−5	−10.5	−6.1	−7.5	−7.4	−12.5	−7.5
2	−5.3	−3.6	−5.5	−4	−8	−5	−7	−6.8	−11.2	−6.3
3	−4.7	−2.9	−5	−3.2	−5.2	−3.5	−6.1	−6	−9.5	−4.9
4	−4.2	−2.3	−4.5	−2.6	−4.8	−2.5	−5.5	−5.3	−8.2	−3.8
5	−3.9	−1.8	−4	−2	−4.5	−2.2	−5	−4.9	−7.8	−3.1
6	0.5	0.92	0.7	0.78	0.7	0.7	−0.4	0.4	−0.7	0.1
7	2.9	2.13	2.9	2.1	3.2	2.1	2.6	2.8	2.5	1.4
8	3	2.2	2.8	2.3	3.1	2.2	3.1	3.1	10	8
9	0.5	0.85	0.3	0.73	0.9	0.6	0.7	0.7	7.8	7.2
10	−4	−2.32	−4.4	−2.6	−5.5	−3	−6.2	−5.8	−14.1	−8.65
11	−4.5	−2.52	−5	−3	−6	−3.4	−6.7	−6.3	−14.2	−8.58
12	−4.9	−3.05	−6	−3.7	−6.9	−4.2	−7.4	−6.9	−14	−8.6
13	−5.3	−3.58	−7	−4.4	−8.2	−5.2	−7.8	−7.4	−14	−8.4

Figure 24 that the vertical ground stress of the left side surrounding rock is greatly reduced due to the water immersion of the left arch foot, and the soil arch effect of the left arch foot is obviously weakened, which greatly weakens the bearing capacity of the surrounding rock.

Comparing the surface settlement after the completion of the three-stage method, it can be found that the surface settlement value decreases significantly after the construction of the cross-centralized next-door method, and the maximum value of surface settlement in each working condition is reduced by about 20%. From Figure 19, it can be observed that the settlement curves of Case 2 and Case 3 show two minimum points because the second relatively large settlement of the water-soaked surrounding rock at the top of the arch occurs after excavation of the B-stage. In both Case 4 and Case 5, the maximum settlement value point is located on the left side of the tunnel under the influence of water infiltration in the left side of the surrounding rock.

4.3. Surrounding Rock Displacement Analysis. The vertical displacement of the tunnel excavated by the three-step method after completion of excavation is shown in Figure 25. It can be seen that the maximum vertical displacement of working condition 1, working condition 2, and working condition 3 always appears at the top of the arch, the vertical displacement of arch shoulder and arch waist decreases in order, the vertical displacement of arch foot appears to be upward, and the displacement of arch bottom is between 2 and 3 cm, which is not much different. The arch top dip width has a certain influence on the arch top settlement, and the arch top settlements for the arch top dip condition in Case 2 and Case 3 are increased by 1.1 cm and 3.1 cm compared with Case 1, which have increase of 15% and 40%.

The maximum settlement of the surrounding rock in Case 4 appears in measurement point 13 between the left arch shoulder and the top of the arch, and the maximum value is 21.5% higher than that in Case 2. It can be seen that, for the same conditions of dip width, the influence of arch shoulder dip on the settlement of the surrounding rock is greater than that of arch top dip. The maximum settlement value of the surrounding rock in Case 5 is greatly increased compared with other cases. The maximum settlement value

is located in the left arch waist and above the lining, and the settlement value reaches 19 cm. It can be seen that the arch footing water immersion is the most unfavorable for tunnel construction settlement control. The existence of the wet zone of the tunnel arch shoulder and arch foot makes the tunnel be in a state of partial pressure, resulting in asymmetric vertical displacement. At the same time, due to the decrease in the bearing capacity of the surrounding rock in the wet zone, the self-supporting capacity of the rock above the tunnel decreases, and the tunnel lining is subjected to more external loads, so there will be a phenomenon of the vertical displacement being greater than other working conditions.

Figure 26 shows the vertical displacement of the tunnel excavated by the CRD method, and Table 6 shows the settlement values of the surrounding rock after excavation by the two excavation methods. It can be seen that, compared with the three-stage excavation method, the settlement of the tunnel using the CRD method is reduced under all conditions, which indicates that the CRD method is more advantageous in controlling the settlement of the surrounding rock.

In Case 2 and Case 3, the difference in the settlement of the arch roof after the completion of construction using two different construction methods is not large, but the settlement values of the shoulder and waist of the arch on both sides are significantly reduced. In Case 2, the settlement of the right lining is reduced by 35%, and the settlement of the left lining is reduced by 20%. In Case 3, the settlement of the right lining is reduced by 40%, and the settlement of the left lining is reduced by 25%.

In Case 4, the maximum settlement value was reduced by 27% by using the CRD method, and the settlement of the left arch shoulder was well controlled. In Case 5, excavation with the CRD method can largely avoid the huge settlement of 20 cm or more on the left arch waist and arch foot, and the maximum settlement is 26% lower than that of the three-step method. At the same time, the use of CRD method can make the overall settlement of the tunnel more uniform, and there will be no local huge settlement.

4.4. Comparative Analysis of Different Excavation Sequences of the Cross-Central Tunnel Method. This section describes the effect of using different excavation sequences on the forces and displacements in shallow buried loess tunnels during the construction of the cross-central tunnel method.

In the second paragraph of Section 4.1, the excavation sequence in the numerical simulation of the CRD method is A-B-C-D. In this section, the tunnel excavated using the A-C-B-D sequence is compared with the tunnel in Section 4.1.

The surface settlement using A-C-B-D sequence excavation is shown in Figure 27, and it can be seen that the surface settlement of each working condition is significantly reduced after using A-C-B-D sequence excavation. The maximum settlement values decreased by 35% for Case 1, 43% for Cases 2 and 3, and 42% for Cases 4 and 5.

Figure 28 shows the displacement of the surrounding rock after excavation using two different excavation sequences. It can be seen that the depth and width of surface settlement are significantly reduced in the case of excavation in the A-C-B-D sequence of excavating the surrounding rock on the submerged side first in Case 4. For tunnels excavated in the A-C-B-D sequence, the width of the surface 2 cm settlement trough is less than double the tunnel width, and the width of the 1 cm settlement trough is about 1.5 times the tunnel width, both of which are less than the settlement of tunnels excavated in the A-C-B-D sequence. This shows that excavating the surrounding rock on one side first and applying support structure can effectively control the surface settlement.

Figure 29 and Table 7 show the settlement values of the surrounding rock after excavation for both excavation sequences. It can be seen that the settlement of the tunnel surrounding rock in the A-C-B-D sequence is better controlled. In Case 1, the maximum settlement value of the surrounding rock decreased by more than 40%, reaching 2.3 cm. The maximum settlement values also decreased by 3.5 cm and 4.4 cm in Case 2 and Case 3, respectively. The overall displacement drop of the surrounding rock in Case 4 is not particularly significant, but the displacement at the left arch shoulder is still controlled to a certain extent. Case 5 is the most unfavorable condition of arch foot dip; after using A-C-B-D sequence excavation, the maximum settlement of tunnel surrounding rock is well controlled, and the overall settlement is reduced by more than 40%.

5. Conclusion

In this paper, numerical simulations of surface water infiltration in shallow buried loess tunnels containing joints in the surrounding rock were carried out to study the mechanical effects of loess tunnels under the influence of joint infiltration, and tunnel excavation simulations under joint infiltration conditions were performed. The following conclusions were drawn:

(1) Large open joints will form a seepage dominant channel when surface water infiltrates, and when the openness gradually increases, surface water will form an instilling effect and quickly form a saturated area in the bottom liner, and the seepage field will change from conical to rectangular. The increase of the number of joints can accelerate the infiltration rate of surface water and form a wider and deeper saturation area.

(2) Under the conditions of uniform surface infiltration and arch top water immersion, which are symmetrically distributed in the infiltration area, the horizontal displacement of the ground and tunnel surrounding rock and lining is not large, and the tunnel is not affected by the bias effect; the surface settlement, settlement trough width, and surrounding rock settlement of arch top water immersion are determined by the width of the water immersion area. Under the condition of arch shoulder submergence, the settlement of arch shoulder on the submerged side increases

significantly, the horizontal displacement of arch waist increases and the horizontal displacement of arch shoulder and arch waist on both sides is asymmetric, and the tunnel is characterized by significant bias force. The most significant effect of wetting on the surface and surrounding rock settlement is on the foot of the tunnel arch, and the surrounding rock and lining of the foot, arch waist, and arch shoulder on the immersed side will produce a large settlement.

(3) CRD method has the advantages of optimizing the lining force and effectively controlling the lining displacement and surrounding rock settlement under various working conditions. The CRD method has no obvious advantage over the three-step method in controlling the vault displacement under the vault flooding condition, but it has good effect in controlling the overall lining displacement. The CRD method can effectively control the settlement of the surrounding rock and reduce the lining under the conditions of waterlogged vault and vault foot, and the settlement of vault and vault shoulder is reduced by 20–30% compared with the three-step method. When using the CRD method of construction, changing the construction sequence can significantly affect the displacement and forces in the surrounding rock [21].

Data Availability

All data and models generated or used during the study are included within the article.

Conflicts of Interest

The authors declare that they have no conflicts of interest.

References

[1] Y. Li, W. Shi, A. Aydin, M. A. Beroya-Eitner, and G. Gao, "Loess genesis and worldwide distribution," *Earth-Science Reviews*, vol. 201, Article ID 102947, 2020.

[2] N. Li and Q. Yang, "Geotechnical engineering problems in water conservancy and civil construction in western China," *Journal of Water Resources and Architectural Engineering*, vol. 17, no. 5, pp. 1–8, 2019.

[3] D. Y. Xie, "Exploration of some new tendencies in research of loess soil mechanics," *Chinese Journal of Geotechnical Engineering*, vol. 23, no. 1, pp. 3–13, 2001.

[4] T. G. Ryashchenko, V. V. Akulova, and M. A. Erbaeva, "Loessial soils of priangaria, transbaikalia, Mongolia, and northwestern China," *Quaternary International*, vol. 179, no. 1, pp. 90–95, 2008.

[5] S. J. Shao, C. Yang, Y. Y. Jiao, and L. si, "Engineering properties of collapsible loess tunnel," *Chinese Journal of Geotechnical Engineering*, vol. 35, no. 9, pp. 1580–1590, 2013.

[6] S. J. Shao, F. Chen, and S. Shao, "Collapse deformation evaluation method of loess tunnel foundation," *Chinese Journal of Rock Mechanics and Engineering*, vol. 36, no. 5, pp. 1289–1300, 2017.

[7] Y. Luo, T. X. Wang, and J. J. Wang, "Finite element seepage flow model for unsaturated loesswith joints," *Journal of Engineering Geology*, vol. 22, no. 6, pp. 1115–1122, 2014.

[8] K. Y. Zhao, Q. Xu, and F. Z. Liu, "Seepage characteristics of preferential flow in loess," *Chinese Journal of Geotechnical Engineering*, vol. 42, no. 5, pp. 941–650, 2020.

[9] X. H. Deng, W. P. Cao, and D. S. Yang, "Stability analysis of shallow loess tunnel considering rainfall infiltration," *Journal of Civil & Environmental Engineering*, vol. 42, no. 2, pp. 45–55, 2020.

[10] Y. H. Zhao, H. Y. Luo, and X. Y. Miao, "Research on the characteristics of steel arch stress and variation of water content of loess tunnel surrounding rock," *Railway Standard Design*, vol. 63, no. 4, pp. 128–131, 2019.

[11] W. L. Zhao, H. P. Lai, and Y. Y. Liu, "Analysis of lining cracking of loess highway tunnel under flooded surrounding rock conditions," *China Journal of Highway and Transport*, vol. 31, no. 5, pp. 117–126, 2018.

[12] E. Wang, Q. G. Liang, and F. Wang, "Study on the influence of different flooding methods onthe deformation of loess metro tunnel," *Journal of Railway Science and Engineering*, vol. 1, no. 15, pp. 156–162, 2018.

[13] S. Xue, D. S. Yang, and X. H. Deng, "Influence of surface water infiltration on stability of shallow buried loess tunnel," *Journal of Xi'an Technological University*, vol. 37, no. 8, pp. 600–606, 2017.

[14] Y. B. Li, C. H. Zhu, and Y. Duan, "Mechanical response of lining structure under wetting effect of surrounding soil in loess tunnel," *Journal of Water Resources and Architectural Engineering*, vol. 18, no. 6, pp. 33–38, 2020.

[15] C. Gong and W. Ding, "A computational framework to predict the water-leakage pressure of segmental joints in underwater shield tunnels using an advanced finite element method," *International Journal for Numerical and Analytical Methods in Geomechanics*, vol. 42, no. 16, pp. 1957–1975, 2018.

[16] M. Lei, B. Zhu, C. Gong, W. Ding, and L. Liu, "Sealing performance of a precast tunnel gasketed joint under high hydrostatic pressures: site investigation and detailed numerical modeling," *Tunnelling and Underground Space Technology*, vol. 115, Article ID 104082, 2021.

[17] C. Gong, W. Ding, K. Soga, K. M. Mosalam, and Y. Tuo, "Sealant behavior of gasketed segmental joints in shield tunnels: an experimental and numerical study," *Tunnelling and Underground Space Technology*, vol. 77, pp. 127–141, 2018.

[18] C. Gong, W. Ding, K. M. Mosalam, S. Günay, and K. Soga, "Comparison of the structural behavior of reinforced concrete and steel fiber reinforced concrete tunnel segmental joints," *Tunnelling and Underground Space Technology*, vol. 68, pp. 38–57, 2017.

[19] C. Gong, W. Ding, and D. Xie, "Parametric investigation on the sealant behavior of tunnel segmental joints under water pressurization," *Tunnelling and Underground Space Technology*, vol. 97, Article ID 103231, 2020.

[20] C. Gong, W. Ding, K. Soga, and K. M. Mosalam, "Failure mechanism of joint waterproofing in precast segmental tunnel linings," *Tunnelling and Underground Space Technology*, vol. 84, pp. 334–352, 2019.

[21] W. Ding, C. Gong, K. M. Mosalam, and K. Soga, "Development and application of the integrated sealant test apparatus for sealing gaskets in tunnel segmental joints," *Tunnelling and Underground Space Technology*, vol. 63, pp. 54–68, 2017.

[22] B. X. Yuan, Z. J. Li, W. J. Chen et al., "Influence of groundwater depth on pile–soil mechanical properties and

fractal characteristics under cyclic loading," *Fractal and Fractional*, vol. 6, no. 4, p. 198, 2022.

[23] B. X. Yuan, Z. H. Li, Y. M. Chen et al., "Mechanical and microstructural properties of recycling granite residual soil reinforced with glass fiber and liquid-modified polyvinyl alcohol polymer," *Chemosphere*, vol. 286, no. 1, Article ID 131652, 2022.

[24] J. Q. Dang and J. Li, "The structural strength and shear strength of unsaturated loess," *Journal of Hydraulic Engineering*, vol. 7, pp. 79–83, 2001.

[25] M. H. Zhang, Y. L. Xie, and B .J Liu, "Analysis of the shear strength characteristics of loess during moisture increase," *Rock and Soil Mechanics*, vol. 27, no. 7, pp. 1195–1200, 2006.

Hindawi
Advances in Civil Engineering
Volume 2022, Article ID 3465281, 12 pages
https://doi.org/10.1155/2022/3465281

Research Article

Study on Mechanical Behavior of Reinforced Concrete Beams under Sulfate Attack

Xiaomeng Zang,[1] Genhui Wang,[1] Zichen Zhang,[1] Xiaolu Duan,[2] and Xiaoying Hu[3]

[1]*School of Civil Engineering, Lanzhou Jiaotong University, Lanzhou, Gansu 730070, China*
[2]*China Railway Eryuan Engineering Group Co. Ltd., Chengdu, Sichuan 610031, China*
[3]*School of Civil Engineering, Lanzhou University of Technology, Lanzhou, Gansu 730050, China*

Correspondence should be addressed to Xiaomeng Zang; zangxm@lzjtu.edu.cn

Received 23 December 2021; Revised 10 February 2022; Accepted 5 April 2022; Published 22 April 2022

Academic Editor: Yonghong Wang

In order to analyze the influence of sulfate corrosion on the mechanical behavior of reinforced concrete beams, the dry-wet cyclic corrosion test was carried out on the model test beams, and the two test beams corroded for 0 d and 60 d were statically loaded, respectively. Then, the changes in flexural mechanical properties of the two test beams corroded for 0 d and 60 d were studied. Finally, the nonlinear finite element model was created by using ABAQUS. The plastic damage model is used to reflect the sulfate corrosion, and the mechanical properties of concrete beams under long-term sulfate corrosion are further analyzed. The results show that the compressive strength of the test beam concrete after 60 days of corrosion is 13.6% higher than that before corrosion, which indicates that the strength of concrete is increased by sulfate corrosion in the early stage. With the increase of sulfate corrosion time, the strength and stiffness of the beam first increase and then decrease. With the change in corrosion time, the cracking load and flexural capacity first increase and then decrease, which is consistent with the mechanism of sulfate densification first and then deterioration of the concrete structure. The calculation formulas of cracking load and bending capacity obtained by fitting are accurate.

1. Introduction

A large number of salt lakes and saline soils are distributed in Northwest China. Salt corrosion caused by these special geographical environments is very common. Due to salt corrosion, many reinforced concrete structures appear diseased and even structural failure may result in advance, which seriously affects the service life of the structure. Among the salt corrosion problems, sulfate corrosion is particularly prominent and needs to be paid attention to. Common sulfate corrosion mainly occurs in industrial buildings (such as chemical plants), underground buildings, coastal buildings, highway and railway facilities in saline soil environment, and hydraulic structures in inland salt lakes. For concrete bridges, not only the foundation pier but also the upper beam body has been seriously corroded by sulfate [1–8]. With the rapid development of the world, China's various highways, railways, and other infrastructures are under vigorous construction, which puts forward higher requirements for the safety and durability of concrete structures. Therefore, it is necessary to study the stress of concrete structures in a sulfate corrosion environment [9, 10]. Nowadays, the research on sulfate corrosion is mostly focused on the level of concrete materials, such as the weight change rate of concrete test block with corrosion time and the change of dynamic elastic modulus and compressive strength [11–15]. However, and there are relatively few studies on the degradation of mechanical properties of concrete beams under sulfate corrosion. It is necessary to combine the existing research results in materials and further explore the content of the research structure level on this basis. At the same time, the specifications and test conditions are limited, and the indoor test is difficult to match the engineering practice, so a more perfect test

scheme needs to be designed [9]; for example, test beam size design, section reinforcement design, test solution configuration, mechanical test scheme, and other specific operation processes need to be further refined.

Based on the existing research, this paper designs the sulfate immersion test of reinforced concrete beam model and compares and analyzes the influence of sulfate corrosion on the mechanical properties of reinforced concrete box girder through static loading test, and the finite element model is established by using ABAQUS nonlinear analysis software [16–25] and reflects the sulfate corrosion by changing the relevant parameters in the plastic damage model. Then, the finite element calculation results are compared with the test results. The change in flexural mechanical properties of the test beam under long-term sulfate corrosion is analyzed by using the finite element model. Finally, the deterioration model of cracking load, flexural bearing capacity with corrosion time, and the degradation of the flexural effective section are obtained. Therefore, it has a certain guiding significance for the prediction of bearing capacity and service life of concrete bridges under similar corrosion conditions.

2. Test Overview

2.1. Test Purpose. In this paper, through experimental research the components were immersed in a 10% Na_2SO_4 solution. In order to speed up the corrosion process, the test was carried out in a dry-wet cycle mode close to the test conditions described in reference [26]. After that, the beams with corrosion time of 0 d and 60 d were tested by static loading failure mechanics. The whole test process is recorded, the test results are analyzed, and the changes in flexural mechanical properties of the two are compared, so as to provide an effective method and means for the study of the mechanical behavior of reinforced concrete beams under sulfate attack.

2.2. Test Scheme

2.2.1. Fabrication of Test Piece. The test beam with box section is designed for the sulfate corrosion test. The length of the test beam is $L = 2000$ mm, the concrete grade is C40, and the shear span ratio is 2.74. An embedded steel plate is set at the left and right of the bottom of the beam to prevent local concrete from being damaged under the action of concentrated force. The section size and reinforcement are shown in Figure 1, and the longitudinal reinforcement adopts Φ_6 ribbed reinforcement and stirrup Φ_6 ribbed reinforcement.

2.2.2. Layout of Measuring Points and Data Acquisition. The concrete strain gauge has been pasted at the midspan section of the test beam, with a resistance value of $120.5 \pm 0.2\%$ and a sensitivity coefficient of $2.032 \pm 0.26\%$ (the strain gauge has been pasted at the reinforcement of the midspan section before pouring concrete). The pasting position and the corresponding serial number of the concrete and reinforcement strain gauge are shown in Figure 2. Two dial indicators of model YHD-100 with a measuring range of 0~30 mm and an accuracy of 0.01 mm are symmetrically installed on the midspan bottom surface of the beam body to measure the midspan displacement of the test beam $f_0 = (f_1 + f_2)/2$. At the same time, the same dial indicators are arranged at the supports at both ends of the beam to measure the settlement f_3 and f_4 of the supports and then the midspan deflection of the beam $f = (f_1 + f_2)/2 - (f_3 + f_4)/2$.

2.2.3. Immersion Model Beam. The beam body cured for 28 d and reaching the corresponding concrete strength shall be placed in a pool with a length of 2.2 m, a width of 1.4 m, and a height of 0.7 m. Pour the prepared 10% sodium sulfate solution into the tank and completely soak the beam. The dry-wet cycle period is 15 days, the sodium sulfate solution is soaked for 7 days, and then the solution in the tank is pumped dry and dried at room temperature for 8 days [27–29], as shown in Figure 3.

2.2.4. Loading of Model Beam. Four-point bending static loading failure tests were carried out on the test beams corroded for 0 d and 60 d, respectively, to study their flexural mechanical properties. The beam numbers are 0 beam and 1 beam, respectively (both beams are cured in the same batch and under the same conditions). The two concentrated forces act on one-third of the beam span. The source of the force is the hydraulic jack, which is distributed through a distribution beam. Step-by-step loading is adopted, and each level stays for 5~10 minutes to obtain a stable measured value. The loading device is shown in Figure 4.

3. Analysis of Test Results

During the loading process of the No. 0 test beam, when the load reaches 24 kN, the first small crack appears at the midspan at the bottom of the beam, with a width of about 0.1 mm, which is regarded as the cracking load, which is close to the theoretical cracking load of 25 kN. With the increasing load, the crack in the middle of the span continues to develop, and then, the inclined crack also occurs in the support, and then, the crack extends upward along the beam height direction. When the load reaches about the yield load, the width of the inclined crack increases obviously; for example, one of the cracks increases from 1 mm to about 2 mm. Some different cracks are connected together to form the main crack, which continuously extends to the beam top, and the average spacing of cracks is 100 mm. With the continuous application of load, when the load reaches 170 kN, it is difficult to apply the load, the load cannot be applied continuously, and there is a gradual downward trend. The deflection in the middle of the span increases rapidly, and the maximum deflection is 3.284 mm. Finally, the concrete in the shear compression zone is damaged, the maximum crack width reaches about 2.5 mm, and the structure fails.

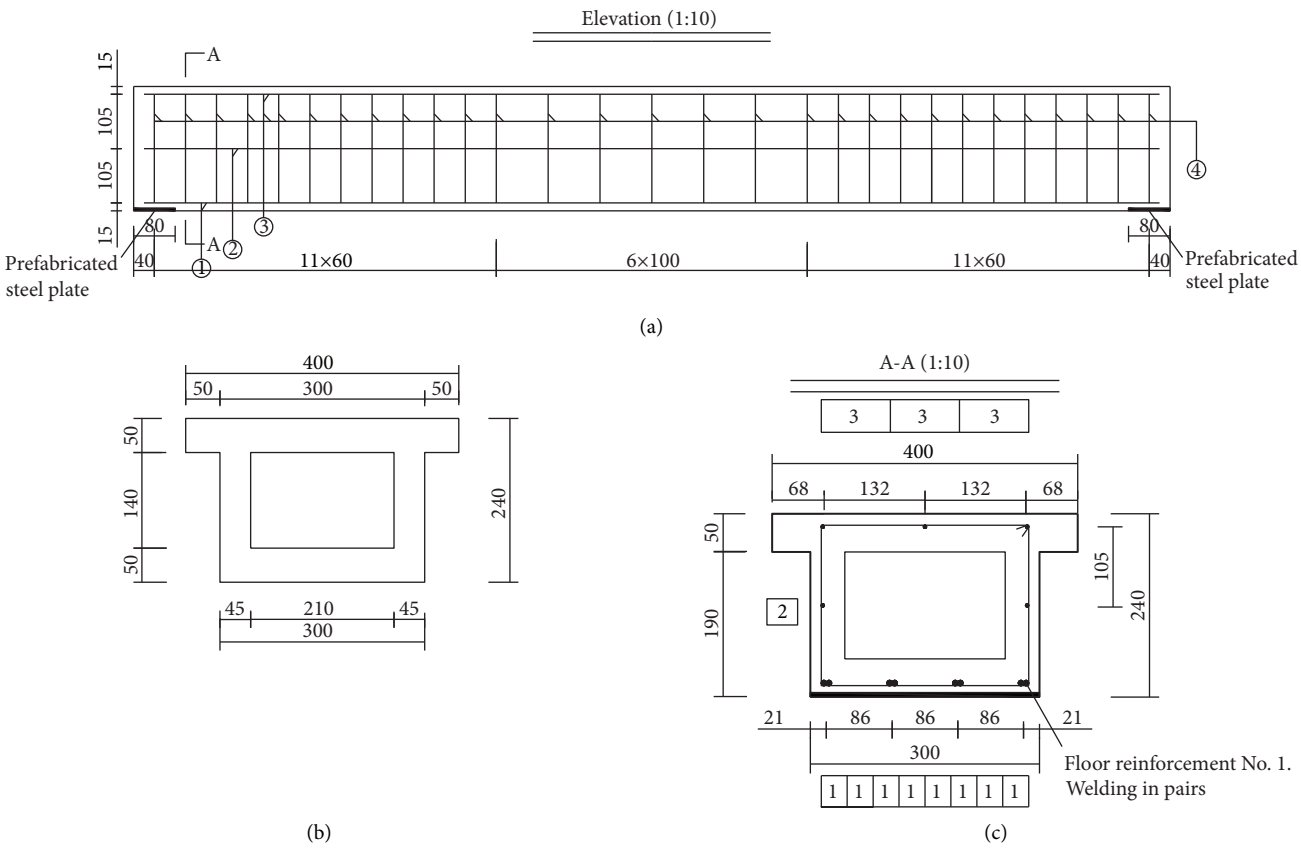

Figure 1: Section size and reinforcement arrangement of test beam (unit: mm). (a) Elevation. (b) Section. (c) Reinforcement layout.

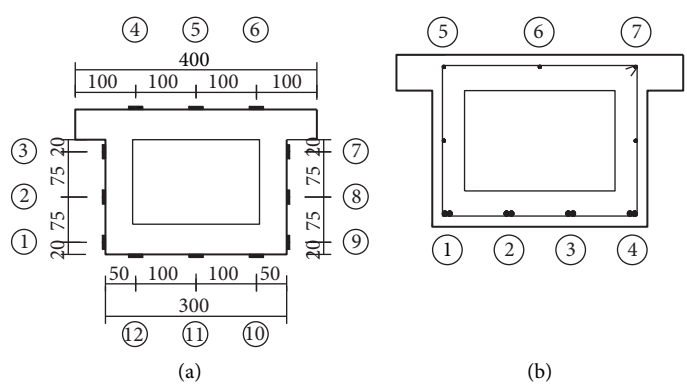

Figure 2: Arrangement of strain gauge of test beam (unit: mm). (a) Arrangement of concrete strain gauges. (b) Arrangement of reinforcement strain gauge.

The rebound value of the No. 1 test beam is measured before and after corrosion, and the change of concrete compressive strength can be obtained by correcting its carbonation depth. Through comparison, it can be found that the concrete compressive strength after 60 days of corrosion is 13.6% higher than that before corrosion, indicating that the concrete compressive strength of the beam body will be improved to a certain extent in the early stage of sulfate corrosion concrete beam. However, due to the short corrosion time, the mechanical test results are only slightly different from those in the noncorroded state. The situation of the whole test process is basically the same as that of the corroded 0 d test beam. When the first crack appears, the loading force is 32 kN, and the crack width is about 0.1 mm. With the continuous increase of the load, the crack at the middle of the span continues to develop, and then, the support also produces oblique cracks. The cracks extend upward in the beam height direction, the vertical cracks and oblique cracks continue to increase, the crack width also gradually increases, and the average spacing of cracks is 105 mm. When the loading force reaches 170 kN, the test beam is still under normal stress. After that, the force

(a) (b)

Figure 3: Immersion test of the model beam. (a) Immersion model beam. (b) 10% Na_2SO_4 solution configuration.

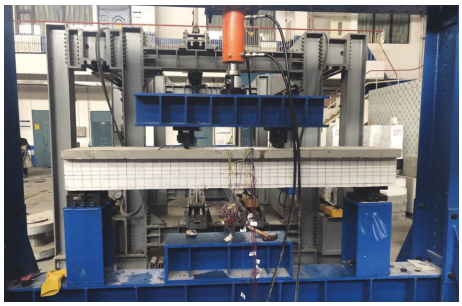

Figure 4: Loading device diagram.

continues to increase, and the deflection continues to increase. When it reaches a certain degree, the force cannot continue to be applied, it is unloaded automatically, the concrete at the inclined section is crushed, the structure fails and destroys, the test beam is damaged by bending, and the crack distribution is shown in Figure 5.

The cracking load is obtained through the test, and the change of yield load is shown in Table 1. The yield load of the test beam is controlled by the yield stress of the tensile reinforcement at the bottom [30, 31].

It can be seen from Table 1 that the cracking load of the current test beam increases with the change of corrosion days; that is, the cracking load of the 60-day corrosion test beam is increased by 33.3% compared with that before corrosion. The reason for this is that the corrosion degree will have a certain impact on the cracking load of the beam. At the initial stage of corrosion, sulfate will react with the concrete to produce expansive products, which will continuously compact the concrete, so as to enhance the crack resistance of the concrete. On the other hand, the expansive products will produce expansive internal stress in the concrete. When the concrete is under load, it is necessary to offset this part of the stress before the concrete is tensioned, so the cracking load increases. Similarly, the yield load of the test beam corroded for 60 days also increases by 3%.

4. Finite Element Model of Structure

4.1. Plastic Damage Model of Concrete. The concrete strength index reduction method is adopted to consider the impact of sulfate immersion corrosion on concrete strength. In ABAQUS software, the plastic damage model is a model based on plastic continuum damage. The principle is to use the combination of isotropic damage elasticity, isotropic tension, and compression plasticity to reflect the inelastic behavior of concrete [32]. In this paper, the plastic damage model is used to study the change of flexural mechanical properties of the test beam with the corrosion time, ignoring the factors such as the corrosion of reinforcement caused by sulfate corrosion and the change of bonding force between reinforcement and concrete [33, 34].

The key of the plastic damage model is to obtain the parameters of concrete CDP (concrete damaged plastic) constitutive relationship corresponding to different corrosion times to reflect the sulfate corrosion. The stress-strain curves of concrete are mainly divided into two types: one is the full stress-strain curve under uniaxial compression and the other is the full stress-strain curve under uniaxial tension.

Through the formula in references [35–37], the eigenvalue reflecting the constitutive relationship of concrete after corrosion can be calculated.

4.1.1. Constitutive Relation of Uniaxial Compression. According to the characteristics of the stress-strain curve of concrete under axial compression, document [36] proposed a curve equation with a cubic polynomial in the rising section and rational formula in the falling section, namely,

$$y = \begin{cases} ax + (3-2a)x^2 + (a-2)x^3, & 0 \le x \le 1, \\ \dfrac{x}{b(x-1)^2 + x}, & x \ge 1, \end{cases} \tag{1}$$

where $x = \varepsilon/\varepsilon_{pr}$, $y = \sigma/\sigma_{pr}$: ε_{pr} is the peak strain of concrete; σ_{pr} is the peak stress of concrete; and a, b are the parameters of rising section and falling section related to materials, respectively.

4.1.2. Constitutive Relation of Uniaxial Tension. According to reference [36], the full tensile stress-strain curve can also be described by a two-stage formula, that is, rising

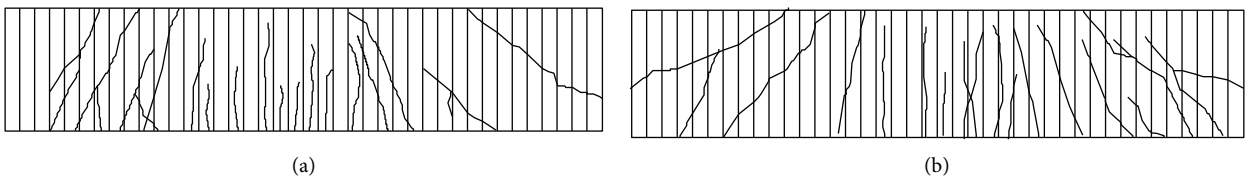

Figure 5: Fracture correlation. (a) Crack distribution in the web of No. 0 test beam. (b) Crack distribution in the web of No. 1 test beam.

Table 1: Test results of cracking load and yield load of test beam.

Number of test beam	Cracking load (kN)	Cracking moment M_{cr} (kN·m)	M_{cr}/M_{cr0}	Yield load (kN)	Yield moment M_y (kN·m)	M_y/M_{y0}
No. 0 test beam	24	8	1	149	49.67	1
No. 1 test beam	32	10.67	1.33	154	51.33	1.03

Note: M_{cr} is the cracking moment of the test beam corroded by sulfate; M_{cr0} is the cracking moment of the test beam not corroded by sulfate; M_y is the yield moment of the test beam corroded by sulfate; and M_{y0} is the yield moment of the test beam not corroded by sulfate.

stage and falling stage. The specific expression is as follows:

$$y = \begin{cases} 1.2x - 0.2x^6, & x \le 1, \\ \dfrac{x}{a_t (x-1)^{1.7} + x}, & x \ge 1. \end{cases} \tag{2}$$

The initial parameters of axial compressive strength are obtained by measuring the cube compressive strength of concrete test blocks with the same batch and strength grade of 100 mm × 100 mm × 100 mm as the test beam and multiplying the corresponding coefficient. The size is 34.1 MPa. Other parameters such as expansion angle 38, eccentricity 0.1, $f_{b0}/f_{c0} = 1.16$, $k = 0.66667$, viscosity parameter 0.05 are selected. The eigenvalues of concrete constitutive relationships corresponding to different corrosion times are shown in Table 2.

By analyzing the data in the table, it can be seen that the variation of each characteristic value of concrete is similar, which increases first and then decreases gradually. By using the relevant calculation tables and inputting the above parameters, the corresponding CDP constitutive relationship can be obtained. The stress-strain curves of concrete test blocks corroded for 0 d, 120 d, 360 d, and 600 d are compared, and the results are shown in Figure 6.

As can be seen from Figure 6, the height of the curve position is ranked as 120 d, 0 d, 360 d, and 600 d, indicating that the compressive stress-strain curve and tensile stress-strain curve belong to an upward trend from 0 to 120 d, and there is an overall downward trend after 120 d, with a greater degree of decline and a faster rate of decline. It shows that the performance of concrete changes with the corrosion time. In the early stage, the corrosion degree of sulfate on concrete is relatively light and even improves its strength to a certain extent. Then, the overall trend is decreased, and the deterioration speed is gradually accelerated, which has a serious impact on the performance of concrete and accelerates the deterioration of overall strength.

4.2. Numerical Analysis Model

4.2.1. Element Selection. The material properties of reinforcement and concrete are quite different. When dividing the calculation unit of the structure, according to the different methods of dealing with the two materials, three methods can be adopted: integral model, separated model, and combined element model [36]. The separated model divides reinforcement and concrete into different types of elements and gives different material parameters.

The characteristic modeling method [38] is used to establish the numerical analysis model of the reinforced concrete beam. The model size and reinforcement layout are consistent with the test concrete beam shown in Figure 1. The concrete adopts an eight-node hexahedral isoparametric element (C3D8) with reduced integral, and the reinforcement adopts a two-node three-dimensional linear truss element (T3D2). The reinforcement cage is built into the concrete by using the method of a built-in unit [39, 40].

4.2.2. Analysis Method and Convergence Criterion. Solid structure analysis is to solve the structural state response quantity that satisfies three kinds of basic equations under external action under given boundary conditions and initial conditions, including stress, strain, and displacement. Implicit algorithm or explicit algorithm can be used to solve the nonlinear equations of reinforced concrete structures. Among them, the implicit algorithm adopts the Newton–Raphson method to solve the nonlinear equation. In the process of solving, it is necessary to inverse the stiffness matrix at the current time.

4.2.3. Loads and Boundary Conditions. Mutual restraint is established between the reinforcement to form a whole, and the three-point loading is carried out on the model according to the test operation. The reference point RP-1 and the loading area are set, as shown in Figure 7. The two are coupled and connected, and then, the load is applied to

Table 2: Constitutive parameters of concrete corresponding to corrosion days.

Days of corrosion (d)	Axial compressive strength (MPa)	Compressive peak strain ($\mu\varepsilon$)	Elastic modulus (MPa)	Tensile strength (MPa)	Tensile peak strain ($\mu\varepsilon$)
0	34.1	1704	34555	3.17	121
60	34.6	1712	34697	3.20	122
120	34.6	1712	34701	3.20	122
240	33.1	1690	34286	3.11	120
360	29.6	1635	33268	2.88	115
480	24.0	1542	31526	2.51	107
600	16.3	1395	28782	1.94	93

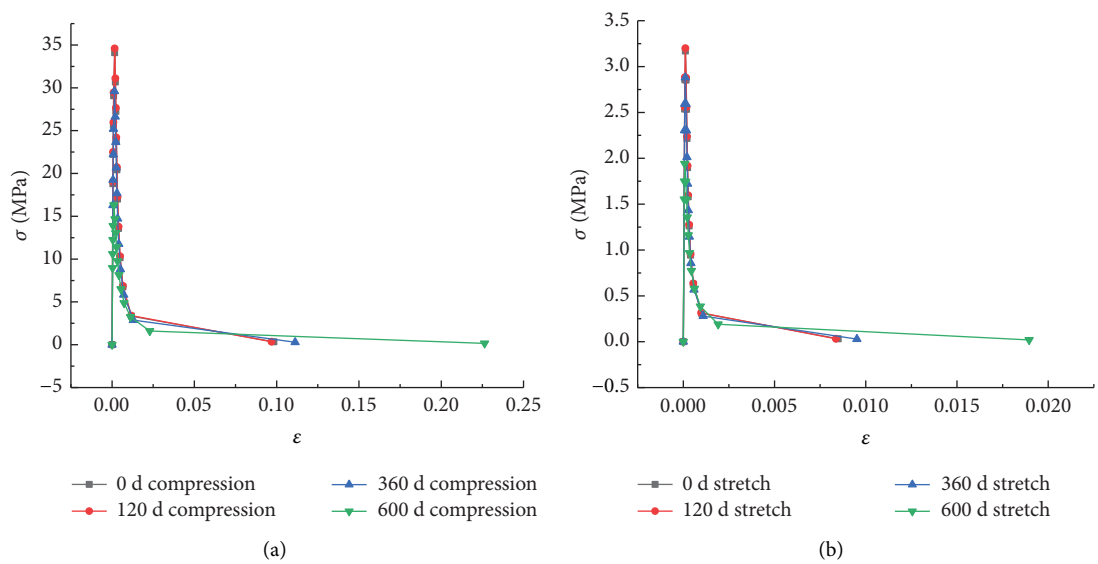

Figure 6: Comparison of stress-strain curves of concrete under different corrosion days. (a) Compressive stress-strain curve of the concrete test block. (b) Tensile stress-strain curve of the concrete test block.

the reference point to avoid stress concentration. The load is applied to the reference point RP-1, and then, the boundary conditions are created according to the simply supported structure.

4.2.4. Contact Conditions. Reinforcement and concrete are set in built-in contact.

4.3. Type of Element and Verification of Mesh Sensitivity. ABAQUS software sets up a rich element library to meet the requirements of different problems for different element types. At present, the commonly used element types in the structural analysis of solid materials include truss element (rod element), beam element, solid element, shell element, rigid body element, and membrane element. In this paper, the concrete adopts a spatial solid element, and the reinforcement adopts a spatial truss element.

Considering that the displacement mode [38] of the spatial 4-node tetrahedral element is a linear function similar to the plane 3-node triangular element, and the strain matrix of each element is constant, and its accuracy is often poor [41]. In this study, the concrete adopts the spatial 8-node hexahedron element, and the reinforcement adopts the

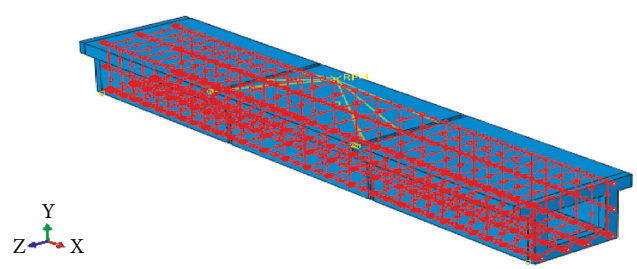

Figure 7: Interaction diagram.

spatial 2-node truss element. The 8-node hexahedron element adopts the displacement mode with three mixed quadratic terms and one mixed cubic term. The maximum number of times of its strain matrix is 2, which can accurately simulate the deformation of the element. Therefore, the spatial 8-node hexahedron element can be used to simulate the strain of the model concrete material.

In order to analyze the influence of element size on the calculation results of the concrete beam, the maximum Mises stress and S33 stress of concrete beam under 6 mm displacement loading are compared and analyzed by using different mesh sizes. The results are listed in Table 3. The

Table 3: Influence of element and mesh size on analysis results.

Mesh scheme	Concrete		Rebar		Mises stress (MPa)
	Element type	Grid size (mm)	Element type	Grid size (mm)	
Mesh 1	C3D8R	25	T3D2	25	6.15
Mesh 2	C3D8R	12.5	T3D2	12.5	9.1
Mesh 3	C3D8R	10.0	T3D2	10.0	10.2
Mesh 4	C3D8R	7.5	T3D2	7.5	10.3
Mesh 5	C3D20R	10.0	T3D3	10.0	10.2

analysis results show that when the concrete element is 10 mm and the reinforcement element is 10 mm, the influence of refining the element size on the analysis results is gentle.

In this paper, the numerical simulation of reinforced concrete beams is carried out by using reinforcement and concrete elements with an approximate size of 10 mm. The box section concrete beam is divided into 55440 spatial 8-node hexahedral reduced integral elements, and the reinforcement skeleton is divided into 2052 spatial 2-node linear truss elements.

4.4. Comparison between Numerical Simulation and Model Test Results. By using ABAQUS software, the nonlinear finite element models under seven corrosion conditions are established. The corrosion days are 0 d, 60 d, 120 d, 240 d, 360 d, 480 d, and 600 d, respectively. Now, the corrosion 0 d model is taken as an example. The whole tensile damage nephogram can reflect the location and development process of cracks. Figure 8 shows the tensile damage in the last frame of the ABAQUS model, and Figure 8 shows the midspan deflection nephogram of the ABAQUS model test beam.

It can be seen from Figure 8 that there is serious tensile damage in the lower midspan of the test beam and its adjacent areas, and there is a tensile stress concentration area at the concentrated loading point, which is consistent with the above mechanical test phenomena. It can be seen from Figure 9 that when the load is 170 kN, the deflection of the middle span of the test beam is large, and the maximum value is at the middle of the span, which is 3.328 mm, which is 1.3% different from the test result of 3.284 mm, indicating that the ABAQUS model is in good agreement with the test.

4.4.1. Load Strain Analysis. The load strain comparison of the concrete at the bottom of the model test beam is shown in Figure 10. It can be seen from Figure 10 that the change trend of corrosion 0 d test value and finite element calculation value is basically the same, and the difference between values is small. Similarly, the fitting degree between the load strain test value of concrete corroded for 60 days and the results of the finite element model is also high, which shows that the test results are reliable, and the method of nonlinear simulation analysis of test beam by using ABAQUS plastic damage model is effective.

4.4.2. Long-Term Sulfate Corrosion. In the previous step, the feasibility of ABAQUS nonlinear simulation is verified. Therefore, with the help of the nonlinear analysis finite element model, the change of flexural mechanical properties of concrete beams under long-term corrosion can be studied, and the load-strain curve corresponding to each corrosion day can be obtained, as shown in Figure 11.

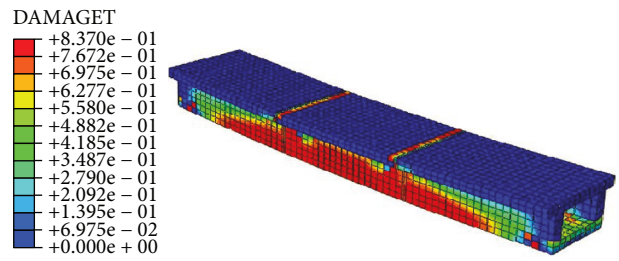

Figure 8: Nephogram of tensile damage of test beam.

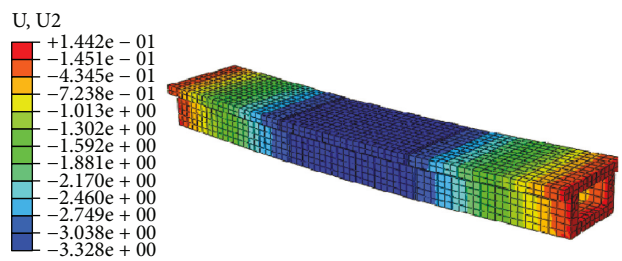

Figure 9: Nephogram of midspan deflection of test beam.

It can be seen from Figure 11 that when the load is small, the concrete strain corresponding to different corrosion times is basically the same or the difference is very small. When the action load is increased, the concrete strain of each corrosion beam is significantly different. The longer the corrosion time is, the greater the concrete strain under the same load, and the maximum increase is about 42%. At this time, the influence on the mechanical properties of the whole structure is obvious. When the load continues to increase to a certain extent, the difference gradually decreases, and the concrete strain value under each corrosion condition is almost equal. On the whole, long-term sulfate corrosion will increase the strain of concrete and reduce the flexural mechanical properties of test beams.

4.4.3. Analysis of Load Deflection Curve of Test Beam. The load-displacement curve corresponding to each corrosion day is obtained by ABAQUS finite element model, as shown in Figure 12.

It can be seen from Figure 12 that with the increase of sulfate corrosion time, the overall curve deviates to the lower

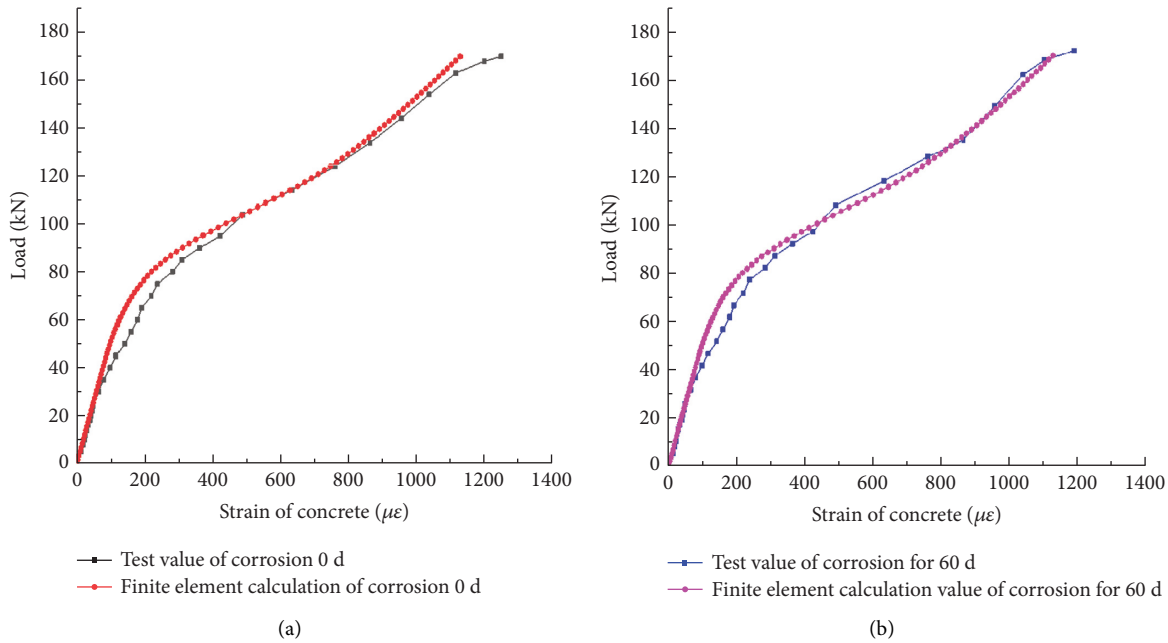

Figure 10: Load strain diagram of beam bottom concrete. (a) Load strain diagram of corrosion 0 d. (b) Load strain diagram of corrosion 60 d.

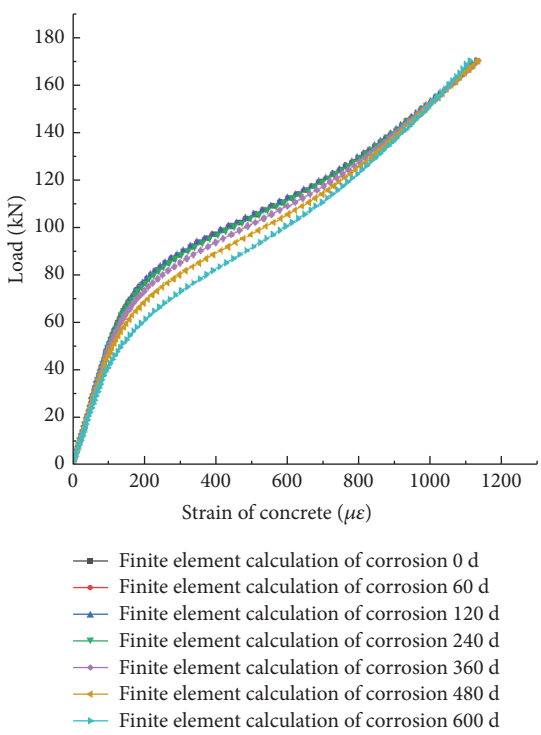

Figure 11: Load strain behavior of concrete at beam bottom.

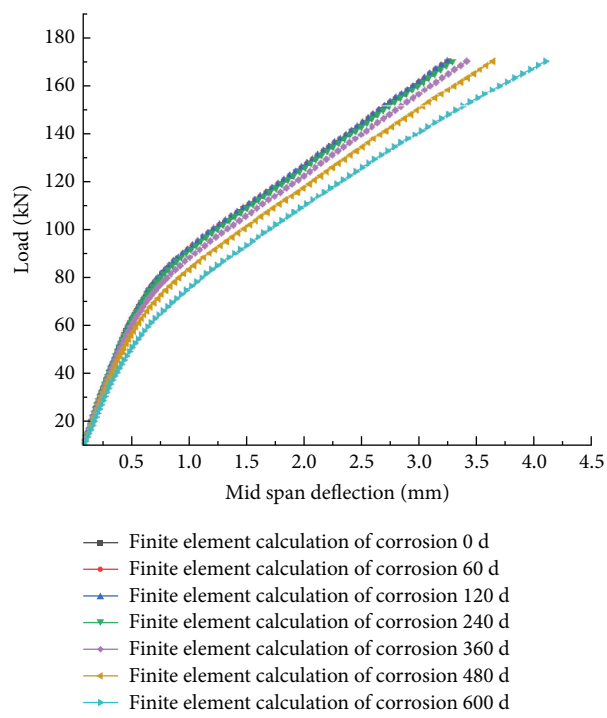

Figure 12: Load deflection curve.

right, indicating that under the condition that the test beam is subjected to the same size of the load, the higher the corrosion degree of the beam body, the smaller the stiffness and the worse the flexural mechanical performance, the greater the corresponding deflection, with the maximum increase of about 28%. Because the coincidence degree of the three curves of 0 d, 60 d, and 120 d is too high, it is difficult to distinguish the changes, so it is necessary to zoom in further. The results show that the corrosion curves of 60 d and 120 d are above the corrosion curve of 0 d, indicating that the deflection is smaller under the same load, indicating that the flexural mechanical properties of the test beam are improved in the corrosion time of 0~120 d. In conclusion, with the increase of sulfate corrosion time, the stiffness of the test beam first increases and then decreases; that is, with the

Table 4: Cracking load and flexural capacity corresponding to different corrosion days.

Corrosion days (d)	Cracking load (kN)	Flexural capacity (kN)
0	24.55	178
60	24.59	179.21
120	24.59	179.21
240	24.53	175.92
360	24.35	171.83
480	24.03	164.84
600	23.35	154.03

Note: the cracking load corresponding to corrosion 0 d in the table is 24.55 kN, which is close to the 24 kN obtained from the test; the cracking load corresponding to 60 days of corrosion is 24.59 kN, which is somewhat different from the 32 kN obtained from the test. It may be due to human factors, and there is an error in the observation of the first crack.

Table 5: Degradation of effective cross-sectional area of flexural section.

Corrosion time t (d)	Flexural capacity (kN)	Bending moment (kN·m)	Effective flexural cross-sectional area (mm^2)	Degradation of the effective cross-sectional area i (%)	Degradation rate of the effective cross-sectional area (10^{-5})
0	178	59.33	47600.00	0	—
240	175.92	58.64	47240.50	0.76	3.17
360	171.83	57.28	46761.17	1.76	8.33
480	164.84	54.95	45922.35	3.52	14.67
600	154.03	51.34	44604.20	6.29	23.08

Note: degradation rate of effective cross-sectional area = $(i_2 - i_1)/(t_2 - t_1)$.

deepening of corrosion, the flexural mechanical properties of the beam first increase and then decrease.

4.4.4. Effective Cross-Sectional Area of Bending Section of Test Beam. By analyzing the results of the ABAQUS finite element model, the cracking load of the test beam under different corrosion times can be obtained. According to the code, the theoretical flexural capacity of the section before corrosion of the test beam is 178 kN, and the corresponding deflection in the finite element model is 3.492 mm. Based on the deflection, the flexural capacity corresponding to each corrosion day can be obtained by applying displacement force. The results are shown in Table 4.

The change in the effective cross-sectional area of the flexural section is obtained according to the degradation of the flexural bearing capacity. Between 0 and 120 d of corrosion, the flexural mechanical properties of the test beam are improved due to the compactness of the concrete structure, so there is no degradation of the effective cross-sectional area of the flexural section. Therefore, from 240 d, the analysis results are shown in Table 5.

It can be seen from Table 5 that through analysis, it is found that with the change of corrosion time, the degradation rate of the effective cross-sectional area of sulfate corrosion test beam is 3.17, 8.33, 14.67, and 23.08, which increases exponentially. That is, the corrosion rate is faster and faster, the degradation degree of effective cross-sectional area is greater and greater, and the attenuation degree of the whole stiffness is stronger and stronger, which finally leads to the decreasing trend of beam bearing capacity. In the actual engineering analysis, the reason for the reduction of the effective cross-sectional area of the bending section is that after the sulfate corrodes the beam body, the part of the

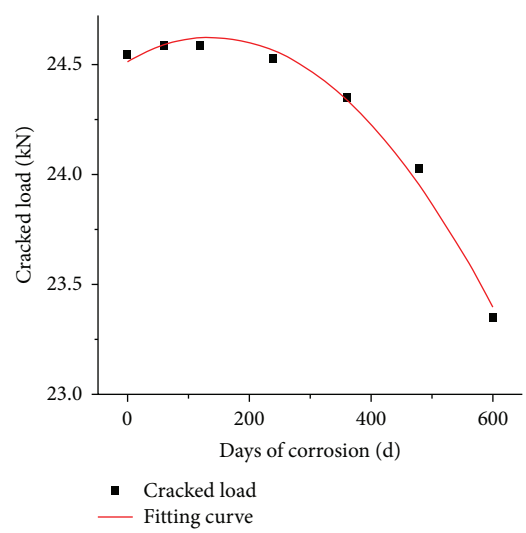

Figure 13: Fitting diagram of a variation of cracking load with sulfate corrosion time.

external concrete in contact with the corrosive environment is eroded, resulting in strength degradation, even cracking and spalling, reducing the effective cross-sectional area, deteriorating the stiffness of the beam body, and deteriorating the bearing capacity.

4.4.5. Calculation of Cracking Load and Flexural Capacity of Test Beam. It can be seen from Table 5 that with the increase of corrosion time, the cracking load increases first and then decreases. In order to better analyze the change of cracking load with corrosion time and study the change degree of mechanical properties of concrete beams under long-term

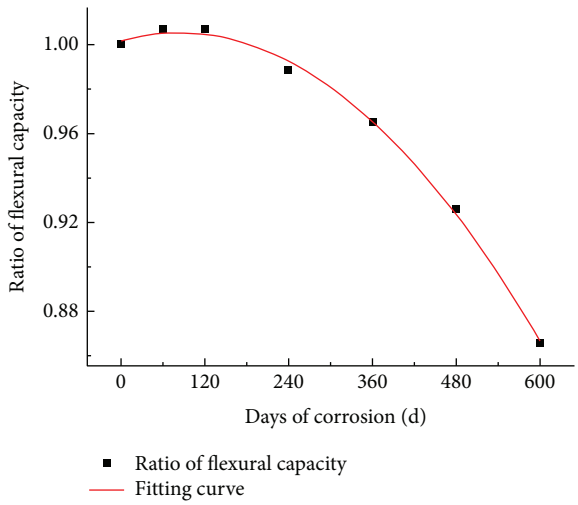

Figure 14: Fitting diagram of bending capacity with sulfate corrosion time.

sulfate corrosion, the quadratic polynomial can be used to fit the above results to obtain the calculation formula of formula (1), and the fitting curve is shown in Figure 13.

$$P_{cr} = 24.52 - 1.59 \times 10^{-3} t - 5.76 \times 10^{-6} t^2, \quad \text{correlation coefficient } R^2 = 0.986. \tag{3}$$

In addition, compared with that before corrosion, the flexural capacity increased by 0.68% at 60 d and 120 d and then showed a downward trend as a whole. It decreased by 1.17% at 240 d, 3.47% at 360 d, 7.39% at 480 d, and 13.47% at 600 d. It can be found that the decline rate of flexural capacity increased exponentially, indicating that the degradation rate of flexural mechanical properties of the test beam is faster and faster. Therefore, another percentage method can be used to reflect the degradation of bearing capacity; that is, the following formula can be obtained by fitting:

$$\frac{P_{ut}}{P_{u0}} = 1.002 + 8.559 \times 10^{-5} t - 5.180 \times 10^{-7} t^2, \quad \text{correlation coefficient } R^2 = 0.997, \tag{4}$$

where the flexural capacity of the test beam without p_{u0} corrosion, $p_{u0} = 178$ kN; and P_{ut} is the flexural capacity of the test beam corroded for t days. The fitting degree is good, and the fitting curve is shown in Figure 14.

5. Conclusion

In the early stage of corrosion, the strength of concrete increases. The main reason is that, in the early stage of corrosion, the expansive products generated by sulfate and concrete fill the pores of the structure, compact the concrete, and produce expansive internal stress, which improves the flexural mechanical properties of the structure to a certain extent. Comparing the test data with the finite element calculation results, it can be found that the calculation results obtained by ABAQUS finite element numerical simulation are in good agreement with the test data. Through the numerical simulation under different corrosion days, it is found that with the increase of sulfate corrosion time, the strength and stiffness of the beam have experienced a process of first increasing and then decreasing. It shows that sulfate corrosion does have a significant impact on the flexural mechanical properties of concrete, and the structural performance will deteriorate under long-term corrosion, which will affect the durability of the beam and reduce its service life. At the same time, the cracking load and flexural capacity also increase first and then decrease, which is consistent with the mechanism of sulfate compacting first and then deteriorating concrete structure. Therefore, the deterioration model of cracking load and flexural capacity with corrosion time is accurate through data fitting.

Sulfate corrosion is a complex and slow process with many influencing factors. This paper only studies 10% sodium sulfate solution. The concentration and type of sulfate have a profound impact on the test results. If magnesium sulfate solution is used, the test results may change greatly. Moreover, due to the time limit, only the mechanical properties of two beams corroded for 0 d and 60 d are studied, and the test data are very limited. Therefore, in future research, it is suggested to increase the corrosion days to 2 years or even 3 years, so as to obtain more data for more practical analysis and research.

Data Availability

The data generated or used during the study are included within the article.

Conflicts of Interest

The authors declare that they have no conflicts of interest.

Acknowledgments

This study was supported by the Science and Technology project of Gansu Provincial Department of Transportation (2020-05), Provincial Natural Science Foundation of Gansu Youth Fund (20JR5RA435), Gansu University Innovation Fund Project (2020A-026), Science and Technology Plan of Gansu Province (21JR7Ra306), and Hongliu Outstanding Young Talents Support Program of Lanzhou University of Technology (062006).

References

[1] D. Niu, *Durability and Life Prediction of concrete Structures*, Science Press, Beijing, China, 2003.

[2] J. Ran, *Study on the Influence of Cracks on the Durability of Bridge Structures in Northwest China*, Lanzhou Jiaotong University, Jiaotong, China, 2018.

[3] Y. Bao and J. Chen, "A new model of damage evolution of concrete under sulfate attack," *Journal of Ningbo University*

(Science and Engineering Edition), vol. 29, no. 1, pp. 98–102, 2016.

[4] L. Jiang, *Study on Deterioration Law of concrete under Sulfate Attack Environment*, Xi'an University of Architecture and Technology, Xi'an, China, 2014.

[5] L. Linlin, *Study on Corrosion of concrete by Sulfate and Inhibition Mechanism of Chloride under Different Mechanisms*, China University of Mining and Technology, Beijing, China, 2016.

[6] B. Bai, R. Zhou, G. Q. Cai, W. Hu, and G. C. Yang, "Coupled thermo-hydro-mechanical mechanism in view of the soil particle rearrangement of granular thermodynamics," *Computers and Geotechnics*, vol. 137, no. 8, Article ID 104272, 2021.

[7] B. Bai, Q. K. Nie, Y. K. Zhang, X. L. Wang, and W. Hu, "Cotransport of heavy metals and SiO2 particles at different temperatures by seepage," *Journal of Hydrology*, vol. 597, Article ID 125771, 2021.

[8] B. X. Yuan, Z. H. Li, Z. L. Su, Q. Z. Luo, M. J. Chen, and Z. Q. Zhao, "Sensitivity of multistage fill slope based on finite element model," *Advances in Civil Engineering*, vol. 2021, Article ID 6622936, 13 pages, 2021.

[9] L. Tao, Z. Sun, and K. Ding, "Research progress on mechanical properties and corrosion products of sulfate eroded concrete," *Concrete and Cement Products*, vol. 273, no. 1, pp. 1–5, 2019.

[10] Z. Jin, *Durability and Life Prediction of concrete under Severe Environment in Western China*, Southeast University, Dhaka, Bangladesh, 2006.

[11] C. D. Lawrence, "Mortar expansions due to delayed ettringite formation. Effects of curing period and temperature," *Cement and Concrete Research*, vol. 25, no. 4, pp. 903–914, 1995.

[12] O. S. B. Al-Amoudi, "Attack on plain and blended cements exposed to aggressive sulfate environments," *Cement and Concrete Composites*, vol. 24, no. 3-4, pp. 305–316, 2002.

[13] S. Chen and B. Wang, "Study on durability of bridge concrete structure under severe corrosion environment," *Journal of railway engineering*, vol. 35, no. 12, pp. 26–30, 2018.

[14] S. Zhang, *Sulfate Corrosion Mechanism of Concrete in Complex Environment*, Qingdao University of Technology, Qingdao, China, 2014.

[15] B. X. Yuan, Z. H. Li, Y. M. Chen et al., "Mechanical and microstructural properties of recycling granite residual soil reinforced with glass fiber and liquid-modified polyvinyl alcohol polymer," *Chemosphere*, vol. 268, Article ID 131652, 2021.

[16] B. Bai, D. Y. Rao, T. Chang, and Z. G. Guo, "A nonlinear attachment-detachment model with adsorption hysteresis for suspension-colloidal transport in porous media," *Journal of Hydrology*, vol. 578, Article ID 124080, 2019.

[17] A. Shishegaran, M. R. Khalili, B. Karami, T. Rabczuk, and A. Shishegaran, "Computational predictions for estimating the maximum deflection of reinforced concrete panels subjected to the blast load," *International Journal of Impact Engineering*, vol. 139, Article ID 103527, 2020.

[18] A. Shishegaran, M. R. Ghasemi, and H. Varaee, "Performance of a novel bent-up bars system not interacting with concrete," *Frontiers of Structural and Civil Engineering*, vol. 13, no. 6, pp. 1301–1315, 2019.

[19] A. Shishegaran, B. Karami, T. Rabczuk, A. Shishegaran, M. A. Naghsh, and M. Mohammad Khani, "Performance of fixed beam without interacting bars," *Frontiers of Structural and Civil Engineering*, vol. 14, no. 5, pp. 1180–1195, 2020.

[20] M. A. Naghsh, A. Shishegaran, B. Karami et al., "An innovative model for predicting the displacement and rotation of column-tree moment connection under fire," *Frontiers of Structural and Civil Engineering*, vol. 15, no. 1, pp. 194–212, 2021.

[21] B. Karami, A. Shishegaran, H. Taghavizade, and T. Rabczuk, "Presenting innovative ensemble model for prediction of the load carrying capacity of composite castellated steel beam under fire," *Structures*, vol. 33, pp. 4031–4052.

[22] A. Shishegaran, M. Saeedi, S. Mirvalad, and A. H. Korayem, "The mechanical strength of the artificial stones, containing the travertine wastes and sand," *Journal of Materials Research and Technology*, vol. 11, pp. 1688–1709, 2021.

[23] A. Shishegaran, B. Karami, E. S. Danalou, H. Varaee, and T. Rabczuk, "Computational predictions for predicting the performance of steel 1 panel shear wall under explosive loads," *Engineering Computations*, vol. 3, pp. 1–19, 2021.

[24] A. Shishegaran, H. Varaee, T. Rabczuk, and G. Shishegaran, "High correlated variables creator machine: prediction of the compressive strength of concrete," *Computers & Structures*, vol. 247, Article ID 106479, 2021.

[25] A. Shishegaran, F. Daneshpajoh, H. Taghavizade, and S. Mirvalad, "Developing conductive concrete containing wire rope and steel powder wastes for route deicing," *Construction and Building Materials*, vol. 232, Article ID 117184, 2020.

[26] J. Liu, S. Song, and M. Gao, "Study on the mechanism of carbon sulfur wollastonite formed by cement-based materials in corrosive environment," *Journal of Building Materials*, vol. 20, no. 6, pp. 846–853, 2017.

[27] A. Atkinson, D. J. Goult, and J. A. Heame, "An assessment of the long-term durability of concrete in radioactive waste repositories," *Materials Research Society*, vol. 50, 1985.

[28] D. Pan, *Research on Key Technologies to Improve the Durability of concrete Bridges in Alpine Areas*, Chongqing Jiaotong University, Shanghai, China, 2010.

[29] F. Zhang, Y. Yuan, and J. Du, "Study on damage detection of concrete members corroded by sulfate," *Journal of China University of Mining and Technology*, vol. 40, no. 3, pp. 373–378, 2011.

[30] Y. Tang, H. Lu, and Y. Zou, "Experimental study on flexural behavior of composite reinforced concrete beams," *Journal of Southeast University (Natural Science Edition)*, vol. 50, no. 05, pp. 822–830, 2020.

[31] F. Zhou, X. Wen, and D. Yunxing, "Flexural behavior of reinforced concrete beams strengthened with TRC plates," *Journal of Central South University*, vol. 49, no. 1, pp. 183–191, 2018.

[32] W. Liu, M. Xu, and Z. Chen, "Parameter calibration and verification of ABAQUS concrete damage plastic model," *Industrial Architecture*, vol. 44, no. S1, pp. 167–171, 2014.

[33] R. Gao, *Study on Micro Macro Deterioration Law of concrete Sulfate Erosion in Complex Environment*, Tsinghua University, Beijing, China, 2010.

[34] X. Wan, *Study on Diffusion Reaction Law and Numerical Simulation of concrete under Sulfate Attack Environment*, Nanjing University of Technology, Nanjing, China, 2010.

[35] Y. Liang and Y. Yuan, "Constitutive relation of concrete under uniaxial compression after sulfate corrosion," *Journal of Harbin Institute of Technology*, vol. 40, no. 4, pp. 532–535, 2008.

[36] G. Zhenhai and S. Xudong, *Principle and Analysis of Reinforced concrete*, Tsinghua University Press, Beijing, China, 2003.

[37] D. Niu, *Durability of Concrete in Complex Environment*, Science Press, Beijing, China, 2020.

[38] P. Zeng, *Finite Element Analysis and Application*, pp. 166–376, Tsinghua University Press, Beijing, China, 2004.
[39] P. Zhao, "Study on restoring force model of precast concrete frame beam column joints," *Earthquake Resistance and Reinforcement of Engineering*, vol. 38, no. 6, pp. 55–59, 2016.
[40] F. Wang, Z. Luo, and X. Lan, "Finite element analysis of axial compression performance of reinforced concrete beam column corner joints with built-in steel tube reinforced circular steel tube," *Journal of Building Structures*, vol. 36, no. S1, pp. 367–374, 2015.
[41] J. Jiang, F. He, and Y. He, *Finite Element Method and its Application*, pp. 54-55, China Machine Press, Beijing, China, 2006.

Hindawi
Advances in Civil Engineering
Volume 2022, Article ID 1595651, 12 pages
https://doi.org/10.1155/2022/1595651

Research Article

Study on Environmental Effects Induced by Quasirectangle Shield Tunnelling with Analytical Stiffness Matrix

Jianguo Xu,[1] **Fengyang Miao**,[1] **Lei Kou**,[1] **and Jinpeng Zhang**[2]

[1]*School of Water Conservancy Engineering, Zhengzhou University, Zhengzhou 450001, Henan, China*
[2]*Henan Puze Expressway Company Limited, Puyang 457000, Henan, China*

Correspondence should be addressed to Lei Kou; klyhe@163.com

Received 4 January 2022; Accepted 21 March 2022; Published 9 April 2022

Academic Editor: Yonghong Wang

During the quasirectangle shield tunnelling, the soil around the tunnel is inevitably disturbed which results in different degrees of additional stresses and displacement of the soil. In this paper, the environmental effects caused by the construction of quasirectangle shield are analyzed by the analytical stiffness matrix method, focusing on the law of the additional stress field and the deformation of the multilayered soil induced by the construction of a quasirectangle shield. The results show that the additional stresses field has localized characteristics around the quasirectangle shield. The further away from the excavation face, the smaller the stress is. Also, shell friction and synchronous grouting pressure have a significantly greater influence on the additional stress field. Finally, the horizontal settlement groove of the quasirectangle shield is roughly symmetrical and parabolic along the tunnel axis, with a groove width range of about 20m. Synchronous grouting pressure has a greater effect on longitudinal ground deformation.

1. Introduction

With the gradual exploitation of underground space in the city, reasonable and efficient use is very important. In order to save the occupancy rate of urban underground space, civil engineers are constantly improving the construction process and proposing new construction technologies. The quasirectangle shield construction technology, which is based on the new structural section of the rectangular tunnel shield, is a new rail transportation construction technology. Compared to the rectangular shield tunnel, the main structure thickness of the quasirectangle shield tunnel is significantly reduced and the structural efficiency is higher. Compared to the circular shield tunnel, oval shield tunnel, and double circular shield tunnel, quasirectangle shield tunnel has higher section utilization rates. The quasirectangle shield tunnel takes up underground space decreased by 35% when the equivalent useable space is the same [1]. The buried depth of the quasirectangle shield tunnel is shallower, and the influence on the surrounding soil is slighter, which greatly improves the possibility of tunnelling through high-rise buildings or narrow roads.

Due to the influence of the shield tunneling to the ground, the soil is definitely disturbed, and the additional stresses are generated on the soil around the tunnel, which may cause ground settlement or uplift, resulting in different degrees of damage to the surface buildings and underground infrastructures [2, 3]. Scholars have paid more and more attention to the prediction of the effect on the building within the influence of the shield tunneling and how to control the ground settlement caused by tunnel excavation. The theoretical analysis of the additional stress field induced by the quasirectangular shield tunnel is mainly based on the Mindlin solution to establish the computational expressions for the additional thrust on the front side of the cutter, the frictional resistance between the shield shell and the soil, and the grouting pressure during the excavation of the shield tunnel in homogeneous stratum [4–7]. The research on ground settlement induced by quasirectangle shield tunneling is mainly based on Peck's formula and stochastic

medium theory to further deduces the formula for calculating and predicting ground settlement [6–9]. Existing literature on the environmental impact of tunnel construction has mostly focused on the analysis and prediction of soil deformation. Li et al. [10] proposed an analytical solution for the additional stresses in the curved tunnel based on Mindlin′s solution. Wu et al. [11] found that the friction force of the cutter head has little influence on the additional stress of the soil around the tunnel. Yuan et al. [12, 13] analyzed the displacement of layered soil through soil model tests and explored the effect of layer thickness on pile-soil interaction. Liang et al. [14] proposed a method based on the Pasternak foundation model and Mindlin′s solution to predict the impact of shield tunnel construction on nearby tunnels. Lai et al. [15] predicted soil deformation through artificial neural networks. Zhang et al. [16] considered the interaction mechanism between the tunnel liners and the surrounding soils and established a soil-liner interaction and nonuniform convergence model, which can predict the disturbed soil movements and tunnel liner deformation due to tunnel excavation. Zhao et al. [7] proposed the cut-off functions of ground surface settlement caused by double-O-tube tunnel shield construction. Wang et al. [17] provided a methodology for obtaining the analytical solutions of ground response induced by noncircular tunnel excavation. Zeng and Zuo [18] derived the theoretical solution of soil deformation considering the rolling of DOT shield by polar coordinate transformation and multi-subdomain integration method. Based on the virtual image technique, stress function solution and Bossiness's solution, Zou and Zou [19] proposed an elastic solution for the vertical nonaxisymmetric displacement boundary condition for the simultaneous grouting of the shield tunnel. Based on extreme gradient boosting and artificial neural network, Zhang et al. [20] established a prediction model to evaluate the surface settlement caused by EPB tunnel, which supports vector machine and multiple adaptive regression spline. However, natural strata exhibit multilayered properties during deposition, and the soil properties of different layers vary greatly. Existing studies usually simplify the complex multilayered problem to a homogeneous stratigraphic problem, which seldom considers the influence of the multilayered properties of the strata on the additional stress field and displacement of the soil around the tunnel induced by the shield tunnel construction.

This paper uses the analytical stiffness matrix method to analyze the additional stress field and displacement of the soil around the tunnel induced by the excavation of a quasirectangle shield in the multilayered soft soils, which is important theoretical guidance for determining the construction dynamic parameters of quasirectangle shield and protecting the safety of the buildings around the tunnel.

2. Analytical Stiffness Solution for the Loading of Multilayered Soil

Kou and Bai [21] deduced the unitary stiffness matrix for the three-dimensional spatial problem of laminar soil layer under loading in the Cartesian coordinate system.

$$K = \begin{pmatrix} k_{11} & \cdots & k_{14} \\ \vdots & \ddots & \vdots \\ k_{41} & \cdots & k_{44} \end{pmatrix}. \tag{1}$$

$$k_{11} = -\frac{2G\xi(2G+\lambda)\left[\left(1-e^{-4\xi z}\right)(\lambda+3G)+4\xi z e^{-2\xi z}(\lambda+G)\right]}{(\lambda+3G)^2\left(1+e^{-4\xi z}-2e^{-2\xi z}\right)-4\xi^2 z^2 e^{-2\xi z}(\lambda+G)^2}. \tag{1a}$$

$$k_{12} = \frac{2G\xi\left[4e^{-2\xi z}\xi^2 z^2(\lambda+G)^2-(\lambda+3G)G\left(1+e^{-4\xi z}-2e^{-2\xi z}\right)\right]}{\left(\lambda+3G^2\right)\left(1+e^{-4\xi z}-2e^{-2\xi z}\right)-4\xi^2 z^2 e^{-2\xi z}(\lambda+G)^2}. \tag{1b}$$

$$k_{13} = \frac{4G\xi e^{-\xi z}(2G+\lambda)\left[(3G+\lambda)\left(1-e^{-2\xi z}\right)+(G+\lambda)\left(1+e^{-2\xi z}\right)\xi z\right]}{(\lambda+3G)^2\left(1+e^{-4\xi z}-2e^{-2\xi z}\right)-4\xi^2 z^2 e^{-2\xi z}(\lambda+G)^2}. \tag{1c}$$

$$k_{14} = \frac{4G\xi^2 z e^{-\xi z}(2G+\lambda)(G+\lambda)\left(1-2e^{-2\xi z}\right)}{(\lambda+3G)^2\left(1+e^{-4\xi z}-2e^{-2\xi z}\right)-4\xi^2 z^2 e^{-2\xi z}(\lambda+G)^2}. \tag{1d}$$

$$k_{22} = \frac{2G\xi e^{-\xi z}(2G+\lambda)\left[(3G+\lambda)\left(e^{-4\xi z}-1\right)+4\xi z e^{-2\xi z}(G+\lambda)\right]}{(\lambda+3G)^2\left(1+e^{-4\xi z}-2e^{-2\xi z}\right)-4\xi^2 z^2 e^{-2\xi z}(\lambda+G)^2}. \tag{1e}$$

$$k_{24} = -\frac{4G\xi e^{-\xi z}(2G+\lambda)\left[(3G+\lambda)\left(e^{-2\xi z}-1\right)+(G+\lambda)\left(1+e^{-2\xi z}\right)\xi z\right]}{(\lambda+3G)^2\left(1+e^{-4\xi z}-2e^{-2\xi z}\right)-4\xi^2 z^2 e^{-2\xi z}(\lambda+G)^2}. \tag{1f}$$

$$\begin{aligned} &k_{21} = k_{12}, k_{23} = -k_{14}, k_{31} = k_{13}, k_{32} = k_{23} = -k_{14}. \\ &k_{33} = k_{11}, k_{34} = -k_{12}, k_{41} = k_{14}, k_{42} = k_{24}. \\ &k_{43} = k_{34} = -k_{12}, k_{44} = k_{22}, \end{aligned} \tag{1g}$$

where

$$\xi^2 = \xi_x^2 + \xi_y^2, \tag{1h}$$

$$\tilde{f}\left(\xi_x, \xi_y, z\right) = \int_{-\infty}^{+\infty}\int_{-\infty}^{+\infty} f(x, y, z) e^{-i\xi_x x} e^{-i\xi_y y} dx\, dy, \tag{1i}$$

i is imaginary, G represents shear modulus, z is the depth of soil, λ describes the Lamé constant, K is the unit stiffness matrix of the plane strain problem for stratified strata subjected to load in the right-angle coordinate system, and the matrix elements of K are k_{11} and k_{12}.

The calculation model for the three-dimensional spatial problem of multilayered soil under loading is shown in Figure 1. According to the characteristics of the natural soil layer and calculation the foundation is divided into n layers, and H_i^- and H_i^+ are the vertical distances from the top and bottom of the layer i to the ground surface, and $\Delta h_i = H_i^+ - H_i^-$ is the thickness of the layer i. The applied load at the layer i is $q_i(x, y, z)$.

For the three-dimensional spatial problem of the multilayered soil under loading, at the surface of the foundation:

$$\sigma_x = \tau_{xz} = \tau_{yz} = 0, \tag{2}$$

At the base of the ground:

$$u = v = w = 0, \tag{3}$$

Assuming complete contact between adjacent calculation layers, the continuity condition for calculation layers without external load is as follows:

$$\begin{aligned} &M(\xi, H_i^+) = M(\xi, H_{i+1}^-), W(\xi, H_i^+) = W(\xi, H_{i+1}^-), N(\xi, H_i^+) = N(\xi, H_{i+1}^-). \\ &X(\xi, H_i^+) = X(\xi, H_{i+1}^-), Y(\xi, H_i^+) = Y(\xi, H_{i+1}^-), Z(\xi, H_i^+) = Z(\xi, H_{i+1}^-). \end{aligned} \tag{4}$$

The continuous conditions between the calculated layers with external load acting at $z = H_i$ are as follows:

$$\begin{aligned} &M(\xi, H_i^+) = M(\xi, H_{i+1}^-),\ W(\xi, H_i^+) = W(\xi, H_{i+1}^-), N(\xi, H_i^+) = N(\xi, H_{i+1}^-), \\ &X(\xi, H_{i+1}^-) = X(\xi, H_i^+) + q_{iX}(\xi, H_i), Y(\xi, H_{i+1}^-) = Y(\xi, H_i^+) + q_{iY}(\xi, H_i), \\ &Z(\xi, H_{i+1}^-) = Z(\xi, H_i^+) + q_{iZ}(\xi, H_i), \end{aligned} \tag{5}$$

where

$$\begin{aligned} &M = \frac{\xi_x \tilde{u} + \xi_y \tilde{v}}{\xi}, N = \frac{\xi_y \tilde{u} - \xi_x \tilde{v}}{\xi}, W = \tilde{w}. \\ &X = \frac{\xi_x \widetilde{\tau_{xz}} + \xi_y \widetilde{\tau_{yz}}}{\xi}, Y = \frac{\xi_y \widetilde{\tau_{xz}} - \xi_x \widetilde{\tau_{yz}}}{\xi}, Z = \tilde{\sigma_z}, \end{aligned} \tag{6}$$

where H_i^- and H_i^+, respectively, represent the depth of the upper and lower surfaces of the layer i; $q_{iX}(\xi, H_i)$, $q_{iY}(\xi, H_i)$, and $q_{iZ}(\xi, H_i)$ are the Fourier integral transformed load components acting at the i-th layer of soil.

Divide the natural layered ground into n calculation layers and apply the analytical element stiffness matrix to each calculation layer. By following the alignment principle of finite elements and combining it with the calculation of the continuous conditions between the layers, the overall analytic stiffness matrix for the three-dimensional spatial problem of the entire laminated foundation with loading can

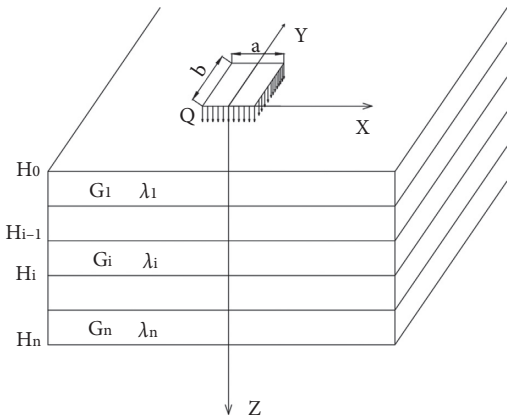

Figure 1: The calculation model of the three-dimensional spatial problem of layered stratum under loading.

be obtained, thus establishing the algebraic equations of stress and strain.

$$\begin{bmatrix} -Z(\xi,0) \\ -iX(\xi,0) \\ \vdots \\ -q_{iZ}(\xi,H_n) \\ -iq_{iX}(\xi,H_n) \\ \vdots \\ Z(\xi,H_n) \\ iX(\xi,H_n) \end{bmatrix} = \begin{bmatrix} K^{(1)} & & & & & & \\ & \ddots & & & & & \\ & & \ddots & & & & \\ & & & K^{(i)} & & & \\ & & & & \ddots & & \\ & & & & & \ddots & \\ & & & & & & K^{(n)} \end{bmatrix} \begin{bmatrix} W(\xi,0) \\ iM(\xi,0) \\ \vdots \\ W(\xi,H_i) \\ iM(\xi,H_i) \\ \vdots \\ W(\xi,H_n) \\ iM(\xi,H_n) \end{bmatrix}. \tag{7}$$

$$\begin{bmatrix} -Y(\xi,0) \\ \vdots \\ -q_{iY}(\xi,H_i) \\ \\ Y(\xi,H_n) \end{bmatrix} = \begin{bmatrix} K^{'(1)} & & \\ & K^{'(i)} & \\ & & K^{'(n)} \end{bmatrix} \begin{bmatrix} N(\xi,0) \\ \\ N(\xi,i) \\ \\ N(\xi,n) \end{bmatrix}. \tag{8}$$

In equations (7) and (8), $K^{(i)}$ and $K^{(i)}$ is the analytical stiffness matrix of layer i.

Combining the stress equation (7) and strain equation (8) to solve the stress and strain with boundary conditions, the solution to the three-dimensional space problem of the multilayered soil foundation under load in the Fourier integral transform domain can be obtained, and then invert the Fourier transform to derive the displacement component and stress in the real physical domain.

3. Model Analysis and Assumptions for Quasirectangle Shield

3.1. Overview of Quasirectangle Shield. As shown in Figure 2, without changing the basic geometry of the quasirectangle shield length, width, and height, the cross section of the quasirectangle shield is simplified to a combination of rectangular ABCD and two semicircles $\widehat{AECO_1}$ and $\widehat{BFDO_2}$. Compared with the actual geometry, the error of the frontal excavation area of the simplified model is 3.5%, and the error of the outer area of the shield shell is 1.5%, which is smaller and can meet the requirements of calculation accuracy.

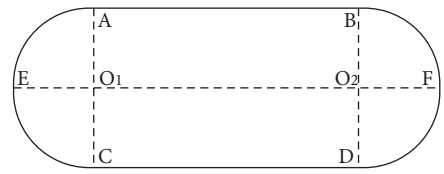

Figure 2: Cross section of the quasirectangle shield.

3.2. Analytical Models and Assumptions. An analytical model for quasirectangle shield tunneling in layer N is shown in Figure 3. Three types of interaction forces between the quasirectangle shield and the surrounding soil during the shield tunneling process are as follows: the additional thrust of the quasirectangle shield propeller to the soil q, the friction between the shell and the soil f, the synchronous grouting pressure p. The grouting pressure is not considered to be attenuated along the radial and longitudinal directions of the tunnel.

In order to calculate and analyze the magnitude and distribution of the additional stresses and displacements in the surrounding soil caused by the quasirectangle shield tunneling, the following assumptions were made:

(1) The quasirectangle shield machine excavated along the tunnel axis in a straight line, regardless of the influence of the shield deviation correction and rotation.

(2) Considering only the effects of shield excavation, the foundation is undrained during shield tunneling. When considering the influence of time changes, the foundation is drainage consolidation.

(3) According to the deposition process of a natural foundation, which is regarded as a semi-infinite space composed of n horizontal layers, each layer has a finite thickness and the soil in the layer is homogeneous and isotropic.

(4) The concentration of frontal additional thrust is q, the concentration of tunneling friction is f, and the concentration of grouting pressure is p. The directions of the frontal additional thrust, tunnelling friction, and grouting pressure are the direction of forces on the surrounding soil during shield tunneling.

4. Additional Stress for Quasirectangle Shield Tunnelling in Multilayered Soil

4.1. Additional Stress due to Additional Thrust on the Front of the Incision. As shown in Figure 2, the coordinates of the left semicircular excavation surface are as follows:

$$\left(0\ ,\ -\frac{K}{2} + r\cos\theta, h - r\ \sin\ \theta\right), \theta \in \left(\frac{\pi}{2}, \frac{3\pi}{2}\right). \tag{9}$$

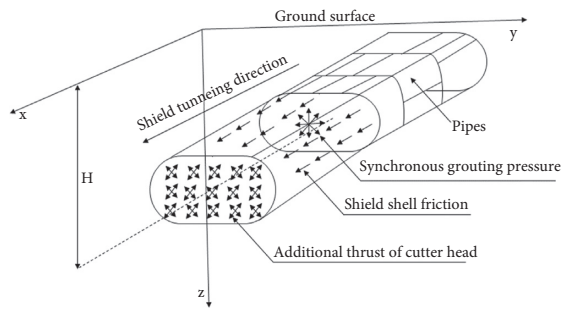

Figure 3: Analysis model of shield tunnel construction.

The coordinates of the right semicircular excavation surface are as follows:

$$\left(0\ ,\ \frac{K}{2}+rcos\theta, h-r\ \sin\ \theta\right), \theta \in \left(\frac{3\pi}{2}, \frac{5\pi}{2}\right). \tag{10}$$

The coordinates of the middle rectangular partial excavation surface are $(0, \zeta, \eta)$. Integrating over the entire excavation surface, the additional stresses in the horizontal direction σ_x^1, σ_y^1 and the additional vertical stress σ_z^1 caused by the frontal additional thrust at any position in the soil (x, y, z) are as follows:

$$\sigma_x^1 = \iint_{S_1} q\Omega(\xi, \zeta, \theta) r\ dr\ d\theta, \tag{11}$$

$$\sigma_y^1 = \iint_{S_1} q\Psi(\xi, \zeta, \theta) r\ dr\ d\theta, \tag{12}$$

$$\sigma_z^1 = \iint_{S_1} q\Phi(\xi, \zeta, \eta) r\ dr\ d\theta, \tag{13}$$

where S_1 is the area of the excavation surface of the shield tunneling, and its integration area is as follows:

$$x = 0, H - \frac{D}{2} < z < H + \frac{D}{2}. \tag{14}$$

and

$$y = -\frac{K+D}{2} - \sqrt{\frac{D^2}{4} - (z-h)^2} \le y \le \frac{K+D}{2} + \sqrt{\frac{D^2}{4} - (z-h)^2}. \tag{15}$$

K is the width of the shield tunnel, D is the diameter of the shield; H is the depth of the tunnel center axis; $\Phi(r, \theta)$, $\Omega(r, \theta)$ and $\Psi(r, \theta)$ are, respectively, the z additional stress of x, y, z at any point in the soil caused by the unit frontal additional thrust, which can be calculated by the analytical stiffness matrix method.

The value of the frontal additional thrust q plays a key role in accurately calculating the magnitude of additional stresses and displacements in the foundation caused by the disturbance of the shield excavation [22]. In the existing studies, many researchers assume that the additional thrust force is 20 kPa, underestimating the additional stresses generated by the shield cutter squeezing the soil [23]. WANG et al. [24]believed that the soil squeezed by the shield was mainly composed of two parts: one was the pressure force on the excavated soil generated by the rotation of the cutter head, and the other was the squeezing force generated by the incision into the soil and proposed the frontal additional thrust q is calculated by the following:

$$q = \frac{10.13\pi(1-\nu)E_u v_t (1-\xi)^2}{(1+\nu)(3-4\nu)D_s k w} + \Delta q. \tag{16}$$

where Δq is the extrusion pressure generated by the shield cutter cutting the soil, generally 10 ~ 25 kPa; E_u is the elastic modulus of nondrainage of the soil (KPa) , which can be calculated by $E_u = E_s = 2.5 \sim 3.5E_{s0.1\sim0.2}$, ν is the Poisson's ratio of the soil, E_s is the elastic modulus of the soil, $E_{s0.1\sim0.2}$ is the compressive volume of the soil (MPa); v_t is the shield tunneling speed (cm/min); k is the number of closed portions of the cutter head; w is the cutter rotational speed (rad/min), D_s is the cutter diameter, and ξ is the cutter opening ratio (%).

When constructing in multilayered soil, the additional frontal thrust should be calculated in layers due to the differences of the soil properties in each layer.

4.2. Additional Stresses due to Frictional Resistance in Tunnelling. As shown in Figure 2, pick any tiny unit on the contact surface between the shield shell and the ground. The unit area is $D\ d\ l\ d\theta/2$, where the tunneling friction is $f\ Dd\ l\ d\theta/2$, f is the trenching frictional resistance load, D is the shield diameter, and l is the integration parameter of the shield machine in the excavation direction. The additional stress in the horizontal direction σ_x^2, σ_y^2 and the additional vertical stress σ_z^2 caused by the frictional resistance between the shield shell and the soil during shield tunneling at any position in the soil (x, y, z) are as follows:

$$\sigma_x^2 = \iint_{S_2} f\ D\Omega \frac{(l, \theta)}{2} dl\ d\theta. \tag{17}$$

$$\sigma_y^2 = \iint_{S_2} f\ D\Psi(l, \theta)/2\ dl\ d\theta \tag{18}$$

$$\sigma_z^2 = \iint_{S_2} f\ D\Phi \frac{(l, \theta)}{2} dl\ d\theta, \tag{19}$$

where S_2 is the side area of the shield shell in contact with the soil; its integration area is as follows:

$$-L \le x \le 0, H - \frac{D}{2} \le z \le H + \frac{D}{2},$$

$$-\frac{K+D}{2} - \sqrt{\frac{D^2}{4} - (z-h)^2} \le y \le \frac{K+D}{2} + \sqrt{\frac{D^2}{4} - (z-h)^2}, \tag{20}$$

L is the length of the shield. $\Phi(r,\theta)$, $\Omega(r,\theta)$ and $\Psi(r,\theta)$ are, respectively, the additional stress of z, x, y at any point in the soil caused by the unit frictional resistance of the excavation, which can be calculated by the analytical stiffness matrix method.

The frictional resistance of the excavation at any position on the contact surface between the shield shell and the ground soil is calculated by the formula for the frictional resistance between the pile and the soil proposed by ALONSO et al. [25].

$$f = \tau_{sr} = \beta_s \sigma_\theta \tan\delta, \tag{21}$$

where σ_θ is the positive radial stress acting on the shield shell,

$$\sigma_\theta = \sigma_v \sin^2\theta + \sigma_h \cos^2\theta, \tag{21a}$$

σ_v, σ_h is the vertical and horizontal ground soil pressure,

$$\sigma_h = K_0 \sigma_v, \tag{21b}$$

$$\sigma_v = \gamma H - \gamma D \sin\frac{\theta}{2}, \tag{21c}$$

K_0 is the horizontal static soil pressure coefficient; δ is the friction angle between the shield shell and the surrounding soil body, which can be obtained through the interfacial shear test.

4.3. Additional Stresses due to Grouting Pressure. As shown in Figure 3, pick a tiny unit in the tunnel surface, the unit area is $D\,d\,s\,d\theta/2$, the grouting pressure on the unit area is $p\,Dd\,s\,d\theta/2$, in which p is the grouting pressure load, s is the integration parameter of grouting in the excavation direction. The additional stresses in the horizontal direction σ_x^2, σ_y^2 and the additional vertical stress σ_z^2 caused by the grouting pressure of the shield construction are as follows:

$$\sigma_x^3 = \iint_{S_3} p\,D\Omega\frac{(s,\theta)}{2}ds\,d\theta, \tag{22}$$

$$\sigma_y^3 = \iint_{S_3} p\,D\Psi\frac{(s,\theta)}{2}ds\,d\theta, \tag{23}$$

$$\sigma_z^3 = \iint_{S_3} p\,D\Phi\frac{(s,\theta)}{2}ds\,d\theta, \tag{24}$$

where S_3 is the area where the grouting pressure acts, and its integral area is as follows:

$$-L - s \le x \le -L, \tag{25}$$

$$H - \frac{D}{2} \le z \le H + \frac{D}{2}, \tag{26}$$

$$-\frac{K+D}{2} - \sqrt{\frac{D^2}{4} - (z-h)^2} \le y \le \frac{K+D}{2} + \sqrt{\frac{D^2}{4} - (z-h)^2}, \tag{27}$$

s is the grouting length; $\Phi(r,\theta)$, $\Omega(r,\theta)$ and $\Psi(r,\theta)$ are, respectively, the additional stress of z, x, y at any point in the soil caused by the grouting pressure of the shield construction, which can be calculated by the analytical stiffness matrix method.

4.4. Total Additional Stress of Soil. Adding the additional soil stresses caused by the additional frontal thrust, shield shell friction, and grouting pressure, the total additional stresses in the soil caused by the construction of the quasirectangle shield are obtained.

$$\sigma_x = \sigma_x^1 + \sigma_x^2 + \sigma_x^3, \tag{28}$$

$$\sigma_y = \sigma_y^1 + \sigma_y^2 + \sigma_y^3, \tag{29}$$

$$\sigma_z = \sigma_z^1 + \sigma_z^2 + \sigma_z^3, \tag{30}$$

5. Displacement for the Quasirectangle Shield Tunnelling in Multilayered Soil

The displacements of the foundation were caused by the stratum loss and soil disturbance when the shield was excavated. In this paper, the analytical stiffness matrix method is used to calculate the displacements caused by the quasirectangle shield tunnel construction in multilayered soil.

According to equations (2) to (6), we can get the following:

$$\begin{aligned} \tilde{u} &= \frac{\xi_x M + \xi_y N}{\xi}, \\ \tilde{v} &= \frac{\xi_y M - \xi_x N}{\xi}, \\ \tilde{w} &= W(\xi, H_i). \end{aligned} \tag{31}$$

$$\begin{aligned} \tilde{u}_i &= \frac{iM(\xi,H_i)\xi_x + N(\xi,i)\xi_y}{\xi}, \\ \tilde{v}_i &= \frac{iM(\xi,H_i)\xi_y - \xi_x N(\xi,i)}{\xi}, \\ \tilde{w}_i &= W(\xi,H_i). \end{aligned} \tag{32}$$

Use the inverse Fourier transform to obtain the displacement of each soil layer and the sum of the displacement of each soil layer to obtain the entire stratum displacements during the Quasirectangle Shield tunneling.

$$u = \sum_{1}^{n} \tilde{u}_i, v = \sum_{1}^{n} \tilde{v}_i, w = \sum_{1}^{n} \tilde{w}_i. \quad (33)$$

where u and v are the deformations of the soil layer in the horizontal direction, w is the settlement of the soil layer in the vertical direction.

6. Project Examples and Discussion

6.1. Project Overview. The shield of the Ningbo Metro Line 3 used a quasirectangular Earth pressure balance shield machine made in China for construction. The dimension of the shield machine is shown in Table 1.

The soil layers traversed by the shield tunnel mainly consist of Sludge ④ and Sludge-Clay ⑤, and the main physical and mechanical properties of each layer are shown in Table 2.

Several monitoring sections are arranged along the tunnel axis in this project. In view of the soil disturbance and deformation caused by the quasirectangle shield construction, this paper uses the 241st ring monitoring section data for comparative analysis. The surface elevation of the section is 2.6 m, the center elevation of the tunnel is -8.581 m, and the buried depth of the tunnel axis is 11.2 m. According to the method proposed in Sections 2 and Sections 4, the additional stress on the ground caused by the disturbance of the shield construction is calculated.

6.2. Additional Stress Analysis

6.2.1. Comparison with Monitoring Data. The comparison between the calculated value and the monitoring data of the additional stress σ_x and σ_y of the soil above the tunnel axis when the shield machine arrived the 241st ring, as shown in Figure 4. Along the direction of buried depth of the tunnel, the distribution pattern of the calculated values of σ_x and σ_y is consistent with the monitoring data. Since the theoretical analysis cannot fully simulate the actual situation, there are some differences between the theoretically calculated values and the actual engineering measurements, but the differences are small. Therefore, the distribution pattern of the calculated values of σ_x and σ_y can provide a theoretical basis for discussing the additional stresses in the soil around the tunnel caused by the quasirectangle shield.

6.2.2. Additional Stress σ_x. Figure 5 shows the distribution of additional stresses σ_x induced by additional frontal thrust, shell frictional resistance, and grouting pressure at 6 m above the tunnel axis from the surface ($y = 0$, $z = 6$). The additional stress σ_x is approximately distributed antisymmetrically along the central axis of the shield tunnel. During the shield tunneling, the front soil is under pressure, and the pressure reaches the maximum at the position 5 m in front of the excavation; the back soil is under tension, and the tension reaches the maximum at the shield tail position. Frontal additional thrust and shell frictional resistance affect σ_x similarly due to their different positions of action. Their antisymmetric points do not coincide. Compared with the frontal additional thrust and synchronous grouting pressure, the shell friction has a greater effect on σ_x, so that the additional stress distribution curve caused by three together is close to the additional stress distribution curve caused by the shell friction.

The distribution of the additional stress σ_x along the X-axis is shown in Figure 6. σ_x is approximately antisymmetric along the shield direction, and the front and back influence range of $y = d$ is roughly -25m ~ 25 m. During the shield tunneling, the soil at the front of the shield is compressed, and the maximum value of σ_x is concentrated at 5m in front of the shield, and the soil at the middle and back of the shield is under tension, and the maximum value of σ_y is concentrated on the tail of the shield. As the distance from the excavation surface increases, the additional stress value gradually decreases. Obviously, the additional stress σ_x hardly changes in the range $y = 0$ to $y = d$, and the additional stress σ_x increases significantly in the range $y = d$ to $y = d + R_1$.

Figure 7 illustrates the distribution of σ_x along the Y axis. σ_x is distributed symmetrically about the tunnel axis, and the influence range of σ_x is 20 m away from the shield axis. The farther away from the shield axis, the additional stress will be smaller and the attenuation will be slower. About 10 m away from the tunnel axis, the additional stress changes little and the curve is relatively flat, indicating that due to the quasirectangle shield, the extrusion range of the front soil is concentrated within the width of the shield.

6.2.3. Additional Stress σ_y. Figure 8 shows the distribution of additional stresses σ_y induced by additional frontal thrust, shell frictional resistance, and grouting pressure at 6 m above the tunnel axis from the surface. The frontal additional thrust and shell friction have similar effects on σ_y, both of which make the soil at the front of the shield laterally compressed, and the soil at the back is laterally under-tension. Under the grouting pressure, the lateral tension on the soil above the tunnel axis is greater and reaches a maximum at the tail position of the shield. Obviously, the effect of synchronous grouting pressure on σ_y is much greater than the effect of additional thrust and shell frictional resistance, resulting in σ_y distribution curve similar to that of σ_y when synchronous grouting acts alone. Thus, synchronous grouting, the grouting volume, and slurry pressure shield tunneling should be strictly controlled.

As can be seen from Figure 9, the distribution of additional stresses σ_y before and after excavation varies greatly and depends on the distance from the excavation surface. At the tail of the shield, the additional stress σ_y suddenly changes to the maximum. Locations near the excavation surface, the front of the excavation is in lateral compression with additional stresses reaching a maximum. and the back of the excavation is in lateral tension. σ_y is mainly affected by synchronous grouting pressure.

It can be seen from Figure 10 that σ_y presents the symmetrical distribution of "arches" on the shield axis. The soil directly in front of the excavation surface is obviously squeezed. The value of σ_y is larger at a certain distance before

Table 1: The dimensions of the quasirectangle shield machine.

Shield width K/m	Shield height H/m	Shield length L/m	Shield radius R/m
11.83	7.26	11.61	3.37

Table 2: Main physical and mechanical properties of the soil layer.

No.	Soil layer	Soil thickness = / m	Gravity/ KN·m3	Compression modulus/ MPa	Poisson's ratio	Static side pressure coefficient K0
1	Miscellaneous soil	1.50	18.0	3.41	0.38	0.60
2	Sludge	1.70	16.4	1.65	0.42	0.72
3	Clay	0.80	18.3	3.15	0.37	0.63
4	Sludge	4.40	16.5	1.63	0.42	0.72
5	Sludge-clay	8.40	17.2	2.02	0.40	0.67
6	Silt-clay	3.70	18.3	3.03	0.32	0.47
7	Sludge-silt-clay	7.30	18.0	2.84	0.35	0.54
8	Clay	5.70	17.4	3.87	0.35	0.55

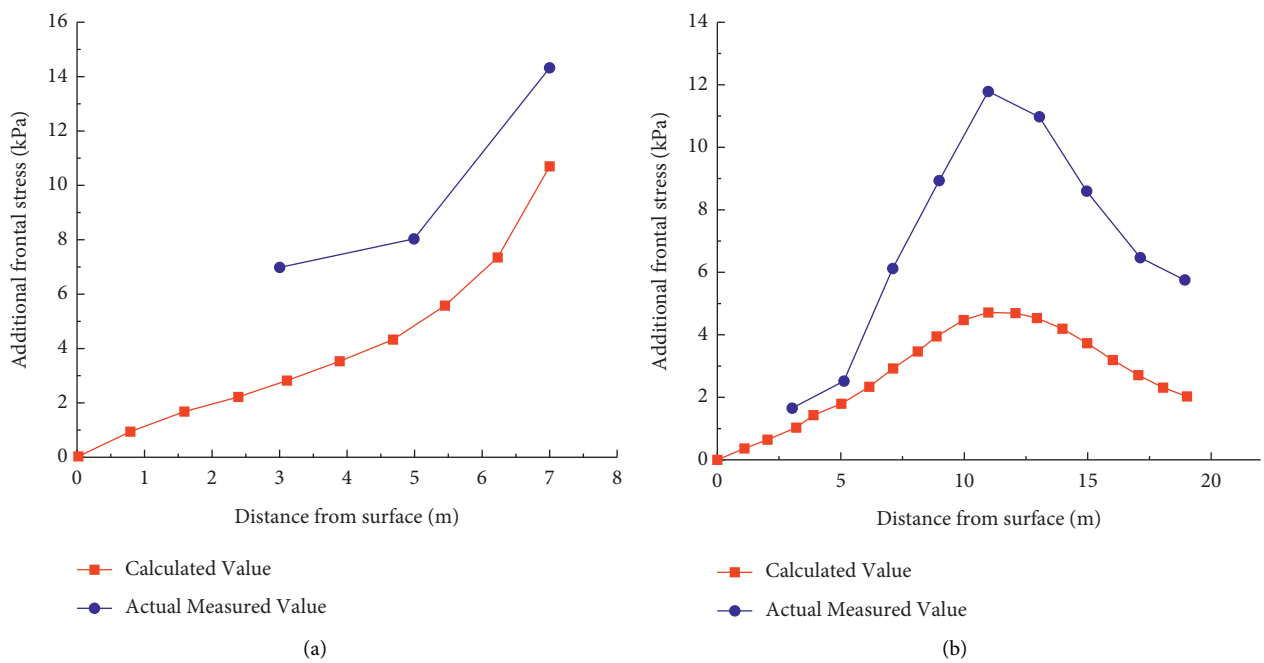

Figure 4: Comparison of calculated and monitoring data of σ_x (a) and σ_y (b).

excavation and the maximum value is located at the shield axis. As the distance from the excavation surface gets farther and farther, the peak point gradually moves to both sides of the shield, the additional stress spread tends to slow down, and the stress tends to be evenly distributed.

6.3. Displacement Analysis

6.3.1. Comparison with Monitoring Data. The comparison between the theoretical value of the lateral displacement of the soil and the monitoring data of the inclined tube CX-241-2 when the shield reached the 241st ring is shown in Figure 11. The monitoring of horizontal displacement fluctuates greatly. As the theoretical analysis cannot fully simulate actual construction which is influenced by many factors, the monitoring data is smaller than the calculated value, but the trends of the two are similar. The horizontal and longitudinal deformation patterns of the surface obtained in this paper can provide some theoretical basis for reducing the surface deformation caused by quasirectangle tunneling.

6.3.2. Horizontal Displacement. Figure 12 shows the theoretical value of the horizontal displacement of the soil at the side inclined tube CX-241-2 when the shield reached the 241st ring, which is located on the right side of the tunnel in the forward direction and which has a horizontal distance of about 1.25 m ($y = 7$ m) from the tunnel. The additional

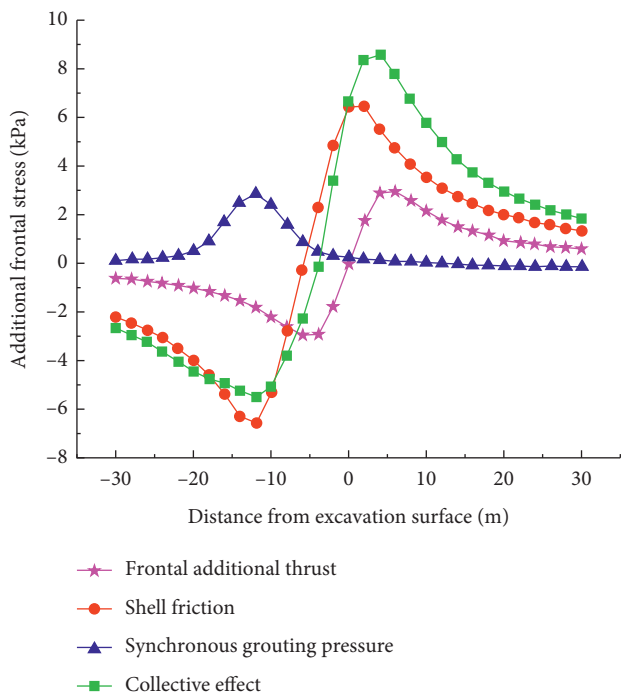

Figure 5: The effect of additional frontal thrust, shell frictional resistance, and synchronous grouting force on σ_x.

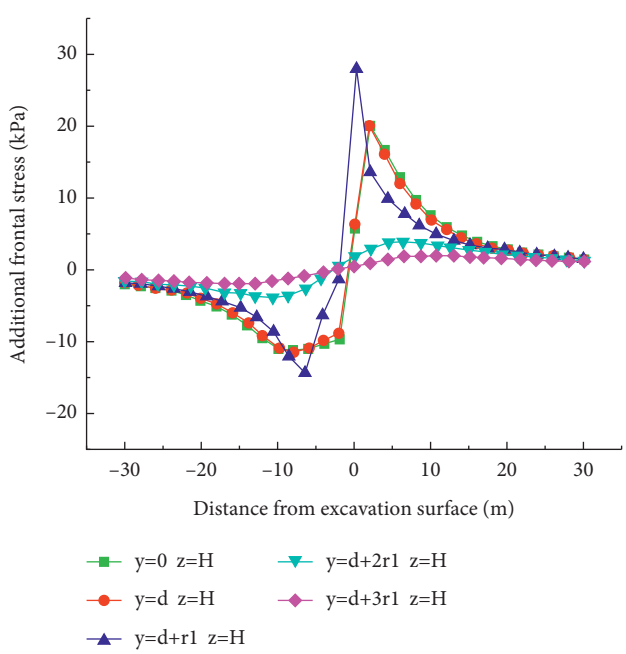

Figure 6: The distribution of the additional stress σ_x along the X axis.

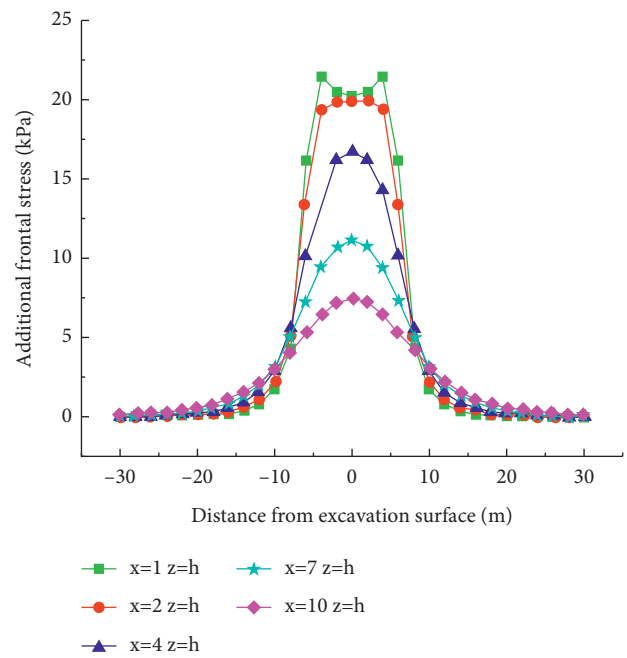

Figure 7: The distribution of the additional stress σ_x along the Y axis.

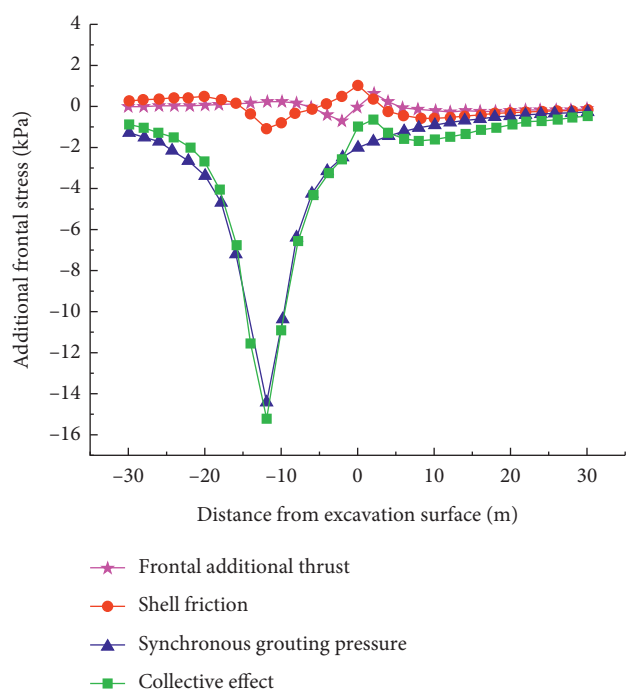

Figure 8: The effect of additional frontal thrust, shell frictional resistance, and synchronous grouting force on σ_y.

frontal thrust acts on the position $x = 0$, and the horizontal displacement is $v = 0$. Therefore, when the shield reaches this position, the additional frontal thrust does not cause lateral horizontal displacement. Since the cutter of the shield is far away from the position of synchronous grouting at the shield tail, the lateral horizontal displacement caused by synchronous grouting is small and can be almost neglected.

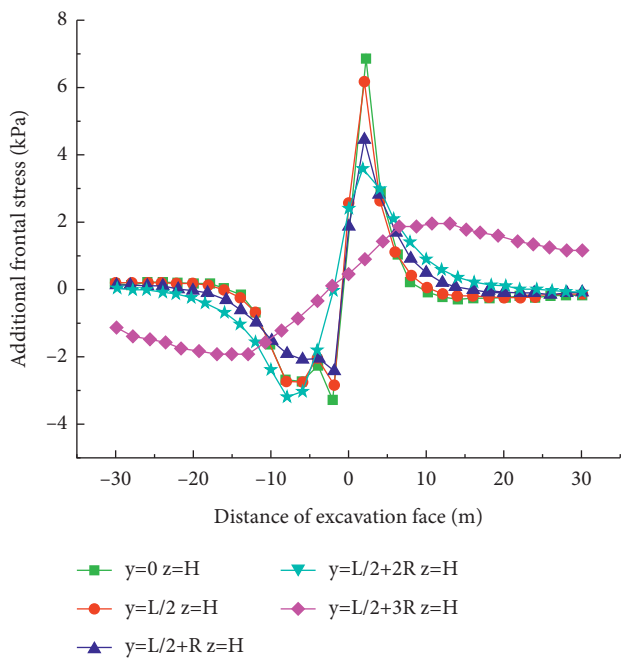

Figure 9: The distribution of the additional stress σ_y along the X axis.

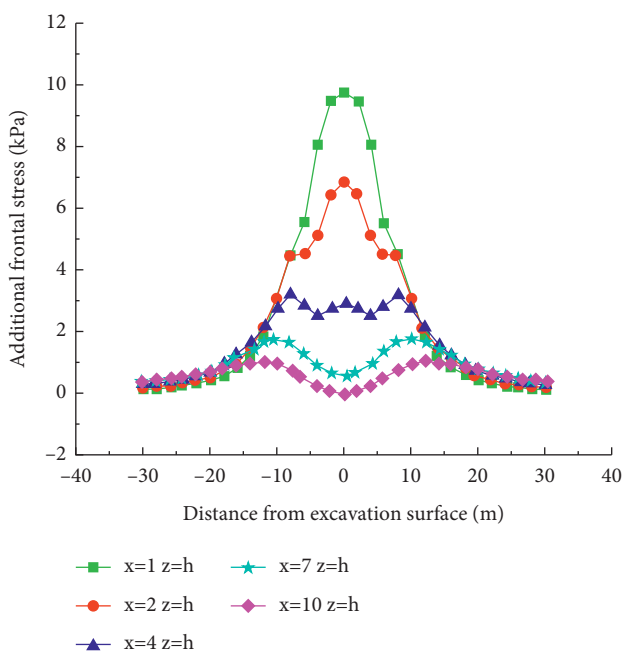

Figure 10: The distribution of the additional stress σ_y along the Y axis.

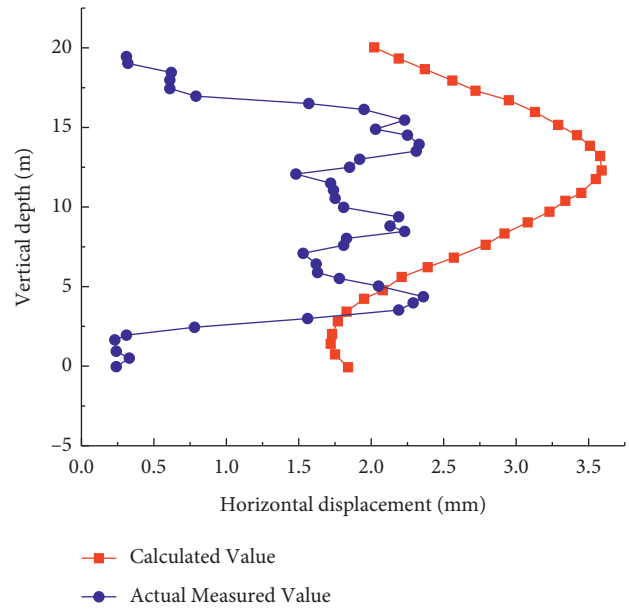

Figure 11: Comparison of calculated value and monitoring data of horizontal displacement.

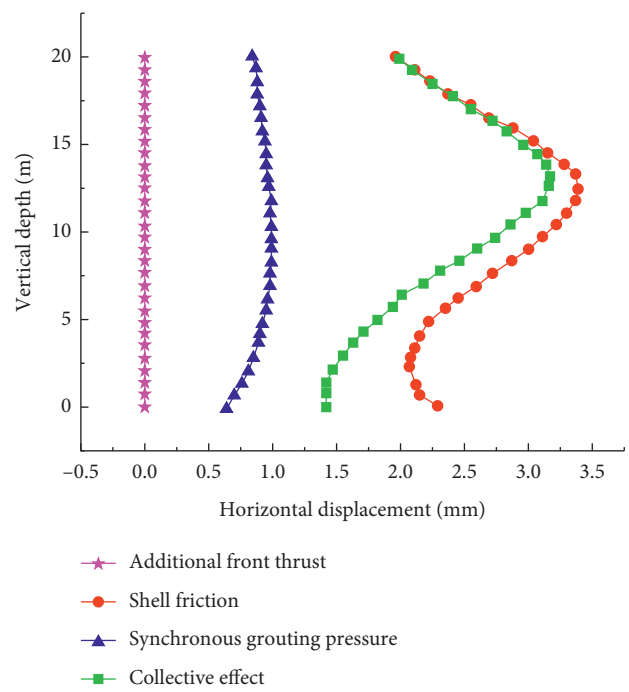

Figure 12: Horizontal deformation of the soil around the shield tunnel.

As been seen in Figure 12 that the shell frictional resistance causes a large horizontal displacement towards the outside of the tunnel, which can reach a maximum 3 mm.

6.3.3. Longitudinal Ground Deformation. The analysis results of the longitudinal deformation of the ground caused by three factors are shown in Figure 13. Under the additional frontal thrust and shell friction, the soil in front of the excavation is raised and the soil at the rear is settled, but the values are small. The peak point of surface deformation differs due to the difference in the action range. The peak point of the longitudinal deformation of the surface caused by the frontal additional stress is located roughly 5 m before and after the excavation, and the peak displacement is about 1 mm; the

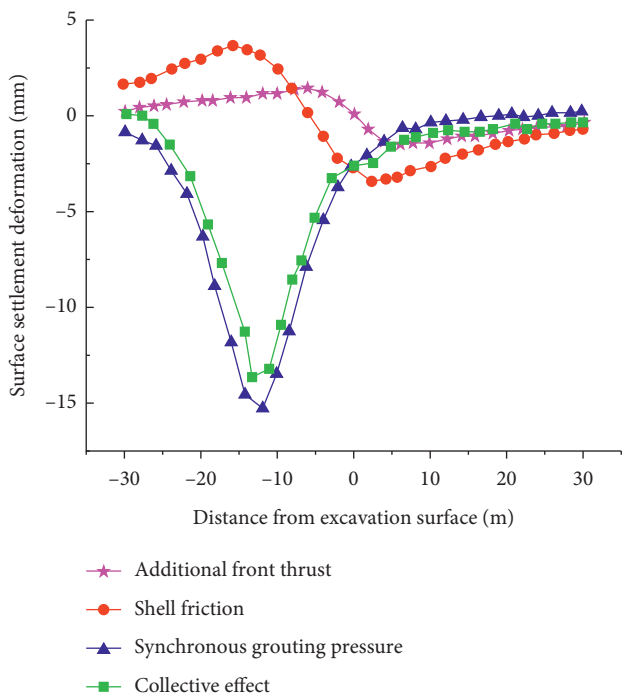

Figure 13: Longitudinal deformation of the ground surface caused by quasi-rectangle shield construction.

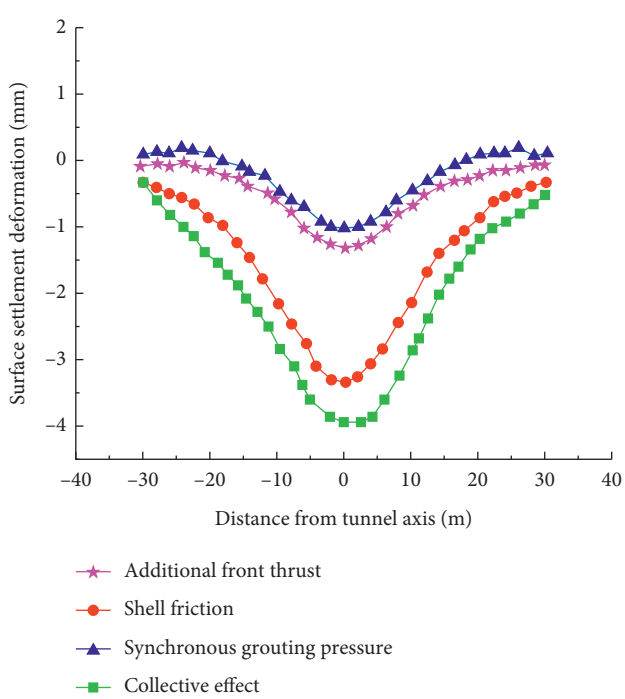

Figure 14: Lateral surface deformation of the ground surface caused by quasirectangle shield construction.

peak point of the longitudinal deformation of the surface caused by the frictional resistance of the shell is located roughly at the tail of the shield and at the face of the excavation, and the peak displacement is about 3.5 mm. The longitudinal deformation of the ground surface caused by synchronous grouting pressure causes a large bulge in the shield tail position, and the maximum value can reach 15 mm, and then rapidly spread to the front and rear of the shield tail.

6.3.4. Lateral Ground Deformation. Figure 14 illustrates the result of the lateral trough settlement caused by the three factors of frontal additional thrust, shell friction, and synchronous grouting pressure at 5 m away from the front of the shield excavation. Obviously, the lateral deformation of the surface is symmetrically distributed about the tunnel axis with an influence range of roughly 20 m on each side of the axis. The three factors have similar effects on the lateral deformation of the surface. Because this position is far from the synchronous grouting position of the shield tail, the influence of synchronous grouting factors is small, and it is close to the front additional thrust. The impact of shell friction on lateral surface deformation is large, up to 3.5 times that of the frontal additional thrust.

7. Conclusion

In this paper, based on the quasirectangular shield tunnelling of Ningbo Metro Line 3, the theoretical calculation formula is used to study the additional stress and ground deformation of the soil caused by the quasirectangle shield excavation. The following conclusions can be summarized:

(1) Based on the basic solution of the analytical stiffness matrix method, the distribution pattern of additional stress and deformation of the soil around the shield caused by the additional thrust on the frontal side of the excavation, the frictional force between the shield shell and the soil body, and the synchronous grouting pressure of the quasirectangular shield in multilayered soft soils are analyzed. The theoretical results are consistent with the monitoring data indicating that the analytical stiffness matrix method can be applied to analyze the environmental effects induced by the construction of a quasirectangular shield.

(2) The influence range of the additional stress is 25 m before and after the shield excavation, which is about 2.2 times the length of the shield, and its range along the horizontal direction of the shield is 20 m on each side of the shield axis, which is about 1.7 times the width of the shield. The farther away from the excavation surface or shield axis, the smaller the additional stress value.

(3) The shell friction and synchronous grouting pressure have a significantly greater influence on the additional stress, assuming that the shell friction and synchronous grouting pressure are uniformly distributed along the excavation surface, in most of the existing studies, a large error compared to the actual situation.

(4) The horizontal settlement curve of the quasirectangle shield is roughly symmetrical along the tunnel axis, with a groove width range of about 20 m. Case friction has a greater effect on horizontal displacement.

(5) Synchronous grouting pressure has a greater effect on longitudinal surface deformation. Synchronous grouting pressure causes a large bulge displacement in the shield tail, the maximum value of which can reach 15 mm, and then spreads rapidly to the front and back of the shield tail.

Data Availability

The data presented in this study are available in the main text of the article.

Conflicts of Interest

The authors declare that they have no conflicts of interest regarding the publication of this paper.

Acknowledgments

This work was supported by the Natural Science Foundation of China (grant no. 52079128) and Science and Technology Project of Henan Province (grant no. 212102310289).

References

[1] Y. H. Zhu, Y. F. Zhu, D. Z. Huang, and P. N. Li, "Development and application of the technical system for quasi-rectangular shield tunnelling," *Mod. Tunn. Technol*, vol. 53, no. S1, pp. 01–12, Apr. 2016.

[2] Q. Fang, J. Du, J. Li, D.-l. Zhang, and L.-q. Cao, "Settlement characteristics of large-diameter shield excavation below existing subway in close vicinity," *J. Cent. South Univ.*vol. 28, no. 3, pp. 882–897, 2021.

[3] H. Qiu, X. Zhang, and M. Daddow, "Prediction of ground settlement induced by slurry shield tunnelling in granular soils," *Civil Engineering Journal*, vol. 6, no. 12, pp. 2273–2289, 2020.

[4] X. Zhang, J. Chen, Y. Bai, A. Chen, and D.-z. Huang, "Ground surface deformation induced by quasi-rectangle EPB shield tunneling," *Journal of Zhejiang University*, vol. 52, no. 2, pp. 317–324, 2018.

[5] X. Jiang, X. Zhang, A. Chen, J. Chen, and Y. Bai, "Ground surface deformation analysis of quasi rectangular EPB shield tunneling," in *Proceedings of the GeoShanghai 2018 International Conference: Tunnelling and Underground Construction*, pp. 103–111, Springer, Singapore, 2018.

[6] G. Wei, H. Zhang, F. Xu, and Z. Wang, "Prediction of ground settlement due to excavation of a quasi-rectangular shield tunnel based on stochastic medium theory," *Geotechnical & Geological Engineering*, vol. 37, no. 5, pp. 3605–3618, 2019.

[7] W. Zhao, P.-j. Jia, L. Zhu et al., "Analysis of the additional stress and ground settlement induced by the construction of double-O-tube shield tunnels in sandy soils," *Applied Sciences*, vol. 9, no. 7, p. 1399, 2019.

[8] D. Hu, Y. Li, X. Liang, Y. Wu, S. Zhang, and Q. Yao, "Analysis and prediction of pavement settlement caused by jacking construction of ultra-shallow rectangular shield frame bridge," *Mathematical Problems in Engineering*, vol. 2020, Article ID 9624927, 14 pages, 2020.

[9] H. Li and F. Li, "Analytical solutions to ground settlement induced by ground loss and construction loadings during curved shield tunneling," *Journal of Zhejiang University - Science*, vol. 22, no. 4, pp. 296–313, 2021.

[10] S. Li, P. Li, and M. Zhang, "Analysis of additional stress for a curved shield tunnel," *Tunnelling and Underground Space Technology*, vol. 107, Article ID 103675, 2021.

[11] C. F. Wu, C. Wei, and F. F. Qiao, "Analysis of additional soil stress caused by shield construction under existing superstructure loads," *Chinese Journal of Rock Mechanics and Engineering*, vol. 37, pp. 1708–1720, 2018.

[12] B. Yuan, Z. Li, Z. Zhao, H. Ni, Z. Su, and Z. Li, "Experimental study of displacement field of layered soils surrounding laterally loaded pile based on Transparent Soil," *Journal of Soils and Sediments*, vol. 21, no. 9, pp. 3072–3083, 2021.

[13] B. Yuan, Z. Li, Y. Chen et al., "Mechanical and microstructural properties of recycling granite residual soil reinforced with glass fiber and liquid-modified polyvinyl alcohol polymer," *Chemosphere*, vol. 286, Article ID 131652, 2022.

[14] R. Liang, W. Wu, F. Yu, G. Jiang, and J. Liu, "Simplified method for evaluating shield tunnel deformation due to adjacent excavation," *Tunnelling and Underground Space Technology*, vol. 71, pp. 94–105, 2018.

[15] J. Lai, J. Qiu, Z. Feng, J.-x. Chen, and H.-b. Fan, "Prediction of soil deformation in tunnelling using artificial neural networks," *Computational Intelligence and Neuroscience*, vol. 2016, Article ID 6708183, 16 pages, 2016.

[16] Z. Zhang, M. Huang, X. Xi, and X. Yang, "Complex variable solutions for soil and liner deformation due to tunneling in clays," *International Journal of Geomechanics*, vol. 18, no. 7, Article ID 04018074, 2018.

[17] H. N. Wang, G. S. Zeng, and M. J. Jiang, "Analytical stress and displacement around non-circular tunnels in semi-infinite ground," *Applied Mathematical Modelling*, vol. 63, pp. 303–328, 2018.

[18] B. Zeng and D. Huang, "Soil deformation induced by Double-O-Tube shield tunneling with rolling based on stochastic medium theory," *Tunnelling and Underground Space Technology*, vol. 60, pp. 165–177, 2016.

[19] J. Zou and S. Zuo, "Similarity solution for the synchronous grouting of shield tunnel under the vertical non-axisymmetric displacement boundary condition," *Advances in Applied Mathematics and Mechanics*, vol. 9, no. 1, pp. 205–232, 2017.

[20] W. G. Zhang, H. R. Li, C. Z. Wu, Y. Q. Li, Z. Q. Liu, and H. L. Liu, "Soft computing approach for prediction of surface settlement induced by earth pressure balance shield tunneling," *Underground Space*, vol. 6, no. 4, pp. 353–363, 2021.

[21] L. Kou and Y. Bai, "Analytical stiffness matrixes for biot consolidation of multilayered viscoelastic foundations in the cartesian coordinate system," *Applied Mathematics and Mechanics*, vol. 37, no. 1, pp. 84–96, 2016.

[22] R. Z. Liang, T. D. Xia, C. G. Lin, and F. Yu, "Analysis of ground surface displacement and horizontal movement of deep soils induced by shield advancing," *Chinese Journal of Rock Mechanics and Engineering*, vol. 34, no. 3, pp. 583–593, 2015.

[23] C. G. Lin, Z. M. Zhang, S. M. Wu, Z.-l. Li, and G.-s. Liu, "Study of ground heave and subsidence induced by shield tunnelling in soft ground," *Chinese Journal of Rock Mechanics and Engineering*, vol. 30, no. 12, pp. 2583–2592, 2011.

[24] H. X. Wang, "Effect of cutterhead compressing the front soil and influence of head aperture ratio on contact pressure of EPB shield to the front soil," *China Civil Engineering Journal*, vol. 42, no. 7, pp. 113–118, 2009.

[25] E. E. Alonso, A. Josa, and A. Ledesma, "Negative skin friction on piles: a simplified analysis and prediction procedure," *Géotechnique*, vol. 34, no. 3, pp. 341–357, 1984.

Hindawi
Advances in Civil Engineering
Volume 2022, Article ID 6997343, 9 pages
https://doi.org/10.1155/2022/6997343

Research Article

Investigation on the Height Calculation of Water Flowing Fracture Zone during Coal Mining under Ordovician Limestone Nappe Aquifer

Chengcheng Chu

Department of Earth and Environment, Anhui University of Science and Technology, Huainan, Anhui 232001, China

Correspondence should be addressed to Chengcheng Chu; chu_cheng_cheng@126.com

Received 14 December 2021; Accepted 4 February 2022; Published 23 February 2022

Academic Editor: Yonghong Wang

This paper focused on the height calculation of water flowing fracture zone during mining under the Ordovician limestone nappe aquifer. According to the critical conditions of crack arresting under the action of compression-shear stress, a formula for calculating the height of water flowing fracture zone during mining under the Ordovician limestone nappe aquifer was proposed, which takes tectonic stress, the influence of fault, the mechanical effect of the seepage field on the stress field, and the rock softening with water into consideration. The formula was applied to calculate the height of water flowing fracture zone above panel E3213 in the first eastern mining area of the Qianyingzi coalmine. The comparison between the theoretical calculation and the measured result shows that the formula proposed in this paper is closest to the measured value and further improves the calculation accuracy compared with the previous formulas. This study not only has important theoretical and practical significance for the safe mining of Qianyingzi coalmine, but also has important theoretical and practical significance for the coalmine facing the double threat of Ordovician limestone confined aquifer and reverse fault.

1. Introduction

The North China coalfield occupies a very important position in the distribution pattern of coal resources in China at the present stage, with abundant reserves. Especially under the action of thrust nappe structure in the southwest strong compression deformation area, the deep coal resources have great potential. However, due to thrust fault, the Ordovician limestone aquifer was pushed to the above coal roof in this area, which has characteristics of karst fissure development and good water abundance. In this case, the Ordovician limestone aquifer becomes a great threat to coal mining.

As we all know, coal seam mining will cause the movement and destruction of strata above the working face. When the mining depth reaches a certain depth (100 m), the movement of strata above the stope can be divided into caving zone, fault zone, and bending subsidence zone from bottom to top, as shown in Figure 1. The height of water flowing fracture zone refers to the sum of the caving zone and the fault zone, which is an important index to analyze the movement and deformation of overlying rock and predict roof water inrush.

Researchers have conducted many studies to predict the development height of water flowing fracture zone in stope, including theoretical calculation, numerical simulation, physical experiments, and other methods [1–22]. In the early 1980s, on the basis of the measured data of coal mines in North China, Liu Tianquan academician put forward an empirical formula for the height of water flowing fracture zone. However, the formula has certain requirements for the depth and thickness of the coal seam mining, which is mainly applicable to the height calculation of the water flowing fracture zone of the thin coal seam with small mining depth (less than 300 m). With the increasing depth of coal mining in China, the applicability of the formula has been greatly restricted. At present, the formula of water flowing fracture zone widely used by field technical staff of

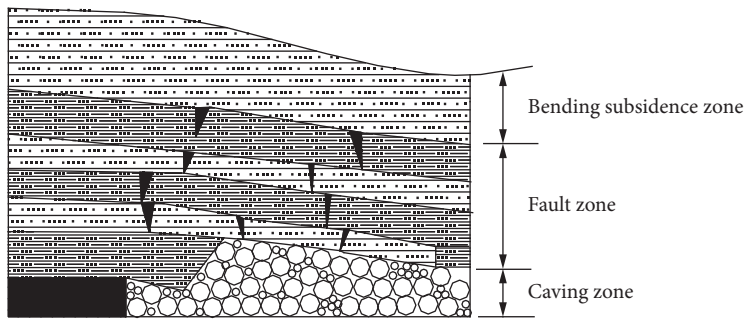

Figure 1: "Three-Zone" model of rock mass movement.

coal mines in China is mainly based on the experiential formula proposed in "Procedures for coal pillar reservation and coal mining of buildings, water bodies, railways and main roadways" [23]. As shown in Table 1, these formulas only consider the influence of coal seam dip angle, roof lithology of coal seam, and mining thickness of coal seam on the development height of water flowing fracture zone. Therefore, there is a certain gap between the calculated results and the actual height.

Due to the limitation of traditional empirical formulas, some scholars have studied the height calculation of water flowing fracture zone in recent years and put forward many new calculation methods. Based on the division theory of "four zones" of roof, Liu et al. [24] pointed out that the rock stratum above the separation zone is in an elastic bending state, and the height of the separation zone can be regarded as the maximum height of water flowing fracture zone. It is concluded that the expression of water flowing fracture zone height is

$$h \approx z = \frac{1}{\eta}\left(1 + C_x L_0 - \frac{\tau}{\gamma H}\right), \tag{1}$$

where h is the height of the water flowing fracture zone; z is the height of the separation zone; C_x is the rock beam transfer coefficient; L_0 is the working face span; γ is the weighted average weight of the roof rock stratum; H is the buried depth of the unbroken rock stratum; τ is the maximum shear strength of the unbroken rock stratum; η is the peak attenuation coefficient of the roof.

Equation (1) shows that the mining depth of coal seam and the working face span are the important factors controlling the development height of roof water flowing fracture zone.

Based on equation (1), Shi et al. [25] pointed out that, under the condition of large mining depth, $\tau/\gamma H$ tends to 0, and $1 + C_X L_0 \approx C_X L_0$. Therefore, the calculation formula of the height of water flowing fracture zone can be expressed as

$$h = \frac{C_X L_0}{\eta}. \tag{2}$$

Equation (2) shows that the development height of water flowing fracture zone is proportional to the working face span under the condition of large mining depth.

In addition, considering the influence of seepage field, Shi et al. [25] further deduced the development height of water flowing fracture zone under the condition of large mining depth and the coupling of seepage field and stress field. The formula is as follows:

$$h = \frac{k}{\eta k_w \sigma_0 - p} L_0, \tag{3}$$

where p is the water pressure of aquifer; k_w is the softening coefficient of rock; σ_0 is the compressive strength of rock without water; k is the proportion coefficient.

According to equation (3), the higher the water pressure in aquifer is, the higher the development height of the water flowing fracture zone will be. In addition, under the same geological conditions, the height of water flowing fracture zone under the coupling effect of seepage field and stress field is larger than that under the condition of only considering the stress field.

Based on the in-depth study of the influence law of key overburden layers on the development height of water flowing fracture zone, Xu et al. [26] proposed that only when the position of key layer is less than a certain critical height from the mining coal seam, the breaking fracture of key layer will develop into water flowing fracture, and the critical height of breaking fracture of key layer can be estimated by 7 to 10 times of mining thickness.

These research results have laid an important theoretical foundation for the research of this paper. However, there are few formulas for calculating the development height of water flowing fracture zone, which comprehensively consider the influence of geological structure characteristics and fluid-solid coupling. In this paper, according to critical conditions of crack arresting under the action of compression-shear stress, and from the perspective of the evolution of the crack propagation of the damaged rock mass, a formula for calculating the height of water flowing fracture zone with mining under a double threat from both the fault and roof confined water was proposed, which takes tectonic stress, the influence of fault, the mechanical effect of the seepage field on the stress field, and the rock softening with water into consideration.

2. Critical Conditions of Crack Growth under the Action of Compression-Shear Stress

Due to different stress conditions, cracks can be divided into three types: open crack (type I), slip crack (type II), and tear crack (type III), as shown in Figure 2.

Table 1: Experiential computing formula of the height of water flowing fracture zone from the "Procedures for coal pillar reservation and coal mining of buildings, water bodies, railways and main roadways."

Dip angle of coal seam	Roof lithology	Compressive strength (MPa)	Formula (1)	Formula (2)
0~54°	Hard	40~80	$100\sum M/1.2\sum M + 2.0 \pm 8.9$	$30\sqrt{\sum M} + 10$
	Medium hard	20~40	$100\sum M/1.6\sum M + 3.6 \pm 5.6$	$20\sqrt{\sum M} + 10$
	Soft	10~20	$100\sum M/3.1\sum M + 5.0 \pm 4.0$	$10\sqrt{\sum M} + 5$
	Ultrasoft	<10	$100\sum M/5.0\sum M + 8.0 \pm 3.0$	—

ΣM refers to cumulative production thickness.

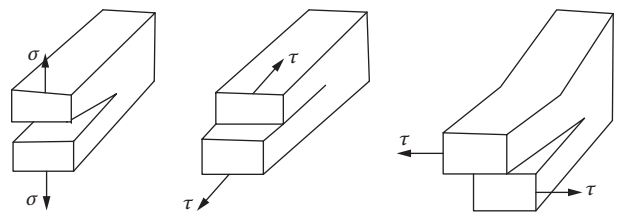

(a) (b) (c)

Figure 2: Three types of cracks. (a) Open crack; (b) slip crack; (c) tear crack.

According to the study of rock fracture mechanics, it is found that the geological rock mass is usually under compression, so the fracture is mostly compression-shear fracture [27]. A large number of experimental results and theoretical analysis show that the compressive shear crack begins to crack along the direction of maximum tensile stress, so the crack is propagated in type I [28, 29].

The theory of fracture mechanics puts forward the critical condition of crack instability propagation expressed by the stress intensity factor (K_I) at the crack tip, also known as the K criterion of brittle fracture. Stress intensity factor is a physical quantity that represents the strength of the stress field at the crack tip, which is determined by the load and the shape and size of the crack. The formula is as follows:

$$K_I = K_{IC}, \tag{4}$$

where K_I is the stress intensity factor at the crack tip; K_{IC} is the plane strain fracture toughness of the material, which indicates the ability of the material to resist brittle fracture. It is a material constant and is generally measured by experiments.

As shown in Figure 3, there is a crack in the infinite plane (plane stress) under biaxial compression, with a length of $2a$ and an azimuth of ϕ. In the figure, σ_1 and σ_3 are maximum compressive stress and the minimum compressive stress, respectively. When the far-field stresses σ_1 and σ_3 increase to a certain value, the primary crack surface compresses and slides, and a branch crack formed at the tip. In order to simplify the calculation, the branch crack is idealized as a straight line with a length of l. When the primary crack surface slides, because the sliding displacement occurs only on the primary crack surface and the normal displacement is zero, only the driving force (T_s) on the crack surface does work. For the branch crack, because it is only affected by the tensile force perpendicular to the crack propagation direction, the tangential displacement is zero and only the normal force (T_n) does work.

If the primary crack and branch crack in Figure 3 are pulled straight to form a straight crack with a length of $2(a+l)$, the maximum sliding displacement on the primary crack surface (δ) can be regarded as the vector sum of the vertical displacement acting on the center of the straight crack (δ_n) and the shear displacement in the crack surface (δ_s). Their relationship can be expressed by the following formula:

$$\delta^2 = \delta_n^2 + \delta_s^2. \tag{5}$$

The type I stress intensity factors produced by δ_n at the center of the straight crack and δ_s at the tip of the branch crack are as follows:

$$\begin{aligned} K_I^n &= \frac{B_n E_0 \delta_n}{(l+a)^{1/2}} \left(B_n = 0.4\right), \\ K_I^s &= \frac{B_s E_0 \delta_s}{(l+a)^{1/2}} \left(B_s \approx 1.0\right), \end{aligned} \tag{6}$$

where K_I^n is the type I stress intensity factor produced by the vertical displacement acting on the center of the straight crack; K_I^s is the type I stress intensity factor produced by the shear displacement in the crack surface; E_0 is the elastic modulus of rock mass.

According to the theory of fracture mechanics, the crack initiation is along the direction at an angle of 70.5° with the primary crack. At this time, the stress intensity factor at the crack tip is K_I^s. However, when the crack propagation length is greater than a, the branch crack turns to the direction of the maximum principal stress, and the crack growth is dominated by the stress intensity factor K_I^n. This transformation can be multiplied by the factor $(1+L)^{1/2}$ $(L = 1/a)$. This assumption has an impact on the results when l is small and has little impact on the results when l is large.

In conclusion, the total stress intensity factor at the crack tip can be expressed as

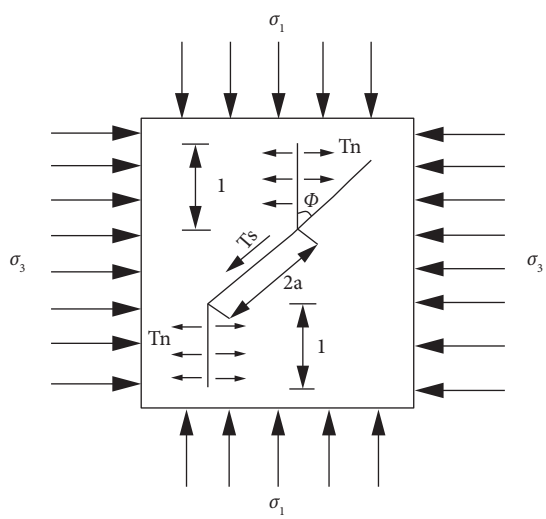

Figure 3: Branch crack propagation.

$$K_I = K_I^n + K_I^s (1+L)^{1/2},$$
$$= \frac{\sqrt{\pi a}}{(1+L)^{3/2}} \left(\frac{2}{\sqrt{3}} T_s^{(\text{primary})} + \frac{\sigma_3 L}{B_n} \right) \left[B_n L + \frac{1}{(1+L)^{1/2}} \right], \tag{7}$$

where $T_s^{(\text{primary})}$ is the driving force on the primary crack surface.

According to the K criterion of crack instability propagation in brittle materials, the critical condition for crack stop propagation under compressive shear stress is as follows:

$$\frac{\sqrt{\pi a}}{(1+L)^{3/2}} \left(\frac{2}{\sqrt{3}} T_s^{(primary)} + \frac{\sigma_3 L}{B_n} \right) \left[B_n L + \frac{1}{(1+L)^{1/2}} \right] = K_{IC}. \tag{8}$$

3. The Formula for Calculating the Height of Water Flowing Fracture Zone under the Action of Stress Field

Tectonic stress field refers to a local singular stress field produced by the interaction between a structure or a group of structures in the Earth and their forces. The direction of tectonic stress is horizontal or near horizontal, so it is also called horizontal stress field. The original rock stress in the tectonic stress field is concentrated and the horizontal stress increases. According to the measured results of global in situ stress, the horizontal stress in the tectonic development area is usually several times or even dozens of times the vertical stress [30, 31]. The tectonic stress field has obvious directionality and regionality.

Without considering the action of tectonic stress field, when the surface is nearly horizontal, the vertical stress (σ_V) at any point in the rock mass is equal to the weight of the overburden.

$$\sigma_V = \gamma H, \tag{9}$$

where γ is the gravity of the rock, and H is the buried depth.

The corresponding horizontal stress is

$$\sigma_h = \lambda \gamma H = \frac{\mu}{1-\mu} \gamma H. \tag{10}$$

where λ is the static lateral pressure coefficient of rock; μ is Poisson's ratio of the rock.

For most hard rock masses, $\lambda = 0.25 \sim 0.43$; that is, the horizontal stress is about 1/3~4/5 of the vertical stress. However, the existence of faults will cause great differences between local stress field and regional stress field, and the lateral pressure coefficient of local stress field around reverse faults $\lambda > 1$.

According to the distribution law of stope support pressure after coal seam mining [32], the maximum value of roof rock support pressure can be expressed as

$$\sigma_h = K \gamma H, \tag{11}$$

where K is the peak coefficient of bearing pressure of roof rock stratum; H is the height of unbroken rock stratum; γ is the weighted average gravity of roof rock stratum.

The peak coefficient of bearing pressure of roof rock stratum (K) decreases linearly with the increase of roof normal height based on the coal seam roof interface (Z), and its expression is

$$K = K\prime - \eta Z, \tag{12}$$

where η is the peak attenuation coefficient of roof, which is mainly affected by mining thickness and roof lithology combination; $K\prime$ is the peak concentration factor of bearing pressure.

According to the practical mine pressure control theory [33], the relationship between the peak concentration factor of bearing pressure and the inclined length of working face is

$$K' = 1 + L_0 C_x, \tag{13}$$

where L_0 is the inclined length of working face; C_x is the transfer coefficient of rock beam.

By combining equations (11)–(13), the relationship between the maximum bearing pressure of roof rock and the height of water flowing fracture zone can be obtained. The expression is as follows:

$$\sigma_h = (1 + L_0 C_x - \eta h) \gamma H, \tag{14}$$

where σ_h is the maximum bearing pressure of roof rock; h is the height of water flowing fracture zone.

According to the fracture strength criterion of rock mass, when the peak stress of roof rock mass (σ_h) is equal to the fracture strength of rock mass ($[\sigma_1]$), the height of water diversion fracture zone reaches the maximum.

Then the expression of the maximum height of the development of the water flowing fracture zone in stope is

$$h = \frac{1}{\eta} \left[1 + L_0 C_x - \frac{[\sigma_1]}{\gamma H} \right]. \tag{15}$$

When the primary fracture or mining fracture in the roof rock is closed or filled, there is a reverse shear stress (friction resistance) between the two walls of the fracture. According

to the Mohr Coulomb strength criterion, the reverse shear stress (τ_0) is

$$\tau_0 = f\sigma + C = \sigma_1 \tan\phi_0 + C_0, \tag{16}$$

where ϕ_0 and C_0 are the original cohesion and friction angle of rock, respectively.

At this time, the driving force on the primary fracture surface is

$$T_s^{(\text{Primary})} = \frac{\sigma_1 - \sigma_3}{2}\sin 2\phi - \sigma_1 \tan\phi_0 - C_0, \tag{17}$$

and substituting equation (17) into equation (8) we can obtain the following expression:

$$\sigma_1 = \frac{K_{IC}/\sqrt{\pi a}/(1+L)^{3/2}\left[B_n L + 1/(1+L)^{1/2}\right] + (2/\sqrt{3})C_0}{1 - \lambda/\sqrt{3}\sin 2\phi + L/B_n\lambda - 2/\sqrt{3}\tan\phi_0}. \tag{18}$$

Substituting equation (18) into equation (15) we can obtain the maximum height of water flowing fracture zone under the action of stress field.

$$h = \frac{1}{\eta}\left\{1 + L_0 C_x - \frac{K_{IC}/\sqrt{\pi a}/(1+L)^{3/2}\left[B_n L + 1/(1+L)^{1/2}\right] + 2/\sqrt{3}\,C_0}{\left[1 - \lambda/\sqrt{3}\sin 2\phi + L/B_n\lambda - 2/\sqrt{3}\tan\phi_0\right]\gamma H}\right\}. \tag{19}$$

With the advancement of the working face to the fault direction, the fragmentation degree of the roof rock mass of the coal seam continues to increase and the compressive strength of the rock decreases. Because $K_{IC} = Y\sigma_{IC}\sqrt{\pi a}$ (σ_{IC} is the critical compressive strength of rock fracture) for the infinite plane, $Y = 1$, the fracture toughness of the rock also decreases. Considering the influence of fault on rock fracture toughness, equation (19) is modified as follows:

$$h = \frac{1}{\eta}\left\{1 + L_0 C_x - \frac{tK_{IC}/\sqrt{\pi a}/(1+L)^{3/2}\left[B_n L + 1/(1+L)^{1/2}\right] + (2/\sqrt{3})C_0}{\left[1 - \lambda/\sqrt{3}\sin 2\phi + L/B_n\lambda - 2/\sqrt{3}\tan\phi_0\right]\gamma H}\right\}. \tag{20}$$

t represents the reduction coefficient of rock fracture toughness (rock strength) under the influence of fault, which can be obtained from the test data of borehole core.

4. The Formula for Calculating the Height of Water Flowing Fracture Zone under the Action of Seepage and Stress Fields Coupling

4.1. Coupling Mechanism of Seepage Field and Stress Field. The deformation and failure of overlying strata in stope are affected not only by mine pressure and mining effect, but also by seepage field.

The influence of stress field on seepage field is mainly because the stress field controls the pore change of porous medium or the geometric shape change of discontinuity in fractured medium, which affects the hydraulic characteristics of medium; the influence of seepage field on stress field includes mechanical action, physical action, and chemical action [24, 34]. Among them, the mechanical action of groundwater on rock mass includes hydrostatic pressure and hydrodynamic pressure. Hydrostatic pressure is the normal stress acting on the fracture structural plane, which belongs to surface force. The hydrostatic pressure per unit area is

$$p_w = \gamma_w H_1, \tag{21}$$

where γ_w is the gravity of water; H_1 is the head height.

Hydrodynamic pressure, also known as osmotic pressure, is a kind of volumetric force due to the hydraulic gradient of groundwater. Under the condition of homogeneous isotropy, the hydrodynamic pressure per unit volume is

$$D = \gamma_w J, \tag{22}$$

where J is the hydraulic gradient.

Literature [35] points out that the mechanical effect of seepage on the stress field of rock mass is that the seepage volume force is generated from the macropoint of view, and from the micropoint of view, the seepage pressure increases the stress intensity factor at the crack tip in rock mass, which has the effect of splitting. When the stress intensity factor at the crack tip reaches the critical value, the crack penetrates, propagates, and destroys, which reduces the stability of rock mass.

Physical action will have a great impact on the physical and mechanical properties of rock mass. This impact first depends on the mineral composition of rock and then depends on the composition, existing form, and content change of structural water in minerals. Chemical action includes chemical erosion, softening, and redox. When the rock mass contains soluble salt minerals, the seepage flow may dissolve and take them away, form cavities, or reduce the cohesion and shear strength in the rock mass; when the content of clay minerals in rock mass, such as shale, mudstone, and clayey siltstone, is high, the softening effect of fluid is more prominent, and the compressive strength will be reduced after the rock absorbs water.

The derivation of the calculation formula in this paper will focus on the mechanical action and the softening effect

of water on rock when considering the influence of seepage field on stress field.

4.2. Calculation Formula for the Height of Water Flowing Fracture Zone. When there is seepage pressure p in the fracture, assuming that the rock block does not conduct water, considering the mechanical effect of seepage field on rock mass and the softening effect on rock, the development height of roof water flowing fracture zone under fluid-solid coupling is analyzed.

The relationship between the effective normal stress of fracture surface σ and σ_1 is

$$\sigma = \sigma_1 - p, \tag{23}$$

where σ is the effective normal stress of fracture surface; σ_1 is maximum compressive stress; p is the seepage pressure in the fracture.

According to the mine pressure control theory (Song 1998), the rock beam transfer coefficient is related to the strength of coal seam and the strength and movement of rock beam itself.

$$C_x = \beta \frac{\sigma_{\text{coal}}}{\sigma_{\text{rock}}}, \tag{24}$$

where β is the scale factor; σ_{caol} is coal seam strength; σ_{rock} is rock beam strength.

Considering the softening effect of water on rock, the compressive strength of rock under fluid-solid coupling is $\sigma_{\text{rock}}' = b\sigma_{\text{rock}}$, where b is the softening coefficient of rock, which is an indicator of rock resistance to water softening. The smaller the softening coefficient of rock, the stronger the softening of rock.

The maximum height of water conducting fracture zone under the coupling action of seepage field and stress field is

$$h = \frac{1}{\eta}\left\{1 + L_0\beta\frac{\sigma_{\text{coal}}}{b\sigma_{\text{rock}}} - \frac{tbK_{IC}/\sqrt{\pi a}/(1+L)^{3/2}\left[B_nL + 1/(1+L)^{1/2}\right] + (2/\sqrt{3})C_0 - p}{\left[1 - \lambda/\sqrt{3}\sin 2\phi + L/B_n\lambda - 2/\sqrt{3}\tan\phi_0\right]\gamma H}\right\}, \tag{25}$$

where t is the reduction coefficient of rock fracture toughness (rock strength) under the influence of faults, which can be obtained from the test data of drilled cores; σ_{caol} is coal seam strength; σ_{rock} is rock beam strength.

It can be seen that, under the coupling action of seepage field and stress field, the greater the water pressure of aquifer, the greater the development height of water flowing fracture zone; the greater the softening coefficient of rock, the better the water resistance of rock, and the smaller the development height of water conducting fractured zone.

When the geological conditions and mining methods of the stope are certain, the development height of water flowing fracture zone is directly proportional to the mining depth of the coal seam and the inclined length of the working face. Therefore, reasonably determining the mining depth of coal seam and the inclined length of working face is an effective measure to control the development of water flowing fracture zone.

5. Case Study

E3213 working face is the trial mining working face in the first eastern mining area of Qianyingzi coalmine. Qianyingzi coalmine is located in the southwest of Suzhou City, Anhui Province, and it is a stratigraphic type of Huaibei coalfield, belonging to North China stratigraphic category. The mining depth of 3_2 coal seam in the first eastern mining area of Qianyingzi coalmine is -280 to -650 m; the average thickness of 3_2 coal seam is 3.3 m. Drilling in mining area reveals that the strata from the bottom to the top are Ordovician, Carboniferous, Permian, Neogene, and Quaternary. As shown in Figure 4, DF200 fault pushes the Ordovician limestone to the top of 3_2 coal seam directly, which is a reverse fault in research area. The dip angle of DF200 fault is about 45°. The roof lithology of 3_2 coal seam is interbed of soft and hard strata. The results of pumping experiments in the Ordovician limestone aquifer show that the aquifer has a hydraulic connection with the surrounding aquifer and is a medium water-rich aquifer. Therefore, 3_2 coal seam mining is threatened by both DF200 fault and Ordovician limestone aquifer.

According to the drilling data, when E3213 working face is pushed 130 m, the measured height of water flowing fracture zone is 72.05 m. The mining depth of the coal seam in the working face is 420 m, and the water pressure of the roof confined aquifer is 6.22 MPa. According to the main physical and mechanical parameters of each rock stratum in the mining area, the weighted average method is used to calculate that the average weight of the overlying rock stratum of the coal seam is 2.2×10^4 N/m^3, internal friction angle $\varphi_0 = 35°$, cohesion = 5.95 MPa, and rock softening coefficient $b = 0.9$. According to the test data of the compressive strength of the drill core, the ratio of the compressive strength of the rock in the fracture zone to the compressive strength of the complete core is 0.33~0.75, that is, $t = 0.33$~0.75, and the average value is 0.54. According to the measured results of in situ stress in Qianyingzi coalmine, the lateral pressure coefficient of rock in the first eastern mining area is 1.65, that is, $\lambda = 1.65$. According to the analysis of the test data of drill core, the plane strain fracture toughness of roof rock (K_{IC}) is 59.43 MPa m$^{1/2}$. According to the data of the mining area, most of the fractures of the roof rock stratum are 0.2 m, which refers to $a = 2$ m and $l = 5$ m.

According to statistics and similar simulation experiments [36], when the mining height is 3~7 m and the working face span is 100~200 m, the values of various coefficients between roof rock beams are $C_x = 1$~1.75 and $\eta = 2$~3.5.

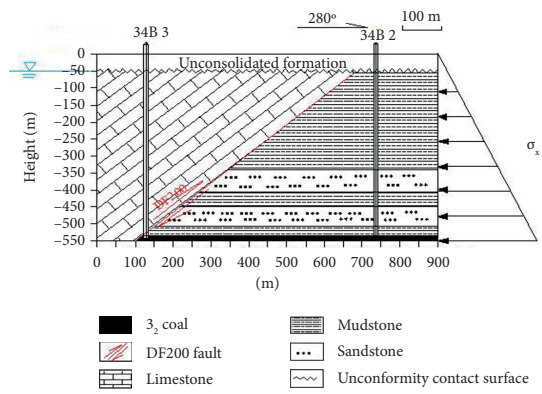

Figure 4: Mining hydrogeological and engineering geological model in the study area.

Based on this, this paper takes $C_x = 1$ and $\eta = 2$ to calculate the development height of water flowing fracture zone considering different influencing factors and the results are shown in Table 2. The different conditions corresponding to No. 1–5 in the table are as follows: (1) only the influence of the self-weight stress field being considered; (2) considering the influence of confined aquifer; (3) considering the influence of tectonic stress field; (4) considering the influence of tectonic stress field and confined aquifer; (5) confined aquifer, tectonic stress field, and the influence of the fault on rock fracture toughness being considered.

As can be seen from Table 2:

(1) Compared with group 1, the theoretical values of the height of the water flowing fracture zone obtained by group 2, group 3, group 4, and group 5 increased by 15.2%, 18.9%, 31.6%, and 32.6%, respectively. Therefore, the water pressure of confined aquifer, fault, and tectonic stress promote the development of water conducting fracture zone.

(2) By comprehensively comparing the theoretical values obtained from the five groups of calculation schemes with the measured values of the height of the water diversion fracture zone in stope, the calculation result of scheme 5 is closest to the actual value. Therefore, the height of water flowing fracture zone of coal seam mining under Ordovician nappe aquifer should comprehensively consider the influence of confined aquifer water pressure, tectonic stress field, and fault.

In addition, using the empirical formula (1) and empirical formula (2) for calculating the height of water flowing fracture zone in medium hard roof slate given in Table 1, it can be obtained that the development height of water flowing fracture zone in overburden of E3213 working face is 30.1~41.3 m and 44.6 m, respectively. Because the influencing factors considered in the traditional empirical formulas are relatively simple, the theoretical value of the development height of the water flowing fracture zone of the coal seam under the Ordovician limestone nappe aquifer calculated by these formulas is less than the actual value. If the risk assessment of water inrush from the stope roof is carried out based on these calculated values, the possible risks will be ignored and the safety production of the coal mine will be affected.

Table 2: Statistics of the height of water flowing fracture zone.

Number	Pressure of confined aquifer p (MPa)	Rock lateral pressure coefficient λ	Influence coefficient of fault on rock fracture toughness t	Height of water flowing fracture zone h (m)
1	0	0.25	1	54.65
2	6.22	0.25	1	62.96
3	0	1.65	1	64.20
4	6.22	1.65	1	71.94
5	6.22	1.65	0.54	72.45

6. Conclusions

A formula for calculating the height of water flowing fracture zone during mining under the Ordovician limestone nappe aquifer was proposed. The formula was on the basis of critical conditions of crack arresting under the action of compression-shear stress and from the perspective of the evolution of the crack propagation of the damaged rock mass, taking tectonic stress, the influence of fault, the mechanical effect of the seepage field on the stress field, and the rock softening with water into consideration. The derived formula for calculating the height of water flowing fracture zone during mining under the Ordovician limestone nappe aquifer was used to calculate the height of water conducting fractured zone of panel E3213 under different conditions. Under the gravity stress field, the calculated value was 54.65 m. Taking the confined aquifer into consideration, the calculated value was 62.96 m and taking tectonic stress into consideration, the calculated value was 64.20 m. Considering influences of both tectonic stress and confined aquifer, the calculated value was 71.94 m. Taking tectonic stress, confined aquifer, and the influence of fault on rock fracture toughness into comprehensive consideration, the calculated value was 72.45 m. The results show that these three factors could promote the growth of water conducting fractured zone. The comparison between the theoretical calculation and the measured result shows that the formula proposed in this paper is closest to the measured value and further

improves the calculation accuracy compared with the previous formulas. Therefore, the height of water flowing fracture zone of coal seam mining under Ordovician nappe aquifer should comprehensively consider the influence of confined aquifer water pressure, tectonic stress field, and fault.

Data Availability

The data used to support the findings of this study are available from the corresponding author upon request.

Conflicts of Interest

The authors declare no conflicts of interest.

Acknowledgments

This work was supported by the Natural Science Foundation of Anhui Science and Technology Department of China under Grant no. 1908085QE248 and the Natural Science Foundation of Anhui Education Department of China under Grant no. KJ2018A0100. Many faculty members at the School of Resources and Geosciences, China University of Mining and Technology, reviewed the manuscript and provided helpful comments. Their support is gratefully acknowledged.

References

[1] W. H. Sui, "Safety geology and geological education for mining engineers," in *Proceedings of the International Symposium and 9th Asian Regional Conference of the International Association for Engineering Geology and the Environment*, Beijing, China, September 2013.

[2] C. He, W. Lu, W. Zha, and F. Wang, "A geomechanical method for predicting the height of a water-flowing fractured zone in a layered overburden of longwall coal mining," *International Journal of Rock Mechanics and Mining Sciences*, vol. 143, Article ID 104798, 2021.

[3] M. Alber, R. Fritschen, M. Bischoff, and T. Meier, "Rock mechanical investigations of seismic events in a deep longwall coal mine," *International Journal of Rock Mechanics and Mining Sciences*, vol. 46, no. 2, pp. 408–420, 2009.

[4] G. F. Hofmann and L. J. Scheepers, "Simulating fault slip areas of mining included seismic tremors using static boundary element numerical modeling," *Mining Technology*, vol. 120, no. 1, pp. 53–64, 2011.

[5] J. G. Ni, J. Wang, Y. L. Tan, and Q. Xu, "Mechanical mechanism of overlying strata breaking and development of fractured zone during close-distance coal seam group mining," *International Journal of Mining Science and Technology*, vol. 30, pp. 207–215, 2020.

[6] W. P. Huang, Y. F. Gao, B. Wang, and J. R. Liu, "Evolution rule and development height of permeable fractured zone under combined-strata structure," *Journal of Mining and Safety Engineering*, no. 2, pp. 330–335, 2017.

[7] C. C. Chu, *Investigation on the Responses of Overburden Stress and Water Pressure to Mining under the Ordovician Nappe*, China University of Mining and Technology, Xuzhou, China, 2016.

[8] B. B. Yang, J. Liu, X. Zhao, and S. Zheng, "Evaporation and cracked soda soil improved by fly ash from recycled materials," *Land Degradation & Development*, vol. 32, no. 9, pp. 2823–2832, 2021.

[9] B. B. Yang, D. Li, S. Yuan, and L. Jin, "Role of biochar from corn straw in influencing crack propagation and evaporation in sodic soils," *Catena*, vol. 204, Article ID 105457, 2021.

[10] B. B. Yang, S. Yuan, Y. Liang, and J. Liu, "Investigation of overburden failure characteristics due to combined mining: case study, Henan Province, China," *Environmental Earth Sciences*, vol. 80, p. 143, 2021.

[11] B. B. Yang, S. T. Du, X. M. Zhao, D. Tang, and C. Yang, "Decision making of curriculum attainment degree for engineering geology based on fuzzy set theory," *Advances in Civil Engineering*, vol. 2021, Article ID 1743778, 6 pages, 2021.

[12] B. B. Yang, Z. P. Zhang, W. L. Ma, M. Hu, and Y. Zhang, "Effect of tea waste on cracking of foundation soil," *Advances in Materials Science and Engineering*, vol. 2021, Article ID 7525811, 2021.

[13] B. B. Yang, K. Xu, and Z. Zhang, "Mitigating evaporation and desiccation cracks in soil with the sustainable material biochar," *Soil Science Society of America Journal*, vol. 84, no. 2, pp. 461–471, 2020.

[14] B. X. Yuan, Z. H. Li, Z. Q. Zhao, and H. Ni, "Experimental study of displacement field of layered soils surrounding laterally loaded pile based on transparent soil," *Journal of Soils and Sediments*, vol. 21, no. 9, pp. 3072–3083, 2021.

[15] B. X. Yuan, Z. H. Li, Z. L. Su, Q. Luo, M. Chen, and Z. Zhano, "Sensitivity of multistage fill slope based on finite element model," *Advances in Civil Engineering*, vol. 2021, Article ID 6622936, 13 pages, 2021.

[16] B. X. Yuan, Z. H. Li, Y. Chen et al., "Mechanical and microstructural properties of recycling granite residual soil reinforced with glass fiber and liquid-modified polyvinyl alcohol polymer," *Chemosphere*, vol. 286, Article ID 131652, 2021.

[17] B. X. Yuan, M. Sun, Y. X. Wang, and L. Zhai, "Full 3D displacement measuring system for 3D displacement field of soil around a laterally loaded pile in transparent soil," *International Journal of Geomechanics*, vol. 19, no. 5, Article ID 04019028, 2019.

[18] B. X. Yuan, M. Sun, L. Xiong, Q. Luo, S. P. Pradhan, and H. Li, "Investigation of 3d deformation of transparent soil around a laterally loaded pile based on a hydraulic gradient model test," *Journal of Building Engineering*, vol. 28, no. 6, Article ID 101024, 2019.

[19] B. Bai, R. Zhou, G. Q. Cai, W. Hu, and G. Yang, "Coupled thermo-hydro-mechanical mechanism in view of the soil particle rearrangement of granular thermodynamics," *Computers and Geotechnics*, vol. 137, no. 8, Article ID 104272, 2021.

[20] B. Bai, Q. K. Nie, Y. K. Zhang, X. Wang, and W. Hu, "Cotransport of heavy metals and SiO_2 particles at different temperatures by seepage," *Journal of Hydrology*, vol. 597, Article ID 125771, 2021.

[21] B. Bai, G. C. Yang, T. Li, and Y. Gao-Sheng, "A thermodynamic constitutive model with temperature effect based on particle rearrangement for geomaterials," *Mechanics of Materials*, vol. 139, Article ID 103180, 2019.

[22] Y. Wu, J. Cui, J. Huang, and W. Zhang, "Correlation of critical state strength properties with particle shape and surface fractal dimension of clinker ash," *International Journal of Geomechanics*, vol. 21, no. 6, Article ID 04021071, 2021.

[23] State Coal Industry Administration, *Procedures for Coal Pillar Reservation and Coal Mining of Buildings, Water Bodies, Railways and Main Roadways*, China Coal Industry Press, Beijing, China, 2017.
[24] X. L. Liu, *Study on the Theory and Application of Water Rock Coupling Process and its Multi-Scale Behavior*, Tsinghua University, Beijing, China, 2008.
[25] L. Q. Shi, H. Q. Xin, P. H. Zhai et al., "Calculating the height of water flowing fracture zone in deep mining," *Journal of China University of Mining and Technology*, vol. 41, no. 1, pp. 37–41, 2012.
[26] J. L. Xu, W. B. Zhu, and X. Z. Wang, "New method to predict the height of fractured water-conducting zone by location of key strata," *Journal of China Coal Society*, vol. 37, no. 5, pp. 762–769, 2012.
[27] S. M. Yi and D. Z. Zhu, *Introduction to Damage Mechanics of Fractured Rock Mass*, Science Press, Beijing, China, 2005.
[28] M. F. Ashby and S. D. Hallam, "The failure of brittle solids containing small cracks under compressive stress states," *Acta Metallurgica*, vol. 34, no. 3, pp. 497–510, 1986.
[29] H. Horii and S. Nemat-Nasser, "Compression-induced microcrack growth in brittle solids: axial splitting and shear failure," *Journal of Geopgysical Research*, vol. 90, no. B4, pp. 3105–3125, 1985.
[30] S. R. Su, *Influence of Fault Structure on In-Situ Stress Field and its Engineering Significance*, Chengdu Institute of Technology, Chengdu, China, 2001.
[31] Q. D. Xie, *Characteristics of Tectonic Stress Field in Fault Area and its Influence on Tunnel Surrounding Rock Stability*, Central South University, Changsha, China, 2010.
[32] M. G. Qian, W. P. Shi, and J. L. Xu, *Mining Pressure and Strata Control*, China University of mining and Technology Press, Xuzhou, China, 2010.
[33] Z. Q. Song, *Practical Mine Pressure Control Theory*, China University of mining and Technology Press, Xuzhou, China, 1998.
[34] L. Q. Shi and J. Han, *Mechanism and Prediction of Floor Water Inrush*, China University of mining and Technology Press, Xuzhou, China, 2004.
[35] D. Z. Zhu and H. X. Guo, *Hydraulic Foundation of Fractured Rock Mass*, Science Press, Beijing, China, 2007.
[36] M. D. G. Salamon, "Behaveior and design of coal pillars," *Australia Coal Journal*, vol. 32, no. 32, pp. 11–22, 1991.

Hindawi
Advances in Civil Engineering
Volume 2022, Article ID 9965974, 10 pages
https://doi.org/10.1155/2022/9965974

Research Article

Experimental Investigation of the Impact of Necking Position on Pile Capacity Assisted with Transparent Soil Technology

Qingnian Yang,[1,2] Jianli Shao,[1] Zhijun Xu,[3] and Yu Miao[1]

[1]*School of Civil Engineering, Nanyang Institute of Technology, Nanyang 473004, China*
[2]*Henan International Joint Laboratory of Dynamics of Impact and Disaster of Engineering Structures, Nanyang Institute of Technology, Nanyang,473004, China*
[3]*College of Civil Engineering, Henan University of Technology, Zhengzhou 450001, China*

Correspondence should be addressed to Zhijun Xu; zj.xu_hust@qq.com

Received 11 November 2021; Revised 14 December 2021; Accepted 3 January 2022; Published 7 February 2022

Academic Editor: Qian Chen

Necking in different positions of a pile body has a significant influence on the bearing performance of a single pile. The transparent soil model experiment was adopted to investigate the impacts of necking positions on the vertical bearing capacity of a single pile and the soil deformation around the pile, and subsequently, the causes of the variation of bearing capacity were analyzed. The results show that the existence of necking does not change the bearing behavior of single pile as pile friction resistance. The bearing capacity of piles decreased by 8.21% and increased by 7.30% when the necking is located in the shallow and middle pile body, respectively, while it did not change significantly when the defects were in the deep part of the pile. The necking position has a significant effect on the deformation and deformation range of soil. The soils at the top, side, and near the end of a pile were mainly influenced by shallow necking, middle necking, and deep necking, respectively. The soils at the location of necking had apparent settlement phenomenon as the piles subsided. The soils at shallow necking's locations were relatively loose, which reduced the side friction force of piles and finally resulted in a reduction of bearing capacity of a single pile. With the increase of the load, the soil around piles gradually developed penetration phenomenon (large deformation), while the soil at the end of pile moved up against pile settlement, which made the necking soil in the middle denser. The loss of side friction resistance was less than the resistance from the necking, which gave birth to an increase in the bearing capacity of a single pile. It was finally found that the side friction resistance and the resistance caused by necking were the main factors governing the bearing capacity of necking single piles.

1. Introduction

As an important form of deep foundation, pile foundation has the advantages of high bearing capacity and low settlement rate and is widely used in high-rise buildings, bridges, and ports. Due to the influences of construction technology and other factors, cavity, crack, diameter reduction (necking), and other defects may develop in pile bodies. Such defects were proved to be in presence by integrity inspection of foundation piles [1, 2]. The existence of these defects will affect the bearing capacity of foundation piles and lead to engineering safety hazards [3–5].

At present, the research on necking piles mainly focuses on the monitoring and identification of the necking. Svetinskii et al. [6] analyzed the reasons and monitoring methods of necking about the concrete and reinforced concrete piles during the settlement and construction. The position of the defect is determined by Ni et al. [7] by the usage of complex continuous wavelet transform and the analysis of time-frequency phase diagrams of different frequency bands. Schilder et al. [8] proposed a device to detect the integrity of pile body by installing Fabry–Pérot interferometer sensor and fiber Bragg grating sensor at the outside of the pile body. Wang et al. [9] found that necking position had a great influence on the vertical bearing capacity by performing indoor model experiment on the vertical bearing characteristics of normal and necking pile. Zhang [10] found that the formation of necked pile is mainly

caused by one or more factors, such as improper construction operation, unreasonable mud density design, poor workability of concrete, or unknown soil layer and groundwater in the stratum. However, there is still a lack of systematic research on the bearing capacity of necking pile and the deformation of soil around pile, and therefore it is difficult to reveal the vertical bearing capacity of necking single piles and guide the engineering design.

Transparent soil testing technology overcomes the shortcomings of conventional geotechnical tests in geotechnical engineering [11, 12]. Ezzein and Bathurst [13] proved that transparent soil had typical mechanical properties of granular soil by the results of laboratory shear test, triaxial compression test, and permeability test. For the research of foundation pile, Kong et al. [14] investigated the influence of pile displacement under inclined uplift force on soil mass by using transparent soil test. Xiang et al. [15] studied the influence of rock strength and buried depth on deformation and failure mechanism by conducting transparent soil test and PFC numerical simulations. Yang et al. [16] obtained the refractive index of transparent soil under different porosities and observed the microscopic characteristics of transparent soil by using scanning electron microscope. Liu et al. [17] performed model tests of static-pressure sinking pile by using transparent soil and the particle image velocimetry method. The advantages of full model test over half model test were outlined and the penetration mechanism of static-pressure pile with different pile tip shapes was investigated. Yuan et al. [18, 19] developed a measurement system to configure the three-dimensional displacement field of soil around piles in transparent soil with the help of particle image velocimetry technology. Liu et al. [20] studied the simulation ability of transparent soil model by comparing the boundary soil displacement field of transparent soil and natural soil model. The test results show that transparent soil can simulate the natural soil. With the development of transparent soil test technology (TSTT), the shortcoming of nonvisualization of geotechnical test has been overcome, and TSTT has become a favorable tool in the geotechnical engineering model testPO. Many scientists have studied and confirmed the preparation method and geotechnical properties of transparent soil. PIV technology is also widely used in geotechnical engineering research, especially in transparent soil test.

To discuss the influence of different neck position on the bearing capacity of single pile, a set of vertical bearing test equipment for single piles using transparent soil was developed. Vertical loading tests were performed using one group of intact piles and three groups of necking single piles at different positions. Load-settlement curves were obtained for the four groups of tests to analyze the influence of necking position on the vertical bearing capacity of single piles. The displacement vector diagram and contour map of four groups of soil around pile corresponding to different loads were calculated by using MatPIV software. The deformation characteristics of soil around piles were studied and the causes for the change of bearing capacity were obtained.

2. Experimental Work

2.1. Experimental Setup. The experimental equipment in the present investigation is mainly composed of three parts: loading system, model box, speckle image making system, and image acquisition system. The loading platform can provide a maximum vertical load of 500 N through a vertical loading rod controlled by a stepper motor. High-strength transparent plexiglass with 5 mm thickness was adopted to construct the model box. The box had an inner size $320 \times 180 \times 350$ mm (length × width × height) [21–23]. The speckle image making system required by the test is placed on the right side of the model box and mainly consists of a 532 nm laser light source and optical prism. The image acquisition system includes industrial CCD camera and camera control computer. Data collection of the test includes mechanical sensors. One located at the end of the loading rod and its accuracy is 0.3 N. The other one was used to calculate the axial force and the displacement of the loading rod. In the tests, the pressure exertion of the loading system and the control of automatic acquisition scheme were realized by a self-developed computer software. The experimental system is shown in Figure 1.

2.2. Experimental Materials. The fused silica solid particles with particle sizes of 0.5–2 mm and purity of 99.9% were selected as solid particles of transparent soil. The size distribution curve is shown in Figure 2. The pore fluid was prepared with *n*-dodecane and 90# white oil with a volume ratio of 1 : 9.5. Finally, the pore fluid with a refractive index of 1.4590 was obtained at indoor temperature 20° C. The physical and mechanical parameters are listed in Table 1. All the piles were made of organic glass. Plexiglass is employed as pile material can make the laser side pass through the pile and accurately observe the movement of soil particles, avoid the error caused by the reflecting surface, and the relative strength is low. It can more accurately simulate the actual situation in the small model test. According to the similarity theory [24], a ratio of 1 : 50 was adopted to reduce the size of the pile studied by Li [25]. The piles had a length and diameter of 200 mm and 20 mm, respectively. The position and size of necking were designed in the shallow, middle, and deep part of the pile shaft, and the distances from the pile top were 60, 100, and 160 mm, respectively, as shown in Figure 3. During the tests, the model pile experiment was repeated three times and the average magnitudes of three testing results were recorded as the loading data. Since the results of the three tests are basically the same, they will not be displayed. This paper shows the results of the average. In the analysis of soil deformation, the images from the test which had a loading data close to the average value were selected for further analysis.

2.3. Experimental Process. The model pile was placed in the middle of the model box and was embedded to a depth of 200 mm. The laser light was turned on and adjusted to an appropriate position to obtain the soil speckle field required for the experimental, as shown in Figure 4. In this scheme,

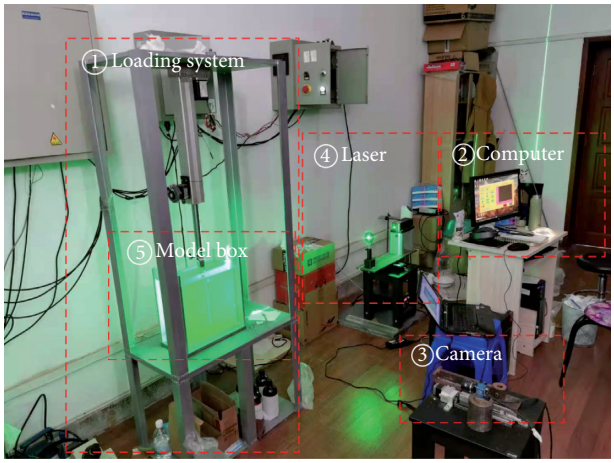

Figure 1: Experimental system.

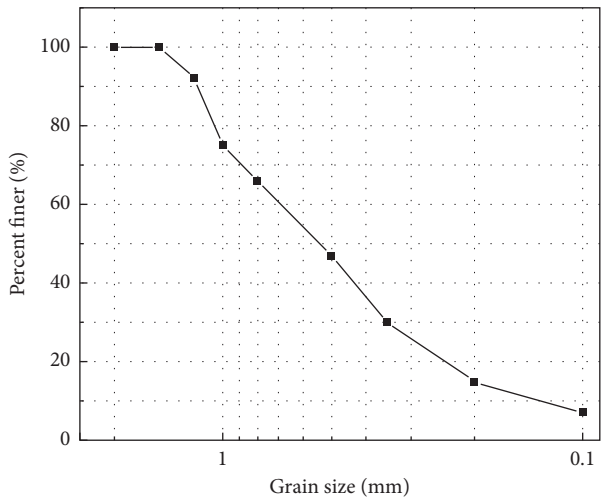

Figure 2: Gradation curve of the fused quartz sand.

Table 1: Parameters of transparent soil.

C_u	C_c	ρ_d (g/cm^3)	ρ_{dmax} (g/cm^3)	ρ_{dmin} (g/cm^3)	γ (kN/m^3)	φ_{dry} (^{o})	φ_{soil} (^{o})	E_s (MPa)	τ_f (kPa)
6	1.354	1.438	1.481	1.239	2.51	37.3	38.3	11.1	10

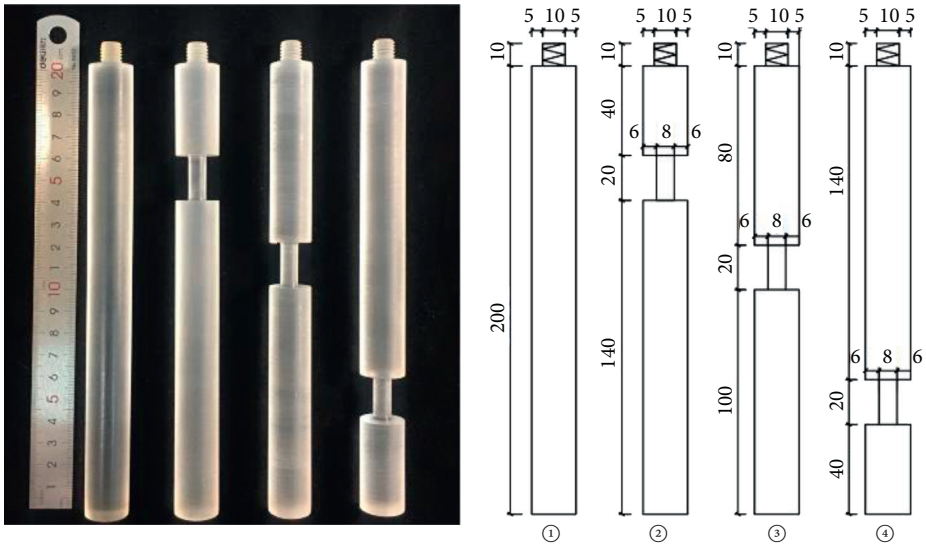

(a) (b)

Figure 3: Physical and dimensions of model piles. (a) Physical model piles. (b) Dimensions of model piles.

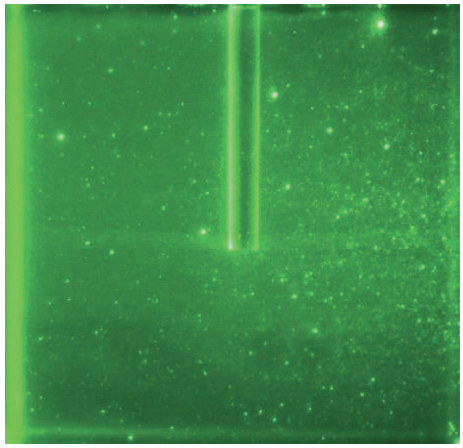

Figure 4: Speckle pattern of transparent soil.

the width of the glass box is about 80 mm away from the pile side, which is 4 times of the pile diameter. The width of the glass box is about 150 mm away from the pile side, which is 7.5 times of the pile diameter. The height of the glass box is 100 mm at the pile bottom, which is 5 times of the pile diameter. According to Liu's research results [17], this scheme can eliminate the boundary effect in the test. During the test, transparent soil was laid according to three layers and the thickness of each layer was 100 mm. The model pile was vertically placed into the soil sample when the transparent soils with 50 mm thickness were laid on the second floor. After that, the subsequent laying was performed. The layout schemes of the model box and pile-soil are shown in Figure 5. To ensure the consistency of the experimental results, the consistency of quality and height of the transparent soil in each model tank should be controlled to ensure the same density of the transparent soil during each experimental preparation. At the same time, to exclude the gas in the granular pores and the internal pore pressure of the soil, the transparent soil after packing was vacuumed.

According to the testing technical code of Building Foundation Piles (JGJ106-2014), the slow-velocity maintenance loading method was adopted to carry out the compressive test of a single pile. The load was applied step by step. The magnitude of loading for each step was 20 N. The loading stability was determined to be stable when the settlement rate of pile top is less than 0.1 mm/h for consecutive two times. The settlement of pile top was recorded, and the speckling field of soils was photographed. Then, loading at the next step was applied. When the settlement of pile reached the maximum or the pile body was damaged, the loading ends. The maximum settlement of pile top is limited to 30 mm.

3. Experimental Results

3.1. Analysis of Vertical Ultimate Bearing Capacity of Piles. Four groups of load-settlement curves recorded at the pile top were obtained in the tests, as shown in Figure 6. Obvious steep drop can be seen in the curve. According to Testing Technical Code of Building Foundation Pile (JGJ106-2014), the loading magnitude corresponding to the starting point of an apparent steep drop was taken as the ultimate bearing capacity in the steep load-settlement curve. It can be concluded that the vertical ultimate bearing capacity of Nos. 1–4 piles' bodies was 219, 201, 235, and 218 N, respectively. Compared with No. 1 pile (the intact pile), the vertical ultimate bearing capacity (VUBC) of Nos. 2 and 3 piles was reduced by 8.21% and increased by 7.30%, respectively. For No. 4 pile, the VUBC was almost the same as the intact pile. Before reaching the ultimate loading point, the settlement of the pile top increased almost linearly with the loading applied in the pile top. When the ultimate loading was reached, the settlement in the pile top increased sharply, showing the bearing behavior of friction piles. Therefore, the existence of necking did not change its bearing behavior of friction piles. Before the vertical ultimate load was reached, the settlement magnitudes of necking single piles at the same loading level were all greater than that of No. 1 pile. In total, the necking reduced the side friction, and thus the settlement magnitudes of the necking single piles were greater than those of the intact pile before reaching the vertical ultimate bearing capacity. Although the vertical ultimate bearing capacity of the necking single pile in the middle was improved, the settlement magnitude was still greater than that of the intact pile.

According to the above results, the vertical ultimate bearing capacity of single piles at different necking positions may decrease or increase in comparison with the intact single pile. Therefore, besides side friction, the bearing capacity of single piles should be affected by some other factors. In the following section, the influencing factors will be analyzed in combination with the load-settlement curve of single piles and the soil deformation around the pile.

3.2. Analysis of Soil Deformation under Vertical Loading of Single Piles. The displacement vector map and contour map of soil deformation around piles under different loading levels were obtained by MatPIV software [16, 26]. The loading transfer law of necking single piles and the intact pile under vertical loading was analyzed. The soil deformation field around the pile under 140, 220, and 260 N loading levels

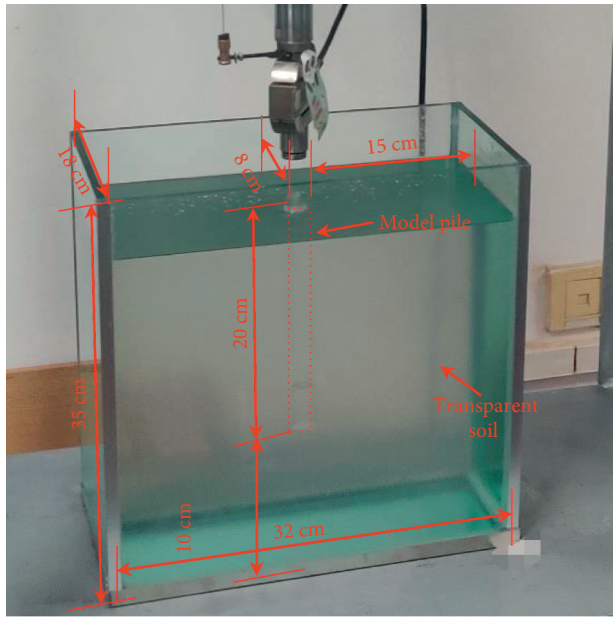

Figure 5: Layout of the model box and pile soil.

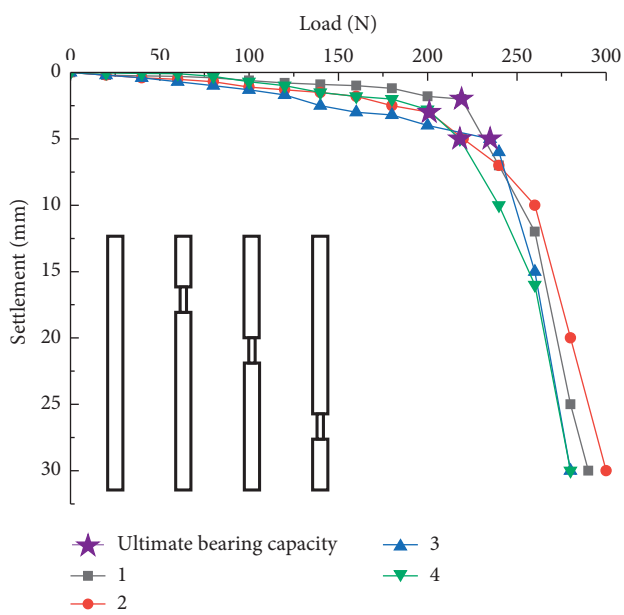

Figure 6: Load-settlement curves.

was selected for analysis. The three load levels stated above were based on the loading of No. 1 pile: 140 N corresponds to the load before the vertical ultimate bearing capacity of a single pile is reached, 220 N is the vertical ultimate bearing capacity of a single intact pile, and 260 N is the load after the vertical ultimate bearing capacity of a single pile. The soil deformation around the three groups of necking piles were compared with each other and also the intact pile. The deformation law of soil around the pile under different loading levels was comprehensively analyzed.

3.2.1. Analysis of Soil Deformation around the Pile under 140 N Vertical Loading. Each single pile was in the normal bearing range under the 140 N loading level, and the top settlement magnitudes of Nos. 1–4 single piles were 1, 1.5, 2.5, and 1.5 mm, respectively. The displacement vector and contour map of the soil around Nos. 1–4 single piles are shown in Figures 7 and 8 under the present loading level 1.

The soils at the pile top and around the pile moved downwards as the sinking of foundation pile under the action of relative friction based on the analysis of Figure 7.

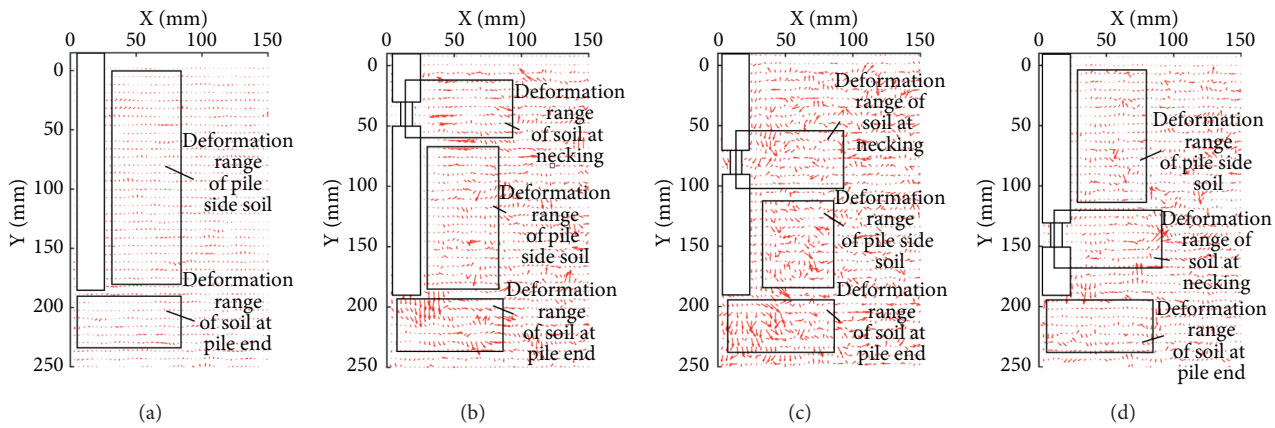

Figure 7: Displacement vector diagram of soil around the single pile under 140 N load level. (a) Intact pile. (b) Necking in the shallow pile body. (c) Necking in the middle pile body. (d) Necking in the deep pile body.

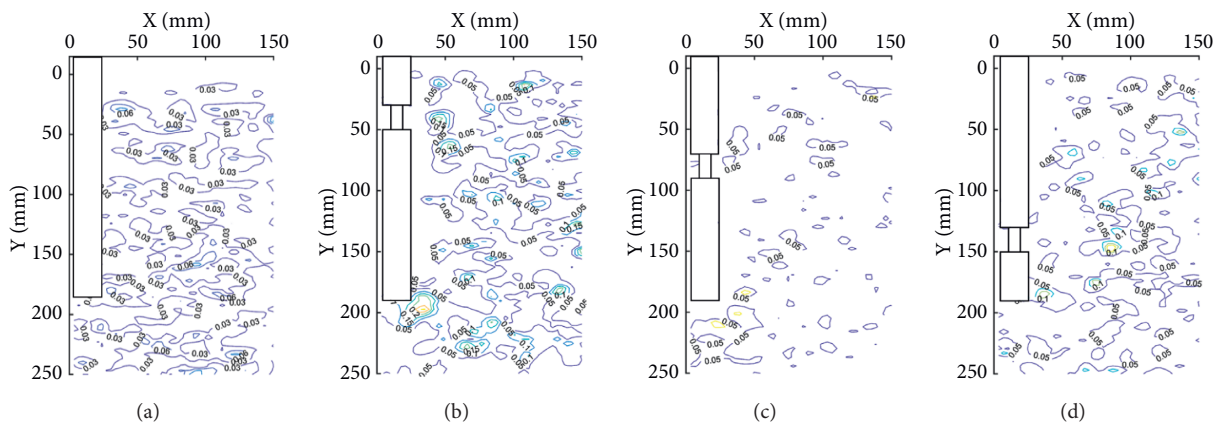

Figure 8: Displacement contour map of soil around the single pile under 140 N load level. (a) Intact pile. (b) Necking in the shallow pile body. (c) Necking in the middle pile body. (d) Necking in the deep pile body.

The closer the distance between the soil around the pile and the foundation pile, the more obvious the movement of the soil around the pile. By analyzing the test results of Nos. 1–4 pile, the following can be concluded. (1) An increase in the soil deformation around the pile shaft and at the pile top of single necking piles appeared in comparison with the intact pile. Especially, the soil at the necking locations of piles suffered from obvious settlement at the pile shaft. (2) The influence of shallow necking on the soil around the pile is less than that in the middle and deep necking cases.

According to Figure 8, the soil around the pile subsided with the settlement of foundation pile under 140 N loading. The deformation of the soil around the pile was independent small deformation, while the deformation of the soil at the pile tip was roughly "pear shaped." Compared with No. 1 pile, there was local but relatively limited concentrated deformation at the necking locations of No. 2 pile. Meanwhile, at the pile tip, the deformation was obviously larger than that of the intact pile. For No. 3 pile, there was a large concentrated deformation area in the soils at the necking position, and the deformation of the soil at the pile tip was larger than that of the intact pile, as well as No. 4 pile. But the deformation is smaller than those appeared at the necking locations in the middle. At a close necking position to the pile top, the soil deformation at the pile top had a trend of connecting with the soil deformation at the necking position.

3.2.2. Analysis of Soil Deformation around the Pile under 220 N Vertical Loading. All single piles had reached their vertical bearing limit except for No. 3 pile at the loading level of 220 N. The settlement magnitudes at the top of Nos. 1–4 piles were 2.8, 5, 5, and 5.0 mm, respectively. Displacement vector and contour map of soil around Nos. 1–4 piles under this load level are, respectively, shown in Figures 9 and 10.

According to Figure 9, the pile top settlement of all piles increased with increasing vertical loading. At the same time, the soil around the pile suffered from large deformation. By comparison and analysis of Nos. 1–4 piles, soils at the shallow and middle necking locations moved horizontally away from the foundation pile and moved upwards against the settlement of the pile. At the same time, the soil at the pile top also has a large displacement, and some soils at

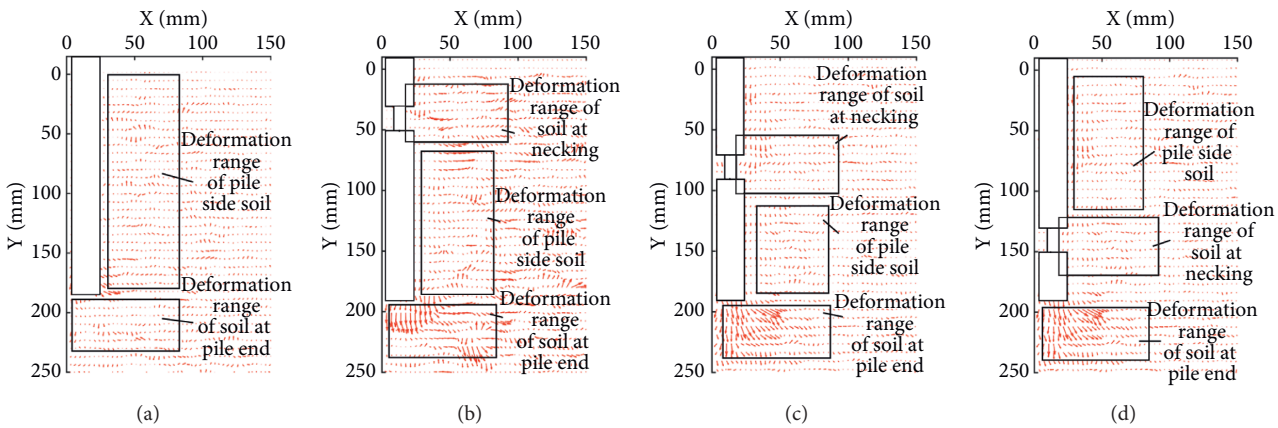

Figure 9: Displacement vector diagram of soil around the single pile under 220 N load level. (a) Intact pile. (b) Necking in the shallow pile body. (c) Necking in the middle pile body. (d) Necking in the deep pile body.

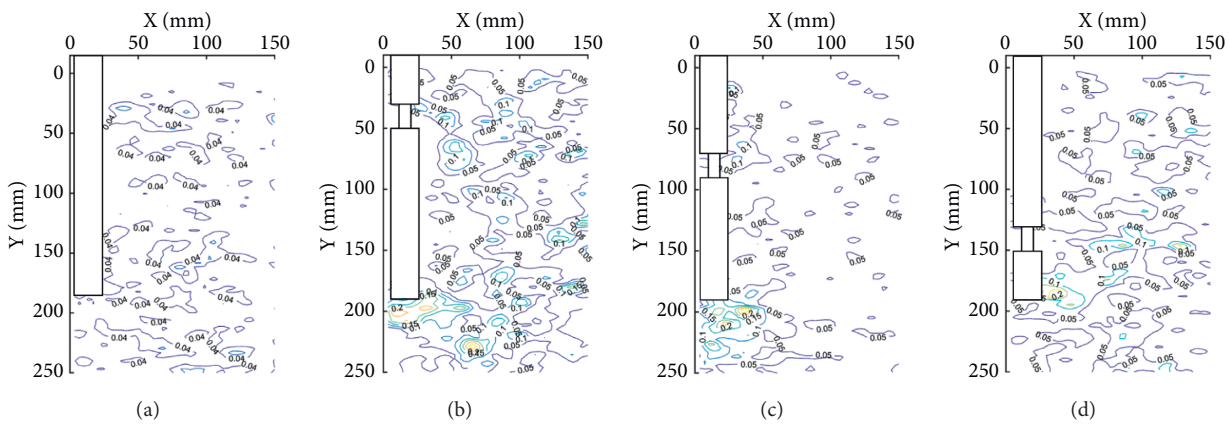

Figure 10: Displacement contour map of soil around the single pile under 220 N load level. (a) Intact pile. (b) Necking in the shallow pile body. (c) Necking in the middle pile body. (d) Necking in the deep pile body.

the pile top moved upwards around the pile top against the pile settlement. For the deep necking pile, there was a tendency that the deformation of soil around the pile shaft connected with the soil at the pile tip, and a larger part of the soil around the pile from the necking position to the pile top was involved in deformation.

According to Figure 10, with an increase of the load, the deformation magnitude and range of the soil around the pile shaft increased and tended to be gradually through, respectively, while the deformation of the soil at the pile tip gradually changed from the original "pear shape" to the "butterfly shape." Compared with results of No. 1 pile, an increase of the local concentrated deformation in the necking position was observed for No. 2 pile. The soil around the pile forms a circular deformation from the necking position to the pile tip. For No. 3 pile, the concentrated deformation of the soil at the reduced diameter position increased, which resulted in an increase of the affected range of the soil around the pile compared to that of the intact pile. The soil deformation at the necking position of pile No. 4 was connected with the soil deformation at the pile tip, so the soil deformation range near the pile tip increased. For the single pile with a shallow necking (No. 2 pile), when the settlement of the foundation pile was large, the soil at the necking position had obvious concentrated large deformation, and the soil around the pile formed a circular deformation from necking position to the pile tip. For the single pile (No. 3 pile) with middle necking, the affected range of soil at the necking position was larger, which accordingly made the affected range of soil around the pile larger than that of the intact pile. For the single pile with deep necking (No. 4 pile), the deformation range of soil near the pile tip increased as the soil deformation at the necking position was connected with that at the pile tip.

3.2.3. Analysis of Soil Deformation around the Pile under 260 N Vertical Loading. Each single pile was destroyed under the loading level of 260 N, and the settlement at the pile top increased sharply. The settlement magnitudes of Nos. 1–4 single piles were 18, 10, 15, and 16 mm, respectively. Figures 11 and 12 show the displacement vector and contour map of the soil around Nos.1–4 single piles under this loading level.

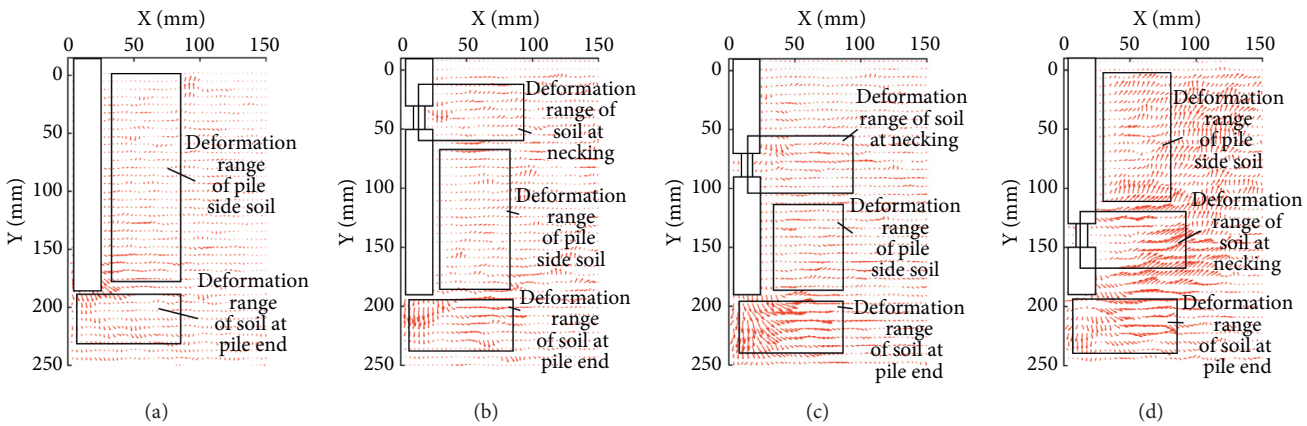

Figure 11: Displacement vector diagram of soil around the single pile under 260 N load level. (a) Intact pile. (b) Necking in the shallow pile body. (c) Necking in the middle pile body. (d) Necking in the deep pile body.

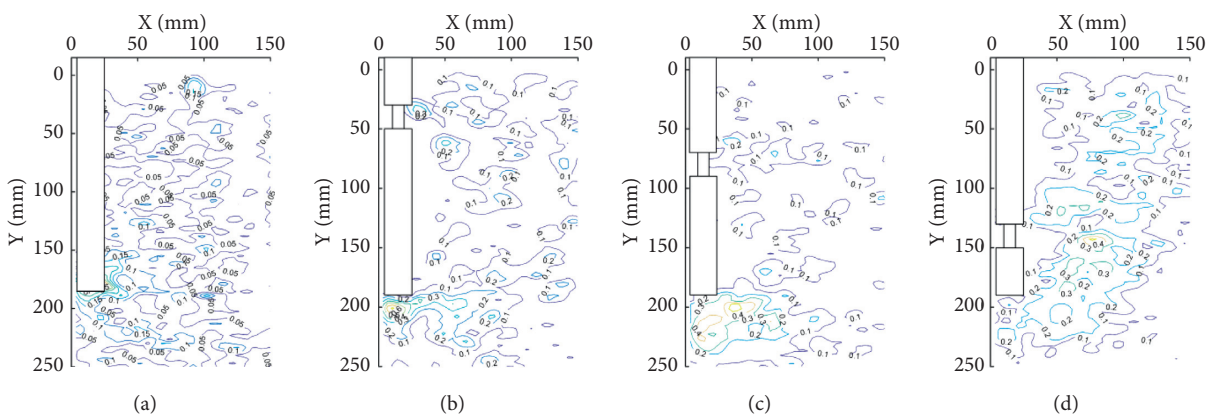

Figure 12: Displacement contour map of soil around the single pile under 260 N load level. (a) Intact pile. (b) Necking in the shallow pile body. (c) Necking in the middle pile body. (d) Necking in the deep pile body.

It can be found from Figure 11 that the settlement of the single piles increased rapidly when the loading magnitude reached the corresponding vertical bearing capacity of the pile. This subsequently resulted in bulge of soil at the side of piles, settlement of some soil at the tip of piles, horizontal outward movement of some soil around the pile shaft, and upward movement of some soil around the pile end. The bearing capacity of the single piles was lost due to the whole shear damage of soil around the piles. In comparison with the Nos. 1–4 piles and the intact pile, some soil around the necking position settled downward, some soil moved outward in the horizontal direction, and some soil moved upward around the necking tip. Meanwhile, the deformation degree and range increased. For the single pile with deep necking, the soil at the necking location was linked up with the soil at the pile tip and the global deformation range of the soil around the piles increased.

According to Figure 12, combined with the load-settlement curve, each single pile lost bearing capacity with the increase of the load, and the deformation field of the soil around the pile evolved from the original independent deformation to the overall deformation. A failure due to overall deformation occurred and the soil at the pile top completely changed to a "butterfly shape." At this time, the side friction and the pile top resistance of each single pile had reached the maximum. Compared with No. 1 pile, concentrated deformation presented at the necking position of No. 2 pile, the deformation range of the soil between the necking position to the pile tip increased, and the overall deformation range increased. For No. 3 pile, there was concentrated large deformation around the necking position, and the deformation range and magnitude of the soil at the pile top were also large. For No. 4 pile, the deformation of the soil at pile tip decreased slightly. However, the deformation of soil at the pile top was connected with soil at necking position, which resulted in an increase of the deformation range of the soil from the necking location to the pile top.

By analyzing the vertical bearing capacity of single pile and the two-dimensional deformation field of soil under vertical load, it can be concluded that the influence of necking on the vertical bearing capacity of pile comes from pile side friction and necking resistance. For the vertical bearing capacity of single pile, the necking resistance makes

up for the loss of transverse friction resistance, and the degree of compensation depends on the compaction of soil. The side friction of pile gradually plays a role from top to bottom. For the complete pile, there is no defect in the pile body, so it has greater friction. For a single pile with shallow necking, the upper part of the pile does not provide friction resistance, and the necking resistance cannot make up for the lost side friction, which leads to the reduction of the vertical bearing capacity of the pile compared with the complete pile. For the single pile with middle necking, the soil around the necking position is dense, and the transverse friction resistance at the necking position plays an important role. Therefore, the transverse friction resistance loss is less than the necking resistance, which leads to an increase in the vertical bearing capacity compared with the complete pile. For a single pile with deep necking, the transverse friction loss is equal to the necking resistance, so the bearing capacity of a single pile with deep necking is the same as that of a complete pile. For the soil around the pile, the necking resistance leads to the concentrated deformation of the soil at the necking. With the increase of load, the range of concentrated deformation increases. With the increase of necking depth, the deformation of soil at the necking and the deformation of soil at the pile end increase. This leads to increased deformation of the soil around the pile.

4. Conclusions

The influence of the necking position on the vertical bearing capacity of single piles was investigated by using the transparent soil test and PIV image processing technology in the present paper. The influence of necking position on the deformation of soil around the pile under vertical load was intuitively analyzed, and the mechanism of the bearing capacity variation was revealed. The following conclusions were derived:

(1) The load-settlement curves of each single pile showed an obvious steep-drop characteristic. According to the soil deformation diagram, the soil around the pile moves downward with the settlement of the pile foundation before the failure. The single pile loses its bearing capacity due to the shear failure of soil around the pile. Therefore, for friction pile, necking will not change the bearing behavior of single pile as friction pile, nor will it change the failure mode of single pile.

(2) The effect of necking on the vertical loading bearing capacity of a pile comes from side friction and necking resistance. While the two resistances are determined by the compactness of the soil at the necking position of the pile. Compared with the intact pile, the vertical bearing capacity of the middle and shallow necking single pile increases by 7.30% and decreases by 8.21%, respectively. While for the deep necking single pile, the capacity remains unchanged. The settlement magnitude of the necking single piles is greater than that of the intact pile before the ultimate bearing capacity.

(3) Concentrated deformation at the necking position was observed for the soil around the pile shaft and a large soil deformation range was identified. The main deformation range of the soil around the pile is controlled by the necking position. The shallow necking affects the deformation of the soil near the pile tip, the middle necking affects the deformation of the soil around the pile, and the deep necking affects the deformation of the soil near the pile end.

(4) Combined with transparent soil and PIV technology, this paper studies the variation law of the bearing capacity of reduced diameter pile and the soil around the pile, which provides a certain theoretical and technical reference for the rational design and reinforcement of foundation pile. However, the study is only for a single sandy soil, and other soil conditions have not been studied. The study only considers the variation law and causes of bearing capacity under vertical load, not horizontal load. The theoretical calculation of the influence of shrinkage on bearing capacity has not been deeply studied, and the next research will be carried out in the future.

Data Availability

The data used to support the findings of this study are available from the corresponding author upon request.

Conflicts of Interest

The authors declare that there are no conflicts of interest regarding the publication of this paper.

Acknowledgments

The authors express their gratitude to the National Natural Science Foundation of China (no. 51978247) and Key Science and Technology Projects of Henan Province (no. 202102310242).

References

[1] Z. Li and Y. Gao, "Effects of inner soil on the vertical dynamic response of a pipe pile embedded in inhomogeneous soil," *Journal of Sound and Vibration*, vol. 439, no. 2, pp. 129–143, 2019.

[2] M. O'neill and H. Sarhan, "Structural resistance factors for drilled shafts considering construction flaws," in *Proceedings of the Current Practice Future*, pp. 166–185, Trend Deep Foundation, California, USA, July 2004.

[3] H. A. Sarhan, M. W. O'Neill, and K. M. Hassan, "Flexural performance of drilled shafts with minor flaws in stiff clay," *Journal of Geotechnical and Geoenvironmental Engineering*, vol. 128, no. 12, pp. 974–985, 2002.

[4] H. Sarhan, M. O'neill, and S. Tabsh, "Structural capacity reduction for drilled shafts with minor flaws," *ACI Structural Journal*, vol. 101, no. 3, pp. 291–297, 2004.

[5] M. O'neill, S. Tabsh, and H. Sarhan, "Response of drilled shafts with minor flaws to axial and lateral loads," *Engineering Structural*, vol. 25, no. 1, pp. 47–56, 2003.

[6] E. V. Svetinskii and M. S. Gaidai, "Defects of precast and cast-in-place piles in foundation engineering," *Soil Mechanics and Foundation Engineering*, vol. 32, no. 2, pp. 63–65, 1995.

[7] S.-H. Ni, Y.-Z. Yang, P.-H. Tsai, and W.-H. Chou, "Evaluation of pile defects using complex continuous wavelet transform analysis," *NDT & E International*, vol. 87, no. 4, pp. 50–59, 2017.

[8] C. Schilder, H. Kohlhoff, D. Hofmann, F. Basedau, and M. Herten, "Static and dynamic pile testing of reinforced concrete piles with structure integrated fibre optic strain sensors," in *Proceedings of the Fifth European Workshop Optical Fibre Sensors*, pp. 47–62, Krakow, Poland, May 2013.

[9] C. Wang, J. Su, and G. Wang, "Model test studies of the vertical bearing behavior of bored piles with breakage defects," *Applied Mechanics and Materials*, vol. 256-259, pp. 65–70, 2013.

[10] M. Zhang, "Experimental researches and numerical analyses of vertical bearing behavior of boredpile foundations including defective piles with stem enlargement or shrinkage," Master Dissertation, Tianjing University, Tianjing, China, 2012.

[11] M. Iskander, "Introduction to transparent soils," in *Modelling with Transparent Soils Visualizing Soil Structure Interaction and Multiphase Flow, non-intrusively*, pp. 1–4, Springer, Berlin, Heidelberg, 2010.

[12] M. Iskander, R. Baturst, and M. Omidvar, "Past, present, and future of transparent soils," *Geotechnical Testing Journal*, vol. 38, no. 5, pp. 393–401, 2015.

[13] F. Ezzein and R. Bathurst, "Transparent sand for geotechnical laboratory modeling," *Geotechnical Testing Journal*, vol. 34, no. 6, pp. 590–601, 2011.

[14] G. Kong, Z. Cao, H. Zhou, and X. Sun, "Analysis of piles under oblique pullout load using transparent-soil models," *Geotechnical Testing Journal*, vol. 38, no. 5, pp. 725–738, 2015.

[15] Y. Xiang, H. Liu, W. Zhang, J. Chu, D. Zhou, and Y. Xiao, "Application of transparent soil model test and DEM simulation in study of tunnel failure mechanism," *Tunnelling and Underground Space Technology*, vol. 74, no. 4, pp. 178–184, 2018.

[16] X. Yang, G. Jin, M. Huang, and K. Tang, "Material preparation and mechanical properties of transparent soil and soft rock for model tests," *Arabian Journal of Geosciences*, vol. 13, pp. 343–352, 2020.

[17] C. Liu, X. Tang, H. Wei, P. Wang, and H. Zhao, "Model tests of jacked-pile penetration into sand using transparent soil and incremental particle image velocimetry," *KSCE Journal of Civil Engineering*, vol. 24, no. 4, pp. 1128–1145, 2020.

[18] B. Yuan, M. Sun, Y. Wang, L. Zhai, Q. Luo, and X. Zhang, "Full 3D displacement measuring system for 3D displacement field of soil around a laterally loaded pile in transparent soil," *International Journal of Geomechanics*, vol. 19, no. 5, Article ID 04019028, 2019.

[19] B. Yuan, M. Sun, L. Xiong, Q. luo, and H. Li, "Investigation of 3D deformation of transparent soil around a laterally loaded pile based on a hydraulic gradient model test," *Journal of Building Engineering*, vol. 28, no. 3, Article ID 101024, 2019.

[20] J. Liu and M. G. Iskander, "Modelling capacity of transparent soil," *Canadian Geotechnical Journal*, vol. 47, no. 4, pp. 451–460, 2010.

[21] J. P. Xu, J. Zhou, C. Y. Xu, and C. Y. Zou, "Model test research on pile driving effect of squeezing against soil," *Rock and Soil Mechanics*, vol. 21, no. 3, pp. 235–238, 2000.

[22] Z. H. Cao, G. Q. Kong, H. L Liu, and H. Zhou, "Model test on deformation characteristic of pile driving in sand using PIV technique," *Engineering Mechanics*, vol. 31, no. no8, pp. 168–174, 2014.

[23] K. R. Massarsch and C. Wersaell, *Cumulative Lateral Soil Displacement Due to Pile Driving in Soft Clay*, Geo-Congress, San Diego, California, US, 2013.

[24] S. Iai, "Similitude for shaking table tests on soil-structure-fluid model in 1g gravitational field," *Soils and Foundations*, vol. 29, no. 1, pp. 105–118, 1989.

[25] Z. Y. Li, "Key problems investigation on non-destructive integrity detection of piles with elevated-cap(beam)," Doctoral Dissertation, Zhejiang University, Hangzhou, China, 2017.

[26] Y. Sang, Z. Wang, S. Yu, and H. Zhao, "The loading test on the singe pile with pile cap in transparent soil model," *Geotechnical Testing Journal*, vol. 42, no. 2, pp. 385–406, 2019.

Hindawi
Advances in Civil Engineering
Volume 2022, Article ID 2269654, 9 pages
https://doi.org/10.1155/2022/2269654

Research Article

Evaporative Cracking Characteristics of the Embankment Soil Affected by the Saline Concentration

Jiawei Liu,[1] **Yingzhi Xia**,[1] **Hui Li**,[1] **Guoping Hu**,[1] **and Mingming Hu**[2]

[1]*School of Civil and Transportation Engineering, Henan University of Urban Construction, Pingdingshan, China*
[2]*School of Civil Engineering, Xuchang University, Xuchang, China*

Correspondence should be addressed to Hui Li; 30070509@hncj.edu.cn and Mingming Hu; hutiaoaini@hotmail.com

Received 5 December 2021; Accepted 24 December 2021; Published 11 January 2022

Academic Editor: Yonghong Wang

Embankment soil affected by saline can not only cause roadbed settlement, frosting, and road cracks but also cause corrosion and cracking of roadbed pipelines, which seriously affects the stability of the road. Water evaporation and dry cracking of the saline soil mainly cause soil swelling, poor water stability, and corrosive characteristics of the embankment soil. In this study, the evaporative cracking characteristics of soil with different saline concentrations were investigated. The results showed that the moisture content decreased linearly with the drying time in the early evaporation process, subsequently decreased slow down in the mid-term evaporation, and finally become got and remain a residual moisture content, which are 46.39%, 44.05%, 42.70%, and 40.27% with the increase of the saline concentration. The evaporation process with different saline concentrations in the soil can be divided into three stages: uniform evaporation stage, slow down evaporation stage, and equilibrium evaporation stage, which was consistent with the moisture content change. With the development of the drying time, the cracks gradually appeared on the soil surface, gradually deepened in the soil, and expanded the crack network. The development of cracks can be divided into three stages: the cracking preparation stage, the crack development stage, and the crack stable stage. The cracking began at high evaporation rate under high saline concentration, and the fractal dimension remained stable under similar saline concentration. The fractal dimension was gradually increased with the decrease of the moisture content and the increase of the saline concentration, respectively. The soil began to crack with larger moisture under high saline concentration. The drying cracks in the nature were consistent with the configuration of the cracks formed in the experimental results.

1. Introduction

Saline soil is widely distributed in China and the world, which seriously harms the industry, agriculture, and infrastructure [1]. The chemical state of the saline soil is changed under the unique arid and semiarid climatic conditions, which can seriously affect the water evaporation and drying and cracking characteristics of the soil [2]. The saline soil showed the characteristics of expansion, poor water stability, and corrosiveness of the soil, which can cause salt expansion, settlement, and muddying of the roadbed [3]. Also, road reflection cracks can cause corrosion and cracking of roadbed pipelines, which seriously affects the stability of the road.

The embankment filled with high liquid limit or expansive soil tends to have a high natural moisture content due to the large plasticity of the soil. Water loss, volume shrinkage, and deformation of the saline soil appeared under the condition of high temperature exposure [4]. The surface water loss rate was much faster than the inner water loss rate in the compacted embankment. The uneven water loss leads to uneven soil shrinkage, which causes the horizontal network cracks on the surface of the embankment soil [5, 6]. The cracks will widen and deepen as the exposure time increases and even will run through the whole layer.

Roadbed soil cracking is a common disease in road engineering, especially the high-filled roadbed with saline soil, causing uneven settlement of the roadbed and causing

cracking. The high groundwater level and salinity degree may produce secondary salinization of the subgrade soil under the action of capillary water in winter and transpiration in summer [7]. The dynamic groundwater can intensify the increase of the soil moisture and salt content, which provide water and salt replenishment for the salt heave and frost heave of the highway [8]. Additionally, the large temperature fluctuation process, especially the cooling process, provides temperature conditions for salt expansion and also provides sufficient temperature stress for the moisture in the roadbed soil to move it to the top of the roadbed, thereby causing roadbed salt cracking [9, 10].

The saline soil is mainly sulfate and chloride salt, which are the main reasons for the failure and destruction of roadbeds. Soil shrinkage and cracking is a complex process, which is affected by various factors and has an important impact on the properties of the soil and causes various engineering problems [11]. Soil cracking reduces the bearing capacity of the soil and increases the compressibility of the soil, which leads to the cracking and destruction of the embankment soil and roadbed [12, 13]. Cracks can also increase the permeability of the soil, adversely affecting the flow of groundwater, which eventually causes damage of the roadbed and embankment soil [14]. The embankment soil cracking circulates with the seasons and the humidity of the environment and is directly related to temperature [15]. These kinds of damage start from the side of the road and gradually develop toward the center of the road, which mainly formed the cracks and bulges with intertwined characteristics [16]. Meanwhile, the development of longitudinal cracks in the road surface is more obvious than the horizontal cracks and will eventually connect with each other to form a network [17].

At present, soil cracking and evaporation are quantitively analyzed using the correlation analysis, image process, and other chemical and biological methods [18–21]. The cracking mechanism was also investigated according to the crack behavior, crack initiation, and development [22]. Furthermore, the measures for controlling the soil cracking were comprehensively studied, such as adding the fiber and biochar into the soil to reinforce and improve the saline soil [23, 24].

However, the cracking and evaporation characteristics of embankment saline soil were barely considered in road engineering, especially the quantitative analysis of the crack development in the laboratory tests. In this study, the evaporation process and characteristics, cracking development, and influencing factors of the embankment saline soil were comprehensively investigated in different saline concentrations based on the experimental process and fractal theory. The moisture content, evaporation rate, and fractal dimension of the cracks were adopted to characterize the saline soil properties which are related to the embankment stability.

2. Materials and Methods

2.1. Materials. In this study, the laboratory experiments were adopted to investigate the cracking features of saline-alkali soil. The soil used in the experiment was collected at a depth of 0.5 m~1.0 m in weak saline-alkaline groundwater environment, which was taken from Hailar Street, Hohhot, Inner Mongolia, China. Hohhot has a typical Mongolian plateau continental climate, with significant seasonal climate change, large annual temperature difference and large daily temperature difference, and sufficient sunshine. The annual average precipitation is 335.2~534.6 mm, mainly in July and August.

The soil samples were dried and crushed outdoors before they were screened through a 2 mm sieve to remove large particles. Then, they were stored in sealed buckets for testing. The physical and mechanical properties of soil are listed in Table 1. Sodium sulfate (Na_2SO_4) with an initial mass fraction of 38% was added to the soil to simulate the impact of saline-alkali pollution.

2.2. Experimental Process. Distilled water was added into the soil first and stirred well and evenly. After that, Na_2SO_4 was added into the soil sample to prepare the saturated mud with an initial moisture content of 100%. The saline-alkali concentration was set as 0, 0.12, 0.24, and 0.36 mol/L, separately. The soil samples were placed in a sealed round glass container with a size of Φ19.5 cm × 5 cm. Then, they were stored in a container with the constant temperature and humidity for 10 days to provide enough time for the saline-alkali to react with the soil and produce uniform sample. The soil sample is shown in Figure 1. A total of 4 groups of samples were prepared for testing with different saline-alkali concentrations, and 3 soil samples in each group were tested in parallel. The experimental parameters are listed in Table 2.

The samples were placed in a constant temperature drying room together with the electronic balance and dried at the temperature of 25°C and a relative humidity of 60%. The weight change was recorded every 3 hours by a computer during the drying process. The evaporation rate and moisture content of the sample were calculated to analyze the evaporation features. The definition of the evaporation is as follows [25]:

$$E_a = \frac{\Delta m}{S \cdot T}, \tag{1}$$

where Δm was the weight change of the soil, which is equal to the weight of the evaporated water, S is the surface area of the soil sample, and T is the evaporation time.

2.3. Image Processing of Cracks in the Samples. A digital camera was used to record the cracking development of the soil sample during the drying process. The recorded images were firstly processed to eliminate digital noise and interference to highlight the cracks using the median filter method to improve the image quality, which can be well used to quantitively analyze the crack features in the soil samples. The color image was converted to the grayscale image which can efficiently extract the crack information. Grayscale is usually divided into 256 grayscale shades, represented by numbers between 0 and 255. The darkest and brightest grayscales were represented by the numbers 0 and 255,

Table 1: Physical and mechanical properties of soil.

Density ($g \cdot cm^{-3}$)	Liquid limit (%)	Plastic limit (%)	Plastic index	Cohesion (kPa)	Internal friction angle (°)	Compressibility coefficient (MPa^{-1})	Compressibility modulus (MPa)
1.68	66.26	38.68	30.42	58.13	22.15	0.267	10.116

Figure 1: Soil sample.

Table 2: Experimental parameters.

Soil group	Saline-alkali concentration ($mol \cdot L^{-1}$)	Number of samples	Thickness of soil samples (mm)
1	0	3	5
2	0.12	3	5
3	0.24	3	5
4	0.36	3	5

respectively. The gradient from black to white is represented by the remaining numbers from 1 to 254. With grayscale, only one number is used to represent the color of each pixel.

The threshold segmentation method was used to binarize the image to further distinguish the cracks from other parts of the soil surface according to the gray threshold difference between the target object (a crack in this case) and the object background (uncracked soil surface). The image was considered as a combination of different gray levels in the target and the background. The target object indicates that the gray value of a pixel exceeds the threshold; otherwise, it belongs to the background.

In this study, the fractal dimension, which is a parameter used to quantitively characterize the irregularity of the system, was used to quantitively characterize the development of the cracks on the soil surface. Of which, similar dimension is a parameter used to characterize the fractal feature of the rock and soil mass and geological structures. Suppose that whole S is composed of N small individuals. These small individuals are denoted as S_i ($i = 1, 2, \ldots, N$). If the small individuals are magnified by $1/r_i$ times, they can be congruent with the whole ($0 < r_i < 1$), and the similarity dimension is expressed as follows [26]:

$$D_S = \frac{\ln N}{\ln (1/r)}. \tag{2}$$

3. Experimental Results

3.1. Evaporation Process of the Saline-Alkali Soil. The evaporation of soil moisture is the process by which water enters the atmosphere from the soil surface, resulting in a decrease in the moisture content of the soil surface and gradual drying, leading to soil cracking, settlement deformation, soil salinization, and desertification. Especially for the embankment soil, evaporation and moisture content not only affect the cracking and deformation of the foundation but also lead to the cracking and subsidence of the pavement. The characteristics of the moisture content varying with the drying time are shown in Figure 2. The moisture content decreased with the drying time. During the first 120 h drying time, the moisture content decreased linearly with the drying time, and with the increase of the saline concentration, the moisture content of the soil was decreased to 65.39%, 62.75%, 61.94%, and 61.19%, respectively. It decreased slow down and presented the curve reduction during the drying time from 120 h to 225 h, and the moisture content was

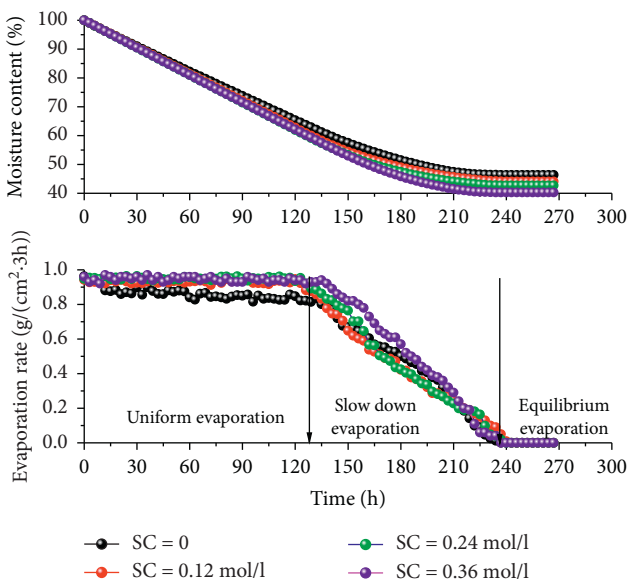

Figure 2: Moisture content and evaporation rate varying with drying time under different saline concentrations.

decreased to 46.57%, 44.58%, 43.07%, and 40.47%, respectively, with the increase of the saline concentration. After 225 h of the drying time, the moisture content of the soil gradually becomes steady and remain a value of 46.39%, 44.05%, 42.70%, and 40.27%, under the saline concentration of 0, 0.12, 0.24, and 0.36 mol/L, respectively. Moreover, the decrease trend of the moisture content gradually increases with the increase of the saline concentration, which indicated that saline may intensify water loss of the soil.

The evaporation was affected not only by the climate and the moisture content but also by the nature of the soil. During the drying time, the evaporation process with different saline concentrations in the soil can be divided into three stages: uniform evaporation stage, slow down evaporation stage, and equilibrium evaporation stage, as shown in Figure 2.

The initial soil sample was in a saturated state under the constant humidity and temperature conditions, which was characterized by uniform evaporation. The capillary water can completely supplement the water reduced by evaporation on the soil surface, which indicates that the evaporation force was greater than or close to the molecular force of water on the soil surface. The evaporation rate was steady in the first 120 h drying time which is consistent with the moisture content change. This indicates that the evaporation in this stage was controlled by the environmental conditions such as humidity and temperature. The average evaporation rate at this stage was about 0.86, 0.93, 0.95, and 0.95 g/(cm^2·3 h), respectively, under the saline concentrations of 0, 0.12, 0.24, and 0.36 mol/L. The evaporation rate decreases with the increase of time, and the soil moisture content continues to decrease with the increase of saline concentration. Due to the low moisture content, the penetration rate of the deep water to the surface of the sample was far behind the loss rate of the surface water molecules, and the water flow from the bottom to the surface of the sample was not enough to maintain a constant evaporation rate, which resulting the decrease of the evaporation rate.

When the moisture content dropped to a certain level, the evaporation began to slow down. Also, with the increase of the saline concentration, the duration of the slow down stage gradually decreased. During the drying time from 120 h to 240 h, the average evaporation rate was decreased to 0.45, 0.45, 0.46, and 0.53 g/(cm^2·3 h) with the increase of the saline concentration. Also, until 240 h of the drying time, the soil stopped evaporating, which was consistent with the change of the moisture content. These indicate that the soil moisture content gradually became a factor controlling the evaporation rate, while the effect of environmental conditions gradually weakens in the slow down stage. This stage will continue until the soil surface dries out.

When the moisture content drops below the ambient humidity, the evaporation and water absorption process was slowly balanced, showing the characteristics of slow equilibrium evaporation. The surface and inside of the soil are so dry that there is no or not enough water in the soil that can be transported to the surface, which leads to the termination of surface evaporation. The water in the soil evaporates and escapes through the dry surface through molecular diffusion. The water evaporation rate was very slow and mainly controlled by the soil moisture content below the surface and the soil water vapor pressure gradient. At this stage, the soil surface moisture content was equal to the residual moisture content, and the evaporation rate was 0. Also, the saline concentration has no significant effect on the evaporation rate.

3.2. Cracking Characteristics of the Soil under Different Saline Concentrations. The soil in nature consists of liquid, solid, and gas phases, which is a three-phase structure. The pores are filled with liquid water under the saturated state. Due to evaporation and water loss process, the liquid phase and the moisture content gradually decrease and then lead to the cracking on the soil surface. The developed cracks may become the preferential path for water migration and increase the permeability of the soil, resulting in a decrease in the mechanical strength of the soil and reducing the stability of the road subgrade. Figure 3 shows the cracks on the soil. With the development of the drying time, the cracks gradually appeared on the soil surface, gradually deepened in the soil, and expanded the crack network.

The effect of saline concentration on the degree of fracture development is significantly different. During the drying process, the decrease of the moisture content causes suction reduction and volume shrinkage of the soil body, which destroyed the skeleton structure and generates tensile stress due to the unevenness of the internal water loss and shrinkage of the soil body. The cracks will appear when the tensile stress exceeds the tensile strength of the soil. The fractal dimension can quantitatively characterize the degree of crack development. As shown in Figure 4, the cracks could not form during early drying which indicated that the fractal dimension was 0. Also, with the increase of the saline

Figure 3: Cracks on the soil surface.

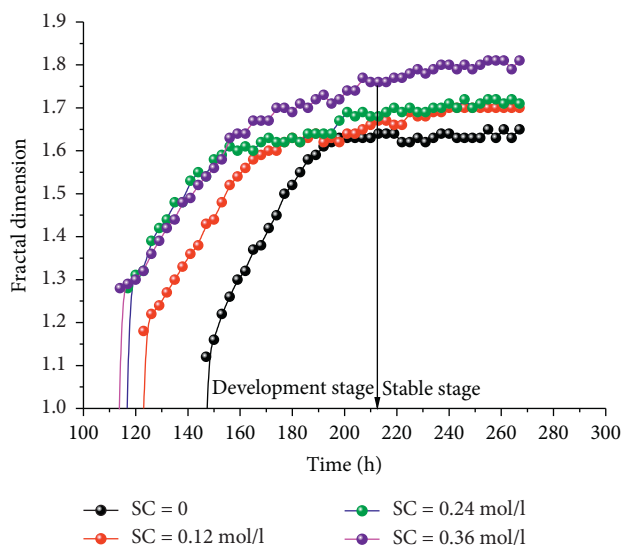

Figure 4: Fractal dimension varying with drying time under different drying times.

concentration, the cracking time was lagging. During the drying time of 100 h and 220 h, the fractal dimension gradually increased, and the higher the saline concentration, the longer the cracking time. After the drying time of 220 h, the fractal dimension remained unchanged as the cracks no longer developed. With the increase of the saline concentration, the final fractal dimension was gradually increased. According to the cracking characteristics, the development of cracks can be divided into three stages: the cracking preparation stage, the crack development stage, and the crack stable stage. With the increase of the saline concentration, the time for cracks to occur gradually decreases, and the time for cracks to develop gradually increases.

With the decrease of the moisture content, the tensile stress gradually increased and accumulated energy to crack readily. With the development of drying time, the cracks firstly appeared on the soil surface. Due to the suction in the soil, the adjacent cracks were connected and formed the main crack in the soil. The new cracks began to branch out from the main cracks, forming secondary cracks during the development stage. The branch cracks further developed in the large-area block formed by the secondary cracks, thereby forming a complete secondary crack network. During the stable phase of the development of the crack network, no new cracks appear on the soil surface even if the evaporation continues. As the drying continued, the existing cracks gradually expanded until they eventually stabilized. The surface crack network basically has no change in the surface crack network morphology, but the cracks widen and deepen.

4. Discussion

4.1. Relationships between the Fractal Dimension and Moisture Content and Evaporation Rate. Figure 5(a) shows the fractal dimension varying with the moisture content under different saline concentrations. With the decrease of the moisture content, the fractal dimension gradually

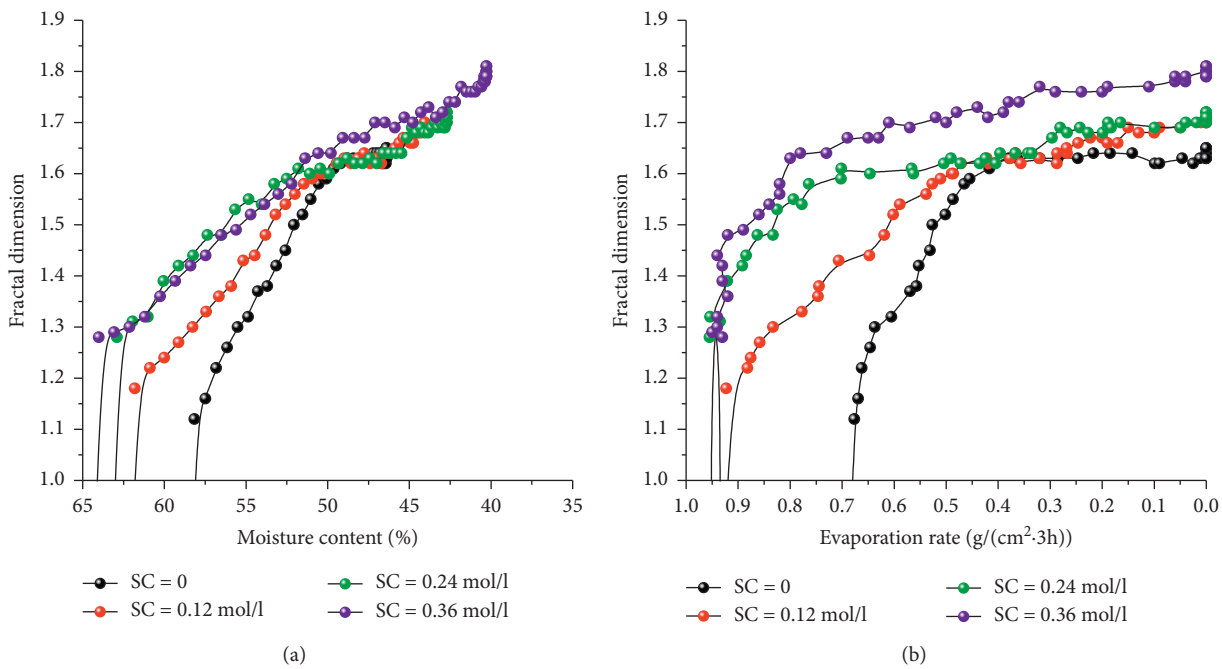

Figure 5: Fractal dimension varying with moisture content and evaporation rate under different saline concentrations. (a) Fractal dimension varying with moisture content. (b) Fractal dimension varying with evaporation rate.

increased. Also, the fractal dimension increased with the increase of the saline concentration, which indicated that the saline can promote the development of the cracks. The higher the evaporation rate was, the faster the fractal dimension developed, as shown in Figure 5(b). With the decrease of the evaporation rate, the fractal dimension was gradually stable. The cracking began at high evaporation rate under high saline concentration, and the fractal dimension remained stable under similar saline concentration, which indicated that the evaporation rate has little effect on the cracking during the stable stage.

4.2. Effect of Saline on the Moisture Content and Cracking Time. Figure 6 shows that the cracking moisture content and the cracking time increased with the saline concentration, while the residual moisture content decreased. The cracking moisture content was 58.16%, 61.8%, 62.9%, and 64.01%, respectively, under the saline concentrations of 0, 0.12, 0.24, and 0.36 mol/L, while the residual moisture content was 46.39%, 44.05%, 42.70%, and 40.27%, respectively. Results indicated that the saline reacted with the soil which reduced the hydrophilic properties and adsorbability of the soil, resulting in lower residual moisture content and longer cracking time. With the increase of the cracking time, the cementation between soil particles reduced which in turn promoted the development of cracks. The soil began to crack with the larger moisture under high saline concentration which indicated that saline can reduce the tensile strength of the soil and weaken the stability of the structure of the soil [27].

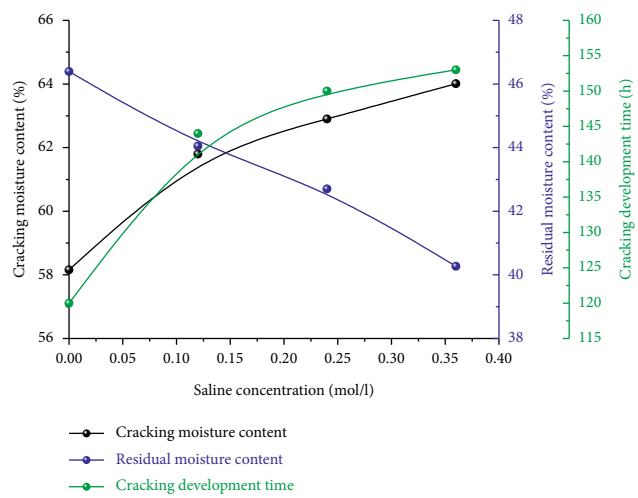

Figure 6: Cracking moisture content, residual moisture content, and cracking duration varying with saline concentration.

4.3. Effect of Saline on the Cracking Degree and Evaporation Rate. Figure 7 shows that maximum fractal dimension and the average evaporation rate increased with the increase of the saline concentration. During the crack stable stage, the maximum fractal dimension was 1.65, 1.7, 1.71, and 1.81, respectively, with the increase of the saline concentration, which indicated that the saline may aggravate the development of cracks and finally affect the stability of embankment soil. The saline in the soil may induce the disintegration of the soil aggregate structure which provided the space and channel for the water evaporation and lead to the high evaporation rate.

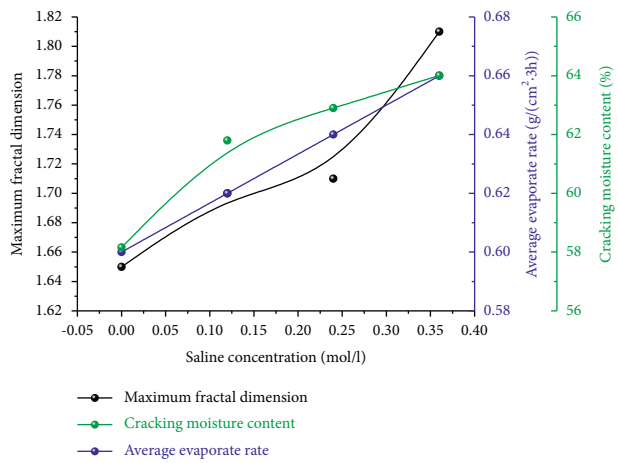

Figure 7: Maximum fractal dimension, average evaporation rate, and cracking moisture content varying with saline concentration.

(a) (b)

Figure 8: Drying cracks in the nature and the corresponding control measures. (a) Drying cracks in the nature. (b) Control measures for the cracks by tree planting.

The drying cracks were common in nature, as shown in Figure 8(a), which was consistent with the configuration of the cracks formed in the experimental results. The crack network was complicated and difficult to characterize, which was suitable for quantization of fractal dimension. In practical engineering processes, tree planting management was commonly used to control the crack development (Figure 8(b)), as the plant roots can effectively keep moisture from losing and reinforce the soil structure.

In the further study, the mechanical and microstructure mechanism of the saline soil affecting the cracking and evaporation characteristics should be addressed.

5. Conclusions

The saline in the soil significantly changed the evaporation characteristics of the soil and the development of dry cracks. The moisture content decreased linearly with the drying time in the early evaporation process, subsequently decreased slow down in the mid-term evaporation, and finally got steady and remain a value of 46.39%, 44.05%, 42.70%, and 40.27% with the increase of the saline concentration. The evaporation process with different saline concentrations in the soil can be divided into three stages: uniform evaporation stage, slow down evaporation stage, and equilibrium evaporation stage, which was consistent with the moisture content change. The evaporation rate was steady in the first 120 h drying time, then gradually slowed down when the moisture content dropped to a certain level, and finally stopped evaporating until the soil surface dried out when the moisture content dropped below the ambient humidity. The evaporation and water absorption processes were slowly balanced, showing the characteristics of slow equilibrium evaporation.

With the development of the drying time, the cracks gradually appeared on the soil surface, gradually deepened in the soil, and expanded the crack network. With the increase of the saline concentration, the final fractal dimension was gradually increased. The development of cracks can be divided into three stages: the cracking preparation stage, the crack development stage, and the crack stable stage. With the increase of the saline concentration, the time for cracks to occur gradually decreases, and the time for cracks to develop gradually increases. The fractal dimension was gradually

increased with the decrease of the moisture content and the increase of the saline concentration, respectively. The cracking began at high evaporation rate under high saline concentration, and the fractal dimension remained stable under similar saline concentration. The cracking moisture content was 58.16%, 61.8%, 62.9%, and 64.01%, respectively, under the saline concentrations of 0, 0.12, 0.24, and 0.36 mol/L. The soil began to crack with the larger moisture under high saline concentration. The drying cracks in the nature were consistent with the configuration of the cracks formed in the experimental results. Also, tree planting management was commonly used to control the crack development in practical engineering processes.

Data Availability

The datasets generated during the current study are available from the corresponding author upon reasonable request.

Conflicts of Interest

The authors declare that they have no conflicts of interest.

Acknowledgments

This study was supported by the Science and Technology Project of Henan Province under grant nos. 212102310596 and 212102310939 and the Henan College Students' Innovation and Entrepreneurship Training Program under grant no. S202110480034. The authors are grateful for the financial support.

References

[1] J. Li, L. Pu, M. Zhu, and R. Zhang, "The present situation and hot issues in the salt-affected soil research," *Acta Geographica Sinica*, vol. 67, no. 9, pp. 1233–1245, 2012.

[2] M. Tejada, C. Garcia, J. L. Gonzalez, and M. T. Hernandez, "Use of organic amendment as a strategy for saline soil remediation: influence on the physical, chemical and biological properties of soil," *Soil Biology and Biochemistry*, vol. 38, no. 6, pp. 1413–1421, 2006.

[3] D. Li, B. Yang, C. Yang, Z. Zhang, and M. Hu, "Effects of salt content on desiccation cracks in the clay," *Environmental Earth Sciences*, vol. 80, no. 19, pp. 1–13, 2021.

[4] B. Yang and J. Yuan, "Influence of soda content on desiccation cracks in clayey soils," *Soil Science Society of America Journal*, vol. 83, no. 4, pp. 1054–1061, 2019.

[5] C.-S. Tang, Y.-J. Cui, B. Shi, A.-M. Tang, and C. Liu, "Desiccation and cracking behaviour of clay layer from slurry state under wetting-drying cycles," *Geoderma*, vol. 166, no. 1, pp. 111–118, 2011.

[6] N. An, C.-S. Tang, S.-K. Xu, X.-P. Gong, B. Shi, and H. I. Inyang, "Effects of soil characteristics on moisture evaporation," *Engineering Geology*, vol. 239, pp. 126–135, 2018.

[7] Z. Xiao, Y. Lai, and M. Zhang, "Study on the freezing temperature of saline soil," *Acta Geotechnica*, vol. 13, no. 1, pp. 195–205, 2018.

[8] X. Zhang, S. Liu, Q. Wang et al., "Experimental investigation of water migration characteristics for saline soil," *Polish Journal of Environmental Studies*, vol. 28, no. 3, pp. 1495–1505, 2019.

[9] B. Bai, Q. Nie, Y. Zhang, X. Wang, and W. Hu, "Cotransport of heavy metals and SiO2 particles at different temperatures by seepage," *Journal of Hydrology*, vol. 597, Article ID 125771, 2021.

[10] B. Bai, G.-C. Yang, T. Li, and G.-S. Yang, "A thermodynamic constitutive model with temperature effect based on particle rearrangement for geomaterials," *Mechanics of Materials*, vol. 139, Article ID 103180, 2019.

[11] B. Yang, D. Li, S. Yuan, and L. Jin, "Role of biochar from corn straw in influencing crack propagation and evaporation in sodic soils," *Catena*, vol. 204, Article ID 105457, 2021.

[12] B. Yuan, Z. Li, Z. Zhao, H. Ni, Z. Su, and Z. Li, "Experimental study of displacement field of layered soils surrounding laterally loaded pile based on transparent soil," *Journal of Soils and Sediments*, vol. 21, no. 9, pp. 3072–3083, 2021.

[13] B. Yuan, Z. Li, Y. Chen et al., "Mechanical and microstructural properties of recycling granite residual soil reinforced with glass fiber and liquid-modified polyvinyl alcohol polymer," *Chemosphere*, vol. 286, Article ID 131652, 2022.

[14] Q. Cheng, C.-S. Tang, D. Xu, H. Zeng, and B. Shi, "Water infiltration in a cracked soil considering effect of drying-wetting cycles," *Journal of Hydrology*, vol. 593, Article ID 125640, 2021.

[15] C.-S. Tang, D.-Y. Wang, B. Shi, and J. Li, "Effect of wetting-drying cycles on profile mechanical behavior of soils with different initial conditions," *Catena*, vol. 139, pp. 105–116, 2016.

[16] B. Yang, J. Liu, X. Zhao, and S. Zheng, "Evaporation and cracked soda soil improved by fly ash from recycled materials," *Land Degradation & Development*, vol. 32, no. 9, pp. 2823–2832, 2021.

[17] B. Yang, K. Xu, and Z. Zhang, "Mitigating evaporation and desiccation cracks in soil with the sustainable material biochar," *Soil Science Society of America Journal*, vol. 84, no. 2, pp. 461–471, 2020.

[18] J. Ren, X. Li, and K. Zhao, "Quantitative analysis of relationships between crack characteristics and properties of soda-saline soils in Songnen Plain, China," *Chinese Geographical Science*, vol. 25, no. 5, pp. 591–601, 2015.

[19] C. Liu, C.-S. Tang, B. Shi, and W.-B. Suo, "Automatic quantification of crack patterns by image processing," *Computers & Geosciences*, vol. 57, pp. 77–80, 2013.

[20] B. Liu, C. Zhu, C.-S. Tang et al., "Bio-remediation of desiccation cracking in clayey soils through microbially induced calcite precipitation (MICP)," *Engineering Geology*, vol. 264, Article ID 105389, 2020.

[21] C.-S. Tang, D.-Y. Wang, C. Zhu, Q.-Y. Zhou, S.-K. Xu, and B. Shi, "Characterizing drying-induced clayey soil desiccation cracking process using electrical resistivity method," *Applied Clay Science*, vol. 152, pp. 101–112, 2018.

[22] J. H. Li and L. M. Zhang, "Study of desiccation crack initiation and development at ground surface," *Engineering Geology*, vol. 123, no. 4, pp. 347–358, 2011.

[23] C.-S. Tang, B. Shi, Y.-J. Cui, C. Liu, and K. Gu, "Desiccation cracking behavior of polypropylene fiber-reinforced clayey soil," *Canadian Geotechnical Journal*, vol. 49, no. 9, pp. 1088–1101, 2012.

[24] Y. Zhang, K. Gu, J. Li, C. Tang, Z. Shen, and B. Shi, "Effect of biochar on desiccation cracking characteristics of clayey soils," *Geoderma*, vol. 364, Article ID 114182, 2020.

[25] B. Yang, Z. Zhang, W. Ma, M. Hu, and Y. Zhang, "Effect of tea waste on cracking of foundation soil," *Advances in Civil Engineering*, vol. 2021, Article ID 7525811, 7 pages, 2021.

[26] B. Yang, S. Du, X. Zhao, D. Tang, and C. Yang, "Decision making of curriculum attainment degree for engineering geology based on fuzzy set theory," *Advances in Civil Engineering*, vol. 2021, Article ID 1743778, 6 pages, 2021.

[27] B. Yuan, M. Sun, L. Xiong, Q. Luo, and H. Li, "Investigation of 3d deformation of transparent soil around a laterally loaded pile based on a hydraulic gradient model test," *Journal of Building Engineering*, vol. 28, no. 6, Article ID 101024, 2019.

Hindawi
Advances in Civil Engineering
Volume 2021, Article ID 1936635, 7 pages
https://doi.org/10.1155/2021/1936635

Research Article

Three-Dimensional Stochastic Seepage Field Analysis of Multimedia Embankment

Xiaoming Zhao,[1,2] **Shiyu Shang**,[1] **Yuanlin Yang**,[1] **and Mingming Hu**[1]

[1]*School of Civil Engineering, Xuchang University, Xuchang, Henan 461000, China*
[2]*The Scientific Research Innovation Team of Xuchang University, Xuchang, China*

Correspondence should be addressed to Xiaoming Zhao; zhaoxiaoming@xcu.edu.cn

Received 12 November 2021; Revised 26 November 2021; Accepted 27 November 2021; Published 15 December 2021

Academic Editor: Bingxiang Yuan

The soil hydraulic conductivity of an embankment has strong spatial variability due to the spatiotemporal variation, both natural and artificial. The strong randomness of the hydraulic conductivity can be expressed by the coefficient of variation (COV) and the fluctuation scale θ. Moreover, different coefficients of variation and fluctuation scales correspond to different random field structures. To study the characteristics of the three-dimensional stochastic seepage field in an embankment under different COVs and fluctuation scales, we generate a three-dimensional random field of the hydraulic conductivity of multimedia embankment based on the local average subdivision technique. In particular, a calculation method for a three-dimensional random seepage field based on the Monte Carlo method combined with a three-dimensional multimedia random field and a deterministic analysis is proposed. The results showed that after three thousand realizations and considering the randomness of the hydraulic conductivity, the position of the free surface of each section in the embankment differed. The mean value of the total head decreased when the COV increased. Furthermore, when the COV was small, the change in the total head with anisotropy ratio was not evident, while the COV was large. The mean value of the total head increased with the anisotropy ratio. When the anisotropy ratio increased, the mean value of the standard deviation of the total head increased first and then decreased.

1. Introduction

Research problems related to geotechnical engineering present uncertainties and randomness. For instance, due to the spatiotemporal variation, both natural and artificial, the soil hydraulic conductivity of an embankment has strong spatial variability. In this regard, the study of random field theory appeared earlier in the mathematics and physics fields. From these fields, a particular fast Fourier transform algorithm proposed by Cooley and Tukey has been used to generate random fields [1]. Moreover, Matheron proposed the Turning Bands Method (TBM) to generate a random field [2], and the accuracy of the random field generated by the TBM method was closely related to the number of lines. Moreover, Mantoglou and Wilson developed the TBM random field theory [3] and used this method to simulate various random fields. Vanmarcke [4–6] proposed the local average random field theory in which the local mean value and standard deviation of random variables represented the variation characteristics of the random field in this space. Fenton proposed a random field generation method based on the local average subdivision (LAS) technique [7, 8]. For one-dimensional or two-dimensional random variables, given the probability density function and statistical parameters, such as mean, standard deviation, and fluctuation scale, the random field comprising regular quadrilateral elements could be generated in a rectangular region in one-dimensional or two-dimensional space. This random field generation technique has the advantages of fast convergence and low theoretical error.

Fenton systematically introduces the basic theory of random field and common random field generation methods. It is found that most errors are related to the accuracy of covariance [9–11]. Zhu et al. studied the reliability of undrained slope by using the stochastic finite element method. The research focuses on the spatial

fluctuation scale in the worst case, that is, the fluctuation scale when the slope failure probability reaches its maximum value. The results show that the worst case is most likely to occur when the average safety factor is low or the coefficient of variation is high [12]. Based on the random field of soil hydraulic conductivity, taking the hydraulic conductivity as a spatial random field variable subject to lognormal distribution, the free surface seepage of a gravity dam is analyzed by the Monte Carlo method [13]. Then, the mean and variance of the total velocity in the gravity dam are obtained. Ahmed [14, 15] considered that the probability density function of hydraulic conductivity obeys lognormal distribution, and the random method is used to analyze the free surface seepage of the gravity dam. The results show that the flow rate in random analysis is smaller than that in deterministic analysis, and the height of free surface in random analysis is lower than that in deterministic analysis. The flow rate and hydraulic gradient have a certain correlation with the COV and fluctuation scale [16, 17]. Literature [18–21] also studied the stable seepage with a random method and obtained similar conclusions. Soil cracking will affect seepage and evaporation [22–25]; then, the stress field and displacement field of other engineering such as pile foundation and slope will be affected [26–31].

The spatial variability of soil hydraulic conductivity changes the distribution of streamline and equipotential line of the seepage field. Compared with deterministic analysis, the elevation of the overflow point, total head, seepage force, and flow have changed significantly, which brings additional risks. In order to improve the accuracy in predicting the risk probability of seepage instability, we need to improve the understanding of the random seepage field of the embankment. In this study, considering the strong variability of embankment soil hydraulic conductivity, a three-dimensional multimedia random field is generated based on the local average subdivision technique, and a calculation method for a three-dimensional random seepage field of an embankment based on the Monte Carlo method combined with a three-dimensional multimedia random field and a deterministic seepage field analysis method is proposed.

2. The Random Field Model of Hydraulic Conductivity

When obtaining random seepage fields, the probability density function of the soil hydraulic conductivity is often considered that follows the lognormal distribution [32–36]. Assume that the mean value of a random field of hydraulic conductivity is μ_k and the variance is σ_k^2; thus, ln k obeys the normal distribution with a mean value of $\mu_{\ln k}$ and a variance of $\sigma_{\ln k}^2$, as shown in the following equation:

$$\begin{aligned} \sigma_{\ln k}^2 &= \ln\left(1 + \frac{\sigma_k^2}{\mu_k^2}\right) \\ \mu_{\ln k} &= \ln(\mu_k) - \frac{1}{2}\sigma_{\ln k}^2. \end{aligned} \tag{1}$$

The hydraulic conductivity of the saturated seepage unit can be obtained using the following equation:

$$k_i = \exp(\mu_{\ln k} + \sigma_{\ln k} g_i), \tag{2}$$

in which k_i is the hydraulic conductivity assigned to the ith unit in the random field and g_i is the local average of a standard Gaussian random field over the domain of the ith unit.

Considering the characteristics of a Gauss–Markov process, the exponential correlation function is selected, which can be written as follows:

$$\rho(\tau) = \exp\left(-\frac{2}{\theta}|\tau|\right), \tag{3}$$

where τ is the distance between any points in the random field and θ is the fluctuation scale of variables in the random field. The fluctuation scale is the distance over which points in the random field are significantly correlated.

The three-dimensional multimedia random field model is generated based on the LAS technique. The Monte Carlo stochastic finite element analysis method was used combined with the deterministic finite element analysis method of the seepage field to analyze the seepage problem several times. According to the statistics of the results, the distribution law of the overflow point elevation and the mean and variance of the total water head in the seepage field were obtained. When the three-dimensional random field was discretized, the value of the COV could be set to change from small to large so that the variation law of each response of the seepage field when the COV changes could be reflected in the random analysis. At the same time, in order to reflect the differences between the random field method and the random variable method, different fluctuation scales can be selected to analyze the variation law of response. The distribution law of the overflow point elevation and the mean and variance of the total water head in the seepage field is obtained.

3. Numerical Calculation Model

The simplified model of a section of Shijiu Lake embankment, located in Nanjing City, Jiangsu Province, and its section is shown in Figure 1. The model is 36 m along the embankment axis. Moreover, the embankment foundation is 144 m wide in the X direction and 24 m high in the Z direction. The foundation is divided into two layers. The upper layer is a relatively thin, heavy silty soil layer with a thickness of 4 m, and the lower layer is a muddy, silty fine sand layer with a thickness of 20 m. The bottom of the embankment is 54 m wide, 8 m high, and 6 m wide at the top of the embankment. The slopes on both sides are graded according to the slope of 1 : 3. During the mesh generation of the model, considering the influence of calculation accuracy and size effect, the mesh size of the embankment body is determined to be 3 m × 1 m × 3 m in the XYZ direction, respectively, foundation 1 is determined to be 3 m × 1 m × 3 m in the XYZ direction, respectively, and foundation 2 is determined to be 3 m × 3.33 m × 3 m in the

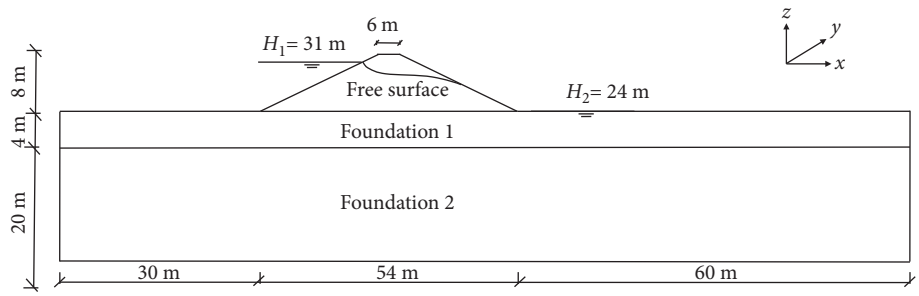

Figure 1: Dimension of the embankment.

XYZ direction, respectively. There are 7,488 units and 8,983 nodes in total. In the analysis, considering the randomness of layered soil parameters, the hydraulic conductivity is regarded as a random field variable of anisotropic heterogeneity. The random field of hydraulic conductivity has correlation only in a single soil layer, different soil layers are independent of each other, and their hydraulic conductivity values are independent in the *XYZ* direction.

The boundary conditions are as follows: the upstream water level elevation was 31 m, the downstream water level elevation was 24 m, and the bottom of the model and the boundaries on both sides are impervious.

When the water flows through the unit with large hydraulic conductivity, the water head decreases slightly. In contrast, when it flows through the unit with small hydraulic conductivity, the water head decreases greatly. When mapping the hydraulic conductivity random field to the embankment model with equation (2), the hydraulic conductivity of each element in the model is uncertain. A realization refers to a single generation of the hydraulic conductivity random field and the subsequent finite element analysis of the seepage field with ABAQUS. A Monte Carlo process involves a large number of realizations that eventually enable statistical statements to be made about the output quantities of the three-dimensional seepage. After 3,000 independent realizations, the results are statistically analyzed, and the variation law of the three-dimensional random seepage field of the embankment is obtained.

In this study, soil samples are obtained by in situ drilling, and then indoor permeability test is conducted for samples in the same soil layer. Table 1 lists the values of hydraulic conductivity at different parts of the embankment. Based on the three-dimensional multimedia random field model, different COVs and fluctuation scales are selected. For the two soil layers of the embankment foundation, the geometric size as shown in Figure 1 is used to discrete the random field. For the embankment body, a random field is generated in a larger three-dimensional space and finally mapped to the embankment body; then, a complete three-dimensional multimedia random field model of the embankment is established.

The hydraulic conductivity of the random field is statistically analyzed. Figures 2 and 3 show the frequency distribution of the hydraulic conductivity of the embankment body and foundation, respectively. As seen in the figures, both coefficients follow the normal distribution and satisfy the spatial distribution characteristics of the hydraulic conductivity. In Figure 2, the value range of the logarithmic hydraulic conductivity is from −15.2 to −19.7. In Figure 3,

Table 1: Hydraulic conductivity of the embankment soil.

Soil	Mean hydraulic conductivity (cm/s)		
	X	*Y*	*Z*
Embankment body	$3.32E-06$	$3.32E-06$	$6.64E-07$
Foundation 1	$1.81E-06$	$1.81E-06$	$4.525E-07$
Foundation 2	$2.26E-05$	$2.26E-05$	$1.13E-05$

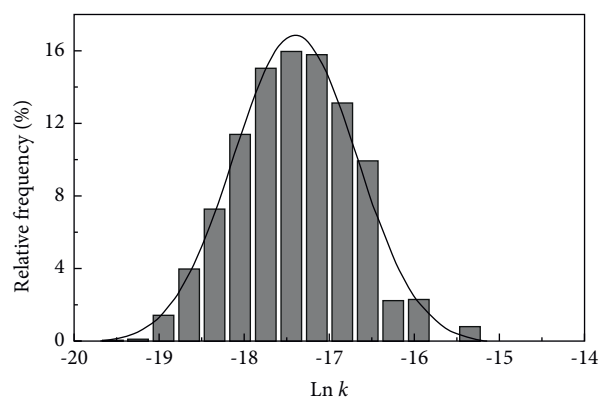

Figure 2: Probability density distribution of the hydraulic conductivity in the embankment body.

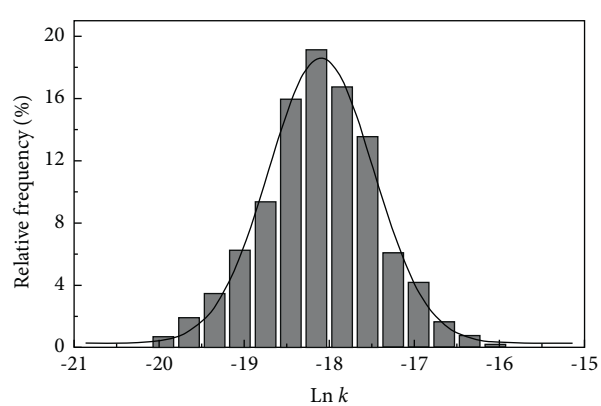

Figure 3: Probability density distribution of the hydraulic conductivity in the foundation.

the value range of the logarithmic hydraulic conductivity is from −15.1 to −20.9. Obviously, compared with the statistical value of the hydraulic conductivity in the embankment body, the value in the embankment foundation has a wider range. The reason may be that when mapping the hydraulic conductivity of the embankment body, the shape of the embankment is trapezoidal. Elements outside the trapezoidal contour do not participate in random field mapping, and because the upper unit of the embankment body is small, the hydraulic conductivity of the two adjacent units may be the same.

In this study, the hydraulic conductivity is regarded as a random field variable, considering that the embankment has the characteristics of long existence period and obvious layered distribution. Soil parameters have strong variability, so the value range of COV of hydraulic conductivity is large. The hydraulic conductivity is regarded as obeying lognormal distribution, and the COV is taken as 0.1, 0.3, 0.5, 0.7, 1.0, 2.0, and 3.0, respectively. Due to the obvious layered distribution of the embankment in the vertical direction and the long time interval between the formation ages of different soil layers, the correlation of soil parameters between different soil layers is weak.

Generally speaking, the fluctuation scale of hydraulic conductivity in the horizontal plane is much higher than that in the vertical direction. In this study, the vertical fluctuation scale is fixed to 3 m, and the horizontal fluctuation scale is fixed to 3 m, 6 m, 12 m, 24 m, 36 m, and 48 m. The anisotropy ratio ζ can be obtained using the following equation:

$$\zeta = \frac{\theta_h}{\theta_v}, \tag{4}$$

where θ_h is the scale of fluctuation in the horizontal plane and θ_v is the scale of fluctuation in the vertical direction.

4. Results

4.1. Free Surface. The main purpose of this section is to obtain the variation law of random seepage field response with COV and fluctuation scale. In order to reflect the influence of COV and fluctuation scale better, it is often changed gradually from small to large in the analysis, and then the curve of random seepage field response with it is obtained. In embankment engineering, the COV and fluctuation scale of different soil layers in a section are certain values, which can be determined by the combination method of experiment and numerical analysis. Based on the results of stochastic finite element analysis of embankment, the mean and standard deviation of free surface position and total head are statistically analyzed, and their distribution laws under different COVs and fluctuation scale combinations are obtained.

Figure 4 shows the free surface calculated in a single time when the COV was 0.3, the vertical fluctuation scale was 3 m, and the horizontal fluctuation scale was 6 m. Moreover, the figure also shows that, due to the spatial variability of the hydraulic conductivity, the overflow point is not a straight line along the embankment axis. Instead, the overflow point fluctuates up and down, similarly to the actual observation. Furthermore, at different embankment sections, the distribution of free surface and the elevation of the overflow point are different. Therefore, when analyzing the seepage stability of the embankment, considering the spatial variability of hydraulic conductivity reflected the actual situation better. The results obtained are sounded. Moreover, they provide novel insights for engineering practice purposes.

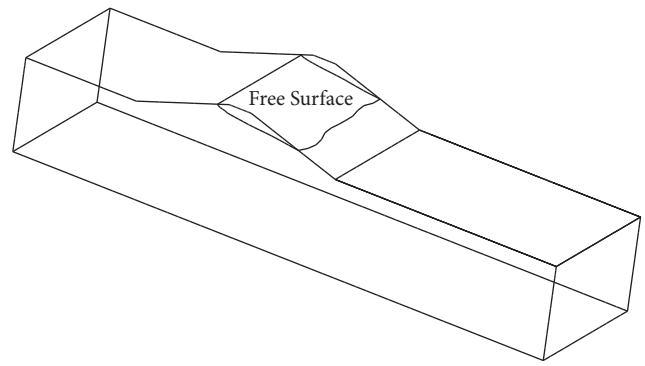

Figure 4: Free surface of three-dimensional random seepage field.

4.2. Random Characteristics of the Total Head. Figure 5 shows that the contour map of the standard deviation of the total head is unevenly distributed, mainly due to the small hydraulic conductivity of the embankment Foundation 1 and the large change of the total head in this soil layer. The slope of the curve varies at the boundary of different soil layers, which agree with the general law of seepage. From the upstream slope to downstream slope, the contour map of the head standard deviation has experienced a process from small to large and then from large to small. The minimum value appears near the upstream slope and downstream slope, and the maximum value appears in the middle of the embankment. The author believes that the reason for this distribution law is that, at the beginning of the analysis, fixed boundary conditions on both sides of the embankment should be given, respectively, that is, at the upstream and downstream boundaries, the standard deviation of the water head is 0. Some studies have obtained similar results under different COVs and fluctuation scales in the stochastic finite element analysis of pressurized seepage [37, 38]. In conclusion, considering the influence of random factors, the standard deviation of the water head reaches the maximum value near the embankment center and gradually decreases to both sides of the model. On the surface of the model, the standard deviation is 0.

In practice, the distribution of the water head in the embankment is the key point to solve other problems. The water head distribution directly affects the distribution of hydraulic gradient and flow rate at each section. Due to the importance of water head distribution, this section analyzes the influence of different COVs and fluctuation scales on water head.

Figure 6 shows the relationship between the mean value of the total head and the COV of the hydraulic conductivity

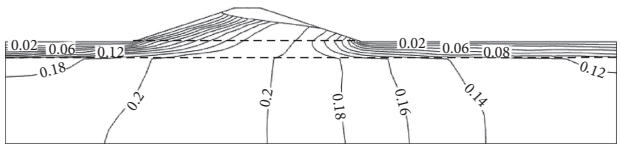

Figure 5: Contour map of the standard deviation of the total head.

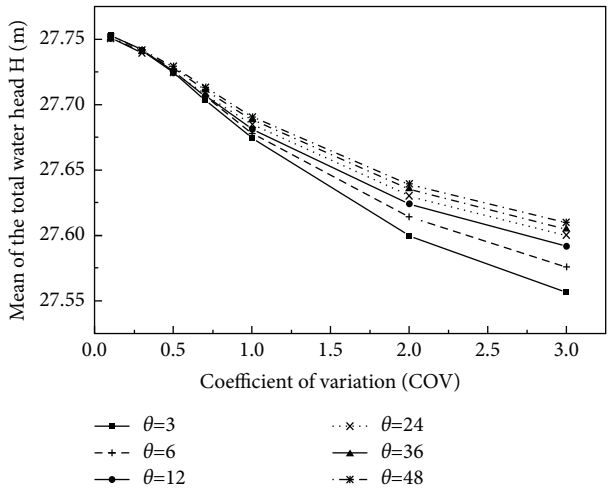

Figure 6: Mean of the total head versus COV of the hydraulic conductivity.

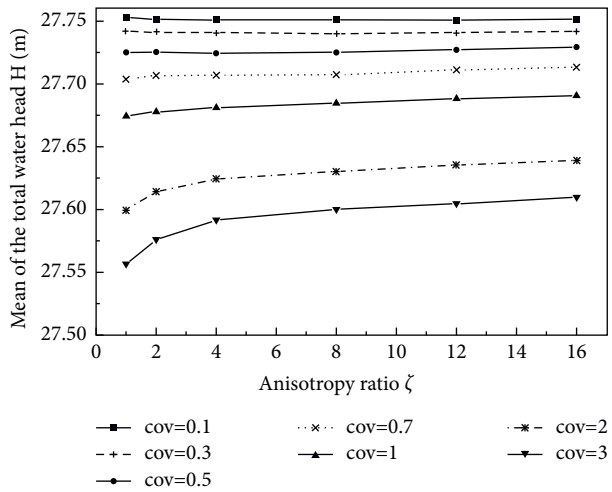

Figure 7: Mean of the total head versus anisotropy ratio of hydraulic conductivity.

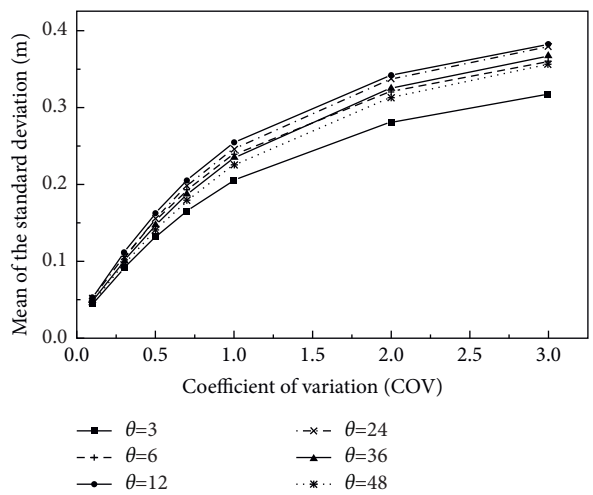

Figure 8: Mean of the total head standard deviation versus COV of the hydraulic conductivity.

at each node in the model. The results indicate that the gradual increase in the COV reduces the mean value of node total head shows. When $\text{cov} \leq 0.3$, the curve slope is relatively small, and the mean value of the total head decreases slowly; when $0.3 < \text{cov} \leq 2$, the slope of the curve is large, and accordingly, the reduction rate of the mean head value is large; when $\text{cov} > 2$, the slope of the curve decreases gradually. Similarly, the rate of reduction of the mean value of the total head also decreases gradually. When the mean value of the total head is large, the overall head distribution in the model is at a high level, which means that when the average value of the node head is high, the overflow point will also be at a higher position and when the mean value of the node head is small, the overflow point will also appear at the lower position on downstream slope.

Figure 7 shows the relationship between the mean value of the total head and the anisotropy ratio of the random field at each node in the model. When the COV is small, the mean value of the total head hardly changes with the increase in the anisotropy ratio. When the COV is large, the value increases notably with the increase in the anisotropy ratio. Moreover, when $1 \leq \zeta \leq 4$, the mean value of the total head increases rapidly, and when $\zeta > 4$, the growth rate of H decreases significantly. In general, the curve shape is similar to the power function form of the exponent in the (0, 1) interval, implying that when the anisotropy ratio reaches a certain degree, obtaining the accurate value of the horizontal fluctuation scale for calculation is not required, and the approximate solution of the relevant problem can be obtained for $\zeta = \infty$. Because the average head distribution can reflect the distribution law of the overflow point elevation to a certain extent, it can be concluded that when the COV is small, the overflow point elevation changes little with the increase in the anisotropy ratio of the random field and when the COV is large, the elevation of the overflow point changes obviously with the change in anisotropy ratio, and the elevation increase rate appears first fast and then slow.

Figure 8 shows the mean value variation curve of the standard deviation of the total head with the COV of the hydraulic conductivity. The figure shows that the mean value of the standard deviation of the total head increases with an increase in the COV of the hydraulic conductivity. Furthermore, the curve slope decreases gradually, indicating that when the COV is small, the mean value of standard deviation is more sensitive to the COV, and the sensitivity decreases with the gradual increase in the COV. Note that the order of the horizontal fluctuation scale represented in each curve is inconsistent with that shown in the legend, indicating that the mean value of the standard deviation of

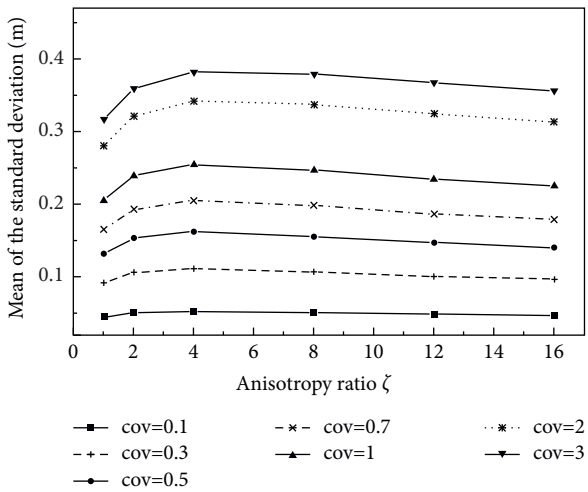

Figure 9: Mean of the total head standard deviation versus anisotropy ratio of hydraulic conductivity.

the total head does not show a consistent law under a specific fluctuation scale.

Figure 9 shows the variation curve of the mean value of the standard deviation of the total head with the anisotropy ratio. The trend of each curve is evident. First, the curves increase and then decrease. The maximum mean value of the standard deviation basically appears at $\zeta = 4$. In particular, when $\zeta \leq 4$, the mean value of the standard deviation of the total head increases with the anisotropy ratio. In contrast, for $\zeta > 4$, the mean value of head standard deviation decreases with an increase in the anisotropy ratio. Approximate results are mentioned in some research studies [13, 39], but the extreme points are different. Also, literature [17] shows that approximate phenomena can be found in soil by observation.

5. Conclusion

In this research, the influence of strong randomness of embankment soil hydraulic conductivity is studied, a three-dimensional multimedia permeability random field is generated, and a Monte Carlo process involves 3,000 realizations that are used to solve the three-dimensional random seepage field of the embankment. Based on this study, the following conclusions can be drawn:

(1) Considering the randomness of the hydraulic conductivity, the position of the free surface of each section in the embankment was different.

(2) The maximum standard deviation of the total head appears near the embankment center. When the total head approaches the outer boundary, the standard deviation decreases rapidly. When the COV increases, the mean value of the total head decreases significantly, and the standard deviation of the total head increases significantly.

(3) When the anisotropy ratio was $1 \leq \zeta \leq 4$, the mean value of the total head increases. In contrast, when the anisotropy ratio was $\zeta > 4$, the growth rate reduces.

(4) When the COV was small, the fluctuation scale less affected the mean and standard deviation of the water head. In contrast, when the COV increases, the effect of the fluctuation scale increases significantly, and the standard deviation of the total water head increases first and then decreases with the increase in the fluctuation scale.

Data Availability

The datasets generated during the current study are available from the corresponding author on reasonable request.

Conflicts of Interest

The authors declare no conflicts of interest.

Acknowledgments

The authors would like to acknowledge financial support from Key Scientific Research Projects of Colleges and Universities in Henan Province under Grant number (22B570002), Henan College Students' Innovation And Entrepreneurship Training Program under Grant no. (S202110480034), and Key Scientific Research in Xuchang University under Grant number (2021HX157).

References

[1] J. W. Cooley and J. W. Tukey, "An algorithm for the machine calculation of complex fourier series," *Mathematics of Computation*, vol. 19, no. 90, pp. 297–301, 1965.

[2] G. Matheron, "The intrinsic random functions and their applications," *Advances in Applied Probability*, vol. 5, no. 3, pp. 439–468, 1973.

[3] A. Mantoglou and J. L. Wilson, *Simulation of Random fields with the Turning Bands Method*, Ralph M. Parsons Laboratory Hydrology and Water Resources Systems, Cambridge, MA, USA, 1981.

[4] E. H. Vanmarcke, *Random Fields: Analysis and Synthesis*, World Scientific, Singapore, 1983.

[5] E. Vanmarcke and M. Grigoriu, "Stochastic finite element analysis of simple beams," *Journal of Engineering Mechanics*, vol. 109, no. 5, pp. 1203–1214, 1983.

[6] E. H. Vanmarcke and G. A. Fenton, "Conditioned simulation of local fields of earthquake ground motion," *Structural Safety*, vol. 10, no. 1–3, pp. 247–264, 1991.

[7] G. A. Fenton, *Simulation and Analysis of Random fields*, Princeton University, New Jersey, NJ, USA, 1990.

[8] G. A. Fenton and E. H. Vanmarcke, "Simulation of random fields via local average subdivision," *Journal of Engineering Mechanics*, vol. 116, no. 8, pp. 1733–1749, 1990.

[9] G. A. Fenton and D. V. Griffiths, "Random field generation and the local average subdivision method," *Probabilistic Methods in Geotechnical Engineering*, pp. 201–223, Springer, Berlin, Germany, 2007.

[10] G. A. Fenton and D. V. Griffiths, "The random finite element method (RFEM) in bearing capacity analyses," *Probabilistic Methods in Geotechnical Engineering*, pp. 295–315, Springer Vienna, Berlin, Germany, 2007.

[11] G. A. Fenton and D. V. Griffiths, "Review of probability theory, random variables, and random fields," *Probabilistic*

Methods in Geotechnical Engineering, pp. 1–69, Springer Vienna, Berlin, Germany, 2007.

[12] D. Zhu, D. V. Griffiths, and G. A. Fenton, "Worst-case spatial correlation length in probabilistic slope stability analysis," *Géotechnique*, vol. 69, no. 1, pp. 85–88, 2019.

[13] G. A. Fenton and D. V. Griffiths, "Statistics of free surface flow through stochastic earth dam," *Journal of Geotechnical Engineering*, vol. 122, no. 6, pp. 427–436, 1996.

[14] A. A. Ahmed, "Saturated-unsaturated flow through leaky dams," *Journal of Geotechnical and Geoenvironmental Engineering*, vol. 134, no. 10, pp. 1564–1568, 2008.

[15] A. A. Ahmed and A. S. Bazaraa, "Three-dimensional analysis of seepage below and around hydraulic structures," *Journal of Hydrologic Engineering*, vol. 14, no. 3, pp. 243–247, 2009.

[16] A. A. Ahmed, "Stochastic analysis of free surface flow through earth dams," *Computers and Geotechnics*, vol. 36, no. 7, pp. 1186–1190, 2009.

[17] A. A. Ahmed, "Stochastic analysis of seepage under hydraulic structures resting on anisotropic heterogeneous soils," *Journal of Geotechnical and Geoenvironmental Engineering*, vol. 139, no. 6, pp. 1001–1004, 2013.

[18] C. L. Winter and D. M. Tartakovsky, "Groundwater flow in heterogeneous composite aquifers," *Water Resources Research*, vol. 38, no. 8, pp. 23–11, 2002.

[19] J. H. He, "Approximate analytical solution for seepage flow with fractional derivatives in porous media," *Computer Methods in Applied Mechanics and Engineering*, vol. 167, no. 1-2, pp. 57–68, 1998.

[20] C. Chuanmiao and H. Hongling, "Global existence of real roots and random Newton flow algorithm for nonlinear system of equations to memorize Qin's method for 770 anniversaries," *Science China Mathematics*, vol. 60, no. 7, pp. 1–12, 2017.

[21] L. Smith and R. A. Freeze, "Stochastic analysis of steady state groundwater flow in a bounded domain: 2. two-dimensional simulations," *Water Resources Research*, vol. 15, no. 6, pp. 1543–1559, 1979.

[22] B. Yang, D. Li, S. Yuan, and L. Jin, "Role of biochar from corn straw in influencing crack propagation and evaporation in sodic soils," *Catena*, vol. 204, Article ID 105457, 2021.

[23] B. Yang, J. Liu, X. Zhao, and S. Zheng, "Evaporation and cracked soda soil improved by fly ash from recycled materials," *Land Degradation & Development*, vol. 32, no. 9, pp. 2823–2832, 2021.

[24] B. Yang, K. Xu, and Z. Zhang, "Mitigating evaporation and desiccation cracks in soil with the sustainable material biochar," *Soil Science Society of America Journal*, vol. 84, no. 2, pp. 461–471, 2020.

[25] B. B. Yang, S. Yuan, Y. Liang, and J. Liu, "Investigation of overburden failure characteristics due to combined mining: case study, Henan Province, China," *Environmental Earth Sciences*, vol. 80, no. 4, p. 143, 2021.

[26] B. Yuan, Z. Li, Z. Zhao, H. Ni, Z. Su, and Z. Li, "Experimental study of displacement field of layered soils surrounding laterally loaded pile based on transparent soil," *Journal of Soils and Sediments*, vol. 21, no. 9, pp. 3072–3083, 2021.

[27] B. X. Yuan, Z. H. Li, Z. L. Su, Q. Z. Luo, M. J. Chen, and Z. Q. Zhao, "Sensitivity of multistage fill slope based on finite element model," *Advances in Civil Engineering*, vol. 2021, Article ID 6622936, 13 pages, 2021.

[28] B. Yuan, Z. H. Li, Y. Chen et al., "Mechanical and microstructural properties of recycling granite residual soil reinforced with glass fiber and liquid-modified polyvinyl alcohol polymer – sciencedirect," *Chemosphere*, vol. 268, Article ID 131652, 2021.

[29] Y. Wu, J. Cui, J. Huang, W. Zhang, N. Yoshimoto, and L. Wen, "Correlation of critical state strength properties with particle shape and surface fractal dimension of clinker ash," *International Journal of Geomechanics*, vol. 21, no. 6, Article ID 04021071, 2021.

[30] B. Bai, Q. Nie, Y. Zhang, X. Wang, and W. Hu, "Cotransport of heavy metals and SiO_2 particles at different temperatures by seepage," *Journal of Hydrology*, vol. 597, Article ID 125771, 2021.

[31] B. Bai, G.-c. Yang, T. Li, and G.-s. Yang, "A thermodynamic constitutive model with temperature effect based on particle rearrangement for geomaterials," *Mechanics of Materials*, vol. 139, Article ID 103180, 2019.

[32] R. A. Freeze, "Influence of the unsaturated flow domain on seepage through earth dams," *Water Resources Research*, vol. 7, no. 4, pp. 929–941, 1971.

[33] R. A. Freeze, "A stochastic-conceptual analysis of one-dimensional groundwater flow in nonuniform homogeneous media," *Water Resources Research*, vol. 11, no. 5, pp. 725–741, 1975.

[34] R. J. Hoeksema and P. K. Kitanidis, "Analysis of the spatial structure of properties of selected aquifers," *Water Resources Research*, vol. 21, no. 4, pp. 563–572, 1985.

[35] E. A. Sudicky, "A natural gradient experiment on solute transport in a sand aquifer: spatial variability of hydraulic conductivity and its role in the dispersion process," *Water Resources Research*, vol. 22, no. 13, pp. 2069–2082, 1986.

[36] H. Huang, B. X. Hu, X. H. Wen, and C. Shirley, "Stochastic inverse mapping of hydraulic conductivity and sorption partitioning coefficient fields conditioning on nonreactive and reactive tracer test data," *Water Resources Research*, vol. 40, no. 1, pp. 1–16, 2004.

[37] D. V. Griffiths and G. A. Fenton, "Seepage beneath water retaining structures founded on spatially random soil," *Géotechnique*, vol. 43, no. 4, pp. 577–587, 1993.

[38] G. A. Fenton and D. V. Griffiths, "Statistics of block conductivity through a simple bounded stochastic medium," *Water Resources Research*, vol. 29, no. 6, pp. 1825–1830, 1993.

[39] D. V. Griffiths and G. A. Fenton, "Probabilistic analysis of exit gradients due to steady seepage," *Journal of Geotechnical and Geoenvironmental Engineering*, vol. 124, no. 9, pp. 789–797, 1998.

Hindawi
Advances in Civil Engineering
Volume 2021, Article ID 5248324, 11 pages
https://doi.org/10.1155/2021/5248324

Research Article

Development Assessment of the Coal Industry of China Based on the Minimum Deviation Comprehensive Weight Evaluation Model

Shihua Ren,[1,2] **Dezhi Zheng**,[2] **Yang Qu**,[3] **Rongjun Qin**,[4] **Xiaomiao Jiao**,[2] **and Jinyan Bai**[5]

[1]*School of Management, China University of Mining and Technology (Beijing), Beijing 100083, China*
[2]*China Coal Research Institute, Beijing 100013, China*
[3]*Coal Industry Planning Institute, Beijing 100120, China*
[4]*China Coal Economic Research Association, Beijing 100013, China*
[5]*China Coal Technology & Engineering Group Corp., Beijing 100013, China*

Correspondence should be addressed to Dezhi Zheng; zhengdezhi@mtghy.com

Received 16 November 2021; Accepted 2 December 2021; Published 13 December 2021

Academic Editor: Yonghong Wang

Coal is the most reliable energy resource in China and has been in existence for a long time. The development model of coal industry is of great significance to carbon emission and environmental protection. In order to evaluate the development mode of China's coal industry, this paper presents the constructed evaluation index system of the development mode of the coal industry from two dimensions, demand pull and factor drive. And, coal consumption is the measurement index of demand pull and selecting resources, capital, technology, human resources, and the energy system form the measurement index of factor drive. By analyzing the evaluation index system of the coal industry development mode and optimal evaluation method, the minimum deviation comprehensive weighting evaluation model, based on the analytic hierarchy process (AHP), and entropy are constructed. The evaluation results show that the coal industry has continued the factor driven growth, driven by demand, in the past decades. Finally, the study analyzes the changes and challenges of the development of China's coal industry from four aspects, development power, development mode, development effect, and development bottleneck, to provide support for revealing the internal mechanism of the development mode of China's coal industry.

1. Introduction

The development of the coal industry is closely related to social economy and energy demand and is affected by multiple factors, such as available resources, available capital, current technology, manpower, and the country's energy system. Energy demand is the driving force behind the development of the coal industry. Evaluating the development mode of the coal industry and revealing the impacts that various factors have on the development of the coal industry and its internal mechanisms have theoretical and practical significance for understanding and promoting the transformation of the development mode of the coal industry [1–5].

At present, qualitative and quantitative evaluation methods mainly include the analytic hierarchy process and the entropy method, which are applied in many fields [6–8]. Naghadehi et al. proposed a fuzzy model, based on the combination of the fuzzy analytic hierarchy process and an advanced type of traditional analytic hierarchy process, which selects the best mining scheme by using effective main criteria and considering the subjective judgment of decision-makers [9]. Underground mining method selection is one of the most important decisions in mining engineering. The selection of appropriate underground mining methods for deposit mining is very important for all stages of mining operations. Yavuz introduced two similar, multiattribute decision-making methods—analytic hierarchy process and fuzzy multiattribute decision-making method—used to select the best underground mining method of Istanbul's lignite mine; they also performed a sensitivity analysis for

each method [10]. Shi et al. proposed an advanced optimization classification method based on fuzzy analytic hierarchy process and tunnel seismic prediction to accurately predict the classification of surrounding rock. The comprehensive weighting method is used to determine the weight of the evaluation index, and the fuzzy analytic hierarchy process model is used for optimal classification of surrounding rock [11]. Based on expert investigation, a three-level, eighteen factor risk evaluation index system for tunnel construction safety evaluation is established through the improved analytic hierarchy process [12]. Qualitative analysis is based mainly on the judgment, knowledge, and experience of one or more experts. In the case of limited available information, the subjective probability based on general professional experience, knowledge, and expert opinions can be used as the basis of analysis. Due to the frequent lack of quantitative data, experience and intuition have always been at the core of mining decision-making [13]. Bi et al. provide an effective method for rectifying potential gaps in the data. The index system is established as the basis of evaluation, and the quantitative evaluation results are obtained by using the matter-element extension method. Centering around the weight value of each index in the matter-element extension method, a comprehensive weight calculation method, based on vague set and entropy, is proposed [14]. In project management, this is an important method to comprehensively evaluate a project's safety risks based on information provided by experts [15–17]. However, the subjective weighting methods, such as analytic hierarchy process and expert consultation, have certain subjective randomness due to the experience or tendencies of decision-makers. The objective weighting methods, such as entropy and grey correlation, make full use of the objective information available, but it is easy to ignore the experience information of experts. Therefore, the use of a combination of quantitative and qualitative evaluation methods, if widely used in various engineering fields, could enhance the evaluation index system [18–21].

To improve the high-tech level of the coal industry, it is necessary not only to find new methods of upgrading power and creating new competitive advantages, an emerging practical problem in the coal industry, but also to solve the core issue of efficiently transforming the economic growth mode of the coal industry in the 12th Five Year Plan, which is key for solving China's energy supply and energy security problem. The coal industry is an important part of China's national economy and provides necessary energy and other resources for economic development. To alleviate China's environmental pressure, it is imperative that changes be made to the national structure of the coal industry through reasonable analysis. Only then, can China realize healthy development of its coal industry, which is of great significance for ensuring national energy security and achieving the objectives of environmental and atmospheric governance [22–24].

Based on factor driven theory, system theory, resource allocation theory, and synergy theory, this study constructs the evaluation index system of the development mode of the coal industry and the minimum deviation comprehensive weighted evaluation model, based on analytic hierarchy process entropy, using the weight calculation method, combining quantitative and qualitative methods, with the aim of providing support for revealing the internal mechanisms of the development mode of the coal industry in China.

2. Methodology

2.1. Model of Evaluation of Development Mode of the Coal Industry

2.1.1. Comprehensive Evaluation Index System. According to the factor driven theory, system theory, resource allocation theory, synergy theory, and other related theories, an index system for the evaluation of the development mode of the coal industry is constructed from the two dimensions of demand pull and factor drive (Figure 1).

Coal consumption is the driving force that best reflects demand. "Coal consumption" was selected as the measurement index of demand pull. Capital, resources, manpower, technology, and energy system, five key elements driving the development of the coal industry, were selected as the measurement index of factor drive. Among the resource indicators, "available resources" indicator was selected as the specific one to measure the resource scale and resource availability potential. Among the capital indicators, "industry fixed asset investment" was selected as the specific indicator to measure the investment scale and investment intensity. Among the technical indicators, there are many indicators to measure the technical level. To judge the overall technical level, the qualitative indicator of "comprehensive technical level" was selected for grading, as it covers multiple subitems such as recovery rate, mechanization degree, and waste resource utilization rate. In the manpower index, "number of employees in the coal industry" was selected as the specific index to measure the scale of employees. In the system indicators, since the system is concentrated in the policy field, "policy suitability" was selected as the specific indicator, as it covers multiple subitems such as policy applicability, policy intensity, and policy implementation effect, and the value is comprehensively evaluated by an expert scoring method.

2.1.2. Minimum Deviation Comprehensive Weighting Evaluation Model. The evaluation model of the coal industry development mode was constructed according to the evaluation index system and optimal evaluation method of the coal industry development mode. The model uses the hierarchy process and entropy method to determine the subjective weight u_j and objective weight v_j of each index. The minimum deviation combination weighting method was used to calculate the comprehensive weight w of resources, capital, technology, manpower, energy system, and other contributing factors, respectively, determine the difference between demand pull and factor drive on the development of coal industry, and quantitatively describe the internal impact mechanism. The minimum deviation comprehensive weighting evaluation model is shown in Figure 2.

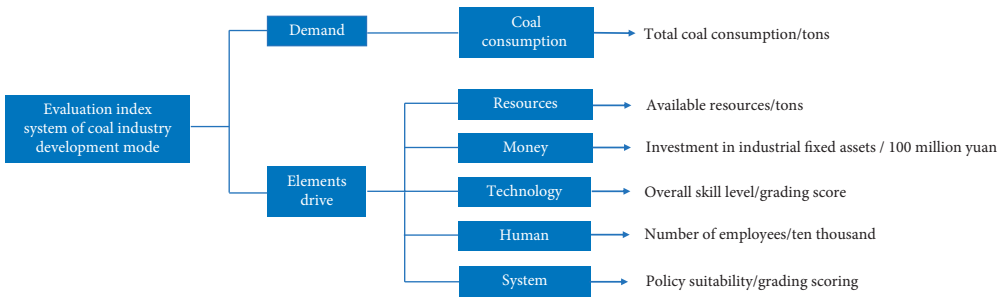

Figure 1: Assessment index system of development mode of the coal industry of China.

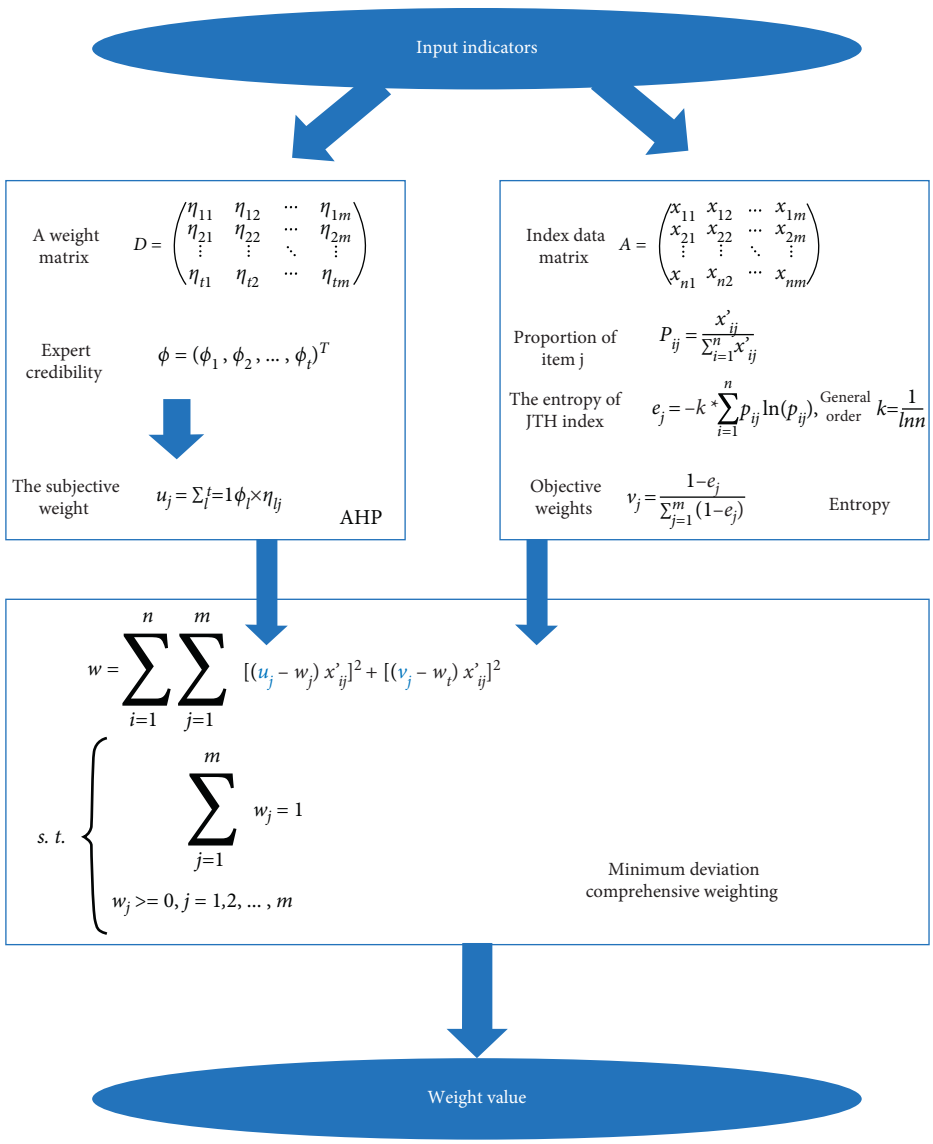

Figure 2: Minimum deviation comprehensive weighting evaluation model (w is weight, e is entropy, and P is probability).

3. Case Study

To reform and transform future development mode of the coal industry, an understanding of the laws (brought out as a response to the past few decades' rapid coal industry developments), power sources, driving factors, and sustainability of development is required. Since the reform and opening of China, with the development of heavy industry and the acceleration of urbanization, the social economy of China has developed rapidly, as has the demand for energy.

Coal has attracted much attention and investment, as China's main source of energy, with the continuous growth of energy demand. Resources, capital, technology, manpower, policies, and other production considerations continue to accumulate in the coal industry, promoting the leapfrog development of the coal industry.

Using the established evaluation model, the review and evaluation of the development mode of the coal industry show that the coal industry has continued the demand driven, factor driven growth in the past few decades. As a core factor, a rate of 39.62% was contributed by demand. And rates of 10.19%, 15.28%, 12.36%, 13.21%, and 9.34% were contributed by resources, capital, technology, manpower, energy system, and other factors, driving the development of the coal industry. However, after experiencing rapid development, the sustainability of driving factors is facing challenges, and the existing development mode of the coal industry has fallen into a bottleneck (Figure 3).

3.1. Development Power

3.1.1. Economy. Since the reform and opening of China, the industrial scale has increased rapidly, along with the economy. According to the process of economic system reform, it can be divided into four stages:

From 1978 to 1992, the exploration stage of market economy was taking place. The economy was dominated by planned economy and supplemented by market regulation. The average annual growth rate of China's economy was 9.46%.

From 1993 to 2002, the market economy was established. China had entered the establishment period of a socialist market economy, with Chinese characteristics. The market vitality had been fully stimulated and the economy had developed vigorously. At this stage, the economy had an average annual growth rate of 9.84%.

From 2003 to 2016, the socialist market economic system was improved. The important goal of this stage of reform was to give greater play to the basic role of the market in resource allocation, enhance the vitality and competitiveness of enterprises, and achieve an average annual economic growth of 9.59%.

From 2017 to now, the economy has transitioned from high-speed growth to high-quality development. Since the 19th National Congress of the Communist Party of China, China has entered a new era of socialism, with Chinese characteristics, and the economy has gradually transitioned from high-speed and medium high-speed growth to high-quality development with medium high-speed growth.

The annual economic growth rate of the first three stages is high and low, and the average economic growth rate of each stage is about 9.6%. In the fourth stage, although the economic growth rate decreased, the absolute growth of gross domestic product (GDP) constantly grew every year.

3.1.2. Energy. Since the reform and opening of China, although energy consumption per unit GDP has decreased year by year, the elasticity coefficient of energy consumption has been maintained at 0.5, which shows the relationship between economic growth and energy consumption. The historical experience of major developed countries also shows that the elasticity coefficient of energy consumption will remain at a high level before the completion of industrialization.

According to the four stages of the process of economic system reform, the elasticity coefficient of energy consumption in different stages represents different defining characteristics. From 1978 to 1992, the average energy consumption elasticity coefficient was 0.77. At this stage, the economic base is low, the development growth rate is high, and the energy consumption elasticity coefficient is relatively high. From 1993 to 2002, the elasticity coefficient of energy consumption decreased, with an average value of 0.46. From 2003 to 2016, due to the rapid growth of high energy-consuming industries and the rapid increase of energy consumption, the average elastic coefficient of energy consumption rebounded to 0.69, and the value was even higher than 1 for three consecutive years, from 2003 to 2005. Since 2017, China has taken the initiative to change the mode of economic development and promote the revolution of energy production and consumption. The growth rate of energy consumption and economic growth have both decreased, and the average elasticity coefficient of energy consumption has dropped to 0.56.

3.1.3. Coal. Due to energy resource endowment, international energy prices, and international situation, China mainly depends on local energy, and coal is the only energy source which can be relied on. At the beginning of the founding of new China, coal consumption accounted for more than 90% of total primary energy consumption. The economy and coal consumption depended on and promoted each other. National coal consumption increased from 400 million TCE in 1978 to 2.829 billion TCE in 2020, an increase of 600%. From 1978 to 1992, with the implementation of the reform and opening-up policy, the demand for energy from coal increased sharply, and the coal consumption increased steadily, with an average annual growth rate of 5.6%. From 1993 to 2002, affected by the Asian financial crisis, China was in a period of economic fluctuation and adjustment. Coal consumption fluctuated from 866 million TCE to 1.162 billion TCE, an increase of 34.2%. The consumption growth rate was negative from 1997 to 1999. From 2003 to 2016, driven by the rapid economic growth, coal demand also increased rapidly, and consumption was nearly doubled, with an average annual growth rate of 6.4%. Since 2017, due to the adjustment of the economic development mode, the growth rate of coal consumption has decreased, and coal consumption has entered the platform period, with an average growth rate of 1.2% (Figure 4).

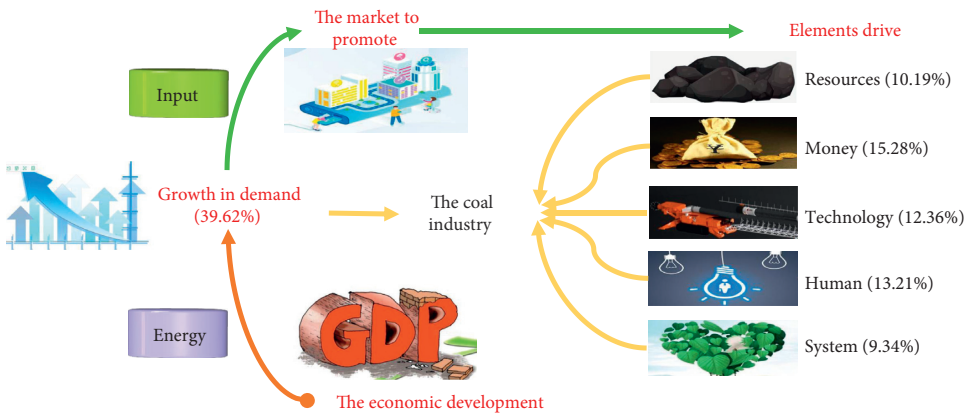

Figure 3: Development mode of the coal industry in the past decades.

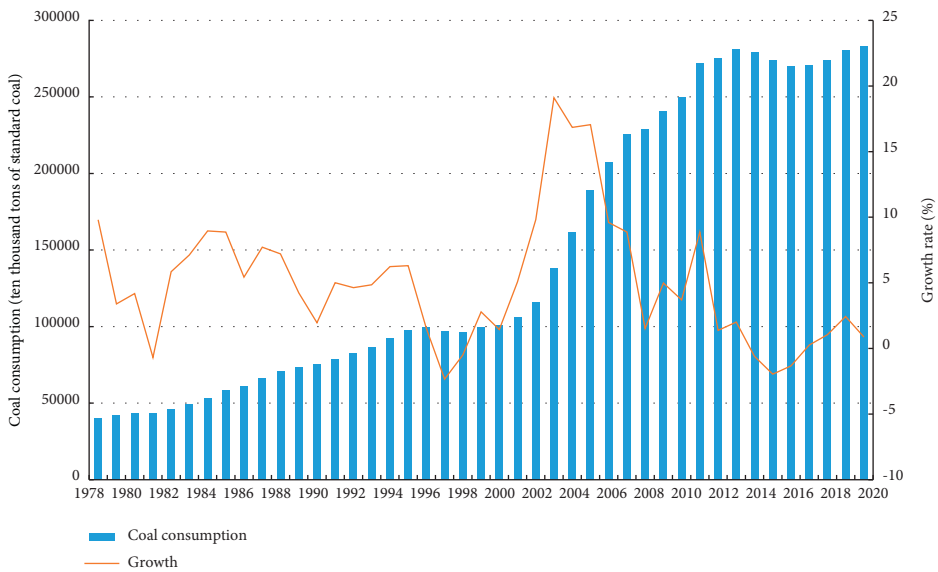

Figure 4: Coal consumption and growth rate from 1978 to 2020 in China.

3.2. Development Mode

3.2.1. Resources. With the increase of resources explored in the western region, the breadth and depth of coal development are gradually shifting from the east to the west. The coal industry was mainly distributed in the eastern regions of China, where there are 21.53 million tons for output and 66.4% of the national coal output. The coal output of Liaoning Province was the first among all provinces in China with 5.44 million tons. In that year, the coal output in the central region was 6.79 million tons, accounting for 21% of the national coal output, and the coal output in the western region was 4.11 million tons, accounting for only 12.7% of the national output. In 2008, the coal output in the western region of China reached 1.171 billion tons, accounting for 43% of the national output, surpassing the central region for the first time and becoming the main coal supplier and important commercial coal transference area in China. The coal output in the central region is 1.073 billion tons, accounting for 40% of the national output. The coal output in the eastern region is 466 million tons, accounting for 17% of the national coal output. The proportion of coal output in the eastern region continues to decline to this day.

In 2018, the coal production in Western China reached 2.283 billion tons, accounting for 59.38% of the national coal output, the coal production in Central China was 1.292 billion tons, accounting for 33.63% of the national output, and the coal output in the eastern region is 269 million tons, accounting for 6.99% of the national coal output. Coal development is further concentrated in the western region (Figure 5).

3.2.2. Capital. Capital is the foundation of the development of every industry. Only through continuous inflow can the industry develop. The coal industry has experienced a roller coaster fluctuation process from rapid inflow, to a sharp decline in investments. 2000 to 2002 was a period of reforming and extricating the coal industry from difficulties. At this stage, the coal industry is vigorously improving conditions of small coal mines, focusing on solving deep-seated problems such as structural contradictions, and the

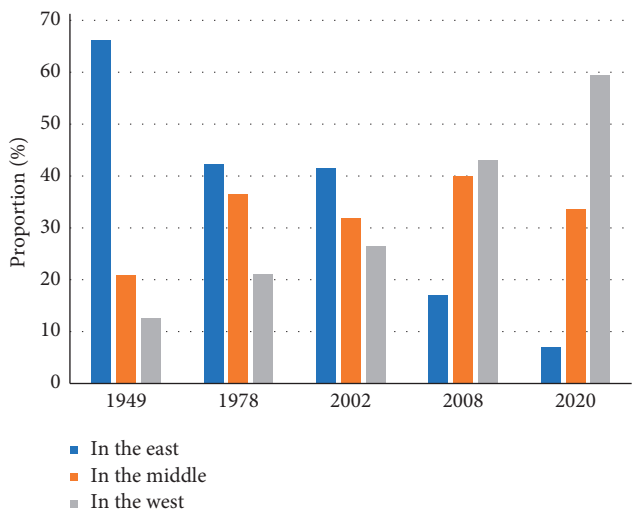

Figure 5: Coal production in different regions of China from 1949 to 2020.

number of total investments is gradually increasing. 2003–2012 was a golden decade of rapid development for the coal industry. At this stage, with the rising demand of the coal market and the profitability of coal enterprises increasing, a large amount of social capital entered the coal industry. During this time, the total number of investments increased rapidly, from 43.7 billion yuan in 2003 to 537 billion yuan in 2012, 12 times what it was in the past decade, with a compound growth rate of 34%. As a result, many projects started on shaky ground, the coal production capacity increased rapidly, and the market overheated. From 2013 to 2016, the national coal industry faced overcapacity, weak demand, falling prices, many losses, and great operating pressure, resulting in the decrease of fixed asset investment in the coal mining and dressing industries for five consecutive years. Since 2016, the coal industry has entered the de-capacity stage. By the end of 2019, the main objectives and tasks of coal de-capacity have been essentially completed. The coal industry has changed from total de-capacity to systematic de-capacity and structural excellent capacity. At the same time, with the continuous improvement of industrial benefits, the fixed asset investment in the coal industry is beginning to be picked up (Figure 6).

3.2.3. Technology. Through the introduction, digestion, absorption, and reinnovation of the coal industry, many scientific researchers have investigated a series of key problems in the technological transformation from mining-focused technology to safety guarantee technology, from process to complete equipment, and from single technology to system integration and achieved fruitful results. The degree of coal mining mechanization in China started late. In the 1960s, the degree of mechanization was less than 10%. With the continuous progress of science and technology in China, the degree of coal mining mechanization in large coal enterprises increased from 3.06% in 1955 to 98.03% in 2019. At the same time, scientific and technological innovation in the coal industry has gradually upgraded from tracking and imitating to paralleling and leading. Intelligent mining technology and equipment, large-scale mine construction, fully mechanized top coal caving mining of extra thick coal seams, and other technologies have reached the international leading level. China has built more than 200 intelligent coal mining faces and created a new intelligent mining mode of "one person inspection and no operation." In addition, the complete sets of large-scale, fully mechanized mining technology and equipment have been exported to Russia, Ukraine, and many other countries realizing the subversive transformation of technology and equipment from input to output.

3.2.4. Manpower. The coal industry has many employees, as it is a typical labor-intensive industry. Before 2000, the average number of employees in the coal mining and washing industry was less than 4 million. With the opening of the "golden decade" of the coal industry, this number exceeded 4 million in 2004 and 5 million in 2008 and reached an all-time high of 6.11 million in 2013. With the industry's overcapacity and increasing losses, coal enterprises have implemented cost reduction and capital increase and started personnel diversion. The average number of coal employees began to fall after 2014. According to the data of the fourth national economic census, in 2018, the number of employees in the coal industry was 3.473 million, which is still the highest number of employees in the world, accounting for 58.27% of the total number of mining industry. Among all 40 industries in the secondary industry, the number of people in the coal industry ranks 12th, accounting for 3% of the total number of people in the secondary industry. Combined with the output data of that year, it can be calculated that the per capita output of China's coal industry is about 1059.6 t, which is far lower than the per capita output of 12800 t in the US coal industry (in 2018, the US raw coal output was 684 million t and 53583 employees). China's coal industry is still driven by labor-intensive development.

3.3. Development Achievements

3.3.1. Supply. After years of development, the productivity level of the coal industry has increased dramatically. The security and stable supply guarantee capacity has been greatly improved, meeting the needs of sustained, rapid development of the national economy, and the coal supply guarantee capacity has been significantly improved (Figure 7). From 2016 to 2019, the newly identified resource reserves of coal increased by 227.9 billion tons. The national coal resource development and production layout have been continuously optimized, and the focus of resource development has gradually shifted to regions with good resource endowment, excellent mining conditions, and low production cost. The focus of coal production has been continuously optimized, the production capacity has been gradually concentrated, and total advanced production capacity has been greatly increased. Regional centralized development of the coal industry has been gradually

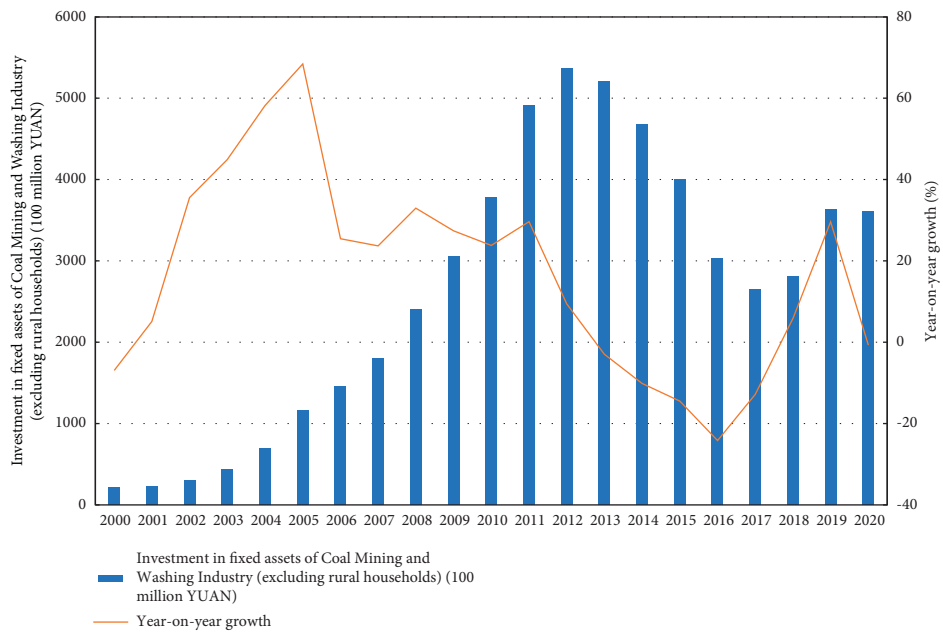

Figure 6: Fixed assets investment of coal mining and dressing industry from 2000 to 2020 in China.

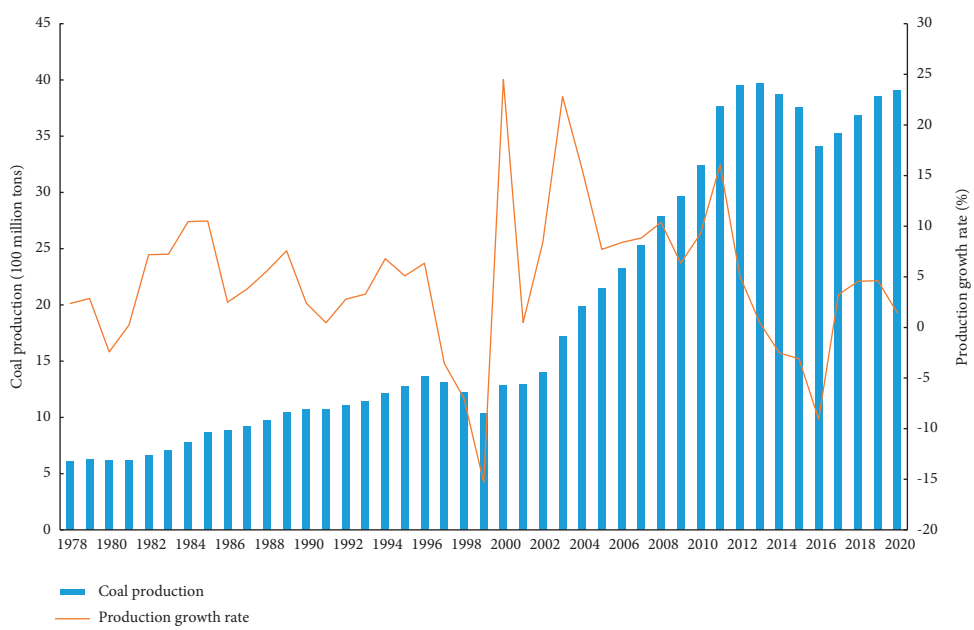

Figure 7: Coal output from 1978 to 2020 in China.

established. As the main coal producing areas, the central and western regions have become more and more prominent in their strategic position. The coal output of Shanxi, Shaanxi, and Inner Mongolia accounts for more than 70% of the total output of the country. The construction of large coal bases has been continuously promoted. The number of coal mines in China has decreased from more than 80000 in the early stage of reform and opening of China to 4700 by the end of 2020, and the advanced production capacity has increased by 600 million t/a. The national coal mine production capacity is 4.1 billion t/a, and the average single well (mine) production capacity has increased to more than 1.1 million t/a. Large modern coal mines have become the main body of national coal production. More than 1200 large modern coal mines, with an annual output of more than 1.2 million tons, have been built in China, accounting for 80% of the country's output. Among them, 52 coal mines, with an annual output of 10 million tons, have been built, with a production capacity of 820 million t/a. The national system of scientific planning, rational development, modern production, and clean, efficient utilization of coal resources has been essentially completed.

3.3.2. Efficiency. In recent years, the coal industry has continuously improved the overall work efficiency of raw coal production by optimizing development layout, developing high-quality production capacity, and promoting mine mechanization and intelligent mining. Some coal mines have even reached the international advanced level. Coal resources are deeply buried in coal seams, and the proportion of open-pit coal mines with favorable congenital conditions is less than 12%. The mines with difficulties account for the vast majority. In addition to the unfavorable conditions, such as many fault structures, thin coal seams, and steep dip angles (which can lead to excessive horizontal stress conditions), some mines in China are also accompanied by disasters such as gas, water, fire and rock burst, limited mining conditions, and frequent safety accidents, which restrict the mining efficiency. However, with the improvement of coal technology, the coal production efficiency has increased from 325.59 t/a in 2000 to 1921.19 t/a in 2020, an increase of 490% (Figure 8). From 2013 to 2020, the annual output of raw coal has been maintained at 3.6 billion tons. But, during this period, the number of employees has dropped sharply from 6.11 million to 4.08 million and 2.03 million, a decrease of 66.8% and an average annual decrease of 11.1%. Compared with 2013, the coal industry completed more workload in 2020 with less than 33% of the original personnel. At the same time, some coal mines have obvious advantages in work efficiency, and the efficiency of the coal industry has been greatly improved.

3.3.3. Safety. Due to the problems of complex coal mine geological conditions, many natural disasters, mining difficulties, and frequent accidents, the coal mine safety regulations gradually improved, and the mortality rate per one million tons has decreased year by year. Overall, the development process of coal mine safety in China is divided into three major periods: 1949–1977 is the period of sharp fluctuation of coal mine safety. During this period, the core task of the coal industry was to ensure coal production and supply. The coal mines built were mostly small or medium-sized, and the coal mine production technology and equipment were relatively backward, resulting in frequent coal mine accidents. The mortality rate per million tons fluctuated between 4.32 and 22.28, and the safety situation was very serious. From 1978 to 2002, the level of coal mine safety continued to improve. During this period, priorities changed from planning mining to ensure coal supply to promoting safe and efficient coal mining through technological progress. Significant progress was made in the construction of large coal bases. The mortality rate per million tons decreased from 9.44 in 1978 to 4.94 in 2002. The overall situation of coal mine safety continued to improve steadily throughout the next several years. 2003–2020 saw a period of rapid improvement to coal mine safety. During this period, after the "golden decade" of industry development, coal mining enterprises' investment in safety production has increased continuously, the degree of coal mining mechanization has increased significantly, and key technologies and equipment for major disaster management have been popularized and applied. The death rate per million tons decreased rapidly from 3.71 in 2003 to 0.059 in 2020 (Figure 9).

3.3.4. Quality. Over the past 60 years, compared with coal production, the increase of the raw coal selection rate in China has increased. In 1952, the raw coal selection rate was approximately 4.4%, and the annual output of washed coal was only a few million tons. In 2020, China's coal selection rate has reached approximately 74.1% (Figure 10). The coal preparation process developed from jigging in the 1950s to the 1970s, to the process of jigging, roughing, and dense medium cyclone cleaning in the 1980s and then to the coexistence of jigging, dense medium separation, water medium cyclone separation, moving screen jigging, air separation, autogenous medium separation, and microbubble flotation in the 1990s. In recent years, with the continuous reduction of capital investment and production cost of heavy medium coal preparation process, after solving the problems of wear resistance of equipment and pipeline, medium recovery, and efficient pumping equipment, heavy medium coal preparation technology has developed rapidly in China. Its characteristics of easy operation and high efficiency have made it more and more popular, and it has become the leading process. In the 21st century, coal preparation, the frontier of clean coal technology, has obvious effects on the improvement of coal quality and utilization efficiency, reduction of ineffective transportation, and reduction of coal pollutant emission. Coal preparation has entered a period of great development. The raw coal capacity of the average coal preparation plant increased from 522 million t/a to 2896 million t/a with an average annual increase of 100 million t from 2000 to 2020.

4. Discussion

4.1. Recoverable Resources of a Shallow Economy Have Been Greatly Reduced. The guaranteed degree of coal resources is low, the recoverable resources of shallow economy are greatly reduced, and the coal resources that can be economically developed and utilized in the future are not rich, which has become the bottleneck restricting the construction of coal modernization. Firstly, after more than 50 years of development in the eastern Huang Huai area, which is rich in coal resources, there are few coal resources left in the Shanxi formation with excellent shallow coal quality, low sulfur content, and other harmful elements and simple hydrogeological conditions. More are turning to the development of the lower coal group, dominated by the Taiyuan formation, which has high sulfur content and complex conditions of Ordovician and Taiyuan limestone water. Secondly, many provinces plan to withdraw from coal production entirely in the next few years. For example, Hebei's coal production capacity withdrew by more than 40% from 2016 to 2019. Jiangxi and Chongqing also plan to significantly reduce coal production and eventually withdraw from the coal production industry. Thirdly, coal resources within the ecological red line will no longer be

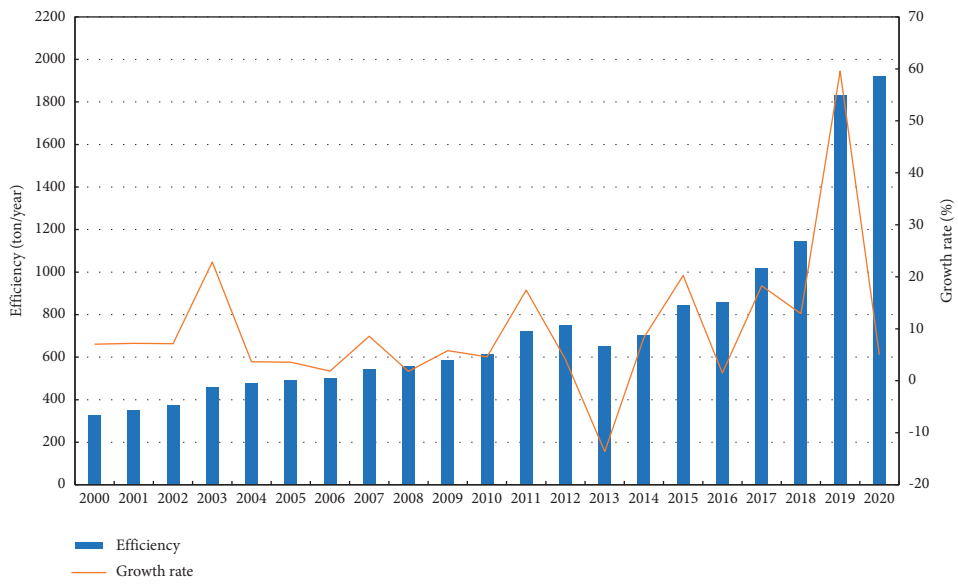

Figure 8: Coal production efficiency of China since 2000.

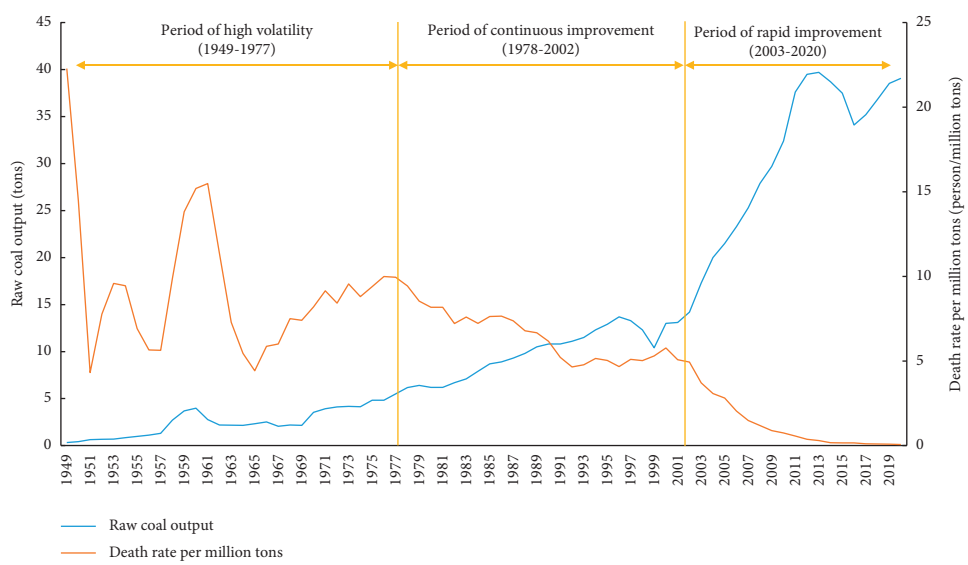

Figure 9: Coal production and death rate per million tons in China.

exploited. From the current situation, many coal resources in Guizhou, Inner Mongolia, Shanxi, Shaanxi, and other provinces will be included in the ecological red line and can no longer be mined. Finally, among the proven 5.57 trillion t coal resources, 2.95 trillion t of them is buried below 1000 m, accounting for 53% of the total coal resources, which is difficult to develop.

4.2. Lack of Independent Innovation, Difficult to Support Future Needs. Coal science and technology play a decisive role in the development of the coal industry and are the foundation of industry development. Although the coal science and technology level have made great progress and significantly improved, there is still a large gap compared with the world's energy science and technology power. The lack of core technology in the coal industry and the dependence on imports of key equipment and materials are still prominent. Based on the principles, standards, and specifications of the United States, the European Union, and other countries, the technical equipment of coal industry was developed. Generally, the process of complete introduction, partial domestic supporting, and domestic R & D and manufacturing is adopted. The core components are independently developed. At present, almost all complete machines such as shearers, scrapers, conveyors, and scraper transfer machines in China can be assembled. However, many core components are still imported. For example, the large scraper conveyor produced in China is internationally leading, but the reducer above 2000 kW still needs to be purchased from PW, a company in Germany. The 5 m diameter raise boring machine is internationally leading, but

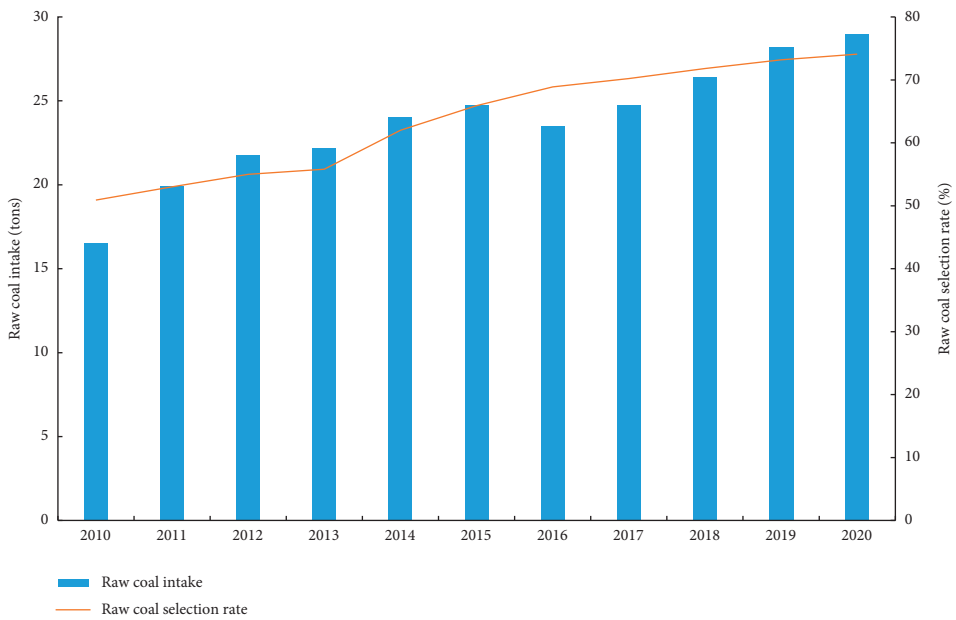

Figure 10: Coal selection rate and quantity in China from 2010 to 2020.

the hydraulic motor still needs to be purchased from Buckland, a company in France, the 8.8 m shearer is internationally leading, but the high-speed and large load bearing still needs to be purchased from the United States, etc. We must understand the huge gap in the scientific and technological levels regarding the coal industry, especially high-end manufacturing. Many technical pieces of equipment are still controlled by people, and there is insufficient independent innovation, which makes it difficult to support the future development of the coal industry.

4.3. Employees Are Too Old and the Improvement of Personnel Quality Is Limited. The contradiction between the low overall quality of employees in the coal industry and the demand for high-quality personnel is becoming more and more prominent. Although the number of employees in the coal industry is large, the overall quality is low. With the continuous improvement of industry automation and intelligence, the requirements of industry development on personnel quality will be higher and higher. As it is, the existing human structure level cannot meet the needs of industry development. First, the employees are too old, and the reserve labor force is insufficient. The proportion of people over 40 years old in mining industry accounts for 56.8%, exceeding the average level of the whole industry. Second, the overall quality is not high and there is a shortage of senior technicians. At present, the employees are mainly technical secondary school students, nearly half of them have an education at or below the technical secondary school level, and less than 30% have a college education or above. The demand for high-quality and high-tech talent is becoming stronger and stronger. In the United States, only those with a professional education can enter the coal industry. Nearly 90% of employees come from vocational schools. The employees have high professional quality and rich practical experience. These high-quality talent teams support the intelligent level of the American coal industry. At present, the personnel structure, with low education, in the coal industry cannot meet future needs. There is a prominent contradiction between the large number of surplus personnel and the shortage of senior skilled talents.

5. Conclusion

From the two dimensions of demand pull and factor drive, this paper presents the evaluation index system of the development mode of the coal industry, with "coal consumption" as the measurement index of demand pull. Select resources, capital, technology, manpower, and energy system as factor driven measurement indicators. According to the evaluation index system and optimal evaluation method of coal industry development mode, the model of the coal industry development mode evaluation is constructed. The model uses the analytic hierarchy process and entropy method to determine the subjective weight u_j and objective weight v_j of each index.

Based on the constructed model, the development mode of the coal industry is reviewed and evaluated. The results show that the coal industry has continued the demand driven factor driven growth in the past few decades. Demand pull is the core factor, with a contribution rate of 39.62%; resources, capital, technology, manpower, energy system, and other factors specifically drive the development of the coal industry, with contribution rates of 10.19%, 15.28%, 12.36%, 13.21%, and 9.34%, respectively.

After experiencing rapid development, the sustainability of driving factors is facing challenges. The bottlenecks of the existing development mode of the coal industry are analyzed in detail from five aspects: resources, capital, technology, manpower, and system.

Data Availability

The datasets generated during the current study are available from the corresponding author on reasonable request.

Conflicts of Interest

The authors declare no conflicts of interest.

Authors' Contributions

The manuscript was approved by all authors for publication.

Acknowledgments

This work was supported by China Coal Technology and Engineering Group (Grant number 2018-2-ZD008) and the strategic research and consulting project of Chinese Academy of Engineering (Grant number 2021-XY-25).

References

[1] Q. Li, "The view of technological innovation in coal industry under the vision of carbon neutralization," *International Journal of Coal Science and Technology*, vol. 1-11, 2021.

[2] M. Zhou and T. Hu, "Analysis of carbon emission status under the carbon neutral target in China for Earth's atmospheric balance," *IOP Conference Series: Earth and Environmental Science*, vol. 804, no. 4, Article ID 042082, 2021.

[3] M. S. Wang and Y. F. Yao, "Development situation and Countermeasures of oil and gas industry under the constraint of carbon neutralization," *Petroleum Drilling Techniques*, vol. 49, no. 5, pp. 1–6, 2021.

[4] C.-M. Li and R. Nie, "An evaluating system for scientific mining of China's coal resources," *Resources Policy*, vol. 53, pp. 317–327, 2017.

[5] X.-M. Chen, Q.-M. Liang, L.-C. Liu, C. Wang, and M.-M. Xue, "Critical structural adjustment for controlling China's coal demand," *Journal of Cleaner Production*, vol. 235, pp. 317–327, 2019.

[6] B. Yang, K. Xu, and Z. Zhang, "Mitigating evaporation and desiccation cracks in soil with the sustainable material biochar," *Soil Science Society of America Journal*, vol. 84, no. 2, pp. 461–471, 2020.

[7] B. Yuan, Z. Li, Z. Zhao, H. Ni, Z. Su, and Z. Li, "Experimental study of displacement field of layered soils surrounding laterally loaded pile based on transparent soil," *Journal of Soils and Sediments*, vol. 21, no. 9, pp. 3072–3083, 2021.

[8] B. X. Yuan, Z. H. Li, Z. L. Su, Q. Z. Luo, M. J. Chen, and Z. Q. Zhao, "Sensitivity of multistage fill slope based on finite element model," *Advances in Civil Engineering*, vol. 2021, Article ID 6622936, 13 pages, 2021.

[9] M. Z. Naghadehi, R. Mikaeil, and M. Ataei, "The application of fuzzy analytic hierarchy process (FAHP) approach to selection of optimum underground mining method for Jajarm bauxite Mine, Iran," *Expert Systems with Applications*, vol. 36, no. 4, pp. 8218–8226, 2009.

[10] M. Yavuz, "The application of the analytic hierarchy process (AHP) and Yager's method in underground mining method selection problem," *International Journal of Mining, Reclamation and Environment*, vol. 29, no. 6, pp. 453–475, 2015.

[11] S.-s. Shi, S.-c. Li, L.-p. Li, Z.-q. Zhou, and J. Wang, "Advance optimized classification and application of surrounding rock based on fuzzy analytic hierarchy process and Tunnel Seismic Prediction," *Automation in Construction*, vol. 37, pp. 217–222, 2014.

[12] X. X. Chen, R. H. Chen, K. Lin, and M. W. Zhang, "Application of the improved analytic hierarchy process in the risk management of tunnel construction," in *Applied Mechanics and Materials*p. 696, Trans Tech Publications Ltd, Kapellweg, SZ, Switzerland, 2015.

[13] V. N. Kazakidis, Z. Mayer, and M. J. Scoble, "Decision making using the analytic hierarchy process in mining engineering," *Mining Technology*, vol. 113, no. 1, pp. 30–42, 2004.

[14] A. Bi, Z. Luo, Y. Kong, and L. Zhao, "Comprehensive weighted matter-element extension method for the safety evaluation of underground gas storage," *Royal Society Open Science*, vol. 7, no. 4, Article ID 191302, 2020.

[15] N. Wang, C.-s. Xu, X.-l. Du, and M.-j. Zhang, "A risk assessment method of deep excavation based on Bayesian analysis and expert elicitation," *International Journal of System Assurance Engineering and Management*, vol. 9, no. 2, pp. 452–466, 2018.

[16] C. Liu, S. Yang, Y. Cui, and Y. Yang, "An improved risk assessment method based on a comprehensive weighting algorithm in railway signaling safety analysis," *Safety Science*, vol. 128, Article ID 104768, 2020.

[17] B. Meng and G. Chi, "New combined weighting model based on maximizing the difference in evaluation results and its application," *Mathematical Problems in Engineering*, vol. 2015, Article ID 239634, 9 pages, 2015.

[18] B. B. Yang, S. Yuan, Y. Liang, and J. Liu, "Investigation of overburden failure characteristics due to combined mining: case study, Henan Province, China," *Environmental Earth Sciences*, vol. 80, 2021.

[19] B. Yuan, Z. H. Li, Y. Chen et al., "Mechanical and microstructural properties of recycling granite residual soil reinforced with glass fiber and liquid-modified polyvinyl alcohol polymer–sciencedirect," *Chemosphere*, vol. 268, Article ID 131652, 2021.

[20] B. Yang, J. Liu, X. Zhao, and S. Zheng, "Evaporation and cracked soda soil improved by fly ash from recycled materials," *Land Degradation & Development*, vol. 32, no. 9, pp. 2823–2832, 2021.

[21] B. Yang, D. Li, S. Yuan, and L. Jin, "Role of biochar from corn straw in influencing crack propagation and evaporation in sodic soils," *Catena*, vol. 204, Article ID 105457, 2021.

[22] Z. Gao, "Sustainable development and upgrading mode of coal industry in China," *International Journal of Mining Science and Technology*, vol. 22, no. 3, pp. 335–340, 2012.

[23] Y. Li, B. Zhang, B. Wang, and Z. Wang, "Evolutionary trend of the coal industry chain in China: evidence from the analysis of I-O and APL model," *Resources, Conservation and Recycling*, vol. 145, pp. 399–410, 2019.

[24] L.-T. Zhao, Z.-T. Liu, and L. Cheng, "How will China's coal industry develop in the future? a quantitative analysis with policy implications," *Energy*, vol. 235, Article ID 121406, 2021.

Hindawi
Advances in Civil Engineering
Volume 2021, Article ID 4245051, 12 pages
https://doi.org/10.1155/2021/4245051

Research Article

Comparisons of Two Approaches for Geotechnical Model Calibration with Scarce Data

Yuanxin Lei, Huifen Liu, and Zhixiong Lu

School of Transportation Civil Engineering and Architecture, Foshan University, Foshan 52800, Guangdong, China

Correspondence should be addressed to Huifen Liu; liuhuifen99@163.com

Received 8 November 2021; Revised 20 November 2021; Accepted 22 November 2021; Published 10 December 2021

Academic Editor: Yonghong Wang

Geotechnical models are usually built upon assumptions and simplifications, inevitably resulting in discrepancies between model predictions and measurements. To enhance prediction accuracy, geotechnical models are typically calibrated against measurements by bringing in additional empirical or semiempirical correction terms. Different approaches have been used in the literature to determine the optimal values of empirical parameters in the correction terms. When measured data are abundant, calibration outcomes using different approaches can be expected to be practically the same. However, if measurements are scarce or limited, calibration outcomes could differ significantly, depending largely on the adopted calibration approach. In this study, we examine two most commonly used approaches for geotechnical model calibration in the literature, namely, (1) purely data-catering (PDC) approach, and (2) root mean squared error (RMSE) method. Here, the purely data-catering approach refers to selection of empirical parameter values that minimize coefficient of variation of model factor while maintains its mean value of one, based solely on measured data. A real case of calibrating the Federal Highway Administration (FHWA) simplified facing load model for design of soil nail walls is illustrated to thoroughly elaborate the differences in practical calibration and design outcomes using the two approaches under scarce data conditions.

1. Introduction

It has been well recognized that model uncertainty plays a key role in reliability-based design of geotechnical structures [1–5], as it is usually much larger than uncertainty associated with design parameters (e.g., soil cohesion, unit weight, and internal friction angle). Typically, geotechnical models need to be assessed and calibrated against measured or observed data before used for design. However, in many cases, measurements or observations that are available for model assessment and calibration are limited, mainly due to two reasons: first, obtaining in situ geotechnical data is costly and time consuming in general; and second, monitored data were always undervalued and thus not well collected and pooled, although in recent years, geotechnical engineers start to realize the value of data and make effort to make the best use of it [6–13].

Despite of the situation, assessment and calibration of geotechnical models using limited data are far better than doing nothing at all [3]. Usually, calibration of a geotechnical model can be done by following two steps: (1) introduce an empirical or semiempirical correction term to a model and (2) determine the constants in the correction term according to certain criteria. Based on the calibration criteria, there are two methods that have been widely adopted for geotechnical model calibration in the literature. One is the purely data-catering (PDC) approach, and the other is the root mean squared error (RMSE) approach.

The PDC approach calibrates a model by adjusting the constants to satisfying two criteria: keeping the mean of bias equal to one while minimizing the coefficient of variation (COV) of bias. Here, bias is defined as the ratio of measured to the predicted value. Bias, also referred to as model bias or model factor elsewhere, is commonly treated as a random variable and used as an indicator for quantification of model accuracy. Previous geotechnical model calibration using the PDC approach can be seen in, e.g., Lin and Liu [14], Lin et al. [15], Lin et al. [16], Phoon and Kulhawy [17], Phoon and Tang [18], Tang and Phoon [19], Yuan et al. [20], and Yuan et al. [21].

On the other hand, the RMSE approach determines the constants as the set that minimizes the root mean squared error between measurements and predictions. Common examples are geotechnical models developed using the response surface method and machine learning methods, e.g., Bathurst and Yu [22], Lin et al. [16], Liu et al. [23], Yu and Bathurst [24], Zhang et al. [25], Zhang et al. [26], Zhang et al. [27], and Zhang et al. [28]. Obviously, these two calibration approaches are not equivalent, especially when the data for calibration are scarce. This will result in different calibrated values for the constants, which in turn lead to different geotechnical design outcomes. Discussion on the difference of these two approaches will be provided later in this study.

While being extensively used, influences of adoption of the two approaches on geotechnical calibration outcomes and the consequences are not yet thoroughly examined. To fill the gap, this study is focused on investigating the differences in both calibration and practical design outcomes that are resulted by using the above two calibration approaches. To allow comparing model competence from a third angle, the Bayesian information criterion (BIC) is employed [29]. A case study of calibrating the default Federal Highway Administration (FHWA) facing load model for facing design of soil nail walls is shown to elaborate the influences.

2. Approaches for Model Calibration and Ranking

This section introduces in detail the PDC and RMSE approaches for calibration of geotechnical models against observed data. The commonalities and differences of the two approaches are discussed. A likelihood-based model ranking method called Bayesian information criterion (BIC) is also introduced, which will be used later to quantify the competences of the calibrated models.

2.1. Purely Data-Catering Approach. Suppose $y = f(x)$ be the geotechnical model to be calibrated. Here, y is the model output which is taken to be a scalar for simplicity; and x is the model input parameter vector, $x = (x_1, x_2, \ldots, x_n)$. Note that the input parameter vector x is the same across different design scenarios, while the values of its elements could vary. For convenient, we denote y_k and x_k for design scenario k.

Let $D = (d_1, d_2, \ldots, d_m)$ be m observed or measured values for y from m real cases, and λ be the model factor (which is a random variable) for $y = f(x)$. Then, based on the method of moment, the sample mean and sample standard deviation of λ, denoted as $\overline{\lambda}$ and s_λ, respectively, can be computed as

$$\overline{\lambda} = \frac{1}{m}\sum_{k=1}^{k=m}\frac{d_k}{y_k},$$
$$s_\lambda = \sqrt{\frac{1}{m-1}\sum_{k=1}^{k=m}\left(\frac{d_k}{y_k} - \overline{\lambda}\right)^2}. \quad (1)$$

The purely data-catering (PDC) approach assumes that a model can be adequately (indeed, compromisingly) calibrated in terms of $\overline{\lambda}$ and s_λ that are obtained by the method of moment. The PDC approach introduces an empirical correction term, M, to the original model for calibration purposes, where M is a function of x and C, with C being a vector of empirical constants to be determined using D. In general, the correction term can be written as $M = f_M(x; C)$. As such, the calibrated model can be expressed as

$$y' = M \times f(x) = f_M(x; C) \times f(x), \quad (2)$$

where y' is the model output after calibration. The sample mean and sample standard deviation of the model factor for the calibrated model, denoted as λ', can then be calculated as

$$\overline{\lambda'} = \frac{1}{m}\sum_{k=1}^{k=m}\frac{d_k}{y'_k}, \quad (3)$$

$$s'_\lambda = \sqrt{\frac{1}{m-1}\sum_{k=1}^{k=m}\left(\frac{d_k}{y'_k} - \overline{\lambda'}\right)^2}. \quad (4)$$

The calibration principles of the PDC approach are to adjust the values of the empirical constants in **C** until simultaneously satisfying two criteria: (1) $\overline{\lambda'}$ is equal to 1, and (2) s'_λ is minimized. Evidently, when the data available for calibration are limited, i.e., m in equations (3) and (4) is not sufficiently large, both $\overline{\lambda'}$ and s'_λ could be significantly influenced by m and D, resulting in unstable calibration outcomes.

2.2. Root Mean Squared Error (RMSE) Approach. This method assesses the accuracy of a model by computing its root mean squared error (RMSE) between model predictions (i.e., y_k or y'_k) and measured (true) values (d_k). The RMSE can be computed as

$$r = \sqrt{\frac{1}{m}\sum_{k=1}^{k=m}(y_k - d_k)^2}, \quad (5)$$

for the original model, i.e., $y = f(x)$, and

$$r' = \sqrt{\frac{1}{m}\sum_{k=1}^{k=m}(y'_k - d_k)^2}, \quad (6)$$

for the calibrated (corrected) model, i.e., $y' = f_M(x; C) \times f(x)$.

The calibration principle of the RMSE method is to select C that minimizes r'. Note that this method does not necessarily result in $\overline{\lambda'} = 1$ with minimal COV'_λ, where $\mathrm{COV}'_\lambda = s'_\lambda/\overline{\lambda'}$ is the coefficient of variation of λ'. Although the RMSE method has been widely used for geotechnical model development and calibrations, it does not provide an intuitive impression of model accuracy.

2.3. Model Competence Ranking. The Bayesian information criterion (BIC) is a relative measure of goodness-of-fit among models given observed data and has been widely used in ranking model competence [29, 30]. The BIC is computed as

$$BIC = -2\ \ln\left(L_{\max}\right) + \kappa\ \ln\left(n\right), \tag{7}$$

where $\ln(L_{\max})$ is the log of the maximum likelihood, κ is the number of model parameters, and n is the number of data points.

Typically, the maximum value of the likelihood function (L) and the corresponding maximum likelihood estimators can be found using numerical methods. Technical descriptions of the maximum likelihood estimation method, e.g., the construction of a likelihood function, are not provided here for brevity. Interested readers are directed to, e.g., Juang et al. [31] and Lin and Liu [14] for more details.

The criterion simply states that the smaller the BIC value of a fitting model, the better the model captures the observations. It should be emphasized that the absolute value of the BIC itself is meaningless in terms of model competence; only the difference between BICs helps ranking the models.

2.4. Discussion. Although the above two approaches have been widely adopted for geotechnical model calibrations based on observed data, there are some fundamental differences in calibration outcomes and interpretations, as given in Table 1.

The PDC approach uses two indicators to jointly describe the model accuracy, i.e., $\overline{\lambda'}$ and s'_λ; whereas, the RMSE approach uses only one indicator, r'. Typically, $\overline{\lambda'}$ is interpreted as an indicator for on-average accuracy, while s'_λ is taken as an indicator for dispersive accuracy. The advantage of such an accuracy assessment scheme is that it provides an immediate and general idea of the performance of a model. For example, $\overline{\lambda'} = 0.90$ and $\mathrm{COV}'_\lambda = s'_\lambda/\overline{\lambda'} = 0.30$ suggest that overall model predictions are 10% larger than the corresponding observations, while the dispersion in prediction accuracy is 30%. Clearly, if a model is perfect, then it would have $\overline{\lambda'} = 1$ and $\mathrm{COV}'_\lambda = 0$. The disadvantage is probably the lack of ability to compare accuracies among models. This can be easily seen for two models, for example, A and B, where A has $\overline{\lambda'} = 0.90$ and $\mathrm{COV}'_\lambda = 0.30$ and B has $\overline{\lambda'} = 0.80$ and $\mathrm{COV}'_\lambda = 0.20$. In such a case, model A has a better on-average accuracy, but its prediction is more dispersive; whereas, model B has a less on-average accuracy, but the prediction spreads less. Hence, it is difficult to directly determine which model is more accurate, if without any further analyses.

For the RMSE approach, the smaller the r', the better the model accuracy. For a perfect model, $r' = 0$. As this method uses a single index for model assessment, accuracy comparison among models is straightforward. However, this approach does not provide an intuitive sense of accuracy of the model itself.

Another difference is the criteria set for calibration. The PDC approach minimizes s'_λ or COV'_λ conditioned on $\overline{\lambda'} = 1$. A mean of $\lambda\prime$ of one represents that the calibrated model is unbiased on average, within the context of observations D. The objective of the RMSE approach is to minimize r' to obtain the best accuracy. As has been pointed out earlier, usually this is not necessarily equivalent to the criteria for the PDC approach.

Table 1: Comparisons of the two model calibration approaches.

Approach	Accuracy indicator	Calibration criterion
PDC	$\overline{\lambda'}$ and s'_λ	Maintain $\overline{\lambda'} = 1$ and minimize s'_λ
RMSE	r'	Minimize r'

Generally, both PDC and RMSE approaches can only handle uncensored data. If observation data are censored, then more robust approaches such as the maximum likelihood method or Bayesian inference technique can be employed. However, to do so, the maximum likelihood method and Bayesian approach would have to first assume the probability distribution of λ' so as to construct the likelihood function L. Therefore, the estimators by these approaches are conditioned on the distribution of λ'. For PDC and RMSE approaches, $\overline{\lambda'}$ and s'_λ and r' are computed without any assumptions of distribution of λ'.

Last, it is pointed out that while each measurement or observation is equally weighted in the PDC calibration approach, it is not the case in the RMSE calibration approach. For the RMSE approach, measurements with large values weigh much more than those with small values in the calibration process.

3. Case Study

This section presents a case study to elaborate the difference in model calibration outcomes using the two approaches. The example is to calibrate the default Federal Highway Administration (FHWA) simplified model for computation of facing loads of soil nail walls using a total of 23 measured data. These data were collected by Liu et al. [32] from the literature. They corresponded to facing loads monitored during or at completion of wall constructions. Hence, they should be interpreted as "short-term" facing loads.

In the following, the measured facing load database established by Liu et al. [32] is first introduced, followed by a brief review of the default FHWA simplified facing load model. Section 3.3 presents the calibration results along with comparisons and discussion. Note that calibration of the FHWA facing load model has been done by Liu et al. [32] using the PDC approach. Section 3.4 shows how would the selection of calibration approaches affect the practical designs of facing of soil nail walls.

3.1. Database of Short-Term Facing Loads. Figure 1 shows the side and front views of the facing of a typical soil nail wall. Nails are structurally connected to the facing at their heads. As the wall deforms, lateral active earth pressures act onto the facing, which are then transferred to nails due to the nail-facing connections. In equilibrium state, a nail is responsible for the lateral earth pressure within a tributary area where the nail head centers. The product of the earth pressure and

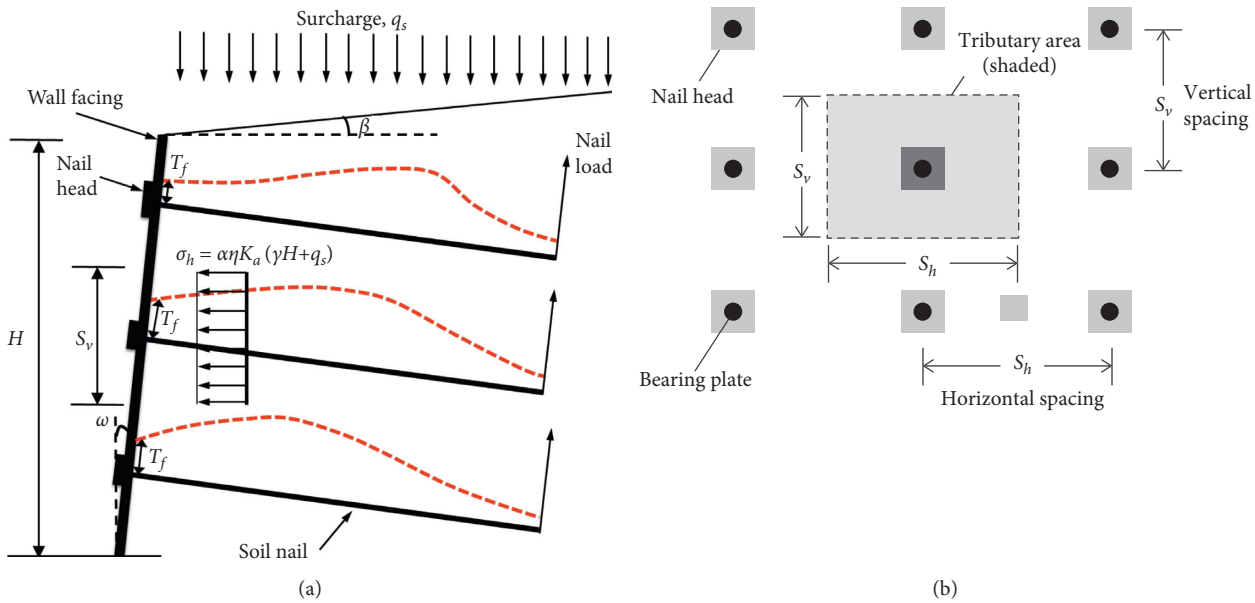

Figure 1: Facing of a typical soil nail wall: (a) side view; (b) front view.

the tributary area is referred to as the nail head tensile load or facing load (Figure 1(a)) in this study. Here, the tributary area is the product of horizontal and vertical nail spacing (Figure 1(b)).

Liu et al. [32] developed a database containing measured long-term and short-term facing loads. The short-term load data are extracted and briefly reviewed here for the reader's convenience to follow. They collected in total 31 short-term load data; however, 8 were identified as questionable data and thus filtered from analyses. Table 2 provides the wall geometry, soil properties, facing type, and nail spacing for soil nail walls where the remaining 23 data were from.

The data were collected from five wall sections, ranging from 4 to 12 m high. All walls had vertical or steep facings and horizontal back slopes. Four walls were in cohesionless soils, while one was in cohesive soil. Two walls were subjected to surcharge, in addition to soil self-weights. The facings were constructed with shotcrete or concrete panels. Nail spacings were set between 1 and 2 m, which are typical. Readers are directed to Liu et al. [32] for detailed description of the collected facing load data.

3.2. FHWA Facing Load Models. The facing of a soil nail wall, as shown in Figure 1, can be simplified as a continuous two-way slab. According to the FHWA soil nail wall design manuals [33], under working conditions, the maximum facing load due to the lateral active earth pressure, T_f, can be calculated as

$$T_f = \alpha\eta K_a(\gamma H + q_s)S_hS_v, \tag{8}$$

where α is the empirical spacing factor expressed as $\alpha = 0.6 + 0.2(S_{\max} - 1)$; $S_{\max}$ (unit: m) is the larger of horizontal and vertical nail spacing S_h and S_v, respectively; η is the empirical depth factor expressed as $\eta = 1.25\,\mathrm{h}/H + 0.5$ for $0 < \mathrm{h}/H \le 0.2$, $\eta = 0.75$ for $0.2 < \mathrm{h}/H \le 0.7$, and $\eta = 2.03 - 1.83\,\mathrm{h}/H$ for $0.7 < h/H \le 1$, where h and H are the depth and wall height, respectively; K_a, γ, and q_s are the Coulomb active earth pressure coefficient, soil unit weight, and surcharge, respectively.

The measured facing loads (T_m) are plotted against the corresponding predicted T_f using equation (8), as shown in Figure 2(a). The data points in the figure appear to be two clusters: one around the 1 : 1 correspondence line and the other below the line. This suggests that the current default FHWA facing load model is conservative as generally it would overestimate the maximum facing loads. This observation is confirmed by computing the sample mean ($\bar{\lambda}$) and sample COV (COV_λ) of λ of equation (8), which are $\bar{\lambda} = 0.77$ and $\mathrm{COV}_\lambda = 0.669$. Hence, on average, equation (8) overpredicts the maximum facing loads by 23%, and the predictions are highly dispersive, according to the ranking scheme proposed by Phoon and Tang [18]. Furthermore, Figure 2(b) shows that λ tends to decrease as T_f increases. The dependency is quantitatively confirmed at a level of significance of 0.05 by Spearman's rank correlation test results that are also given in the figure. Such a dependency is undesirable, and its effects on reliability-based geotechnical design have been investigated by Lin and Bathurst [34]. As a result, it is necessary to perform model calibration for equation (8) for accuracy improvements.

To identify the sources of model errors and the abovementioned dependency, λ are plotted against each input parameter of equation (8), as shown in Figure 3. Spearman's rank correlation test results show that λ are statistically correlated to α, K_a, and S_hS_v at a significance level of 0.05. Therefore, a correction term which is a function of these three parameters can be introduced to the equation for calibration, i.e., $M = f(\alpha, K_a, S_hS_v)$. However, since α and S_hS_v are highly correlated, only S_hS_v is kept, while α is removed from M formulation for simplification. Moreover, K_a is removed from M to further simplify the calibration as

Table 2: Summary of wall geometry, soil properties, facing type, and nail spacing for soil nail walls.

Wall	Soil type	Wall geometry			Soil strength properties			q_s (kPa)	Facing type	Nail spacing	
		H (m)	ω (°)	β (°)	ϕ (°)	c (kPa)	γ (kN/m^3)			S_h	S_v
W1	Heterogenous SM	9.2	0	0	36.5	18.5	16.3	0	Shotcrete	1.85	1.85
W2	Glacial tills	12	10	0	32	0	20	22.5	Shotcrete	1.5–1.9	0.9–1.55
W3	Fill, silt, sand	7.6	0	0	38	0	19.6	0	N/A	1.83	1.22–1.83
W4	Gravelly silty sand	4	0	0	35	0	19.6	0	Concrete panel	1.0	1.05
W5	Gravelly silty sand	5	0	0	35	0	19.6	127	Concrete panel	1.0	1.05

H, wall height; ω, face batter angle; β, back slope angle; ϕ, soil friction angle; c, soil cohesion; γ, soil unit weight; q_s, surcharge; S_h, horizontal nail spacing; S_v, vertical nail spacing.

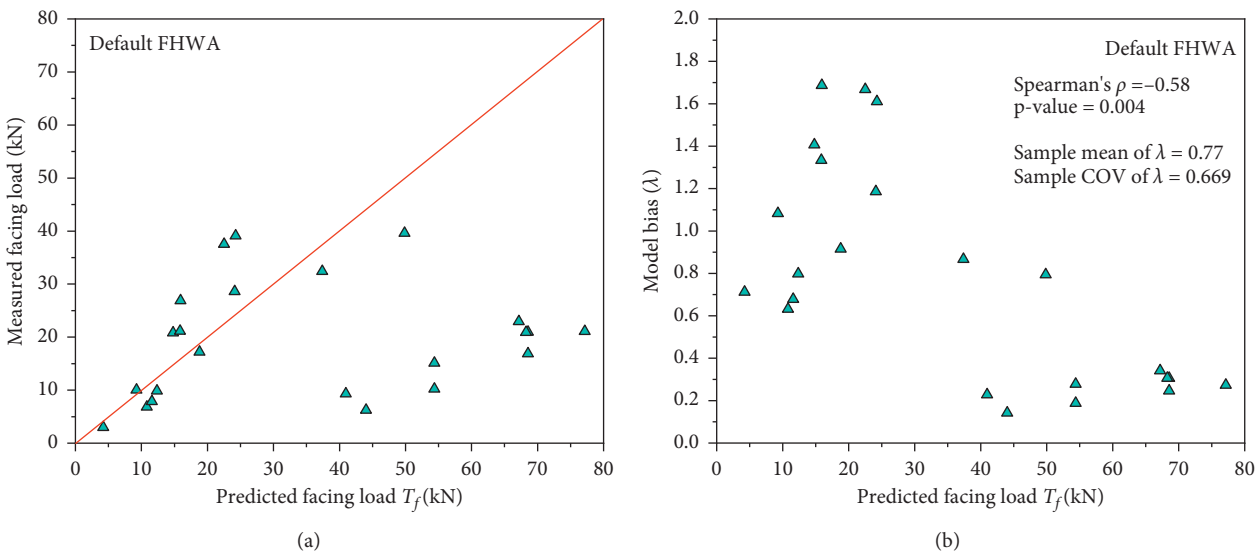

Figure 2: Analyses of accuracy of the default FHWA simplified facing load model: (a) measured versus predicted facing load; (b) model bias versus predicted facing load.

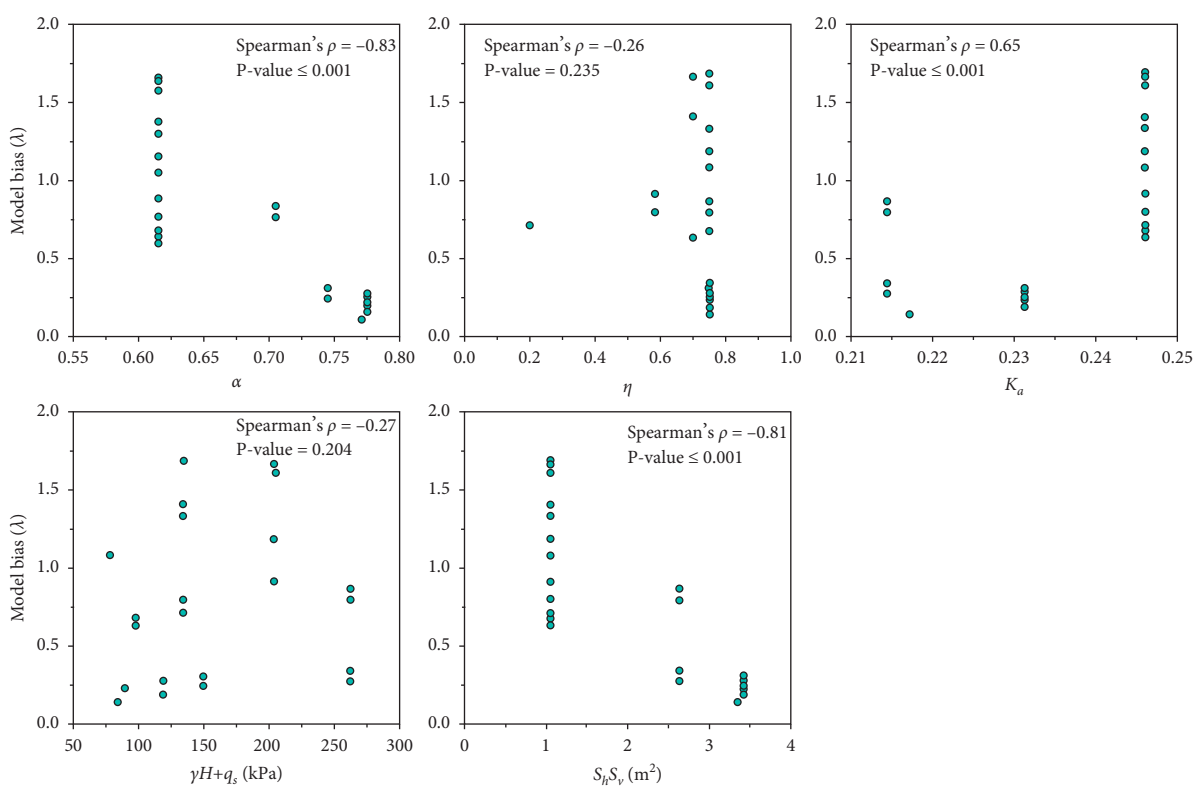

Figure 3: Plots of model bias λ for the default FHWA facing load model against various input parameters.

the focus of this study is on comparison of calibration approaches rather than model development. Last, a power form expression is assumed for M, and thus, equation (8) becomes

$$T_f = M\alpha\eta K_a(\gamma H + q_s)S_h S_v = a\left(\frac{S_h S_v}{A_t}\right)^b \alpha\eta K_a(\gamma H + q_s)S_h S_v, \tag{9}$$

where a and b are the empirical constants to be determined using the 23 measured facing load data; and $A_t = 2.25\,\mathrm{m}^2$ is the typical tributary area used to make M dimensionless. The PDC and RMSE approaches discussed earlier in this study are then used to determine the values of a and b. The results are shown and discussed in the next section.

3.3. Analysis Results. Calibration of equation (9) is carried out in this section. The accuracy of the calibrated model is then compared based on sample mean and sample COV and also root mean squared errors (RMSEs). After that, the accuracy is rescrutinized from a maximum likelihood perspective, which helps understanding the calibration outcomes.

3.3.1. Comparisons between PDC and RMSE Approaches. Table 3 provides the calibration outcomes for equation (9) using the two approaches. By using the PDC approach, the constants in equation (9) are determined as $a = 0.4964$ and $b = -1.0677$, which correspond to $\overline{\lambda\prime} = 1.00$ and a minimal $\mathrm{COV}'_\lambda = 0.432$. The RMSE for this case is computed to be 38.3618. On the other hand, by the RMSE approach, the optimal a and b values are found to be 0.4866 and −1.3118, respectively. The minimal RMSE is 35.9635. The sample mean and sample COV for this case are $\overline{\lambda'} = 0.96$ and $\mathrm{COV}'_\lambda = 0.452$. Several interesting observations can be made from these results.

First, these two approaches are not practically equivalent from the perspective of model calibration when the data volume available for the calibration is small. The resulted a values are close, i.e., 0.4964 versus 0.4866; whereas, the b values are significantly different, i.e., −1.0677 versus −1.3118.

Second, based on bias statistics of equation (9), the PDC approach appears to be superior as its results are unbiased on average and less dispersive compared to those by the RMSE approach (i.e., 4% overestimation and 2% more dispersive). Interestingly, if comparing the RMSEs, one would easily reach a reverse conclusion that the RMSE approach is better than the PDC approach as it gives less RMSE, 35.9635 against 38.3618. Therefore, it is difficult to judge which one is better if based merely on the results given in Table 3. The comparison should be made from a third angle, which will be discussed in the next subsection.

Last, both approaches are effective and efficient in model calibration for accuracy enhancement. The essence of calibration is to move the data points towards the 1 : 1 correspondence line in general, as shown in Figure 4. The difference is that $\lambda\prime$ by the PDC approach seems to be more skewed, while those by the RMSE approach appear to be more uniform. Despite of this, $\lambda\prime$ by the two approaches follow closely along the 1 : 1 correspondence line, and thus, the two methods in general do not lead to fatally different outcomes.

3.3.2. Rescrutinization from a Maximum Likelihood Perspective. The accuracies of the three facing load models, i.e., default FHWA, calibrated FHWA by PDC, and calibrated FHWA by RMSE, are reassessed in this section using the maximum likelihood method. The cumulative distributions of λ and λ' are shown in Figure 5. Kolmogorov–Smirnov tests are applied to the three bias datasets, and the results show that all the datasets can be considered as both normally and log-normally distributed at a significance level of 0.05. Hence, the maximum likelihood estimation (MLE) is carried out assuming normal and log-normal λ and λ'. The estimation outcomes are given in Table 4.

For both cases, the estimated means by MLE are practically the same as the sample means; while, the estimated COVs by MLE are slightly less than the sample COVs, i.e., about 2–4% which are practically neglectable. However, for the default model case (i.e., equation (9)), the estimated bias COV by MLE assuming log-normal λ is much larger than the sample COV or that assuming normal λ, i.e., about 20% higher.

For the normal case, the computed maximum loglikelihood values $\ln(L_{\max})$ are −12.8317 and −12.9868 for the PDC and RMSE approaches, respectively. As for both models, the number of parameters is $\kappa = 2$, and the number of data points is $n = 23$; by using equation (7), the BIC values are correspondingly calculated to be 31.93 and 32.24. This means that, if λ' is a normal random variable, then in this case, the PDC calibration approach is better than the RMSE approach as the BIC value for the former is smaller. On the other hand, $\ln(L_{\max})$ are −9.5680 if using the PDC approach and −8.6353 if using the RMSE approach. The corresponding BIC values are 25.41 and 23.54. This suggests that if λ' is a log-normal random variable, then model calibration using the RMSE approach is preferable. For both approaches, the $\ln(L_{\max})$ values for the log-normal case are always less than those for the normal case; hence, it can be said that λ' is more likely a log-normal random variable. If comparing the four $\ln(L_{\max})$ values, one would conclude that the RMSE-log-normal scenario is the best one as its $\ln(L_{\max})$ is the smallest one.

3.4. Practical Influences. Analyses presented earlier show how the selection of a calibration approach would affect the calibration outcomes, i.e., $C = (a, b)$. In this part, we investigate the influences of the calibration outcomes on practical designs of facing of soil nail walls. The facing design must ensure adequate margins of safety against various limit states, including facing flexural, punching shear, and headed-studs tensile failures. For illustration purposes, here we only consider the facing flexural limit state, which requires estimation of the maximum facing load and the ultimate facing flexure capacity. The primary design parameter for this limit state is the reinforcement ratio cross-sectional area per unit width at the nail head

Table 3: Summary of calibration outcomes of equation (10) using the PDC and RMSE approaches.

Model	Approach	Constant in C		Model bias, λ or λ'		RMSE
		a	b	Sample mean	Sample COV	
Default FHWA	N/A	1	0	0.77	0.669	140.7869
Calibrated FHWA	PDC	0.4964	−1.0677	1.00	0.432	38.3618
	RMSE	0.4866	−1.3118	0.96	0.452	35.9635

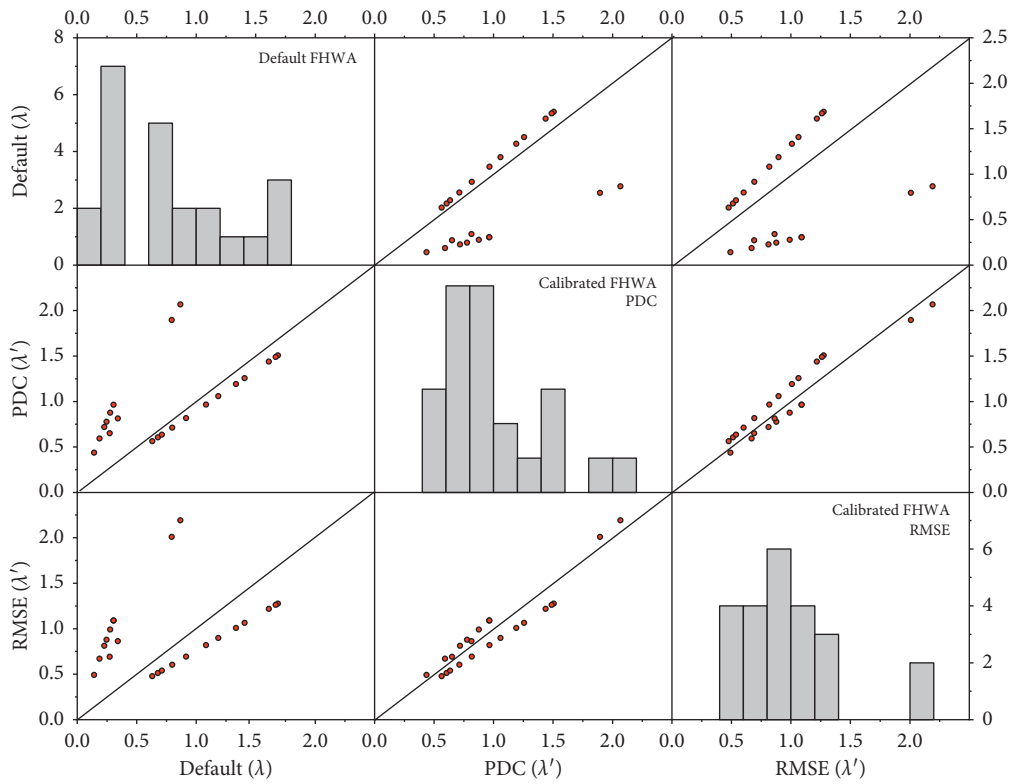

Figure 4: Histograms and comparisons of model biases λ and λ'.

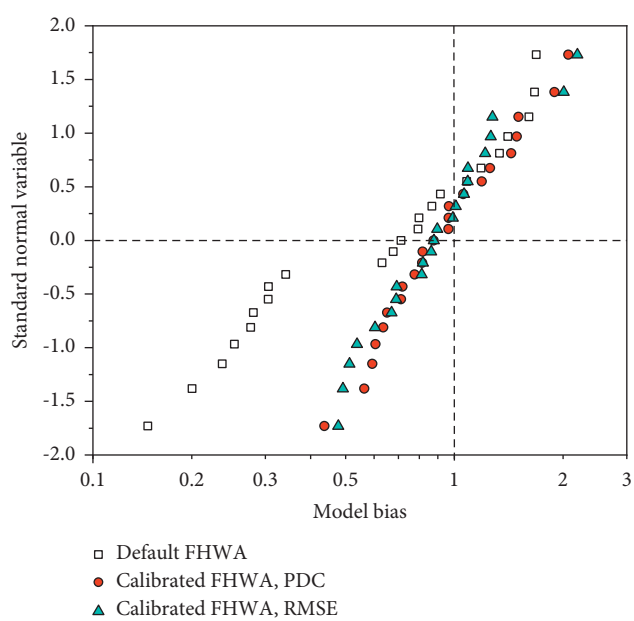

Figure 5: Cumulative distributions of model biases of the default and calibrated FHWA facing load models.

Table 4: Estimated statistics of model bias, λ, or λ' using the maximum likelihood method.

Model	Approach	Normal			Log-normal		
		Mean	COV	$\ln(L_{\max})$	Mean	COV	$\ln(L_{\max})$
Default FHWA	N/A	0.77	0.654	−16.8202	0.79	0.888	−14.3902
Calibrated FHWA	PDC	1.00	0.423	−12.8317	1.00	0.414	−9.5680
	RMSE	0.96	0.442	−12.9868	0.96	0.414	−8.6353

and at midspan. The influences of the two calibration approaches are assessed by using C to compute the maximum facing loads and to determine the reinforcement ratio.

The example wall used for analysis is 10 m in height with a horizontal back slope ($\beta = 0^\circ$) and a vertical facing ($\omega = 0^\circ$). The means of the soil strength parameters are assumed to be $c = 0$ kPa, $\phi = 30^\circ$, and $\gamma = 18\,\text{kN/m}^3$. The COVs are taken as 0.15 for ϕ and 0.075 for γ. Nails are spaced at 1.2 m horizontally and vertically.

3.4.1. On Estimation of Facing Loads. Both equations (9) and (10) are used to compute the nominal facing loads (T_f) along depth (h/H). The results are shown in Figure 6. Visually, T_f along h/H is a trapezoidal shape with larger values in the middle and smaller values at the top and bottom of the wall. The default FHWA model gives the highest facing loads, for example, at $h/H = 0.5$, the nominal T_f is about 42 kN; while, the calibrated FHWA model by the PDC approach gives the smallest T_f, which is about 33 kN. The difference is over 20%. The T_f by the calibrated FHWA model by the RMSE approach is about 36 kN. The difference in T_f using the two approaches is about 8%.

Figure 7 shows the distributions of facing loads corrected by biases, λT_f or $\lambda' T_f$, where the statistics of λ and $\lambda\prime$ are estimated by the method of moment (referred to as sample bias) and maximum likelihood method (referred to as MLE bias). Visually, the distributions of $\lambda' T_f$ by PDC and RMSE approaches are highly similar, regardless of the methods used to compute bias statistics. Compared to the calibrated FHWA cases, the distributions of λT_f for the default FHWA case move leftward, meaning that λT_f overall is smaller than $\lambda' T_f$. There is a noticeable difference in λT_f distributions by sample bias and MLE bias, mainly due to the large difference in COV of λT_f, as given in Table 5, which summarizes computed means and COVs of λT_f and $\lambda\prime T_f$ at $h/H = 0.5$ using different calibration approaches and bias estimation approaches. On the other hand, λT_f for the default FHWA case has longer tails than those for the calibrated FHWA cases; obviously, this is due to the much higher COVs of λT_f, compared to those for $\lambda' T_f$. Last, it is observed that, in general, the differences in the means and COVs of $\lambda' T_f$ based on RMSE and PDC approaches are practically insignificant, as given in Table 5.

3.4.2. On Facing Design. Consider identical reinforcement cross-sectional area per unit width at the nail head and at midspan ($a_n + a_m$) horizontally and vertically, with $S_h = S_v$, the facing flexural capacity, R_F, calculated as [33]

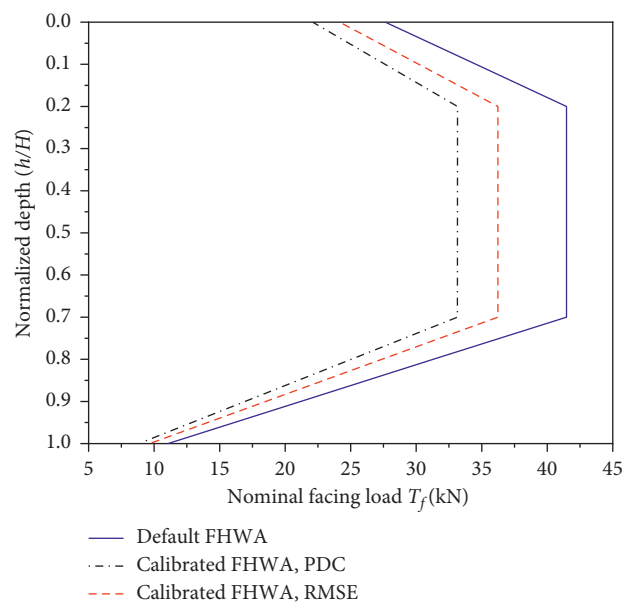

Figure 6: Predicted (nominal) maximum facing loads along depth using the three FHWA models.

$$R_F = \frac{C_F}{265}(a_n + a_m) t f_y. \tag{10}$$

where C_F is the empirical factor accounting for the non-uniformity of soil pressures behind the facing and is equal to 2.0, 1.5, and 1.0 for temporary walls when the facing thickness is $t = 100, 150$, and 200 mm [35], and f_y is the reinforcement tensile yield strength. In this example, the facing thickness is taken as $t = 100$ mm, and thus, $C_F = 2.0$. The nominal value of f_y is taken as 414 MPa. The reinforcement area ($a_n + a_m$) is the main design parameter to be determined given a target margin of safety (e.g., factor of safety or reliability index). The design factor of safety for this limit state can be calculated as

$$FS = \frac{R_F}{T_f}. \tag{11}$$

The performance function, g_F, can be written as

$$g_F = \lambda_R R_F - \lambda_L T_f. \tag{12}$$

where λ_R and λ_L are the model factors (model factors (biases) for R_F and T_f, respectively. In this study, λ_L is λ if using the default FHWA model and λ' if using the calibrated FHWA models. λ_R is taken as a log-normal random variable with mean of 1.1 and COV of 0.1 [36, 37].

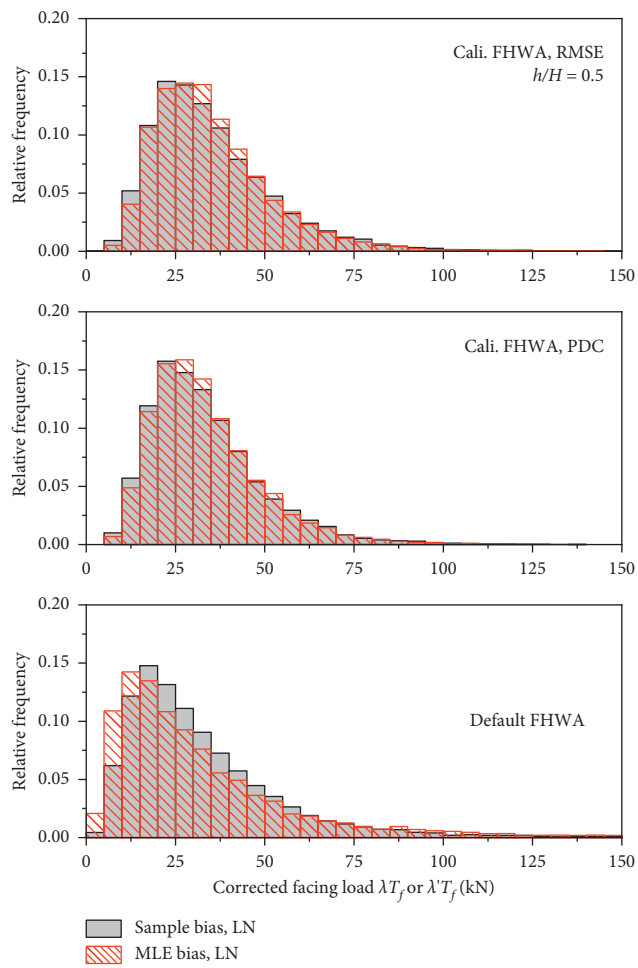

Figure 7: Histograms of facing load at $h/H = 0.5$ corrected by different biases, λT_f or $\lambda' T_f$.

Table 5: Summary of computed means and COVs of λT_f and $\lambda' T_f$ at $h/H = 0.5$ using different calibration approaches and bias estimation approaches.

Bias statistics	λT_f by default FHWA		$\lambda' T_f$ by calibrated FHWA, PDC		$\lambda' T_f$ by calibrated FHWA, RMSE	
	Mean (kN)	COV	Mean (kN)	COV	Mean (kN)	COV
By sample	32.21	0.700	33.39	0.478	35.21	0.500
By MLE	33.11	0.945	33.45	0.457	35.19	0.464

Table 6 provides the design outcomes of $(a_n + a_m)$ using the deterministic approach where the margin of safety is taken as $FS = 2.0$ and using the reliability approach where the margin of safety is taken as $\beta_T = 3.50$. Here, β_T is the target reliability index, and $\beta_T = 3.50$ roughly corresponds to a probability of failure of 1/5000. Note that these FS and β_T values are consistent with those recommended in the FHWA soil nail wall design manual by Lazarte et al. [33] and Aashto [38]. Based on the deterministic approach (equation (11)), using the FHWA facing load model calibrated by the PDC approach gives the least $((a_n + a_m))$, which is 212 mm^2/m; whereas, the default FHWA model gives the highest value, i.e., 266 mm^2/m. The difference is about 20%.

However, based on the reliability approach, the computed $(a_n + a_m)$ values using the default FHWA model are much larger than those using the calibrated FHWA models, i.e., 730 versus 446 and 492 and 1135 versus 430 and 447. The difference is about 40–60%. The design outcomes by the calibrated FHWA models by PDC and RMSE approaches are more or less similar, albeit those by the RMSE approach are slightly higher.

Figure 8 shows the $(a_n + a_m)$ values with respect to FS ranging from 1 to 5 and β_T ranging from 2 to 4 using the default and calibrated FHWA facing load models. It confirms that the difference in $(a_n + a_m)$ is insignificant between the two calibrated FHWA models; both are much less than those obtained by the default model. This highlights the importance of performing geotechnical model calibration while the influence of selection of the model calibration approach is secondary. Tables 5 and 6 and Figure 8 together

Table 6: Comparisons of reinforcement area per unit width for facing design against flexural failures using default and calibrated FHWA simplified facing load models.

Approach	Reinforcement area per unit width, $(a_n + a_m)$ (mm^2/m)		
	$FS = 2.0$	$\beta_T = 3.50$, sample bias	$\beta_T = 3.50$, MLE bias*
Default FHWA	266	730	1135
Cali. FHWA, PDC	212	446	430
Cali. FHWA, RMSE	232	492	447

*Assuming log-normal distribution for bias.

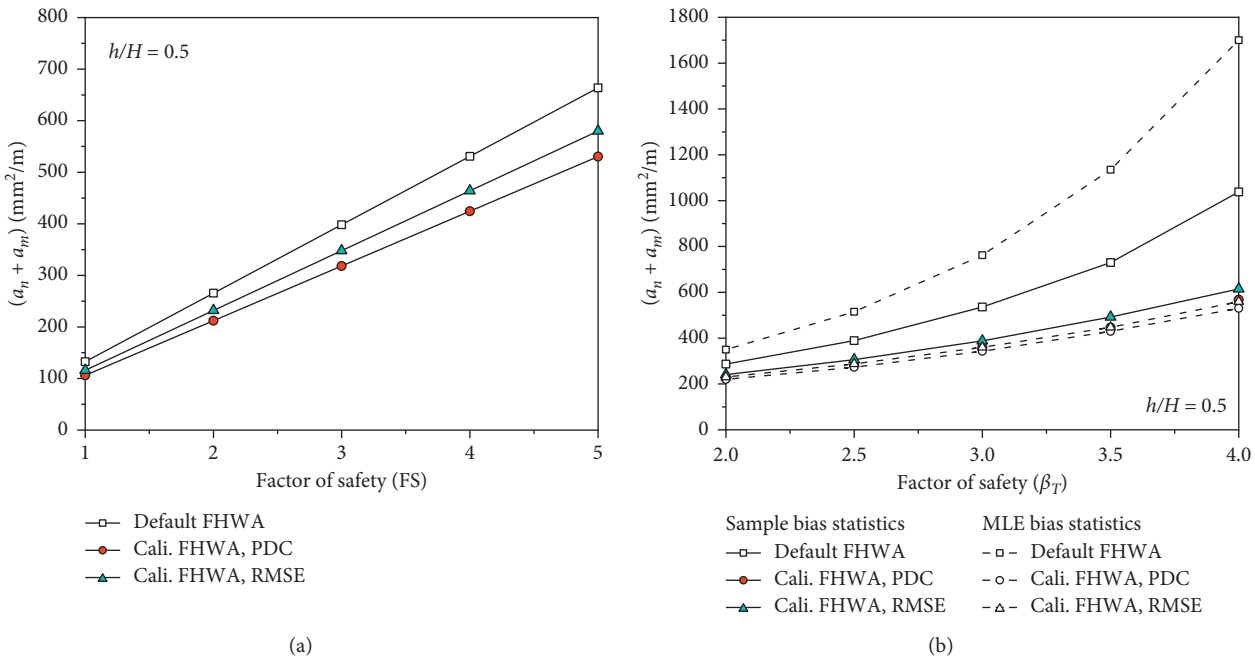

Figure 8: Plots of design outcomes of $(a_n + a_m)$ against FS ranging from 1 to 5 and β_T ranging from 2 to 4.

suggest that adopting the PDC and RMSE approaches for geotechnical model calibration does not result in a fatal difference on practical design outcomes, even under scare data conditions.

4. Conclusions

Calibrations of geotechnical models in many cases have to be carried out with scarce data. This study examines two approaches that have been widely adopted for geotechnical model calibration in the literature, namely, pure data-catering (PDC) approach and root mean squared error (RMSE) approach. The PDC approach calibrates a model by adhering to two criteria: maintaining mean of model bias of one while minimizing COV of model bias, where model bias is defined as the ratio measured to the predicted value. The RMSE approach calibrates a model by minimizing the root mean squared error between measured and predicted values.

A case study is presented to elaborate the influence of selection of model calibration approaches from a practical point of view. The case study is on calibration of the default Federal Highway Administration (FHWA) simplified facing load model for facing design of soil nail walls. A total of 23 measured facing load data collected by Liu et al. [15] are adopted for calibration. Calibration results confirm that the two approaches are not practically equivalent when the data available for calibration are scarce. A model calibrated by the PDC approach usually does not reach minimal RMSE or vice versa. The Bayesian information criterion (BIC) is introduced to rank the competence of the PDC and RMSE-calibrated models fitting to the data. According to BIC, a model calibrated by the PDC approach may or may not be superior to its counterpart by the RMSE approach, depending on the assumption of distribution of model bias.

The two PDC- and RMSE-calibrated models are then used for estimation of facing loads and design of reinforcement ratio against the facing flexure limit state using both deterministic and reliability-based design approaches. It is demonstrated that the estimated facing loads and the determined reinforcement ratios using both calibrated models do not differ significantly from each other. Therefore, in practice, either approach can be adopted for geotechnical model calibration even with scarce data.

Last, there are also other approaches for model calibrations, for example, the Bayesian inference technique. The Bayesian approach provides distributions other than point estimates for estimation of model parameters. This sets the basic differences between the Bayesian approach and the

PDC and RMSE approaches. Discussion on parameter determination using Bayesian approaches can be referenced to, e.g., Lin and Yuan [39] and Lin et al. [40].

Data Availability

The data used to support the findings of this study are included within the article.

Conflicts of Interest

The authors declare that they have no conflicts of interest.

Acknowledgments

The authors are grateful for financial support provided by Guangdong Provincial Key Laboratory of Marine Civil Engineering (LMCE202107).

References

[1] Z. Cao, Y. Wang, and D. Li, *Probabilistic Approaches for Geotechnical Site Characterization and Slope Stability Analysis*, Springer, Verlag Berlin Heidelberg, 2017.

[2] International Organization for Standardization, *General Principles on Reliability of Structures*, ISO2394:2015, Geneva, Switzerland, 2015.

[3] K.-K. Phoon, "The story of statistics in geotechnical engineering," *Georisk: Assessment and Management of Risk for Engineered Systems and Geohazards*, vol. 14, no. 1, pp. 1–23, 2019.

[4] K.-K. Phoon, "The story of statistics in geotechnical engineering," *Georisk: Assessment and Management of Risk for Engineered Systems and Geohazards*, vol. 14, no. 1, pp. 3–25, 2020.

[5] K.-K. Phoon, J. Ching, and T. Shuku, "Challenges in data-driven site characterization," *Georisk: Assessment and Management of Risk for Engineered Systems and Geohazards*, pp. 1–13, 2021.

[6] B. Bai, G.-c. Yang, T. Li, and G.-s. Yang, "A thermodynamic constitutive model with temperature effect based on particle rearrangement for geomaterials," *Mechanics of Materials*, vol. 139, Article ID 103180, 2019.

[7] B. Bai, Q. Nie, Y. Zhang, X. Wang, and W. Hu, "Cotransport of heavy metals and SiO 2 particles at different temperatures by seepage," *Journal of Hydrology*, vol. 597, no. 2, Article ID 125771, 2020.

[8] Y. Wu, J. Cui, J. Huang, W. Zhang, and N. Yoshimoto, "Correlation of critical state strength properties with particle shape and surface fractal dimension of clinker ash," *International Journal of Geomechanics*, vol. 21, no. 6, Article ID 04021071, 2021.

[9] B. Yuan, M. Sun, L. Xiong, Q. Luo, and H. Li, "Investigation of 3D deformation of transparent soil around a laterally loaded pile based on a hydraulic gradient model test," *Journal of Building Engineering*, vol. 28, no. 6, Article ID 101024, 2019a.

[10] B. Yuan, Z. Li, Z. Zhao, H. Ni, and Z. Li, "Experimental study of displacement field of layered soils surrounding laterally loaded pile based on transparent soil," *Journal of Soils and Sediments*, vol. 21, no. 4, pp. 1–12, 2021a.

[11] B. Yuan, Z. Li, Z. Su, Q. Luo, M. Chen, and Z. Zhao, "Sensitivity of multistage fill slope based on finite element model," *Advances in Civil Engineering*, vol. 2021, Article ID 6622936, 13 pages, 2021b.

[12] B. Yuan, Z. Li, Y. Chen et al., "Mechanical and microstructural properties of recycling granite residual soil reinforced with glass fiber and liquid-modified polyvinyl alcohol polymer - ScienceDirect," *Chemosphere*, vol. 286, Article ID 131652, 2021c.

[13] L. Zhang, F. Wu, Y. Zheng, L. Chen, J. Zhang, and X. Li, "Probabilistic calibration of a coupled hydro-mechanical slope stability model with integration of multiple observations," *Georisk: Assessment and Management of Risk for Engineered Systems and Geohazards*, vol. 12, no. 3, pp. 169–182, 2018.

[14] P. Lin and J. Liu, "Evaluation and calibration of ultimate bond strength models for soil nails using maximum likelihood method," *Acta Geotechnica*, vol. 15, no. 7, pp. 1993–2015, 2020.

[15] P. Lin, R. J. Bathurst, and J. Liu, "Statistical evaluation of the FHWA simplified method and modifications for predicting soil nail loads," *Journal of Geotechnical and Geoenvironmental Engineering*, vol. 143, no. 3, Article ID 04016107, 2017.

[16] P. Lin, P. Ni, C. Guo, and G. Mei, "Mapping soil nail loads using Federal Highway Administration (FHWA) simplified models and artifical neural network technique," *Canadian Geotechnical Journal*, vol. 57, no. 6, pp. 1453–1471, 2020.

[17] K.-K. Phoon and F. H. Kulhawy, "Characterisation of model uncertainties for laterally loaded rigid drilled shafts," *Géotechnique*, vol. 55, no. 1, pp. 45–54, 2005.

[18] K.-K. Phoon and C. Tang, "Characterisation of geotechnical model uncertainty," *Georisk: Assessment and Management of Risk for Engineered Systems and Geohazards*, vol. 13, no. 2, pp. 1–30, 2019.

[19] C. Tang and K.-K. Phoon, "Statistics of model factors and consideration in reliability-based design of axially loaded helical piles," *Journal of Geotechnical and Geoenvironmental Engineering*, vol. 144, no. 8, Article ID 04018050, 2018.

[20] J. Yuan, P. Lin, G. Mei, and Y. Hu, "Statistical prediction of deformations of soil nail walls," *Computers and Geotechnics*, vol. 115, Article ID 103168, 2019b.

[21] J. Yuan, P. Lin, R. Huang, and Y. Que, "Statistical evaluation and calibration of two methods for predicting nail loads of soil nail walls in China," *Computers and Geotechnics*, vol. 108, pp. 269–279, 2019c.

[22] R. J. Bathurst and Y. Yu, "Probabilistic prediction of reinforcement loads for steel MSE walls using a response surface method," *International Journal of Geomechanics*, vol. 18, no. 5, Article ID 04018027, 2018.

[23] H. Liu, P. Lin, C. Guo, Z. Li, and X. Qin, "A shallow artificial neural network for mapping bond strength of soil nails," *Marine Georesources & Geotechnology*, vol. 39, no. 3, pp. 1–13, 2019.

[24] Y. Yu and R. Bathurst, "Probabilistic assessment of reinforced soil wall performance using response surface method," *Geosynthetics International*, vol. 24, no. 5, pp. 524–542, 2017.

[25] J. Zhang, H. Huang, and K. Phoon, "Application of the Kriging-based response surface method to the system reliability of soil slopes," *Journal of Geotechnical and Geoenvironmental Engineering*, vol. 139, no. 4, pp. 651–655, 2012.

[26] J. Zhang, H. Chen, H. Huang, and Z. Luo, "Efficient response surface method for practical geotechnical reliability analysis," *Computers and Geotechnics*, vol. 69, pp. 496–505, 2015a.

[27] W. Zhang, A. T. Goh, and F. Xuan, "A simple prediction model for wall deflection caused by braced excavation in clays," *Computers and Geotechnics*, vol. 63, pp. 67–72, 2015b.

[28] W. Zhang, C. Wu, Y. Li, L. Wang, and P. Samui, "Assessment of pile drivability using random forest regression and multivariate adaptive regression splines," *Georisk: Assessment and Management of Risk for Engineered Systems and Geohazards*, vol. 15, no. 1, pp. 1–14, 2019.

[29] G. Schwarz, "Estimating the dimension of a model," *Annals of Statistics*, vol. 6, no. 2, pp. 461–464, 1978.

[30] K. P. Burnham and D. R. Anderson, "Multimodel inference," *Sociological Methods & Research*, vol. 33, no. 2, pp. 261–304, 2004.

[31] C. H. Juang, J. Ching, L. Wang, S. Khoshnevisan, and C.-S. Ku, "Simplified procedure for estimation of liquefaction-induced settlement and site-specific probabilistic settlement exceedance curve using cone penetration test (CPT)," *Canadian Geotechnical Journal*, vol. 50, no. 10, pp. 1055–1066, 2013.

[32] H. Liu, L. Tang, P. Lin, and G. Mei, "Accuracy assessment of default and modified Federal Highway Administration (FHWA) simplified models for estimation of facing tensile forces of soil nail walls," *Canadian Geotechnical Journal*, vol. 55, no. 8, pp. 1104–1115, 2018.

[33] C. Lazarte, H. Robinson, J. Gómez, A. Baxter, A. Cadden, and R. Berg, *Geotechnical Engineering Circular No. 7 Soil Nail walls—Reference Manual*, Rep. No. FHWA-NHI-14-007, Federal Highway Administration, Washington, DC, 2015.

[34] P. Lin and R. J. Bathurst, "Influence of cross correlation between nominal load and resistance on reliability-based design for simple linear soil-structure limit states," *Canadian Geotechnical Journal*, vol. 55, no. 2, pp. 279–295, 2018a.

[35] R. Byrne, D. Cotton, J. Porterfield, C. Wolschlag, and G. Ueblacker, *Manual for Design and Construction Monitoring of Soil Nail walls*, Federal Highway Administration, Washington, DC, 1998.

[36] P. Lin and R. J. Bathurst, "Reliability-based internal limit state analysis and design of soil nails using different load and resistance models," *Journal of Geotechnical and Geoenvironmental Engineering*, vol. 144, no. 5, Article ID 04018022, 2018b.

[37] P. Lin and R. J. Bathurst, "Calibration of resistance factors for load and resistance factor design of internal limit states of soil nail walls," *Journal of Geotechnical and Geoenvironmental Engineering*, vol. 145, no. 1, Article ID 04018100, 2019.

[38] Aashto, *LRFD Bridge Design Specifications*, American Association of State Highway and Transportation Officials (AASHTO), Washington DC, 9th Ed. edition, 2020.

[39] P. Lin and X.-X. Yuan, "A two-time-scale point process model of water main breaks for infrastructure asset management," *Water Research*, vol. 150, pp. 296–309, 2019.

[40] P. Lin, X. X. Yuan, and E. Tovilla, "Integrative modeling of performance deterioration and maintenance effectiveness for infrastructure assets with missing condition data," *Computer-Aided Civil and Infrastructure Engineering*, vol. 34, no. 8, pp. 677–695, 2019.

Hindawi
Advances in Civil Engineering
Volume 2021, Article ID 1743778, 6 pages
https://doi.org/10.1155/2021/1743778

Research Article

Decision Making of Curriculum Attainment Degree for Engineering Geology Based on Fuzzy Set Theory

Binbin Yang,[1] **Shuting Du**,[1] **Xiaoming Zhao**,[1] **Dongqi Tang**,[1] **and Changde Yang**[2]

[1]*School of Civil Engineering, Xuchang University, Xuchang 461000, Henan, China*
[2]*School of Mining Engineering and Geology, Xinjiang Institute of Engineering, Urumqi 830023, Xinjiang Uygur Autonomous Region, China*

Correspondence should be addressed to Binbin Yang; ybb008008@hotmail.com

Received 1 November 2021; Accepted 15 November 2021; Published 26 November 2021

Academic Editor: bingxiang yuan

The study of engineering geology emphasizes the combination of theory and practice, and it highlights the comprehensive cultivation of curricular theory, curricular practice, and comprehensive skills. It is necessary to establish a set of effective methods to evaluate the achievement of training objectives to track, test, and improve the quality of curricular learning. In this paper, the principle of the fuzzy analytic hierarchy process based on entropy is used to construct an evaluation index system for the goal achievement degree of engineering geology courses, and the primary indicators mainly include knowledge, ability, and quality. Based on the actual situation, five curricular achievement levels are determined, that is, the comment set V = {very low, low, medium, high, very high}. Relying on the engineering geology course resource database of Xuchang University, the course goal achievement degree is evaluated, and the results show that the engineering geology course achievement degree is high. This method is suitable not only for the evaluation of the achievement of curricular objectives but also for the evaluation of the achievement of engineering education graduation requirements. This method can also help us find different courses and teaching weak links supporting the index points, indicate the direction and provide support for teachers to continuously improve their teaching and management methods, and effectively promote a continuous improvement in teachers' teaching level and teaching quality.

1. Introduction

With the rapid development in the engineering construction, the relationship between engineering construction and the environment is becoming increasingly prominent, and the geological conditions of engineering construction are becoming increasingly complex [1, 2]. Therefore, the new form has increasingly higher requirements for college students' innovative ability, which strengthens the demand for reform in colleges and universities with regard to the mode of diversified and personalized training of students' innovative ability, and it is necessary to cultivate engineering scientific and technological talent with innovative ability. The concept of outcome-based education (OBE) is student centered and student oriented, and it represents the mainstream direction of reform in the context of engineering education professional certification. Engineering education professional certification advocates the concept of OBE throughout the whole process of talent training. It is an internationally accepted engineering education quality assurance system. Many domestic colleges and universities use this concept and method in specialty construction and talent training [3]. The gradual application of modern information technologies such as the Internet and big data in education and teaching has triggered changes in traditional majors and disciplines such as civil engineering and forced colleges and universities to reconstruct the talent training system for traditional industries. Especially in recent years, due to the impact of global climate change, the frequency and intensity of extreme climate events have increased significantly,

affecting geological bodies in various ways and inducing a series of engineering geological disasters, such as subgrade collapses and house cracking [4–7].

Resource database construction is an important means of realizing educational informatization and a learning society. It relies on network technology, teaching resources, and big data to improve educational modernization and informatization. A Hadoop-based cloud computing platform is built for big data analysis and application course resource management, improves resource utilization and sharing, and provides better services for teachers, students, and employees [8]. The number of web-based continuing education courses has increased significantly, but educators know little about the factors affecting the use of resources in online courses or the relationship between resource use and educational outcomes. The rapid development of online education, knowledge sharing, big data, and artificial intelligence technology has brought innovation to education [9]. Gueudet and Poisard discussed the design and use of curriculum resources brought by the use of the literature method in teaching methods, and they proposed this theoretical method and the related "reflective investigation" method [10]. By referring to the latest studies on digital curriculum resources (DCRs), this paper discusses the design and use (by teachers and students) of digital curricula and electronic textbooks in mathematics education [11, 12]. With the rapid development of network technology and the sharing and promotion of intelligent vocational education platforms, the role of the resource database in "Internet + education" is particularly important [13]. An online course system platform has the function of promoting active, collaborative, interactive, research-based, and autonomous learning and is an important way to form an open, efficient, and convenient new teaching mode [14, 15]. Taking the creation of high-quality resources, network teaching, improved teaching effects, enriched teaching means, and improved teaching effects as the core realizes three-dimensional teaching involving the rapid upload, retrieval, and archiving of resources. A perfect online course system is the basis and guarantee for all-round information-based teaching and for improving the level of school education information [16, 17].

The fuzzy comprehensive evaluation method is a comprehensive bid evaluation method based on fuzzy mathematics. It is characterized by strong systematicness and clear and reliable results. It can better solve fuzzy and difficult-to-quantify problems. It is suitable for quantitative analysis and qualitative research [18]. Chen et al. combined a fuzzy analytic hierarchy process with a fuzzy comprehensive evaluation method and proposed a new teaching performance evaluation framework. The application of this framework can make the evaluation results more scientific, accurate, and objective. It is hoped that this work can help university managers improve the level of educational quality [19]. Liu and Chen constructed a fuzzy matrix through membership determination on the basis of five first-level objectives and second-level corresponding objectives. The matrix can objectively and fairly evaluate students' learning effect, stimulate students' enthusiasm for autonomous learning, and help them build their confidence in employment challenges with an optimistic and positive attitude [20]. The fuzzy comprehensive evaluation method is a method based on fuzzy mathematics. By constructing the weight, the index can be evaluated objectively and scientifically. Using a fuzzy comprehensive evaluation method can help teachers improve their teaching quality in a timely manner, change the time control of teaching quality into process control, and change static management into dynamic management [21–23].

The study of engineering geology courses emphasizes the combination of theory and practice and highlights the comprehensive cultivation of curricular theory, curricular practice, and comprehensive skills. It is necessary to establish a set of effective methods to evaluate the achievement of training objectives to track, test, and improve the quality of curricular learning. Taking the civil engineering students of Xuchang University as the evaluation object, based on the principle of the fuzzy analytic hierarchy process, this paper constructs an evaluation index system for the engineering geology curricular goal achievement degree, carries out a reasonable weight distribution, inspection, and optimization, formulates the evaluation grade evaluation standard, and realizes the goal of curricular achievement degree evaluation considering a variety of evaluation data. It can provide a reference for graduation achievement evaluation for engineering education certification.

2. Methodology

The objects can be evaluated by the fuzzy comprehensive evaluation method based on multiple factors according to the fuzzy relationship synthesis. There is a unique evaluation value for the evaluated object in the fuzzy comprehensive evaluation method, which is not affected by the set of evaluation objects. Each index can be evaluated by the fuzzy comprehensive evaluation method. The weight of each influence index can quantitatively calculate according to the historical statistical data, and the object can be evaluated quantitatively [24]. A fuzzy comprehensive evaluation method was used in this paper to calculate and evaluate the achievement degree of engineering geology courses based on the course resource database. The calculation and evaluation steps of this method are as shown in Figure 1.

2.1. Determining the Evaluation Factor Set and Index System. The factor set is a set composed of various factors affecting the evaluation object as elements, set as $U = \{u_1, u_2, \ldots, u_n\}$. U is the N factor describing the evaluation object, namely, the evaluation index [25]. Based on the role of engineering geology in the curricular system and in combination with the graduation requirements, the curricular objectives are divided into three parts to support the first-class indicators of the graduation requirements, as shown in Table 1 and Figure 2.

2.2. Determining the Comment Set of Comprehensive Evaluation. The comment set is a set of possible results for various indicators, set as $V = \{v_1, v_2, v_3, \ldots, v_n\}$. V refers to N kinds of decisions describing the state of each factor, and N refers to the number of comments, which is generally

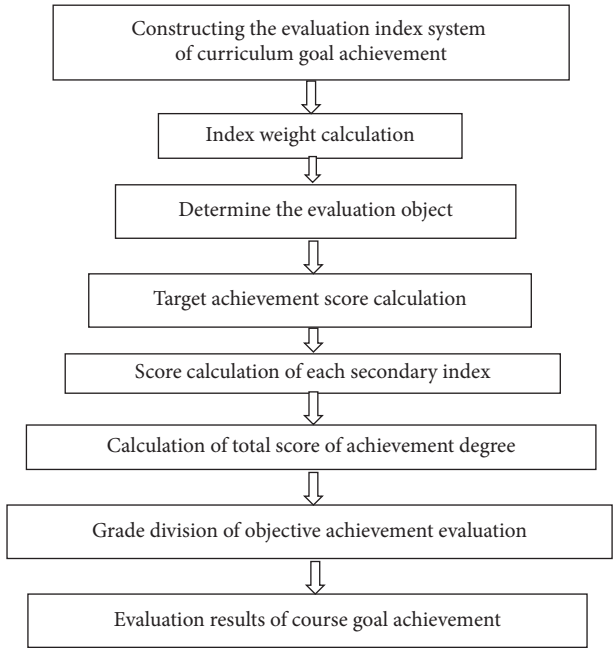

Figure 1: Course goal achievement evaluation process.

Table 1: Correspondence between the course objectives and graduation requirements.

Graduation requirement index	Course objective
Knowledge objectives	To master the basic concepts, principles, and advanced methods of engineering geology to be able to solve complex engineering geological problems in the life cycle of civil engineering
Capability objectives	To improve the ability of engineering practice and innovation, the ability to deal with geological disasters in engineering, and the ability to engage in independent learning and teamwork
Quality objectives	To have good scientific and cultural literacy, ideological, and political literacy and a sense of social responsibility and professional ethics, to have engineer thinking and a craftsman's spirit, and to have the correct outlook on life, values, and world view

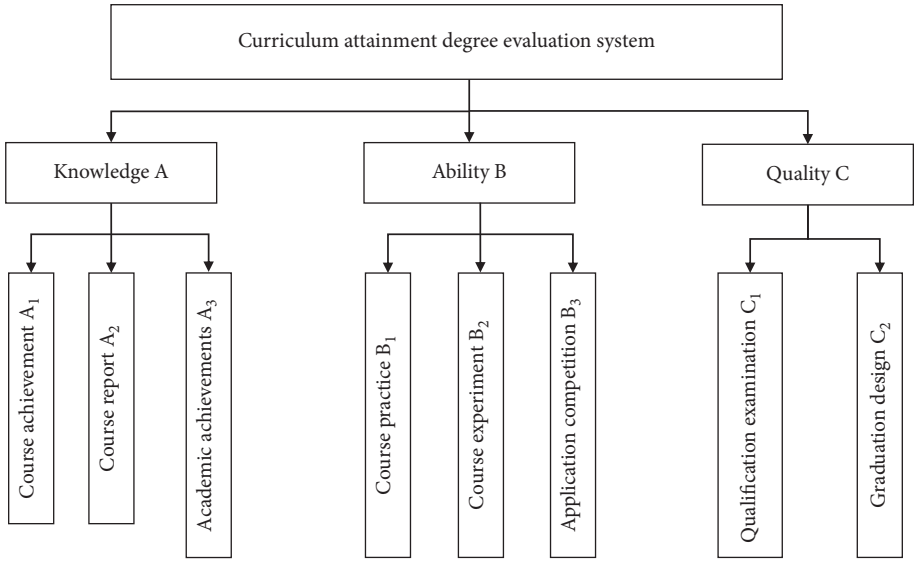

Figure 2: Curricular goal achievement index system.

divided into 3–5 levels [26]. Based on the actual situation, this paper determines five curricular achievement levels, that is, the comment set V = {very low, low, medium, high, very high} [27, 28].

2.3. Determining the Factor Weight Vector. In evaluation, the weight is a measure of the relative importance of factors. If the weight cannot be determined objectively, the evaluation results may be seriously distorted and even cause judges to make the wrong judgment. In this paper, the weight of the evaluation factors is quantitatively determined by the entropy method through statistical empirical data. The weight set of each factor or the weight vector is represented by $A = (a_1, a_2, a_3, \ldots, a_i)$, where $a_i > 0$ and $\sum a_i = 1$, which reflects a trade-off of various factors.

In multifactor evaluation, different weights are taken because different factors have different practical roles in evaluation. In this paper, the weight of each factor is calculated by statistical data on a course resource (Table 2) and the entropy method model. In information theory, entropy is a measure of uncertainty. The greater the amount of information is, the smaller the uncertainty and the smaller the entropy. The smaller the amount of information is, the greater the uncertainty and the greater the entropy [29]. Based on the characteristics of entropy, an event's randomness and disorder degree can be judged by calculating the entropy, and the dispersion degree of an index can also be judged by the entropy. The greater the dispersion degree of the index is, the greater the impact of the index on comprehensive evaluation [30, 31]. The specific calculation is as follows.

Calculate the proportion of this index under the influence of factor j.

$$p_{ij} = \frac{x_{ij}}{\sum_{i=1}^{n} x_{ij}}, \quad (i = 1, 2 \ldots n;\ j = 1, 2 \ldots m). \tag{1}$$

Calculate the entropy of factor j.

$$e_j = -k \sum_{i=1}^{n} p_{ij} \ln\left(p_{ij}\right), \quad k > 0,$$
$$k = \frac{1}{\ln(n)}, \quad e_j \geq 0. \tag{2}$$

Calculate the difference coefficient of index j. For the j-th index, the greater the difference of index X_{ij} is, the greater the impact on safe mining and the smaller the entropy.

Define the difference factor:

$$g_j = \frac{1 - e_j}{m - E_e},$$
$$E_e = \sum_{j=1}^{m} e_j, \quad 0 \leq g_j \leq 1, \tag{3}$$
$$\sum_{j=1}^{m} g_j = 1.$$

The weight results are obtained as follows:

Table 2: Weights of the secondary evaluation indexes.

Primary index	Secondary index	Weight
Knowledge	Course achievements	0.33
	Course reports	0.35
	Academic achievements	0.32
Ability	Course practice	0.25
	Course experiments	0.41
	Application competitions	0.34
Quality	Qualification examinations	0.48
	Graduation design	0.52

$$w_j = \frac{g_j}{\sum_{j=1}^{m} g_j} \ (1 \leq j \leq m). \tag{4}$$

2.4. The Single Factor Fuzzy Evaluation Is Carried Out, and the Evaluation Matrix Is Constructed. First, make a single factor evaluation of the single factor U_i ($i = 1, 2, 3, \ldots, n$) in the factor set. From the membership of the factor U_i to the evaluation grade V_j as R_{ij}, we can obtain the single factor evaluation set of the i-th factor U_i, and $R_i = (R_{i1}, R_{i2}, \ldots, R_{in})$. In this process, the determination of membership is very important. This paper uses the questionnaire method combined with the actual learning situation of students to obtain the membership of the determined factors. Finally, a general evaluation matrix R is constructed from the evaluation set of N factors. That is, each evaluated object determines the fuzzy relationship matrix R from U to V.

2.5. Fuzzy Synthesis and Judgment. A fuzzy subset B of evaluation set V is introduced, which is called the evaluation set, that is, $B = (b_1, b_2, b_3, \ldots, b_n)$. Let $B = A^* R$ (* is the operator symbol), which is the fuzzy comprehensive evaluation model. To make the evaluation results clear, the information concentration principle is adopted and scored based on the percentage system. The information concentration formula is

$$S = B * C^T. \tag{5}$$

Among them, C^T is the grade of the corresponding factors. Based on the final score S, the achievement degree of the course can be judged by comparing and dividing the interval (Table 3).

3. Case Study

Taking the civil engineering students (64 in total) enrolled in the engineering geology course at Xuchang University as an example, the required data are obtained from the online course system. Civil engineering is the earliest undergraduate major in the School of Civil Engineering of Xuchang University which located in Xuchang City, Henan Province, in China. The students trained by civil engineering have solid theoretical foundation and professional knowledge, good scientific and cultural literacy, sense of social responsibility and professional ethics, and practical ability and innovation

Table 3: The assessment grade of achievement.

Achievement rating	Very low	Low	Medium	High	Very high
Achievement score	<40	40–59	60–69	70–89	90–100

ability to independently solve complex engineering problems in the field of civil engineering, as well as international vision and team cooperation ability.

The evaluation indicators are divided into two levels. The first-level indicators mainly include knowledge, ability, and quality. The knowledge indicators are mainly controlled by the second-level indicators: course achievements, course reports, and academic achievements. The relationship matrix is shown in the following equation:

$$R_A = \begin{pmatrix} 0 & 0.12 & 0.27 & 0.29 & 0.32 \\ 0 & 0 & 0 & 0.29 & 0.71 \\ 0.05 & 0.13 & 0.45 & 0.33 & 0.04 \end{pmatrix}. \quad (6)$$

Course practice, course experiments, and application competitions are the main factors affecting the ability index. The constructed relationship matrix is shown in the following equation:

$$R_B = \begin{pmatrix} 0 & 0 & 0 & 0.27 & 0.73 \\ 0 & 0.14 & 0.33 & 0.42 & 0.11 \\ 0 & 0.21 & 0.25 & 0.33 & 0.21 \end{pmatrix}. \quad (7)$$

The main factors affecting the quality indicators are quality examinations and graduation design, and the constructed relationship matrix is shown in the following equation:

$$R_C = \begin{pmatrix} 0.002 & 0.212 & 0.415 & 0.274 & 0.097 \\ 0.001 & 0.245 & 0.365 & 0.285 & 0.104 \end{pmatrix}. \quad (8)$$

Based on the information entropy model, the weights of the secondary indicators are calculated, and the weight values of the secondary indicators are obtained, as shown in Table 2. The weight vectors of each secondary index are (w_{A1}, w_{A2}, w_{A3}) = (0.33, 0.35, 0.32), (w_{B1}, w_{B2}, w_{B3}) = (0.25, 0.41, 0.34), and (w_{C1}, w_{C2}) = (0.48, 0.52). Through the synthesis operation of the membership matrix, the comprehensive evaluation matrix of the primary indexes is obtained, as shown in the following equation:

$$R = \begin{pmatrix} 0.016 & 0.0812 & 0.2331 & 0.3028 & 0.3669 \\ 0 & 0.1288 & 0.2203 & 0.3519 & 0.299 \\ 0.00148 & 0.22916 & 0.389 & 0.27972 & 0.10064 \end{pmatrix}. \quad (9)$$

The setting of the evaluation target value is related to the overall teaching level of the school, reflecting the strictness of the requirements for students. Considering that the school is still dominated by the school year system, the setting of the evaluation target value is based on whether students pass the assessment of corresponding links. The weight vector of the first-level evaluation index is (0.34, 0.33, 0.33). Through the evaluation set $B = (b_1, b_2, b_3, b_4, b_5)$, where $B = A^* R$ (* is the operator symbol), obtain B = (0.005928, 0.1457348, 0.280323, 0.3113866, 0.2566272). B is the comprehensive evaluation result matrix of the evaluation achievement degree, which is the membership degree of different quality levels. b_1, b_2, b_3, b_4, and b_5 represent low, low, medium, high, and high membership, respectively. A is the weight matrix of the evaluation factor, and R is the evaluation matrix. Based on the principle of information concentration, $s = 74.25$ is obtained from equation (5). According to Table 3, the degree of achievement of the engineering geology course is high.

4. Conclusion

Based on the principle of the fuzzy analytic hierarchy process based on entropy, this paper constructs an evaluation index system for the engineering geology curricular goal achievement degree. Relying on the engineering geology curriculum resource database of Xuchang University, this paper evaluates the curricular goal achievement degree and obtains good application results. This method is applicable not only to the evaluation of the degree of achievement of curricular objectives but also to the evaluation of the achievement of graduation requirements for engineering education certification, and it can also help us find different courses and teaching weak links supporting the index points, indicate the direction and provide support for teachers to continuously improve their teaching and management methods, and effectively promote a continuous improvement in teachers' teaching level and teaching quality. Based on the principle of information concentration, $s = 74.25$, the degree of achievement of the engineering geology course is high.

Fuzzy mathematics and information entropy theory essentially solve the problems of unsystematic index selection and the difficult combination of qualitative and quantitative evaluation in the process of curricular goal achievement evaluation. The example application shows that the curricular goal achievement evaluation system constructed in this paper can be used as an effective reference method for university decision-making. Through the evaluation process of the degree of achievement of the curricular objectives in this paper, we see that to achieve the curricular objectives, we should pay attention to the details of the overall curricular teaching quality control and curricular organization to a great extent. We should not only consolidate the accumulation of basic theoretical knowledge and skills but also strengthen the cultivation of practice, training, and competition ability and encourage innovation.

Data Availability

The datasets generated during the current study are available from the corresponding author on reasonable request.

Conflicts of Interest

The authors declare no conflicts of interest in the submission of this manuscript, and the manuscript is approved by all the authors for publication.

Acknowledgments

This work was financially supported by the Pedagogical Research and Practice Project of Xuchang University under Grant No. XCU2021-YB-047 and No. XCU2021-ZB-003.

References

[1] B. Yuan, Z. Li, Z. Zhao, H. Ni, Z. Su, and Z. Li, "Experimental study of displacement field of layered soils surrounding laterally loaded pile based on transparent soil," *Journal of Soils and Sediments*, vol. 21, no. 9, pp. 3072–3083, 2021.

[2] J. He, Y. Xue, J. Xu, D. Zhang, and S. Zhang, "Whole-process monitoring of sinkhole collapse based on distributed optical fiber strain-vibration joint system and its case study in railway subgrade," *Optical Fiber Technology*, vol. 60, Article ID 102380, 2020.

[3] R. M. Harden, "Developments in outcome-based education," *Medical Teacher*, vol. 24, no. 2, pp. 117–120, 2002.

[4] T. C. Su, "Assessment of cracking widths in a concrete wall based on tir radiances of cracking," *Sensors*, vol. 20, no. 17, 2020.

[5] C. A. Pederson, P. M. Santi, and D. R. Pyles, "Relating the compensational stacking of debris-flow fans to characteristics of their underlying stratigraphy: implications for geologic hazard assessment and mitigation," *Geomorphology*, vol. 248, pp. 47–56, 2015.

[6] B. Y. Yuan, Z. H. Li, Z. L. Su, Q. Z. Luo, M. J. Chen, and Z. Q. Zhao, "Sensitivity of multistage fill slope based on finite element model," *Advances in Civil Engineering*, vol. 2021, Article ID 6622936, 13 pages, 2021.

[7] B. Y. Yuan, Z. H. Li, Y. Chen et al., "Mechanical and microstructural properties of recycling granite residual soil reinforced with glass fiber and liquid-modified polyvinyl alcohol polymer – sciencedirect," *Chemosphere*, vol. 268, Article ID 131652, 2021.

[8] Y. Zhao and H. Liu, "Cloud curriculum resource management platform based on Hadoop," *Measurement and Control*, vol. 53, no. 9-10, pp. 1782–1790, 2020.

[9] C. R. Woods and K. J. Kemper, "Curriculum resource use and relationships with educational outcomes in an online curriculum," *Academic Medicine*, vol. 84, no. 9, pp. 1250–1258, 2009.

[10] G. Gueudet and C. Poisard, "Design and use of curriculum resources for teachers and teacher educators: example of the Chinese abacus at primary school," *International Journal of Educational Research*, vol. 93, pp. 68–78, 2019.

[11] B. Pepin, J. Choppin, K. Ruthven, and N. Sinclair, "Digital curriculum resources in mathematics education: foundations for change," *ZDM*, vol. 49, no. 5, pp. 645–661, 2017.

[12] X. Y. Zhang, A. M. Holbrook, L. Nguyen et al., "Evaluation of online clinical pharmacology curriculum resources for medical students," *British Journal of Clinical Pharmacology*, vol. 85, no. 11, pp. 2599–2604, 2019.

[13] A. M. Bodzin, Q. Fu, V. Kulo, and T. Peffer, "Examining the effect of enactment of a geospatial curriculum on students' geospatial thinking and reasoning," *Journal of Science Education and Technology*, vol. 23, no. 4, pp. 562–574, 2014.

[14] B. Y. Chen, D. E. Kern, R. M. Kearns, P. A. Thomas, M. T. Hughes, and S. Tackett, "From modules to MOOCs," *Academic Medicine*, vol. 94, no. 5, pp. 678–685, 2019.

[15] S. Rezat, L. Fan, and B. Pepin, "Mathematics textbooks and curriculum resources as instruments for change," *ZDM - Mathematics Education*, vol. 53, no. 6, pp. 1189–1206, 2021.

[16] Z. Karimi, T. Ashktorab, E. Mohammadi, H. Abedi, and K. Zarea, "Resources of learning through hidden curriculum: Iranian nursing students' perspective," *Journal of Education and Health Promotion*, vol. 4, p. 57, 2015.

[17] M. Misfeldt, A. L. Tamborg, J. Dreyøe, and B. B. Allsopp, "Tools, rules and teachers: the relationship between curriculum standards and resource systems when teaching mathematics," *International Journal of Educational Research*, vol. 94, pp. 122–133, 2019.

[18] S. D. Xian, "A new fuzzy comprehensive evaluation model based on the support vector machine," *Fuzzy Information And Engineering*, vol. 2, no. 1, pp. 75–86, 2010.

[19] J. F. Chen, H.-N. Hsieh, and Q. H. Do, "Evaluating teaching performance based on fuzzy AHP and comprehensive evaluation approach," *Applied Soft Computing*, vol. 28, pp. 100–108, 2015.

[20] S. Liu, P. Chen, and P. Chen, "Research on fuzzy comprehensive evaluation in practice teaching assessment of computer majors," *International Journal of Modern Education and Computer Science*, vol. 7, no. 11, pp. 12–19, 2015.

[21] Y. Jiang and Y. Wang, "Evaluation of teaching quality of public physical education in colleges based on the fuzzy evaluation theory," *Journal of Computational and Theoretical Nanoscience*, vol. 13, no. 12, pp. 9848–9851, 2016.

[22] S. W. Sun and Y. W. Zhai, "The application of fuzzy comprehensive evaluation model in the teaching evaluation system," *Applied Mechanics and Materials*, vol. 303-306, pp. 1452–1455, 2013.

[23] F. Jiang, Q. Zheng, and W. Shi, "The applied research of fuzzy comprehensive evaluation on talent training mode of safety engineering," *Procedia Engineering*, vol. 43, pp. 425–430, 2012.

[24] S. Feng and L. D. Xu, "Decision support for fuzzy comprehensive evaluation of urban development," *Fuzzy Sets and Systems*, vol. 105, no. 1, pp. 1–12, 1999.

[25] Y.-W. Du, S.-S. Wang, and Y.-M. Wang, "Group fuzzy comprehensive evaluation method under ignorance," *Expert Systems with Applications*, vol. 126, pp. 92–111, 2019.

[26] L.-j. Li and L.-t. Shen, "An improved multilevel fuzzy comprehensive evaluation algorithm for security performance," *The Journal of china Universities of Posts and Telecommunications*, vol. 13, no. 4, pp. 48–53, 2006.

[27] H. Zhang, X. He, and H. Mitri, "Fuzzy comprehensive evaluation of virtual reality mine safety training system," *Safety Science*, vol. 120, pp. 341–351, 2019.

[28] K.-L. Wen, "A Matlab toolbox for grey clustering and fuzzy comprehensive evaluation," *Advances in Engineering Software*, vol. 39, no. 2, pp. 137–145, 2008.

[29] Q. S. Zhang and S. Y. Jiang, "A note on information entropy measures for vague sets and its applications," *Information Sciences*, vol. 178, no. 21, pp. 4184–4191, 2008.

[30] D. L. Mon, C.-H. Cheng, and J. C. Lin, "Evaluating weapon system using fuzzy analytic hierarchy process based on entropy weight," *Fuzzy Sets and Systems*, vol. 62, no. 2, pp. 127–134, 1994.

[31] M. Song, Q. Zhu, J. Peng, and E. D. R. G. Santibanez, "Improving the evaluation of cross efficiencies: a method based on Shannon entropy weight," *Computers & Industrial Engineering*, vol. 112, pp. 99–106, 2017.